AFRL-SN-WP-TR-2001-1060

MICROELECTROMECHANICAL SYSTEMS (MEMS) ELECTROSTATIC SWITCHING TECHNOLOGY FOR MICROWAVE SYSTEMS

Richard E. Strawser

AFRL/SNDI, Building 620
2241 Avionics Circle, Ste 20
Wright-Patterson Air Force Base, OH 45433-7322

DECEMBER 2000

FINAL REPORT FOR PERIOD 19 SEPTEMBER 1995 – 10 DECEMBER 2000

SENSORS DIRECTORATE
AIR FORCE RESEARCH LABORATORY
AIR FORCE MATERIEL COMMAND
WRIGHT-PATTERSON AIR FORCE BASE, OH 45433-7318

NOTICE

USING GOVERNMENT DRAWINGS, SPECIFICATIONS, OR OTHER DATA INCLUDED IN THIS DOCUMENT FOR ANY PURPOSE OTHER THAN GOVERNMENT PROCUREMENT DOES NOT IN ANY WAY OBLIGATE THE US GOVERNMENT. THE FACT THAT THE GOVERNMENT FORMULATED OR SUPPLIED THE DRAWINGS,SPECIFICATIONS,OR OTHER DATA DOES NOT LICENSE THE HOLDER OR ANY OTHER PERSON OR CORPORATION; OR CONVEY ANY RIGHTS OR PERMISSION TO MANUFACTURE, USE, OR SELL ANY PATENTED INVENTION THAT MAY RELATE TO THEM

THIS REPORT IS RELEASABLE TO THE NATIONAL TECHNICAL INFORMATION SERVICE (NTIS). AT NTIS, IT WILL BE AVAILABLE TO THE GENERAL PUBLIC, INCLUDING FOREIGN NATIONALS.

THIS TECHNICAL REPORT HAS BEEN REVIEWED AND IS APPROVED FOR PUBLICATION.

RICHARD E. STRAWSER, Project Engineer
Multi-Chip Integration Branch
Aerospace Components & Subsystems Division

ALAN J. TEWKSBURY, Chief
Multi-Chip Integration Branch
Aerospace Components & Subsystems Division

ROBERT T. KEMERLEY, Chief
Aerospace Components & Subsystems Division
Sensors Directorate

Do not return copies of this report unless contractual obligations or notice on a specific document requires its return.

REPORT DOCUMENTATION PAGE

Form Approved
OMB No. 074-0188

1. AGENCY USE ONLY (Leave blank)	2. REPORT DATE	3. REPORT TYPE AND DATES COVERED
	December 2000	Final, 09/19/1995 – 12/10/2000

4. TITLE AND SUBTITLE
Microelectromechanical Systems (MEMS) Electrostatic Switching Technology for Microwave Systems

5. FUNDING NUMBERS
PE: 62204F

6. AUTHOR(S)
Richard E. Strawser

7. PERFORMING ORGANIZATION NAME(S) AND ADDRESS(ES)
AFRL/SNDI, Building 620
2241 Avionics Circle, Ste 20
Wright-Patterson Air Force Base, OH 45433-7322

8. PERFORMING ORGANIZATION REPORT NUMBER

9. SPONSORING / MONITORING AGENCY NAME(S) AND ADDRESS(ES)
SENSORS DIRECTORATE
AIR FORCE RESEARCH LABORATORY
AIR FORCE MATERIEL COMMAND
WRIGHT-PATTERSON AIR FORCE BASE, OH 45433-7318
POC: Richard E. Strawser, AFRL/SNDI, 937-255-4557 x3451

10. SPONSORING / MONITORING AGENCY REPORT NUMBER
AFRL-SN-WP-TR-2001-1060

11. SUPPLEMENTARY NOTES
This final report is a Ph.D. dissertation submitted to the University of Cincinnati in partial fulfillment of its requirements for a Doctor of Philosophy degree.

12a. DISTRIBUTION / AVAILABILITY STATEMENT
Approved for public release; distribution unlimited.

12b. DISTRIBUTION CODE

13. ABSTRACT *(Maximum 200 Words)*

The development of microelectromechanical Systems (MEMS) switch technology and integration of this technology into radio frequency (RF) electronics has created numerous applications for both commercial and military systems. The incorporation of RF MEMS switches into microwave systems offers unprecedented reductions in insertion loss (on-resistance) with extremely low switching power levels as compared with active devices such as field effect transistors (FETs) and positive-intrinsic-negative (PIN) diodes. Achievement of these performance improvements creates new opportunities for radar systems. The overall objective of this research was the design, fabrication, and characterization of MEMS switches fabricated on gallium arsenide substrates with possible application into microwave systems.

14. SUBJECT TERMS
RF MEMS switches

15. NUMBER OF PAGES
234

16. PRICE CODE

17. SECURITY CLASSIFICATION OF REPORT	18. SECURITY CLASSIFICATION OF THIS PAGE	19. SECURITY CLASSIFICATION OF ABSTRACT	20. LIMITATION OF ABSTRACT
Unclassified	Unclassified	Unclassified	SAR

NSN 7540-01-280-5500

Standard Form 298 (Rev. 2-89)
Prescribed by ANSI Std. Z39-18
298-102

TABLE OF CONTENTS

LIST OF FIGURES

LIST OF TABLES

LIST OF SYMBOLS

Symbol	Description
a	zero applied force length
A	beam cross sectional area
b	applied force length
C_{down}	down-state capacitance
C_{up}	up-state capacitance
d	initial gap separation
δ	beam deflection
E	Modulus of Elasticity
$E_{a,b}$	Modulus of Elasticity of films a or b
(EI)eff	effective flexural rigidity of multi layer film
ε	dielectric constant
F_e	electrostatic force
F_s	force due to spring constant
$h_{a,b}$	distance from neutral axis for films a or b
I	Moment of Inertia
$I_{a,b}$	Moment of Inertia of films a or b
k	spring constant
L	overall beam length
L_s	switch inductance
M	beam bending moment
μ	permeability
ν	deflection along the beam length
P	electrostatic pressure
q	force per unit length
R_s	switch resistance
R_y	reaction at point y
S	width of center conductor of coplanar waveguide
σ	conductivity
t	beam thickness
$t_{a,b}$	thickness of films a or b
V	applied voltage
V_{piC}	pull-in voltage of cantilever beam
V_{piB}	pull-in voltage of microbridge
w	beam width
Z_s	switch impedance

ACKNOWLEDGEMENTS

I would like to express my sincere appreciation to my advisor Dr. H. Thurman Henderson for his guidance, encouragement, and patience throughout the course of my doctoral program. I would also like to thank the management of the Aerospace Components and Subsystems Concepts Division of the Air Force Research Laboratory, AFRL/SND, Robert Kemerley and Alan Tewksbury. They provided the opportunity to participate in the Long-term, Full-time training program and offered support and encouragement throughout my program of study. I would also like to thank my dissertation committee members for their support, encouragement, and advice.

Special thanks go to the members of the Aerospace Components Division (AFRL/SND) for their assistance and encouragement. In particular I would like to acknowledge the assistance of Chris Bozada, Dave Via, Dr. Jack Ebel, Dr. Kevin Leedy, Dr. Rebecca Cortez, Dr. Matt O'Keefe, and Chris Lesniak. Chris Bozada provided hands-on training of fabrication and the use of numerous systems within the AFRL clean room. Dave Via provided assistance with the switch mask layout, fabrication process, and SEM images. Drs. Ebel, Leedy, Cortez, and O'Keefe provided constant encouragement, advice, and helpful criticisms throughout the research. Chris Lesniak provided the electromagnetic simulations. Finally, I would like to thank my parents for their support and encouragement throughout my graduate studies.

CHAPTER 1

INTRODUCTION

The development of MicroElectroMechanical Systems (MEMS) using silicon microfabrication processes has created numerous applications for sensors and actuators such as pressure sensors, accelerometers, flow controllers, and chemical analysis systems [1, 2]. MEMS technology has also been investigated for high frequency circuits such as tunable filters and switches for routing radio frequency (RF) and microwave frequency signals [3, 4]. The objective of this research was to develop MEMS switches suitable for microwave applications using gallium arsenide (GaAs) material systems and fabrication processes. The material of choice for microwave systems operating from 1 to 300 GHz is GaAs, due to its high electron mobility and drift velocity. Also, the semi-insulating property of GaAs substrates permits monolithic integration of GaAs semiconductors and passive circuits such as transmission lines. The primary application for this research was space-based phased array radar operating at 8 – 12 GHz.

1.1 Phased Array Radar

Array radar systems offer a number of advantages over the single antenna designs including system flexibility, increased range coverage, multiple target capability, and high data rates. Array systems consist of hundreds or thousands of antenna elements on a common back plane, with each element radiating a few watts of power. The radar remains fixed and the beam is electronically scanned. In comparison, conventional radar consists of a single antenna or dish radiating several hundred or thousand watts of power and the dish is mechanically scanned to cover the intended area. Simplified block diagrams of array and conventional radar systems (Fig. 1.1) show the fundamental differences in their architectures.

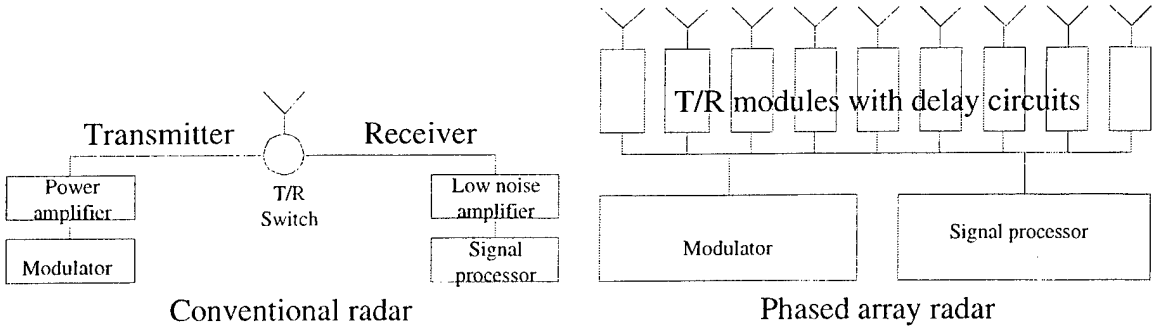

Fig. 1.1. Radar system block diagrams.

The advantages of array radar include reduced power requirements for the individual antenna elements and graceful degradation of the system due to redundancy in the number of Transmit/Receive (T/R) modules. The large number of antenna elements allows for sufficient functionality even if 10% of the elements fail. Also, by combining electronic scanning with subdivided section arrays, multiple targets can be tracked simultaneously [5, 6]. Beam scanning is achieved by changing the time or phase of the signal applied to the individual antenna elements (Fig. 1.2). This beam steering results from the constructive and destructive interference of the electromagnetic waves emitted by each antenna element. By segregating sections of the array, multiple targets can be scanned simultaneously. Conventional radar relies on mechanically positioning the antenna aperture for beam steering and cannot scan multiple targets.

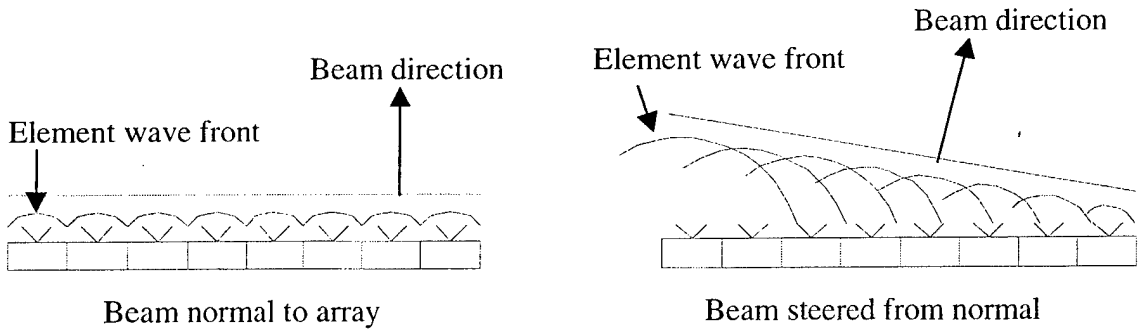

Fig. 1.2. Electronic scanning of a phased array.

Four approaches have been developed to electronically scan the aperture: phase shifting, real-time or time delay, frequency shifting, and electronic feed switching. The least expensive approach, frequency shifting, relies on varying the signal frequency to the antenna elements, but results in a low bandwidth system. The most common approach, phase shifting, relies on varying the phase delay of the signal to each antenna element [5, 7, 8]. Discrete phase delays are switched into the signal path of each antenna element (Fig. 1.3). Typically positive-intrinsic-negative (*PIN*) diodes or field effect transistors (FETs) have been used for the switching elements [9, 10].

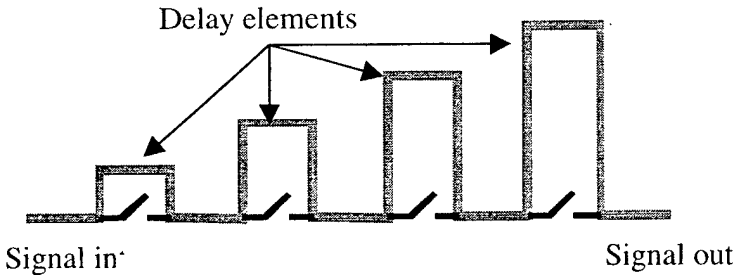

Fig. 1.3. Four-bit phase shift circuit.

1.2 *PIN* Diodes

The structure of *PIN* diodes consists of an intrinsic semiconductor layer sandwiched between heavily doped p-type and n-type regions. At kHz and MHz frequencies, *PIN* diodes function as conventional p-n junctions. However, at microwave frequencies they function as variable attenuators or switches. Under forward bias conditions, the conductivity of the intrinsic region increases, creating an electrically variable resistor. Under reverse bias, the intrinsic region is depleted of charge carriers and functions as an open circuit [11].

Monolithic GaAs *PIN* diodes have been fabricated and tested from 0.1 - 20 GHz [12]. Switches can be configured in a variety of designs including single-pole-double-throw, triple-throw, and quadruple-throw switches. Single-pole-double-throw switches

offer 1.0 dB insertion loss and isolation greater than 40 dB at 10 GHz. Higher performance diodes have been demonstrated, but these devices require unique doping levels and preclude the monolithic integration of the diodes with other active microwave devices. The direct current (DC) power required to bias *PIN* diodes is also large (50 mW). The combination of high insertion loss and large DC power severely impacts the system architecture and make *PIN* diodes less desirable for space-based systems.

1.3 FETs

The operation of FETs relies upon the change of conductivity resulting from an applied transverse electric field. The fabrication of FETs consists of forming a doped region or tub within the undoped semiconductor material. The undoped region serves to isolate the individual FETs. Next, two ohmic contacts, the source and drain, are formed on the doped region. A gate contact placed between the source and drain controls current flow through the device. By applying a voltage to the gate, a depletion region is created under the gate that modulates current flow between the source and drain contacts. At the pinch-off voltage, the depletion region extends to the bottom of the doped region and almost no current will flow between the source and drain. Current will not flow in the bulk undoped regions because the material is semi-insulating.

The application of FETs includes switches, variable capacitors, and amplifiers. A number of FET structures have been developed for microwave applications, but the Insulated Gate FETs (IGFETs) and dual-gate FET, have typically been used in phase shifter circuits. The RF performance of IGFETs is typically an insertion loss of 0.4 dB and isolation of greater than 8 dB at 10 GHz. The isolation decreases over the 8 – 12 GHz region due to the inherently high source-drain capacitance [13]. In addition, FETs require DC power levels of 10 mW for biasing which makes them unattractive as switches. Dual-gate FETs have also been utilized in phase shifter designs, but these designs require carefully matched devices, which complicates the fabrication process. As

part of an amplifier, FETs also provide gain in phase shifter circuits. Operating as amplifiers, gains of up to 3 dB at 10 GHz have been demonstrated. As with FET switches, FET-based amplifier phase shifters also are impacted by the DC power required for device biasing. Amplifier phase shifters based upon FETs are also susceptible to variations of the gain over the frequency range. The phase shifter amplifier supplies signal to the input of the high power amplifier which in turn feeds the antenna aperture. The load impedance seen by the phase shifter varies over the frequency range and is difficult to control without adding additional circuitry that increases the DC power load.

In summary, both *PIN* diodes and FET switches offer high isolation (> 8 dB) and high switching speeds (> 3 nsec), but have a relatively large insertion loss (> 0.4 dB) and DC power consumption (> 10 mW) [11 - 13]. Also, the insertion loss and isolation of FETs and *PIN* diodes vary over the frequency range of interest. Monolithic integration of FETs is easier than *PIN* diodes but the inherent signal gain offered by transistors is difficult to achieve.

1.4 MEMS Switches

MicroElectroMechanical Systems (MEMS) are miniature mechanical devices fabricated using integrated circuit processing. They combine the functionality of electrical and mechanical systems with the fabrication advantages of integrated circuits, including monolithic batch fabrication and precise feature control.

A number of MEMS switch implementations can be used for phase shifters. Metal-to-metal contact switches offer exceptionally low insertion loss (0.1 dB) [3], but the switch lifetime is limited due to reliability problems with the contact metallurgy. Dielectric isolated switches (varactors) offer slightly higher insertion losses (0.2 – 0.5 dB) [3] while overcoming the reliability concern of contact metallurgy.

The actuation methods of MEMS switches include electrostatic, electromagnetic, piezoelectric, and thermal. Electromagnetic and thermal actuation methods offer high

actuation forces, but require high current (> 3.5 mA) and are associated with slower switching response (msec) [14, 15]. Piezoelectric actuation offers low power consumption, but integration of the common piezoelectric materials into the fabrication process is prohibitive [16, 17]. Electrostatic actuation provides ease of integration into the fabrication process, fast switching speed (1 – 10 μsec), and low power consumption (< 0.5 μW) [3]. For RF MEMS switches, switching speeds below 10 μsec are achievable with switching energies on the order of nano-joules or less. Electrostatically activated MEMS switches only draw current during the switching cycle and therefore the DC power consumption is very low, typically < 1 μW [3].

Low insertion loss is achieved by the high capacitive coupling of the dielectric-isolated switches in the "on" state. Insertion losses of < 0.5 dB at 10 GHz are readily achievable [3]. Higher signal isolation values result from the low capacitive coupling between the contacts in the "off" state. Isolation values > 15 dB at 10 GHz have been demonstrated [3]. Capacitive coupling results from the dielectric layer thickness and the air gap of the structure, both of which are functions of the fabrication process and can be varied as part of the design trade-off. Also, unlike active semiconductor devices, this coupling is not a function of doping or carrier concentration and switch performance is relatively constant over the frequency range of interest. These issues will be discussed in more detail in later chapters when the switch design equations are formulated.

The primary disadvantage of MEMS switches as compared to FETs or *PIN* diodes is the slower switching speed due to inertia and damping effects on the moving element. The switching speed for array radar is dependent upon the application, range requirements, and the speed of the platform. For many applications, switching speeds on the order of 10 μsec are acceptable. A comparison of FET switches, *PIN* diodes, and a micromachined switch/varactor is shown in Table 1.1. This table clearly shows the performance advantages offered by MEMS technology.

Table 1.1
COMPARISON OF MICROWAVE SWITCHES [12, 13].

Parameter	FET Switch	*PIN* Diode	Micromachined Switch/Varactor (Goals)
Insertion Loss (dB) at 10 GHz	0.4	1.0	< 0.5
Isolation (dB) at 10 GHz	> 8	> 25	> 25
Switching Speed	3 nsec	3 nsec	< 10 μsec
Voltage (V)	10	8.5	10
Power Consumption (mW)	10	50	< 0.1

A number of organizations have developed RF MEMS switches and reported their results in the literature. Research conducted at Hughes Research Labs, Rockwell Science Center, Raytheon/Texas Instruments, and the University of Michigan will be highlighted below, however the discussion presented here is not inclusive of all MEMS efforts.

1.4.1 Hughes Research Laboratory

Microactuators for microwave systems were first reported by Hughes Research Laboratory (HRL) in 1991 [18, 19]. The Hughes effort focused on developing electrostatically driven cantilever beam and rotary switches (Fig. 1.4). The rotary switches provided an insertion loss of < 0.4 dB and > 35 dB isolation at 2 - 45 GHz. The cantilever beam switches demonstrated an insertion loss of < 0.5 dB and > 25 dB isolation over the same frequency range. The disadvantage of the rotary switch was the high actuation voltages (80-200 V) and slow switching speed (msec). The actuation voltage and switching speed of the cantilever designs were not presented.

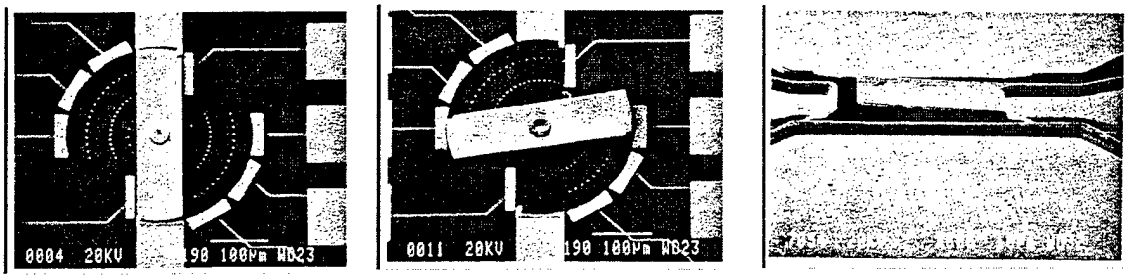

Fig. 1.4. Rotary and cantilever beam switches developed at HRL [18, 19].

1.4.2 Rockwell Science Center

Rockwell Science Center reported an electrostatically activated cantilever switch for 4 GHz telecommunications systems in 1995 [20]. The switch (Fig. 1.5) consisted of a silicon dioxide cantilever beam with gold contacts fabricated on a semi-insulating GaAs substrate. The insertion loss was 0.1 dB and the isolation was 50 dB at 4 GHz. One advantage of this switch design was the separation of the actuation voltage and RF signal. The activation voltage was 28 V with a closure time of 30 μsec.

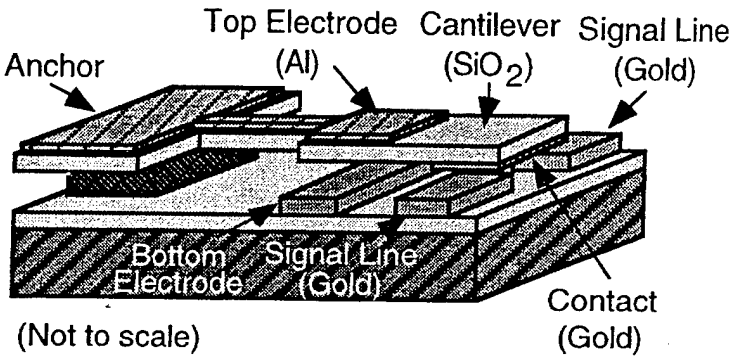

Fig. 1.5. Cantilever beam switch developed at Rockwell Science Center [20].

1.4.3 Raytheon / Texas Instruments

Texas Instruments, now Raytheon reported an electrostatically actuated membrane switch in 1995 [21 - 23]. The switch (Fig. 1.6) was an offshoot of the digital mirror switches and consisted of a thin, 0.3 μm thick aluminum membrane suspended above a high resistivity silicon substrate. The actuation voltage was 10 V, with a switching speed of 8 μsec. The switch provided an insertion loss of 0.3 dB and 15 dB isolation at 10 GHz.

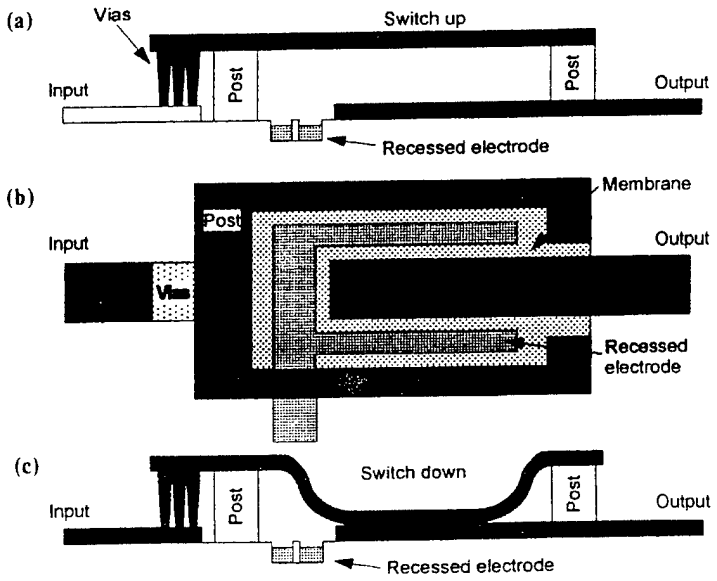

Fig. 1.6. Membrane switch developed at Texas Instruments [21 – 23].

Refinements in the design have resulted in a bow-tie configuration [24, 25] (Fig. 1.7). This switch was also fabricated on a high resistivity silicon substrate (> 5000 Ω-cm) and used an aluminum alloy membrane. The switches were fabricated on top of a 1.0 μm silicon dioxide buffer layer grown on the silicon substrates, increasing the resistivity to greater than 10 kΩ-cm. A plasma enhanced chemical vapor deposition (PECVD) silicon nitride layer was deposited over the lower electrode for dielectric isolation. The membrane consisted of a thin (< 0.5 μm) aluminum alloy that was heavily perforated to minimize air damping and allow for removal of the sacrificial post layer. This switch design employed a shunt configuration in which the "up" position allowed the RF signal to pass and the "down" position shorted the transmission line to ground closing the signal path. The insertion loss was reported to be ~ 0.2 dB at 10 GHz in the "up" position and the isolation was ~ 15 dB at 10 GHz in the "down" position. The switching speed was < 5 μsec with an actuation voltage of 50 V.

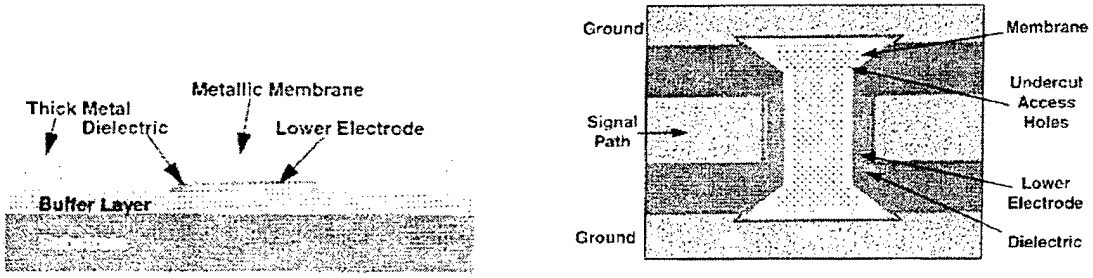

Fig. 1.7. Bow-tie switch developed at Raytheon / Texas Instruments [24, 25].

1.4.4 University of Michigan

The University of Michigan has conducted extensive research into RF MEMS and reported several innovative switch designs and applications [4]. A low voltage switch consisted of a membrane suspended by very flexible spring suspensions (Fig. 1.8) [26]. These designs consisted of a 2 μm thick electroplated gold membrane suspended 4.2 μm above the bottom electrode. The insertion loss was 0.2 dB with 30 dB isolation at 20 GHz. The membranes were highly perforated to achieve low voltage switching and allow removal of the underlying sacrificial post material. The actuation voltage for the serpentine spring design was 14 V while the actuation voltage for the cantilever spring design was 17 V.

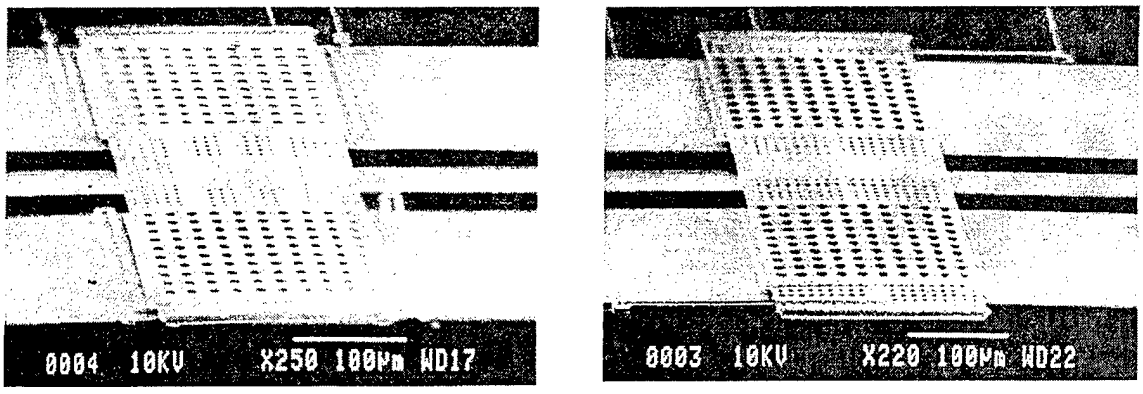

Serpentine springs Cantilever springs

Fig. 1.8. Membrane switches developed at the University of Michigan shown without top electrode present [26].

Low voltage operation of these switches was achieved by the incorporation of very compliant spring suspensions leading to switch instability. To resolve this instability, a top electrode was fabricated over the entire structure to clamp the switch in the "up" position. This switch configuration was also of the shunt variety and required a "holding" voltage for the "on" position and a switching voltage for the "closed" position.

1.5 Research Objectives

Based upon the published efforts, it is clear that RF MEMS switches have numerous potential applications in microwave frequency electronic systems. Presently two major challenges facing the utilization of MEMS switches include the actuation voltage and choice of the most appropriate material system. The power supply voltages available in current T/R modules are less than 15 VDC. Incorporation of 25-35 V MEMS switches would require voltage doubler circuits, which increases overhead costs and complicates the system architecture. The development of MEMS switches operating at less than 15 V would fit directly into the existing architectures. In addition, the choices of material systems, either silicon or gallium arsenide impact the packaging and interconnect approach. For example, a silicon based approach, would require a hybrid construction process when integrated with GaAs electronics, due to the incompatibility of the aluminum and gold metallizations. A GaAs approach would allow for monolithic integration.

This research effort focused on low voltage electrostatic actuated MEMS switches based on GaAs fabrication processes. Electrostatic RF MEMS microswitches in a series configuration were designed, fabricated and tested. Specific issues examined included the interrelationship between switch size and actuation voltage, as well as the electrical

performance based upon size, switch metallization and dielectric material. Stress control of the switch metallization was investigated by using bilayers and trilayers of titanium and gold. Analytical models of the mechanical design were developed and compared with finite element models. Finally, RF designs were developed and compared with both electromagnetic simulations and actual results.

1.6 References

[1]. D.S. Eddy and D.R. Sparks, "Application of MEMS Technology in Automotive Sensors and Actuators", *Proceedings of the IEEE*, Vol. 86, No. 8, (August 1998): 1747-1755.

[2]. C.H. Mastrangelo, M.A. Burns, and D.T. Burke, "Microfabricated Devices for Genetic Diagnostics", *Proceedings of the IEEE*, Vol. 86, No. 8, (August 1998): 1769-1787.

[3]. E.R. Brown, "RF-MEMS Switches for Reconfigurable Integrated Circuits", *IEEE Trans. on Microwave Theory and Techniques*, Vol. 46, No. 11, (November 1998): 1868-1880.

[4]. C.T.C. Nguyen, L.P.B. Katehi, and G.M. Rebeiz, "Micromachined Devices for Wireless Communications", *Proceedings of the IEEE*, Vol. 86, No. 8, (August 1998): 1756-1768.

[5]. D.R. Billetter, "*Multifunction Array Radar*", Artech House Inc., (1989).

[6]. S.A. Hovanessian, "*Radar Detection & Tracking Systems*", Artech House Inc., (1982).

[7]. E. Brookner, "*Radar Technology*", Artech House Inc., (1977).

[8]. E. Brookner, "*Practical Phased-Array Antenna Systems*", Artech House Inc., (1991).

[9]. D.M. Pozar, "*Microwave Engineering*", Addison-Wesley Publishing Company, (1993).

[10]. I. Bahl and P. Bhartia, "*Microwave Solid State Circuit Design*", John Wiley & Sons, (1988).

[11]. K. Chang, "*Handbook of Microwave and Optical Components: Volume 2 Microwave Solid-State Components*", John Wiley & Sons, (1990).

[12]. J. Lee, D. Zych, E. Reese, and D. Drury, "Monolithic 2-18 GHz Low Loss, On-Chip Biased PIN Diode Switches", *IEEE Trans. on Microwave Theory and Techniques*, Vol. 43, (February 1995): 250-255.

[13]. M. Shokrani and V.J. Kapoor, "InGaAs Microwave Switch Transistors for Phase Shifter Circuits", *IEEE Trans. On Microwave Theory and Techniques*, Vol. 42, (May 1994): 772-778.

[14]. W.P. Taylor, O. Brand, and M.G. Allen, "Fully Integrated Magnetically Actuated Micromachined Relays", *Journal of Microelectromechanical Systems*, Vol. 7, No. 2, (June 1998): 181-191.

[15]. J.H. Comtois and V.M. Bright, "Surface Micromachined Polysilicon Thermal Actuator Arrays and Applications", *IEEE Solid-State Sensor and Actuator Workshop*, (June 1996): 174-177.

[16]. S.S. Lee, R.P. Tied, and R.M. White, "Piezoelectric Cantilever Microphone and Microspeaker", *IEEE Solid-State Sensor and Actuator Workshop*, (June 1994): 33-37.

[17]. P. Luginbuhl, G.A. Racine, P. Lerch, B. Romanowicz, K.B. Brooks, N.F. de Rooij, P. Renaud, and N. Setter, "Piezoelectric Cantilever Beams Actuated by PZT Sol-Gel Thin Film", *IEEE Transducers 95*, (June 1995): 413-416.

[18]. L.E. Larson, R.H. Hackett, and R.F. Lohr, "Microactuators for GaAs-Based Microwave Integrated Circuits", *IEEE Transducers 91*, (June 1991): 743-746.

[19]. L.E. Larson, R.H. Hackett, M.A. Melendes, and R.F. Lohr, "Micromachined Microwave Actuator (MIMAC) Technology - A New Tuning Approach for Microwave Integrated Circuits", *IEEE 1991 Microwave and Millimeter-Wave Monolithic Circuits Symposium*, (1991): 27-30.

[20]. J.J. Yao and M.F. Chang, "A Surface Micromachined Miniature Switch for Telecommunications Applications with Signal Frequencies from DC up to 4 GHz", *IEEE Transducers 95*, (June 1995): 384-387.

[21]. C. Goldsmith, T.H. Lin, B. Powers, W.R. Wu and B. Norvell, "Micromechanical Membrane Switches for Microwave Applications", *1995 IEEE MTT-S International Microwave Symposium Digest,* (May 1995): 91-94.

[22]. C. Goldsmith, J. Randall, S. Eschelman, T. Lin, D. Denniston, S. Chen, and B. Norvell, "Characteristics of Micromachined Switches at Microwave Frequencies", *1995 IEEE MTT-S International Microwave Symposium Digest*, (May 1995): 1141-44.

[23]. J.N. Randall, C. Goldsmith, D. Denniston, and T.H. Lin, "Fabrication of Micromechanical Switches for Routing Radio Frequency Signals", *Journal of Vacuum Science Technology*, B 14(6), (Nov/Dec 1996): 3692-3696.

[24]. C. Goldsmith, Z.Yao, S. Eshelman, and D. Denniston, "Performance of Low-Loss RF MEMS Capacitive Switches", *IEEE Microwave and Guided Wave Letters*, Vol. 8, No. 8 (Aug 1998): 269-271.

[25]. Z.J. Yao, S. Chen, S. Eshelman, D. Denniston, and C. Goldsmith, "Micromachined Low-Loss Microwave Switches", *IEEE Journal of Microelectromechanical Systems*, Vol. 8, No. 2 (June 1999): 129-134.

[26]. S. Pacheco, C.T. Nguyen, and L.P.B. Katehi, "Micromechanical Electrostatic K-Band Switches", *1998 IEEE MTT-S International Microwave Symposium Digest*, (June 1998): 1569-1572.

CHAPTER 2

MECHANICAL DESIGN

The mechanical design of MEMS switches was based upon the development of both analytical and two-dimensional Finite Element Models (FEM). Two types of switch structures were investigated, a cantilever beam and a built-in beam (spring-bridge). A systematic study of actuation voltage dependency on microswitch design was made by varying beam lengths while maintaining constant beam width and thickness. The impact of beam length on actuation voltage was compared for the analytical and FEM models.

The cantilever beam design (Fig. 2.1) consisted of a metal switch fabricated on a GaAs substrate. Dielectric material provided DC isolation between the metal contacts when the switch was in the closed position. The fabrication process was based on conventional GaAs airbridge fabrication processes, which use photoresist as the sacrificial material. One unique feature of this design is the inclined rise of the beam, resulting in a spring board cantilever where the actuation voltage is applied over a finite length of the freestanding beam. The deflection equation for the spring cantilever was developed and compared with the typical clamped cantilever model discussed in most Mechanics of Materials texts (see for example, Ref. 1). Details behind the electrical design and fabrication processes are included in Chapters 3 and 4, respectively.

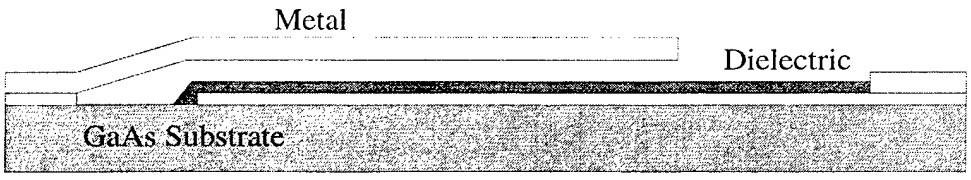

Fig. 2.1. Design of MEMS spring board cantilever beam switch.

2.1 Clamped Cantilever Beam Model

The clamped cantilever beam model (Fig. 2.2) has been analyzed in numerous texts and is the basis for most MEMS cantilever beam designs. In this model, q is the actuation force applied over the length b and a is the zero applied force length. Vertical deflection at the tip is denoted by δ. This model has been analyzed by Timoshenko and Gere [1] and the deflection equation is given by

$$\delta = \left(\frac{q}{24EI}\right)\left(3L^4 - 4a^3L + a^4\right), \tag{2.1}$$

where E is the modulus of elasticity and the moment of inertia is given by

$$I = \frac{wt^3}{12}. \tag{2.2}$$

The beam width is denoted by w and the thickness by t.

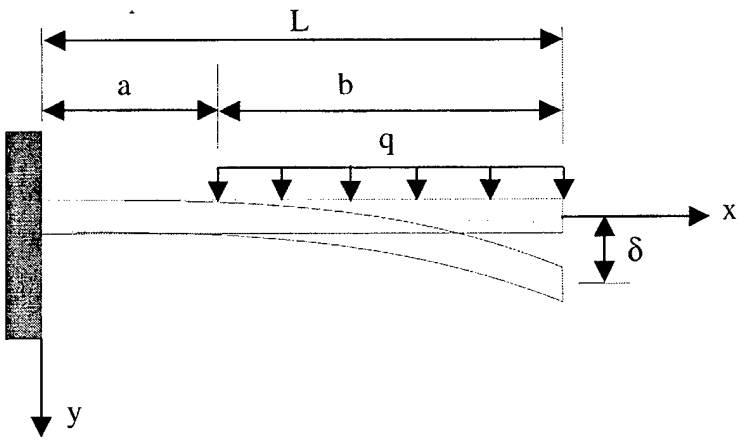

Fig. 2.2. Clamped cantilever beam model.

For a first order approximation, the force per unit length q applied to the cantilever can be represented as an electrostatic pressure P by defining $q = Pw$, with

$$P = \frac{\varepsilon}{2}\left(\frac{V}{d}\right)^2, \tag{2.3}$$

where the actuation voltage is V, ε is the dielectric constant, and d is the separation between the plates. Combining Eqs. (2.2) and (2.3) with (2.1) and rearranging yields the actuation voltage in terms of the physical parameters.

$$V = \sqrt{\frac{48EId^2\delta}{\varepsilon w(3L^4 - 4a^3L + a^4)}} \quad . \tag{2.4}$$

Plotting the actuation voltage versus beam length (Fig. 2.3) shows low actuation voltages can be obtained for beam lengths in excess of 400 μm. Values used in this calculation are included in Table 2.1.

Table 2.1
DESIGN PARAMETERS

Parameter	Value
Young's modulus (E) of gold [2, 3]	78 GPa
Separation distance (d)	5 μm
Tip deflection distance (δ)	5 μm
Beam width (w)	50 μm
Beam thickness (t)	1.5 μm
Pivot arm length (a)	10 μm
Dielectric constant of air (ε)	8.854×10^{-12} F/m

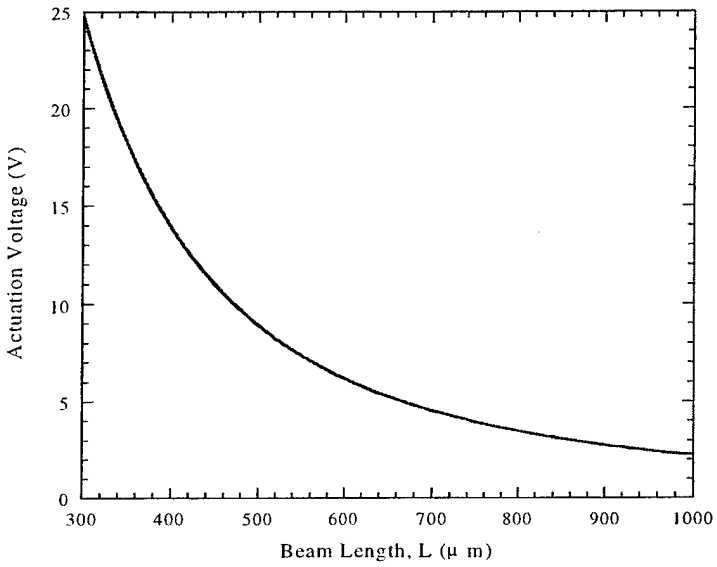

Fig. 2.3. Actuation voltage versus beam length, L (μm).

2.2 Cantilever Spring Model

The cantilever spring model (Fig. 2.4) was developed using the method of successive integration, which relates deflection in term of the bending moment [4]. The procedure consists of determining the bending moment and reactions using free-body diagrams and equations of static equilibrium. The bending moment of the beam M is

$$EI\upsilon'' = -M, \tag{2.5}$$

where υ is the deflection along the length of the beam. Integrating this equation twice and adding the appropriate constants results in the deflection equation for the beam.

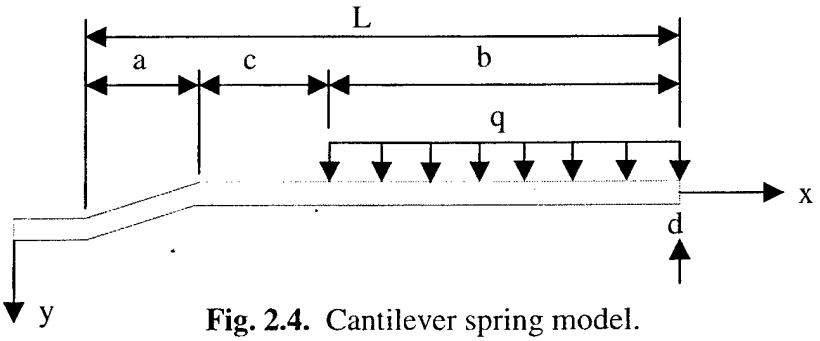

Fig. 2.4. Cantilever spring model.

Using the free-body diagram (Fig. 2.5), the reaction force at point A, R_A, was determined by inspection of the external forces, resulting in $R_A = qb$. The model was then subdivided into three sections and the deflection equation for each section was derived.

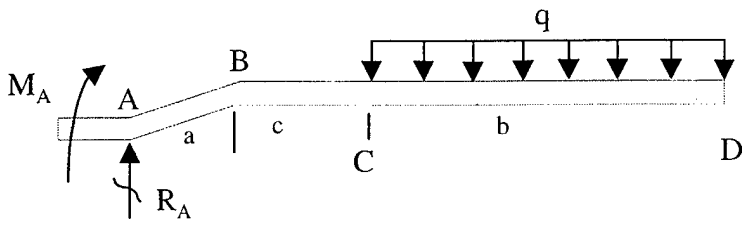

Fig. 2.5. Free-body diagram.

The deflection equation for the inclined segment A-B $(0 < x < a)$ was derived from Fig. 2.6, with the bending moment M_1 given by

$$M_1 = M_A + \frac{R_A x}{\cos\theta} \,. \tag{2.6}$$

The deflection equation is determined by substituting M_1 into Eq. (2.5) and performing two successive integrations.

$$EI\upsilon'' = -M_A - \frac{qbx}{\cos\theta} \tag{2.7}$$

$$EI\upsilon' = -M_A x - \frac{qbx^2}{2\cos\theta} + C_1 \tag{2.8}$$

$$EI\upsilon = -\frac{M_A x^2}{2} - \frac{qbx^3}{6\cos\theta} + C_1 x + C_2 \,. \tag{2.9}$$

From the boundary conditions $EI\upsilon'_{(x=0)} = 0$ and $EI\upsilon_{(x=0)} = 0$, the constants of integration are determined to be $C_1 = 0$ and $C_2 = 0$. The end point conditions at $x = a$ then gives

$$EI\upsilon'_{(x=a)} = -M_A a - \frac{qa^2 b}{2\cos\theta}. \tag{2.10}$$

$$EI\upsilon_{(x=a)} = -\frac{M_A a^2}{2} - \frac{qa^3 b}{6\cos\theta}. \tag{2.11}$$

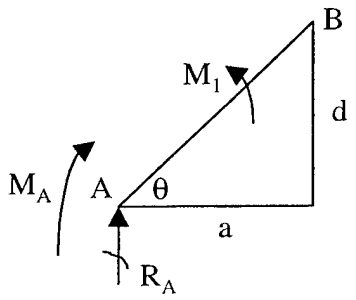

Fig. 2.6. Beam segment A-B *(0 < x < a)*.

The derivation for the segment A-C *(0 < x < a+c)* follows the same procedure and was derived using Fig. 2.7. The bending moment M_2 is given by

$$M_2 = M_A + R_A x \,. \tag{2.12}$$

. The deflection equation is then determined by

$$EI\upsilon'' = -M_A - qbx \tag{2.13}$$

$$EI\upsilon' = -M_A x - \frac{qbx^2}{2} + C_3 \tag{2.14}$$

$$EI\upsilon = -\frac{M_A x^2}{2} - \frac{qbx^3}{6} + C_3 x + C_4 \,. \tag{2.15}$$

The constants C_3 and C_4 were determined by solving Eqs. (2.14) and (2.15) for $x = a$ and equating them with the end point conditions given by Eqs. (2.10) and (2.11) giving

$$C_3 = \frac{qa^2 b}{2}\left(1 - \frac{1}{\cos\theta}\right) \tag{2.16}$$

$$C_4 = -\frac{qa^3 b}{3}\left(1 - \frac{1}{\cos\theta}\right). \tag{2.17}$$

Substituting these results into Eqs. (2.14) and (2.15) and solving for the end point at $x = a+c$ gives

$$EI\upsilon'_{(x=a+c)} = -M_A(a+c) - \frac{qb}{2}(a+c)^2 + \frac{qa^2 b}{2}\left(1 - \frac{1}{\cos\theta}\right) \tag{2.18}$$

$$EI\upsilon_{(x=a+c)} = -\frac{M_A}{2}(a+c)^2 - \frac{qb}{6}(a+c)^3 + \frac{qa^2 b}{2}(a+c)\left(1 - \frac{1}{\cos\theta}\right) - \frac{qa^3 b}{3}\left(1 - \frac{1}{\cos\theta}\right). \tag{2.19}$$

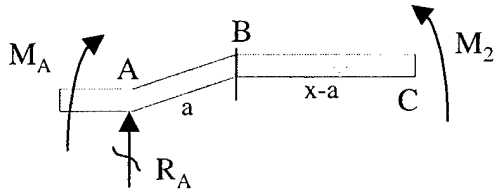

Fig. 2.7. Beam segment A-C *(0 < x < a+c)*.

The derivation of the deflection equation for the entire beam segment A-*D* *(0 < x < L)* was derived from Fig. 2.8, with the moment M_3 given by

$$M_3 = M_A + R_a x - \frac{q(x-a-c)^2}{2}. \tag{2.20}$$

The deflection equation is then determined from

$$EI\upsilon'' = -M_A - qbx + \frac{q(x-a-c)^2}{2} \tag{2.21}$$

$$EI\upsilon' = -M_A x - \frac{qbx^2}{2} + \frac{q(x-a-c)^3}{6} + C_5 \tag{2.22}$$

$$EI\upsilon = -\frac{M_A x^2}{2} - \frac{qbx^3}{6} + \frac{q(x-a-c)^4}{24} + C_5 x + C_6 . \tag{2.23}$$

The constants C_5 and C_6 were determined by solving Eqs. (2.22) and (2.23) for $x = a+c$ and equating them with the end point conditions of Eqs. (2.18) and (2.19), resulting in

$$C_5 = \frac{qa^2 b}{2}\left(1 - \frac{1}{\cos\theta}\right) \tag{2.24}$$

$$C_6 = -\frac{qa^3 b}{3}\left(1 - \frac{1}{\cos\theta}\right). \tag{2.25}$$

Since the bending moment at the beam tip is zero $(EI\upsilon''_{(x=L)} = 0)$, the bending moment M_A can be obtain by substituting $x = L$ into Eq. (2.21) and solving for M_A giving

$$EI\upsilon''_{(x=L)} = 0 = -M_A - qbL + \frac{q}{2}(L-a-c)^2 \tag{2.26}$$

$$M_A = -qbL + \frac{qb^2}{2}, \tag{2.27}$$

where $b = L-a-c$. Finally, substituting C_5, C_6, and M_A into Eq. (2.23) results in the spring beam deflection equation in terms of x.

$$EI\upsilon = \frac{q}{24}\left[12bLx^2 - 6b^2x^2 - 4bx^3 + (x-a-c)^4 + 12a^2bx\left(1 - \frac{1}{\cos\theta}\right) - 8a^3b\left(1 - \frac{1}{\cos\theta}\right)\right]. \tag{2.28}$$

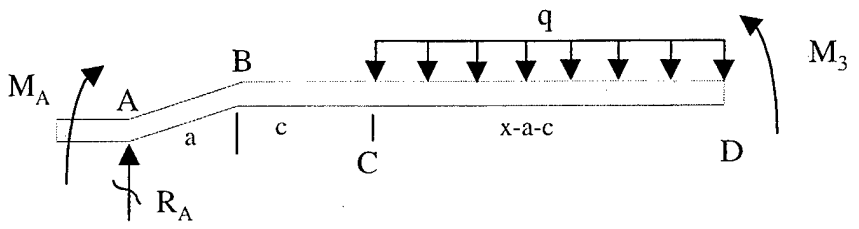

Fig. 2.8. Beam segment A-D *(0 < x < L)*.

Solving for maximum beam deflection *(x = L)* and using

$$\cos\theta = \frac{a}{\sqrt{a^2 + d^2}}, \tag{2.29}$$

Eq. (2.28) can be rearranged to give

$$\delta_{\max} = \frac{q}{24EI}\left[8bL^3 - 6b^2L^2 + b^4 + 4a^2b(3L - 2a)\left(1 - \frac{\sqrt{a^2 + d^2}}{a}\right)\right]. \tag{2.30}$$

Using $q = Pw$ and Eq. (2.3), Eq. (2.30) can be defined in terms of the actuation voltage

$$V = \sqrt{\frac{48EId^2\delta}{\varepsilon w\left[8bL^3 - 6b^2L^2 + b^4 + 4a^2b(3L - 2a)\left(1 - \frac{\sqrt{a^2 + d}}{a}\right)\right]}}. \tag{2.31}$$

2.3 Bilayer Beam Material Characteristics

The fabricated cantilever spring switches were composed of bilayer films of titanium (Ti) and gold (Au) deposited using standard evaporation. Incorporation of the bilayer films into the deflection Eqs. (2.1) and (2.30) was done by calculating the effective flexural rigidity of the bilayer beams $(EI)_{eff}$. Based on Fig. 2.9, $(EI)_{eff}$ is given by [5]

$$(EI)_{eff} = \frac{wt_a t_b^3 E_a E_b}{12(t_a E_a + t_b E_b)} k_1, \tag{2.32}$$

where

$$k_1 = 4 + 6\frac{t_a}{t_b} + 4\left(\frac{t_a}{t_b}\right)^2 + \frac{E_a}{E_b}\left(\frac{t_a}{t_b}\right)^3 + \frac{E_b}{E_a}\frac{t_b}{t_a}. \qquad (2.33)$$

Four bilayer combinations were used throughout this research. The effective flexural rigidity for each combination is included in Table 2.2. Calculations were based on a beam width $w = 50\ \mu m$ and bulk modulus values of E_{Au} = 78 GPa, and E_{Ti} = 110 GPa [6].

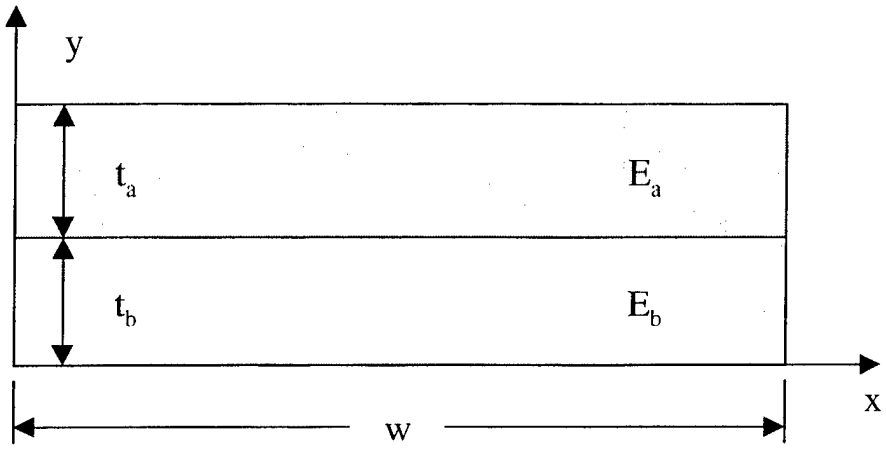

Fig. 2.9. Bilayer beam.

Table 2.2
EFFECTIVE FLEXURAL RIGIDITY.

Ti thickness, t_b (μm)	**Au thickness, t_a (μm)**	**$(EI)_{eff}$ (x 10^{-12} Nm^2)**
1.0	0.5	1.31
0.75	0.75	1.29
0.5	1.0	1.29
0.02	1.5	1.16

Calculation of the effective moment of inertia (I_{eff}) for the bilayer films first involves finding the neutral axis and then determining the moment of inertia about the neutral axis for each layer (I_a and I_b) [7]. As an example, the location of the neutral axis

(h_a and h_b) for the first bilayer combination of Table 2.2 *1.0 μm Ti / 0.5 μm Au* (Fig. 2.10) was determined by taking the first moment of the cross-sectional area using

$$\int_a ydA = \left(t_b + \frac{t_a}{2} - h_b \right)(t_a)w \tag{2.34}$$

$$\int_b ydA = -\frac{h_b^2}{2}w + \frac{(t_b - h_b)^2}{2}w, \tag{2.35}$$

where $t_a = 0.5\ \mu m$, $t_b = 1.0\ \mu m$, and $w = 50\ \mu m$. Solving these integrals results in

$$\int_a ydA = 31.25e^{-18} - 25e^{-12}h_b \quad and \quad \int_b ydA = 25e^{-18} - 50e^{-12}h_b\ . \tag{2.36}$$

Since the stress at the neutral axis is zero, substituting these results into

$$E_a \int_a ydA + E_b \int_b ydA = 0\ , \tag{2.37}$$

provides $h_a = 0.70\ \mu m$ and $h_b = 0.80\ \mu m$. The moments of inertia I_a and I_b were then determined using the parallel-axis theorem [8], which states that the moment of inertia of an area with respect to any axis in the plane of the area is related to the moment of inertia with respect to a parallel centroidal axis (Fig. 2.10)

$$I_y = I_{yc} + Ad_2^2\ , \tag{2.38}$$

where d_2 is the vertical distance between the x-axis and x_c-axis.

Continuing this example,

$$I_a = \frac{w(t_a)^3}{12} + wt_a\left(h_a - \frac{t_a}{2} \right)^2 \tag{2.39}$$

$$I_b = \frac{w(t_b)^3}{12} + wt_b\left(h_b - \frac{t_b}{2} \right)^2\ . \tag{2.40}$$

Using $t_a = 0.5\ \mu m$, $t_b = 1.0\ \mu m$, $w = 50\ \mu m$, $h_a = 0.70\ \mu m$, and $h_b = 0.80\ \mu m$ results in $I_a = 6.09\ \mu m^4$ and $I_b = 8.19\ \mu m^4$. Finally, the effective moment of inertia is given by

$(I_{eff}) = I_a + I_b$. Results of these calculations and the effective elastic modulus obtained by dividing (EI_{eff}) *by* (I_{eff}) are listed in Table 2.3.

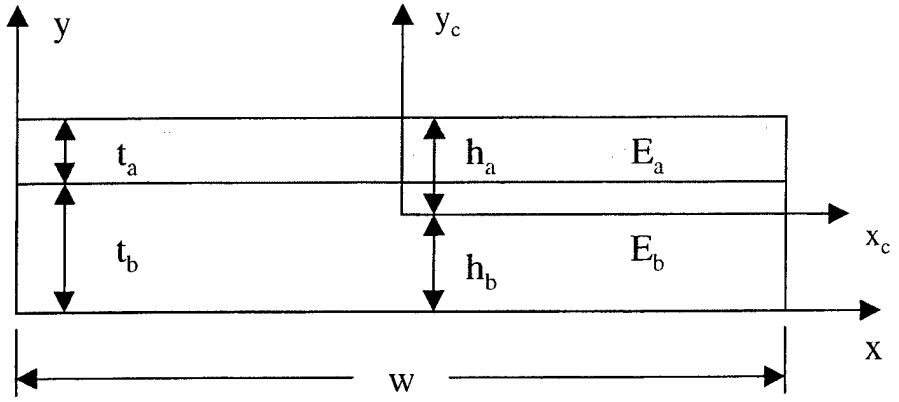

Fig. 2.10. Parallel-axis theorem.

Table 2.3
BILAYER BEAM MATERIAL CHARACTERISTICS.

Ti thickness (μm)	**Au thickness (μm)**	**I_{eff} (μm^4)**	**E_{eff} (GPa)**
1.00	0.50	14.28	91.65
0.75	0.75	14.37	90.01
0.50	1.00	14.33	89.96
0.02	1.50	14.65	79.15

2.4 ANSYS Analysis of Spring Cantilever

Mechanical simulation of tip deflection using Finite Element Analysis (FEA) of a 300 μm long spring cantilever design (Fig. 2.11) was made using ANSYS/ED® Version 5.4. A listing of the input code is provided in Appendix A. The 300 μm beam length was modeled with a sloped portion of 10 μm length and a linear pressure $q = 6.368$ nPa applied over the distributed load length b = 290 μm. The resulting tip deflection was 5 μm (Fig. 2.12). Material values used for this simulation are listed in Table 2.4.

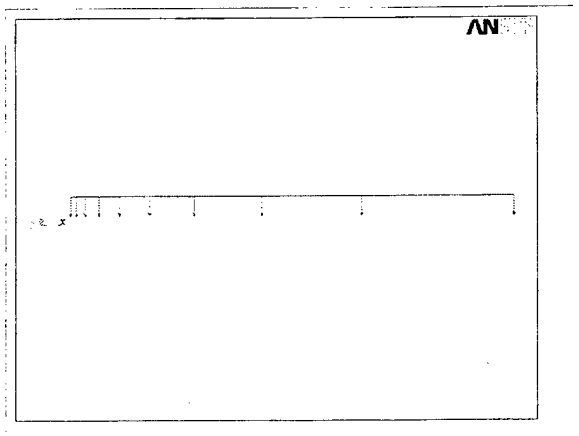

Fig. 2.11. Spring beam with end constraints and applied load.

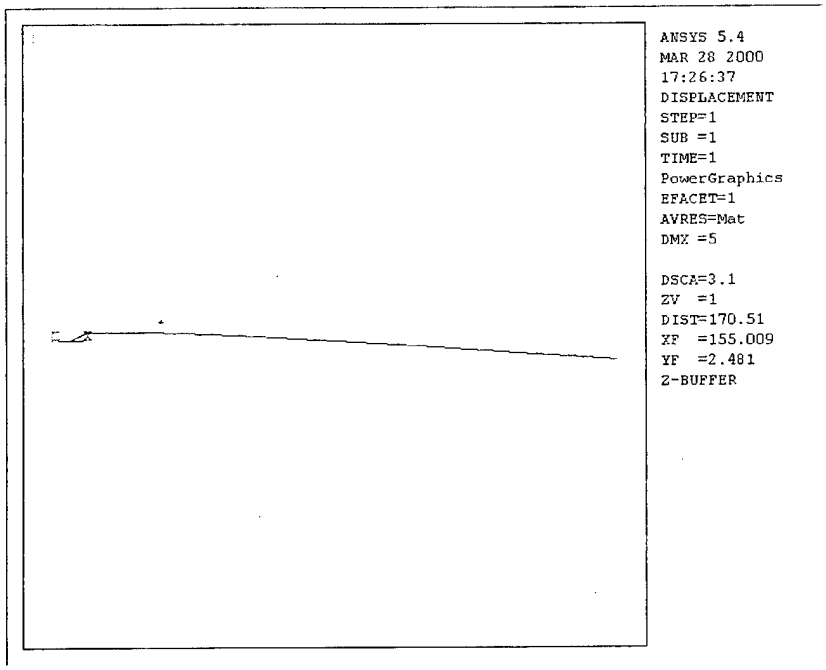

Fig. 2.12. Spring cantilever deflection.

Table 2.4
ANSYS SIMULATION COEFFICIENTS.

Parameter	Value
Cross-sectional area	75 μm^2
Moment of inertia	14.28 μm^4
Total beam height	1.5 μm
Young's modulus	91.65 $N/\mu m^2$

Comparisons of the analytical models for the clamped cantilever (Fig. 2.2), the spring cantilever (Fig. 2.4) and the ANSYS simulation of the spring design (Fig. 2.11) were made for three lengths of cantilevers. The distributed load length *b* was varied to investigate the accuracy of the models with variations of the moment arm. The length *b* was measured from the cantilever tip to within 10 μm of the clamped end. For a 300 μm long cantilever beam, a length b = 10 μm represents a point load at the tip of the cantilever beam while a length b = 290 μm represents a distributed load applied along the entire cantilever except 10 μm from the clamped end. For these conditions, the results (Fig. 2.13 – 2.15) show an excellent agreement of the ANSYS simulations with both analytical models. Also, for the three cantilever beam lengths examined, the actuation voltage quickly converges to a constant value when the distributed load length *b* reaches half the overall cantilever beam length.

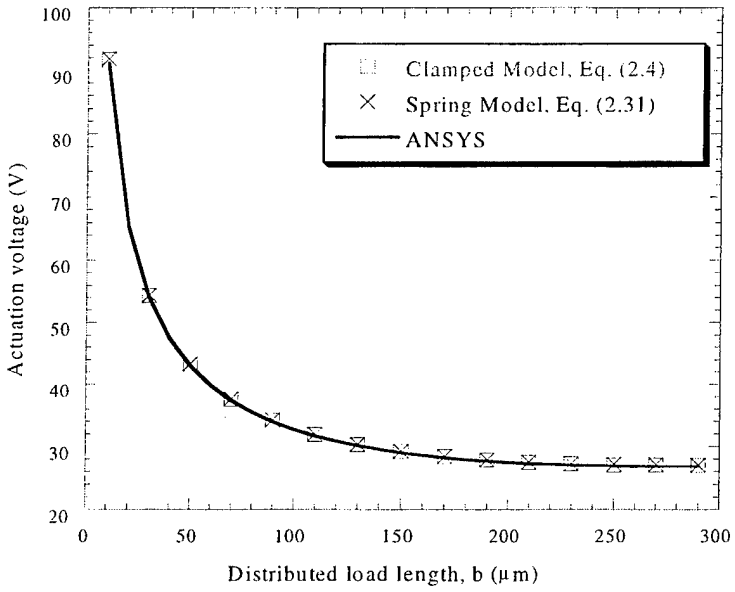

Fig. 2.13. Tip deflection of analytical models and finite element model of 300 μm cantilever, with distributed load applied over variable length, b.

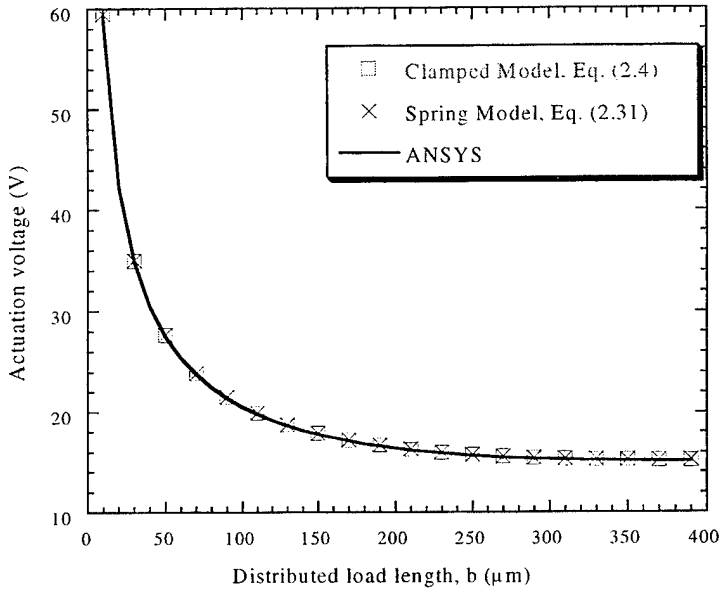

Fig. 2.14. Tip deflection of analytical models and finite element model of 400 μm cantilever, with distributed load applied over variable length, b.

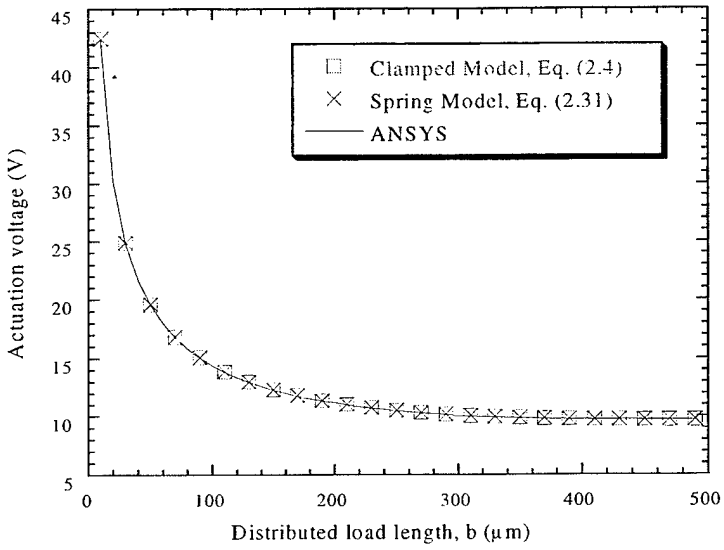

Fig. 2.15. Tip deflection of analytical models and finite element model of 500 μm cantilever, with distributed load applied over variable length, b.

These results show that the clamped model, spring model, and ANSYS simulations of the spring structure provided seemingly identical modeling of the

cantilever structure over the lengths from 300 μm to 500 μm (Fig. 2.1). The inclined slope had a negligible impact on the voltage and the clamped model could be used for initial designs. The inclined model reverts to the clamped model when the incline is reduced to zero *($\theta = 0$)* and the *a* term of Eq. (2.1) is replaced with $a = L\text{-}b$ and simplified. Variations in both the slope of the incline and the gap height are factors of the fabrication process and large variations are impractical. Experimental verification of these results was not possible due to the inability to accurately determine the point of tip contact for the cantilevers.

2.5 Microbridge Model

The microbridge structure was also analyzed using both the double clamped (built-in) model and a spring structure. The built-in beam model (Fig. 2.16) is a statically indeterminate structure with more moments and reactions than can be analyzed using free-body diagrams and solving equilibrium equations. This analysis requires the additional boundary condition that the slope of the deflection curve at the center of the beam is zero ($EI\upsilon'_{(x=L/2)} = 0$). The solution of the built-in bridge structure followed the same procedure as used for the cantilever beam model. The analysis, presented in Appendix B resulted in the deflection equation

$$\delta_{\max} = \frac{qb}{384EI}\left(2L^3 - 2b^2L + b^3\right). \tag{2.41}$$

Using the results $q = Pw$ and Eq. (2.3), the actuation voltage can be given by

$$V = \sqrt{\frac{768EId^2\delta}{\varepsilon wb(2L^3 - 2b^2L + b^3)}}. \tag{2.42}$$

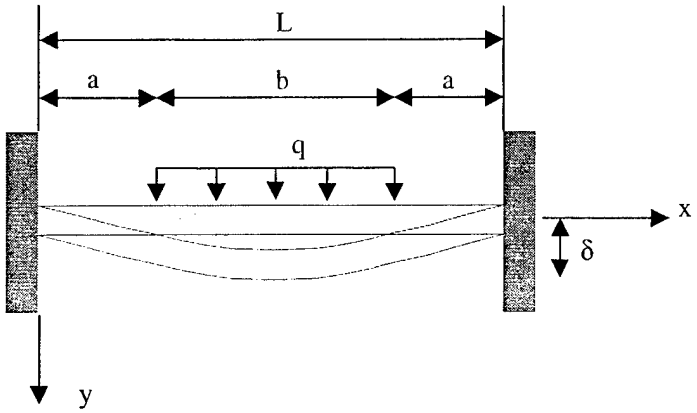

Fig. 2.16. Built-in beam model.

2.6 Spring Bridge Model

The spring bridge model (Fig. 2.17) was also analyzed using the method of successive integration. The analysis, shown in Appendix C, resulted in the deflection equation

$$\delta_{max} = \frac{qb}{384EI}\left[2L^3 - 2b^2L + b^3 + 24a^2L\left(1 - \frac{\sqrt{a^2+d^2}}{d}\right) - 84a^3\left(1 - \frac{\sqrt{a^2+d^2}}{d}\right)\right]. \quad (2.43)$$

Again using $q = Pw$ and Eq. (2.3), the actuation voltage for the spring bridge model is

$$V = \sqrt{\frac{768EId^2\delta}{\varepsilon wb\left(2L^3 - 2b^2L + b^3 + 24a^2L\left(1 - \frac{\sqrt{a^2+d^2}}{d}\right) - 84a^3\left(1 - \frac{\sqrt{a^2+d^2}}{d}\right)\right)}}. \quad (2.44)$$

This equation is similar to the equation for the built-in beam Eq. (2.42) with the addition of the last two terms.

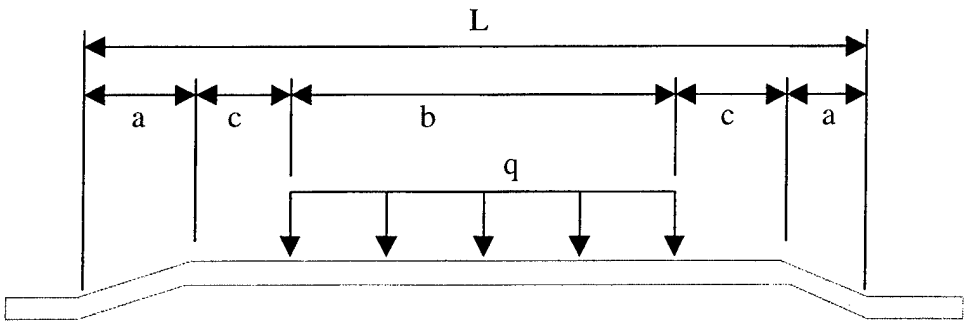

Fig. 2.17. Spring bridge model.

2.7 ANSYS Analysis of Spring Bridge

Comparisons of the analytical models for the built-in bridge (Fig. 2.16) and the spring bridge (Fig. 2.17) were made with ANSYS simulations (Fig. 2.18). As with the previous simulations of the cantilever, to investigate the effect of the moment arm, a distributed load was applied over the length b, which was increased to the full length of the bridge. Using the analytical results of Eq. (2.41) as a guide, a linear pressure of $q = 20.72\ nPa/\mu m$ was applied over the beam length of $b = 500\ \mu m$, resulting in a beam deflection of $\delta = 5.0\ \mu m$ (Fig. 2.19) at the center of the 600 μm long microbridge. A listing of the input code is included in Appendix A. The simulation incorporated the material parameters from Table 2.4.

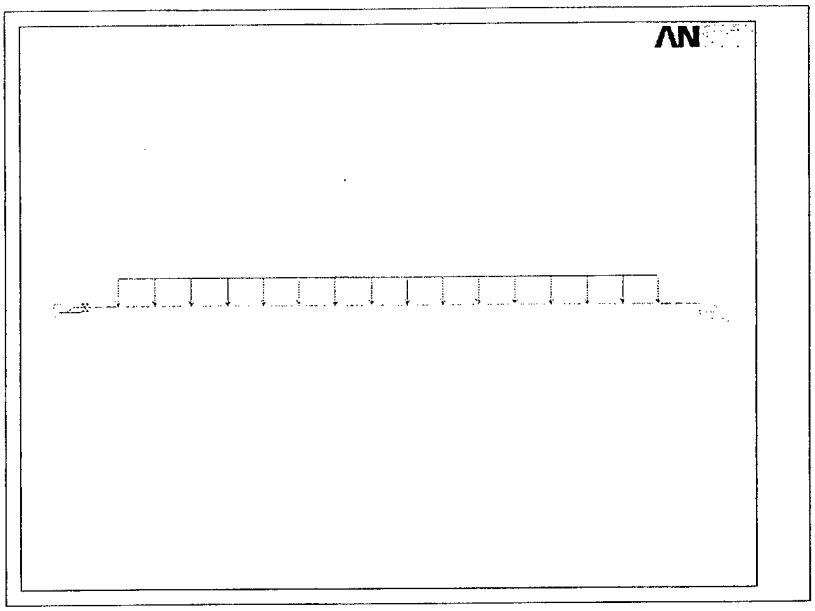

Fig. 2.18. Spring bridge model with end constraints and applied load.

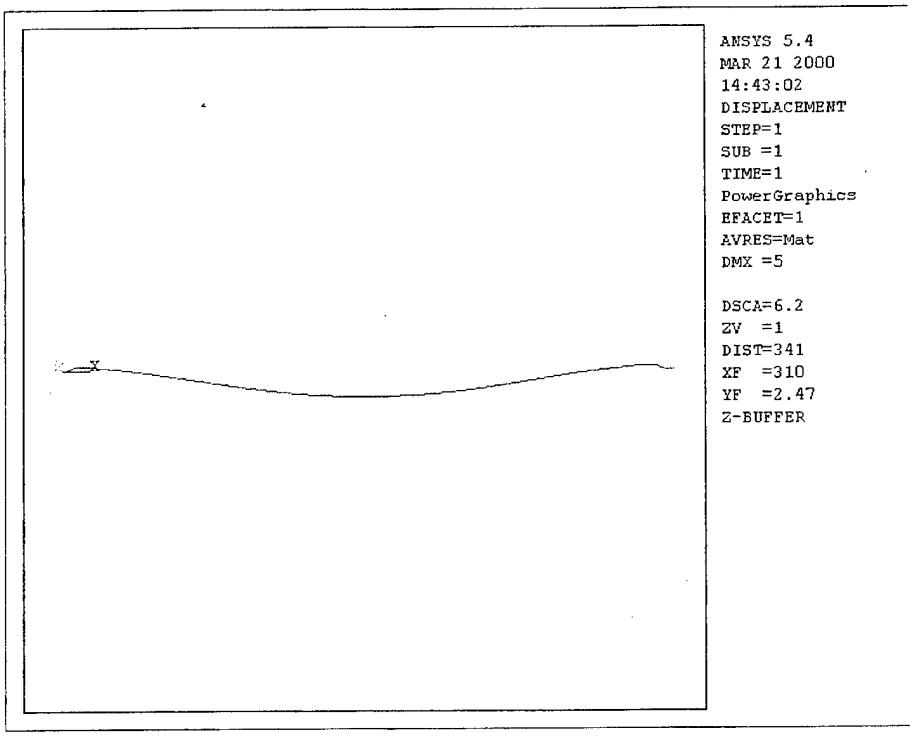

Fig. 2.19. ANSYS deflection of spring beam model.

Comparisons of the analytical models for the built-in bridge (Fig. 2.16), the spring bridge model (Fig. 2.17), and the ANSYS simulations of the spring bridge design

(Fig. 2.18) were made for three lengths of bridge structures. The simulations were also made for distributed load length b, which is the length the pressure is applied to the bridge. These simulation were based upon achieving a $\delta = 5.0\ \mu m$ deflection at the center of the bridges. These results (Fig. 2.20 – 2.22) show an excellent agreement between the analytical models and the simulation results.

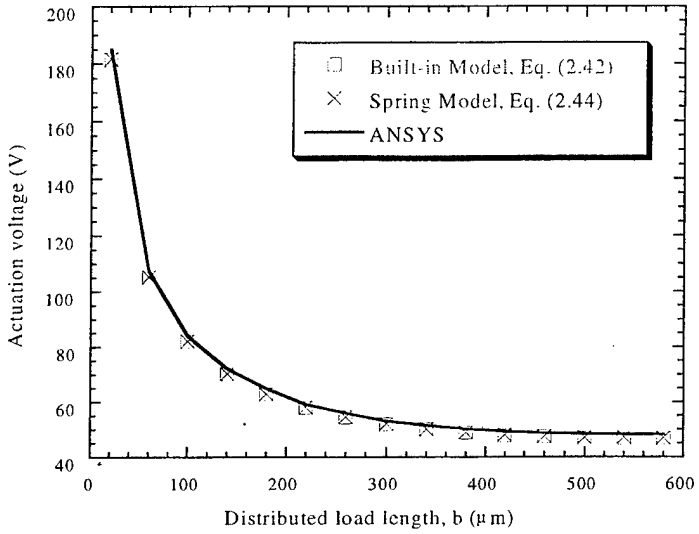

Fig. 2.20. Tip deglection of analytical models and finite element model of 600 μm microbridge, with distributed load applied over variable length, b.

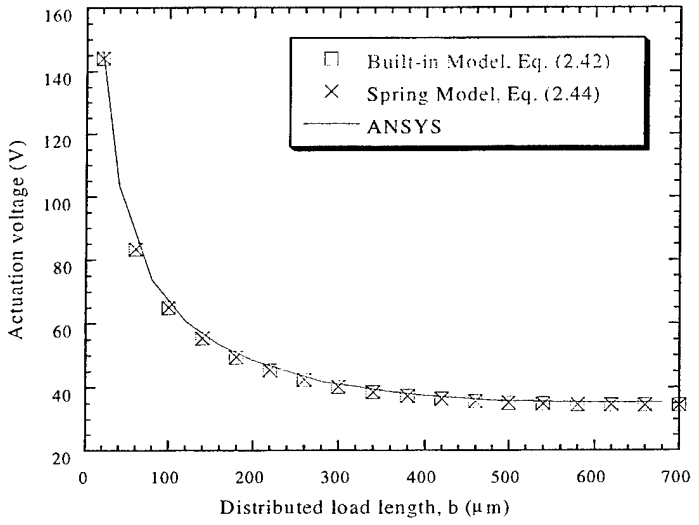

Fig. 2.21. Tip deflection of analytical models and finite element model of 700 μm microbridge, with distributed load applied over variable length, b.

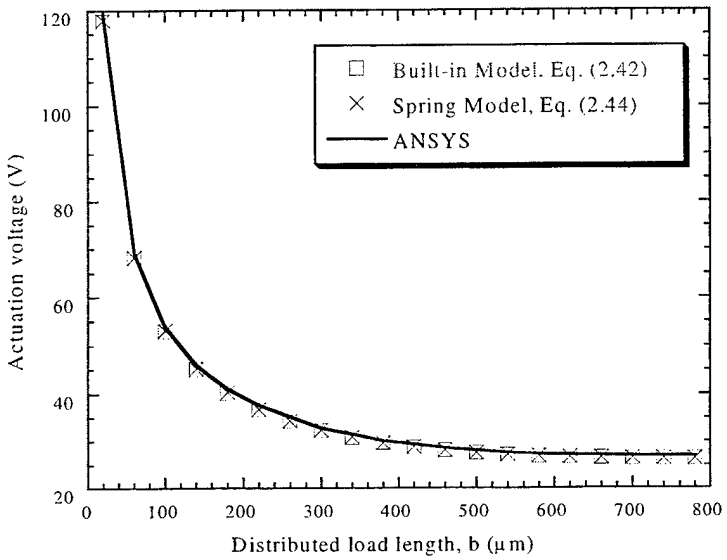

Fig. 2.22. Tip deflection of analytical models and finite element model of 800 μm microbridge, with distributed load applied over variable length, b.

These results show that the built-in model, spring model, and ANSYS simulations of the spring bridge structure also provided seemingly identical modeling of the bridge structures over lengths of 600 μm to 800 μm. The inclined slope had a negligible impact on the actuation voltage and the built-in bridge model could be used for initial designs. The spring bridge model Eq. (2.43) reverts to the built-in beam model Eq. (2.41) when the inclined slope reduces to zero. Variations in both the slope of the incline and the gap height had relatively minor impact on the mechanical design but have a large impact on the fabrication processes. These bridge results were based upon deflections at the center point of the beam. Experimental verification was not possible due to the inability to observe the vertical deflections.

2.8 Pull-in Voltage

The preceding analysis assumed linear deflection of the beam. In practice, as the beam gap spacing decreases, the electrostatic force increases until it exceeds the spring

constant of the beam and the gap collapses. The voltage required to produce this force has been referred to as the pull-in voltage (V_{pi}). Two approaches have been analyzed to investigate the pull-in voltage. The first approach was a modification of the preceding linear beam deflection [9]. The second approach was the electrostatic pull-in process developed at MIT[10].

The first approach was based on equating the electrostatic force equation with the spring force equation of the switch [9]. For a parallel plate capacitor, the electrostatic force is determined by

$$F_E = \frac{\partial W}{\partial y}, \tag{2.45}$$

where W is the work and is given by

$$W = \frac{CV^2}{2}. \tag{2.46}$$

A first order equation for the switch capacitance is given by

$$C = \frac{\varepsilon A}{d_y}, \tag{2.47}$$

where d_y is the variable gap height, which changes as the beam deflects. Substituting Eqs. (2.46) and (2.47) into Eq. (2.45) and taking the derivative results in the electrostatic force

$$F_E = -\frac{\varepsilon A V^2}{2 d_y^2}. \tag{2.48}$$

Using the fundamental equation for the spring constant (F = kx) for the switch gives

$$F_S = k(d_o - d_y), \tag{2.49}$$

where d_o is the initial gap height and k is the spring constant. Equating Eqs. (2.48) and (2.49) results in

$$-\frac{\varepsilon A V^2}{2d_y^2} = k(d_o - d_y). \tag{2.50}$$

Solving for the voltage gives

$$V = \sqrt{\frac{-2kd_y(d_o - d_y)}{\varepsilon A}}. \tag{2.51}$$

At the maximum value of voltage, the spring force is unable to maintain equilibrium and the gap collapses. The maximum value of V can be determined by setting the derivative of Eq. (2.51) to zero, as shown below.

$$\frac{\partial V}{\partial y} = 0 \tag{2.52}$$

$$\sqrt{\frac{-kd_o d_y^2 + kd_y^3}{\varepsilon A}}\left[\frac{-2kd_o d_y + 3kd_y^2}{\varepsilon A}\right] = 0 \tag{2.53}$$

Solving this equation shows that the pull-in voltage occurs when

$$d_y = \frac{2d_o}{3}. \tag{2.54}$$

Based upon this result, the preceding deflection equations were modified for a deflection of $\delta = 2/3\ d$ and the voltage calculated. Since the variation between the clamped and spring model was minimal, the clamped models were used for both the cantilever and bridge. For the cantilever beam, the deflection, in terms of voltage is given by

$$V_{piC} = \sqrt{\frac{32d^3(EI)_{eff}}{\varepsilon_0 w(3L^4 - 4a^3L + a^4)}}. \tag{2.55}$$

The bridge deflection can be determined by substituting $\delta = 2/3\ d$ into Eq. (2.42), resulting in

$$V_{piB} = \sqrt{\frac{512 d^3 (EI)_{eff}}{\varepsilon_0 w b (2L^3 - 2b^2 L + b^3)}}, \tag{2.56}$$

where b is given by

$$b = L - 2a. \tag{2.57}$$

The MIT electrostatic pull-in approached [10] was developed to characterize material properties and was verified using samples prepared in a dielectric-isolated single-crystal silicon wafer-bonded process [11]. The approach was based upon the assumption that the movable conductor (cantilever or bridge) has a negligible stress gradient (i.e. no curl or buckling). An analytic expression for the effective spring constant (K_{eff}) of the structure can be given in terms of two intermediate quantities S and B. The stress quantity, S was defined as

$$S = \sigma' t d^3, \tag{2.58}$$

where σ' is the effective residual stress, t is the film thickness, and d is the gap spacing. The bending quantity, B was defined as

$$B = E' t^3 d^3, \tag{2.59}$$

where E' is the elastic modulus of the material. Using L as the beam length, the effective spring constant was given by

$$K_{eff} = \frac{S}{L^2 \left[1 + \frac{2\left\{1 - \cosh\left(\frac{kL}{2}\right)\right\}}{\left(\frac{kL}{2}\right)\sinh\left(\frac{kL}{2}\right)} \right]}, \tag{2.60}$$

where

$$k = \sqrt{\frac{12S}{B}} \,. \tag{2.61}$$

Applying the MIT approach to the microstructures of the present research, the beams would be considered wide ($w \geq 5t$) and the elastic modulus (E') is replaced by the plate modulus ($E / (1 - \nu^2)$), where ν is Poisson's ratio. For cantilevers, the effective residual stress ($\sigma' = 0$) and ($\sigma' = \sigma_0 (1 - \nu)$) for the bridges. Here σ_0 is the biaxial residual film stress. Using these conditions, the closed form model for the pull-in voltage of the cantilever is given by

$$V_{piC} = \sqrt{\frac{0.28B}{\varepsilon_0 L^4 \left(1+0.42\frac{d}{w}\right)}} \,. \tag{2.62}$$

For the bridge structure, the closed form model for pull-in voltage is given by

$$V_{piB} = \sqrt{\frac{2.79S}{\varepsilon_0 L^2 \left(1+0.42\frac{d}{w}\right)}} \,. \tag{2.63}$$

Using Eqs. (2.55), (2.56), (2.62), (2.63), the physical constants listed in Table 2.5, and the material properties listed in Table 2.6, the pull-in voltages for the cantilever beam and microbridge switches were computed and listed in Table 2.7. Determination of the biaxial residual stress (σ) will be discussed in the next chapter.

Table 2.5
PHYSICAL CONSTANTS.

Parameter	**Value**
Gap spacing (d)	5.0 μm
Permittivity constant (ε_0)	$8.854e^{-12}$ F/m
Beam width (w)	50 μm
Beam thickness (t)	1.5 μm
Zero applied force length (a)	10 μm

Table 2.6
MATERIAL PROPERTIES.

Ti (μm)	Au (μm)	$(EI)_{eff}$ (x 10^{-12} Nm^2)	E (GPa)	ν	σ (MPa)
1.00	0.50	1.31	91.65	0.36	54.175
0.75	0.75	1.29	90.01	0.38	26.80
0.50	1.00	1.29	89.96	0.40	83.60
0.02	1.50	1.16	79.15	0.44	14.00

Table 2.7
PULL-IN VOLTAGES.

	Modified Tip Deflection				MIT M-Test Model			
Ti / Au Bilayer films (μm)	**1.00 / 0.50**	**0.75 / 0.75**	**0.50 / 1.00**	**0.02 / 1.50**	**1.00 / 0.50**	**0.75 / 0.75**	**0.50 / 1.00**	**0.02 / 1.50**
Switch	**Cantilever Pull-in Voltage (V)**							
C-300	14.7	14.6	14.6	13.8	12.9	12.8	12.8	12.0
C-400	8.3	8.2	8.2	7.8	7.3	7.2	7.2	6.7
C-500	5.3	5.3	5.3	5.0	4.6	4.6	4.6	4.3
Switch	**Bridge Pull-in Voltage (V)**							
B-600	25.5	25.5	25.5	25.5	73.9	51.2	88.9	35.1
B-700	18.7	18.7	18.7	18.7	63.3	43.8	76.2	30.1
B-800	14.3	14.3	14.3	14.3	55.4	38.4	66.7	26.4

The notation C-300 represents the 300 μm cantilever and the B-600 represents the 600 μm microbridge.

2.9 Summary

The results of the mechanical modeling show that the clamped models are sufficient to accurately model the spring-like switches. Also, analysis of the pull-in voltage showed that switch actuation can be obtained for reasonable switching voltages, provided the residual stress of the switch metal is closely controlled. Actual comparisons between actuation voltage and modeled pull-in voltage will be presented in Chapter 5.

2.10 References

[1]. J.M. Gere and S.P. Timoshenko, "*Mechanics of Materials*", PWS-Kent Publishing Company, Boston, MA., (1990), 772.

[2]. M. Bauccio, "*ASM Metals Reference Book 3rd Edition*", ASM International, Materials Park, OH (1993), 143 – 147.

[3]. R.E. Bolz and G.L. Tuve, "*CRC Handbook of Tables for Applied Engineering Science, 2nd Edition*, "CRC Press, Cleveland, OH, (1973), 331 – 332.

[4]. J.M. Gere and S.P. Timoshenko, op. cit., 461 – 471.

[5]. W.C. Young, "*Roark's Formulas for Stress and Strain*", McGraw-Hill, Inc., (1989), 117 – 120.

[6]. J.M. Gere and S.P. Timoshenko, op. cit., 779.

[7]. J.M. Gere and S.P. Timoshenko, op. cit., 301 – 308.

[8]. J.M. Gere and S.P. Timoshenko, op. cit., 740 – 743.

[9]. H.C. Nathanson, et. al. "The Resonant Gate Transistor", *IEEE Trans. on Electron Devices*, Vol. ED-14, No. 3, (March 1967): 117-133.

[10]. P.M. Osterberg and S.D. Senturia, "M-TEST: A Test Chip for MEMS Material Property Measurement Using Electrostatically Actuated Test Structures", *Journal Microelectromechanical Systems*, Vol. 6, No. 2, (June 1997): 107-118.

[11]. C.H. Hsu and M.A. Schmidt, "Micromachined Structures Fabricated Using Wafer-Bonded Sealed Cavity Process", *Proc. 1994 Solid-State Sensor and Actuator Workshop,* Hilton Head, SC, (June 1994): 151-155.

CHAPTER 3

ELECTRICAL DESIGN

In addition to the structural integrity requirements discussed in Chapter 2, RF MEMS switches must also satisfy electrical impedance matching requirements of microwave circuits. Unlike circuit theory, which assumes that the physical dimensions of the circuits and conductors are much smaller than the wavelength of the signals, microwave components and transmission lines may be a fraction of the wavelength or several wavelengths in size [1]. This requires careful consideration of field theory and the use of electromagnetic simulations in the design of microwave components.

Microwave components are interconnected using transmission lines. The impedance of transmission lines must be matched to the impedance of the components to reduce signal loss. A number of transmission line approaches are available, but two types are primarily used, microstrip and coplanar waveguide, Fig. 3.1 [2]. Each approach has its own unique advantages and constraints and the selection of the approach is dependent upon component design and processing constraints.

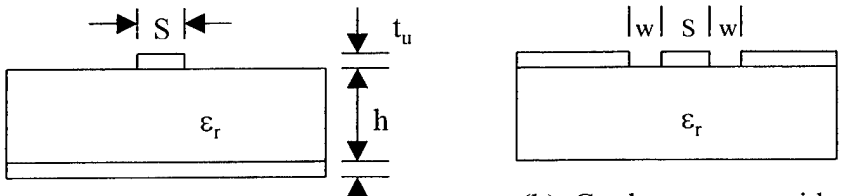

(a) Microstrip (b) Coplanar waveguide

Fig. 3.1. Two types of transmission line design approaches.

Microstrip design, Fig. 3.1a consists of a conducting path of width S on one side of a semi-insulating substrate material and a ground plane on the backside of the substrate. The thickness of the signal path t_u and ground plane t_l are chosen to be multiples of the skin depth δ_s of the signal, which is the depth of penetration of the signal into the conducting metal and is given by [3]

$$\delta_s = \sqrt{\frac{2}{\omega\mu\sigma}}, \tag{3.1}$$

where, $\omega = 2\pi f$, μ_o is the magnetic permeability ($4\pi e^{-7}$ H/m), and σ is the electrical conductivity. For standard gold metallization with a conductivity $\sigma = 4.098e^7$ S/m [4], the skin depth varies from $\delta_s = 0.72$ - 0.88 μm at X-band (8 – 12 GHz). Typical values for microstrip transmission lines at X-band are $t_u = 2\ \mu m$ and $t_l = 3 - 5\ \mu m$. Impedance matching of microstrip is dependent upon the conductor width S, substrate thickness h, and the relative permittivity of the substrate material ε_r. The use of microstrip also requires bringing ground pads from the bottom of the substrate to the top through metallized vias. To achieve electrical, thermal, and processing goals, the substrates are thinned from a nominal thickness of 650 μm for 76.2 mm diameter GaAs wafers to 150 μm, prior to via formation [5]. For processing considerations and compatibility with other research efforts, microstrip design was not employed in this research.

A coplanar waveguide, Fig. 3.1b consists of a central conductor of width S between two ground planes separated by width w. This approach has the advantage of single side processing and greatly reduces the processing complexity by eliminating via formation. Thinning of the substrate for both thermal and electrical considerations may be employed, but as mentioned a via process is not required. A coplanar waveguide

design approach was utilized for this research after consideration of both processing issues and integration with other microwave designs.

3.1 Coplanar Waveguide Design Approach

Design of the MEMS switches was based upon the determination of the characteristic impedance of a coplanar waveguide. Quasi-static analysis of coplanar waveguides was first developed by Wen [6] and modified by Gupta et al.[7] into closed form design equations. The characteristic impedance of coplanar waveguide $Z_{o\text{-}cp}$ is given by

$$Z_{o-cp} = \frac{30\pi}{\sqrt{\varepsilon_{re}}} \frac{K'(k)}{K(k)}. \tag{3.2}$$

The term k is defined by the width of the signal line S and the distance w between the signal line and ground planes, Fig. 3.1b, and is given by

$$k = \frac{S}{S + 2w}. \tag{3.3}$$

The ratio $K'(k)/K(k)$ is given by

$$\frac{K(k)}{K'(k)} = \frac{1}{\pi} \ln\left[2\frac{1+\sqrt{k'}}{1-\sqrt{k'}}\right], \quad for \quad 0.707 \le k \le 1 \tag{3.4}$$

$$\frac{K(k)}{K'(k)} = \frac{\pi}{\ln\left[2\frac{1+\sqrt{k'}}{1-\sqrt{k'}}\right]}, \quad for \quad 0 \le k \le 0.707 \tag{3.5}$$

where k' is

$$k' = \sqrt{1-k^2}. \tag{3.6}$$

The effective relative permittivity ε_{re} is given by

$$\varepsilon_{re} = \frac{\varepsilon_r + 1}{2}\left[\tanh\left\{1.785\log\frac{h}{w} + 1.75\right\} + \frac{kw}{h}\left\{0.04 - 0.7k + 0.01(1 - 0.01\varepsilon_r)(0.25 + k)\right\}\right], \tag{3.7}$$

where h is the thickness of the substrate.

The design procedure is an iterative approach that begins with the determination of a suitable value of k for a desired characteristic impedance ($Z_{o\text{-}cp}$). As an aid, the graph, Fig. 3.2 was developed using

$$Z_{o-cp} = \frac{30}{\sqrt{\frac{\varepsilon_r + 1}{2}}}\left[\ln\left\{2\frac{\left(1 + \sqrt{k'}\right)}{\left(1 - \sqrt{k'}\right)}\right\}\right], \tag{3.8}$$

where k' was determined by Eqs. (3.3) and (3.6). For a characteristic impedance of $Z_{o\text{-}cp} = 50\ \Omega$ on a GaAs substrate ($\varepsilon_r = 13$) [8], $k \sim 0.425$. Choosing a coplanar linewidth of $S = 50\ \mu m$ and using Eq. (3.3), the separation distance can be computed resulting in $w = 33.8\ \mu m$.

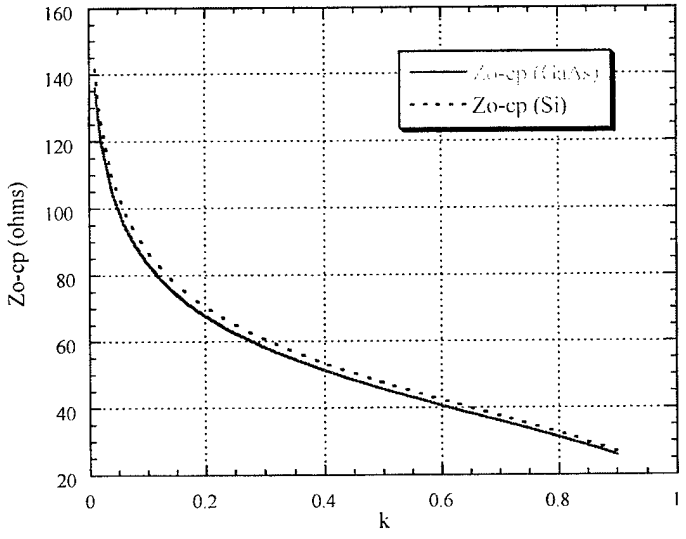

Fig. 3.2. Calculated characteristic impedance of coplanar waveguide.

Using the values given in Table 3.1, a characteristic impedance $Z_{o\text{-}cp} = 50\ \Omega$ was calculated using Eqs. (3.2) to (3.7). A layout of the waveguide for a cantilever switch, Fig. 3.3 shows the overall device layout with the separation $w = 34\ \mu m$ and the line width $S = 50\ \mu m$. The layout of the microbridge waveguide, Fig. 3.4 is similar with the exception that the bottom metal output path is routed around the bridge landing at point *A*. Complete drawings of the switches are included in Chapter 4.

Table 3.1
DESIGN PARAMETERS FOR A GaAs SUBSTRATE.

Parameter	Value
Line width (S)	50 μm
Separation distance (w)	34 μm
Relative permittivity (ε_r)	13
Substrate thickness (h)	650 μm

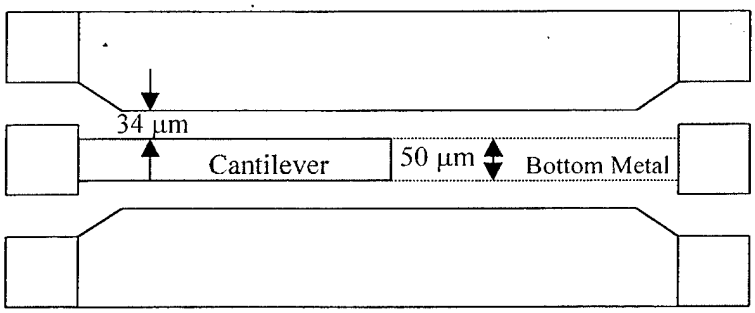

Fig. 3.3. MEMS coplanar cantilever switch layout.

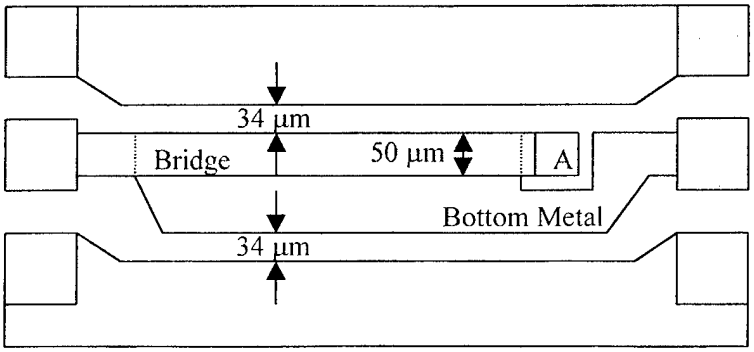

Fig. 3.4. MEMS coplanar bridge switch layout.

3.2 Switch Configuration

MEMS switches can be used in either series or shunt configurations, Fig. 3.5. The switches discussed in Chapter 1 were primarily of the shunt configuration, in which, when actuated, the switch grounds the signal path. The approach to implement this switch, Fig. 3.6 consists of a grounded switch over the coplanar signal line. In the up-state condition, loss is due to coupling from the signal line to the switch and is very low, typically ≤ 0.1 dB. In the down-state, the grounded switch is pulled into contact with the signal line resulting in high isolation ≥ 15 dB [9].

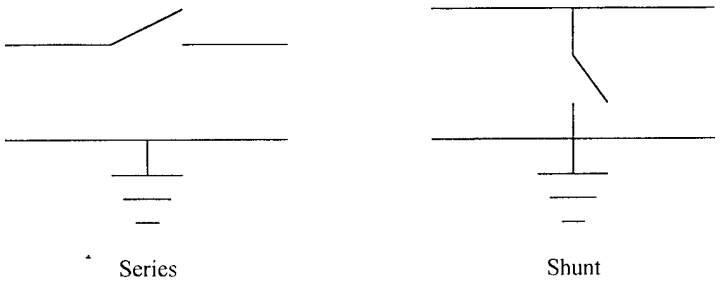

Fig. 3.5. Switch configurations.

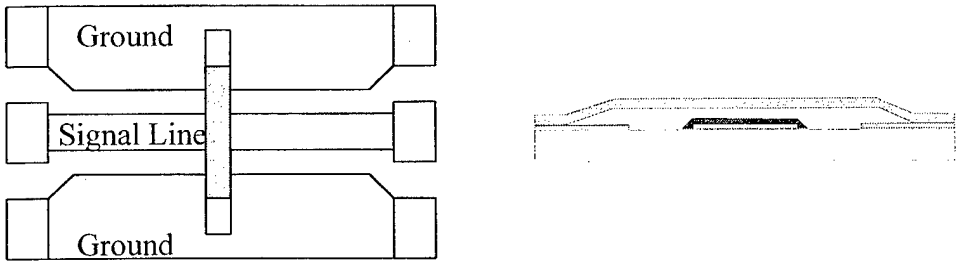

Fig. 3.6. Shunt switch configuration.

The switches developed in this research were in the series configuration which as the name implies the switch is in series with the transmission line, Fig. 3.7. In the up-state, the RF signal has no signal path to the signal out line except by coupling through the airgap. In the down-state, the signal is capacitively coupled through a thin dielectric

to the signal out line. The series configuration places great demands on both the switch design and material properties and was chosen to investigate these effects. The following sections develop analytical equations for the design of series switches and compares them with an electromagnetic simulation.

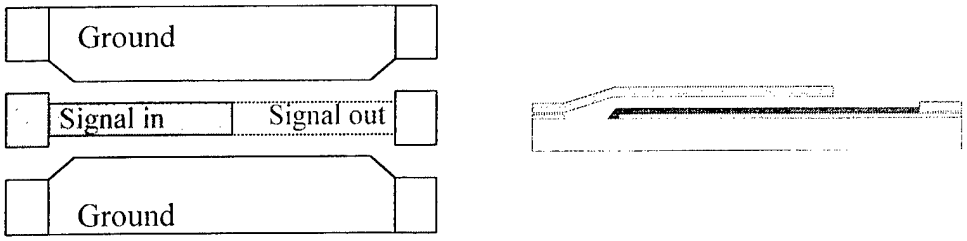

Fig. 3.7. Series switch configuration.

3.3 Series Switch Design Analysis

In the series configuration, the switch impedance can be modeled as the sum of the impedance of the lumped elements of the beam in both the "up" and "down" states. The impedance of the switch Z_S can be given as

$$Z_S = R_S + j\omega L_S + \frac{1}{j\omega C_S}, \tag{3.9}$$

where $\varpi = 2\pi f$, R_s is the series resistance, L_s is the beam inductance, and C_s is the beam capacitance. The series resistance of the beam R_S is given in two parts, the resistance of the beam R_B and the resistance of the transmission line R_T. The series resistance of the beam is [10]

$$R_S = \frac{L_B}{t_B w \sigma} + \frac{L_T}{t_T w \sigma}, \tag{3.10}$$

where σ is the conductivity, L_B is the switch length, L_T is the transmission line length, t_B is the beam thickness, t_T is the transmission line thickness, and w is the beam width. To allow for automated wafer probing, the overall length of the cantilever switch die was fixed at 700 μm and the bridges fixed at 1000 μm. Both the cantilevers and bridges were centered within the die length resulting in symmetry for the beam and transmission lines. The effective lengths are given in Table 3.2, with the notation of C-xxx for cantilevers and B-xxx for microbridges.

Table 3.2
TRANSMISSION LINE LENGTH.

Switch	**Beam Length L_B (μm)**	**Transmission Line L_T Length (μm)**
C-300	500	500
C-400	550	550
C-500	600	600
B-600	800	800
B-700	850	850
B-800	900	900

The beam inductance L_S can be approximated by [11]

$$L_S = \frac{\mu_O h}{w} L, \tag{3.11}$$

where μ_O is the permeability of free space, h is the gap spacing, L is the beam length, and w is the beam width. The beam capacitance [12] can be modeled as a combination of the parallel plate capacitance and the fringing capacitance. In the up-state, the total capacitance C_{up} is given by

$$C_{up} = \frac{\varepsilon_O w L}{h + \frac{t_D}{\varepsilon_R}} \left[1 + \left(\frac{\ln\left(\frac{w\pi}{h + t_D} \right)}{\frac{w\pi}{h + t_D}} \right) + \left(\frac{\ln\left(\frac{L\pi}{h + t_D} \right)}{\frac{L\pi}{h + t_D}} \right) \right], \tag{3.12}$$

where ε_O is the permittivity of free space, t_D is the thickness of the dielectric, and ε_R is the relative permittivity of the dielectric. The parameters L, w, and h represent the beam length, width, and gap height, respectively. In the "down" state, the total capacitance C_{down} is given by

$$C_{down} = \frac{\varepsilon_o \varepsilon_R w L}{t_D} \left[1 + \left(\frac{\ln\left(\frac{w\pi}{t_D}\right)}{\frac{w\pi}{t_D}} \right) + \left(\frac{\ln\left(\frac{L\pi}{t_D}\right)}{\frac{L\pi}{t_D}} \right) \right]. \tag{3.13}$$

Using Eqs. (3.10) to (3.13), the lumped elements of the beams can be calculated using the material parameters and dimensions provided in Table 3.3.

Table 3.3
BEAM PARAMETERS.

Parameter	Value
σ (Au) [13]	$4.098e^{7}$ S/m
μ_O [13]	$4\pi e^{-7}$ H/m
ε_O [13]	$8.854e^{-12}$ F/m
ε_R [14]	8
L	300 – 800 μm
t_B	1.5 μm
t_T	0.25 μm
w	50 μm
h	5.0 μm
t_D	0.25 μm

Given these parameters, the lumped elements of the beams were calculated and listed in Table 3.4.

Table 3.4
BEAM LUMPED PARAMETERS.

Beam	R_S (Ω)	C_{up} (fF)	L_{up} (pH)	C_{down} (pF)	L_{down} (pH)
C300	0.10	30.16	39.59	4.30	1.89
C400	0.13	40.00	52.78	5.73	2.51
C500	0.16	49.83	65.98	7.17	3.14
B600	0.20	59.66	79.17	8.60	3.77
B700	0.23	69.48	92.37	10.03	4.40
B800	0.26	79.30	105.56	11.46	5.03

Based upon these values, the impedance of the switches in both the "up" and "down" states were calculated using Eq. (3.9). The insertion loss of the switch in the "down" state was then determined by modifying the loss of a series configured *PIN* diode [15], resulting in

$$Insertion\ Loss = -10\ Log\left(1+\frac{Z_S}{2Z_O}\right)^2, \tag{3.14}$$

where $Z_O = 50\ \Omega$ is the characteristic impedance of the system. The switch isolation in the "up" state was also determined by modifying the equation for a series configured *PIN* diode [15] resulting in

$$Isolation = -10Log\left[1+\left(\frac{Z_S}{2Z_O}\right)^2\right]. \tag{3.15}$$

The isolation and insertion loss of the switches were computed over X-band (8 - 12 GHz) and shown in Figs. 3.8 - 3.13 for the three cantilever and three bridge switches.

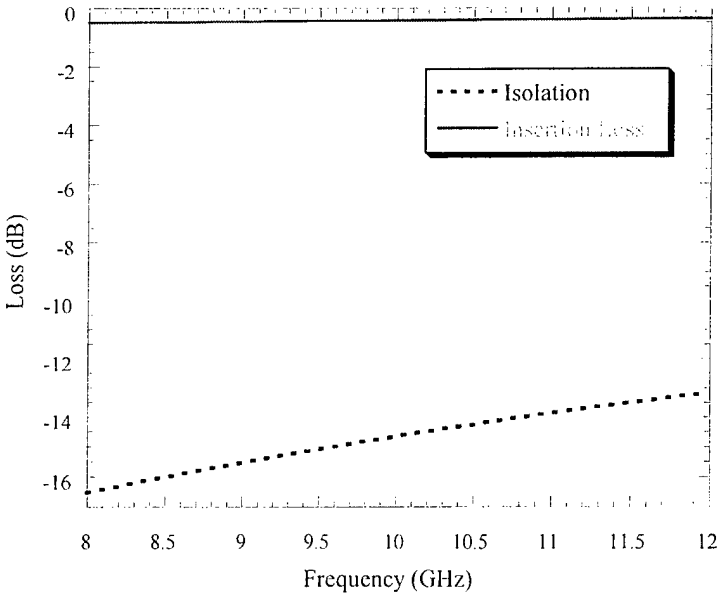

Fig. 3.8. Calculated loss of 300 μm cantilever switch.

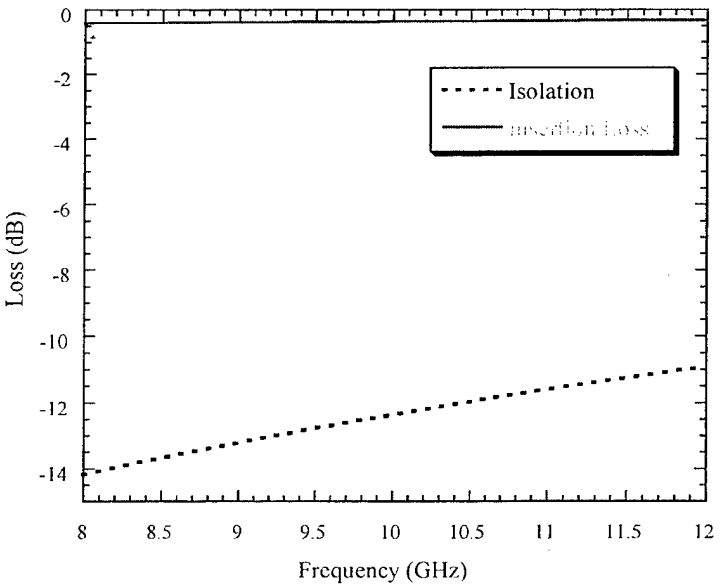

Fig. 3.9. Calculated loss of 400 μm cantilever switch.

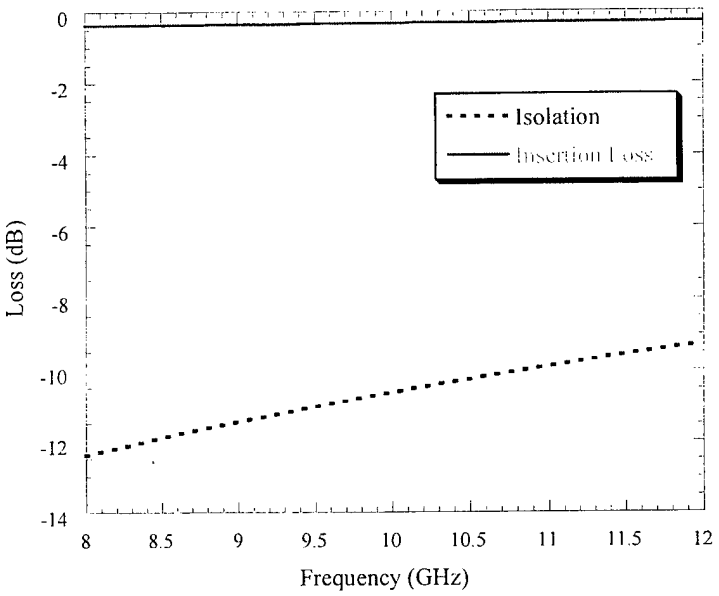

Fig. 3.10. Calculated loss of 500 μm cantilever switch.

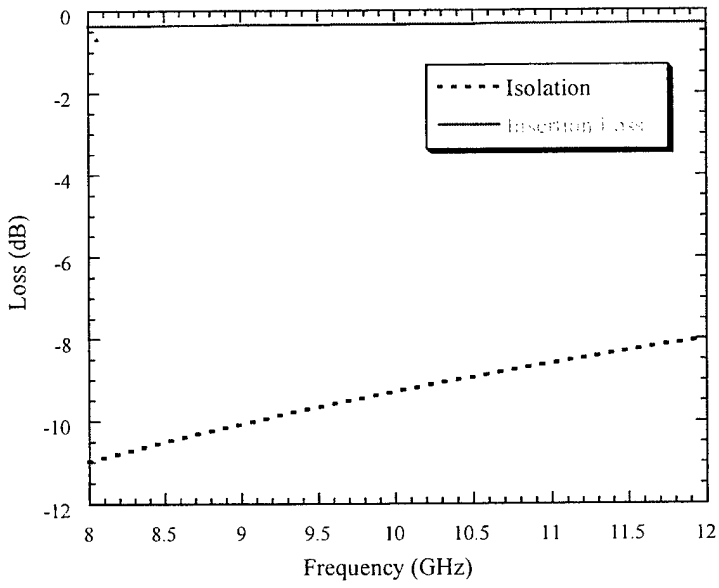

Fig. 3.11. Calculated loss of 600 μm bridge switch.

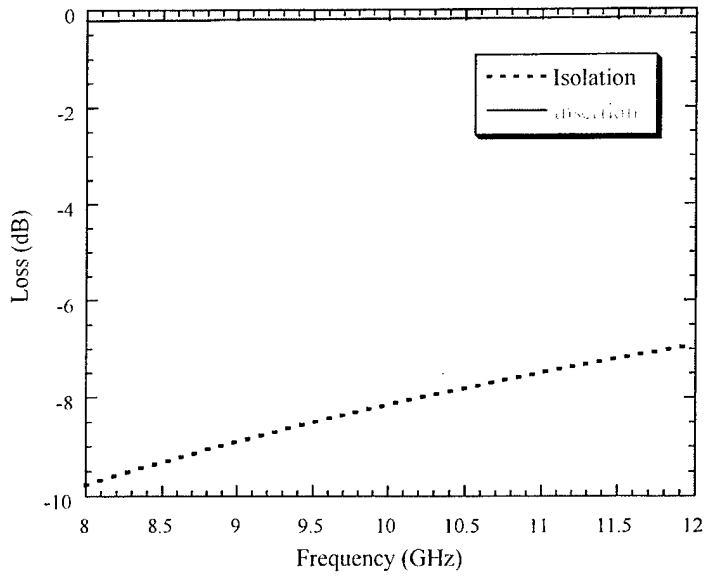

Fig. 3.12. Calculated loss of 700 μm bridge switch.

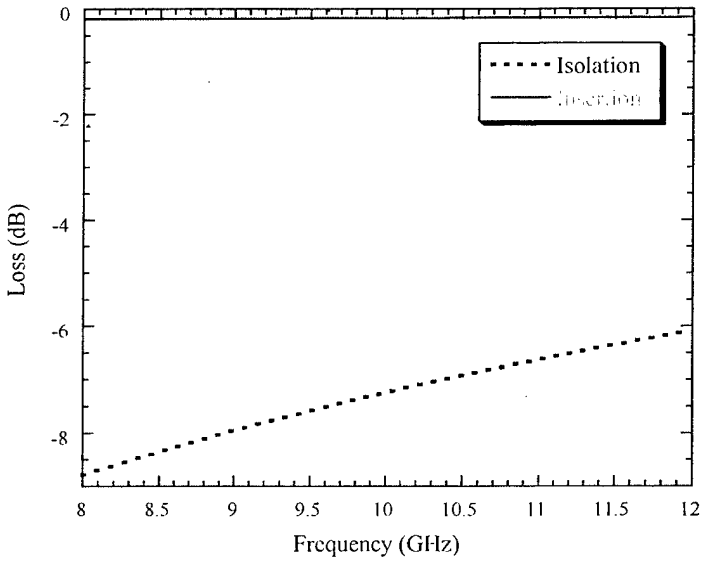

Fig. 3.13. Calculated loss of 800 μm bridge switch.

These results indicate that the insertion loss is reasonably constant, but the isolation decreases with increasing beam length. As the switch length increases, the series resistance increases and the capacitance increases, resulting in lower capacitive impedance.

3.4 Electromagnetic Simulation

Simulations of the switch designs were conducted using the Sonnet $_{em}$® Suite to verify the analytical models. Sonnet $_{cm}$® is a suite of electromagnetic tools used for 3-D planar (microstrip, coplanar, stripline, etc.) analysis. Designs are input through a graphical interface unit *Xgeom* and analyzed using the analysis engine *Em*. *Em* is a full three-dimensional analysis tool based on the Method of Moments and Fast Fourier Transform techniques to simulate the current distribution on the metallization and the electromagnetic coupling on and between dielectric surfaces [16].

Simulations were made for the two switches, the 300 μm cantilever, Fig. 3.14 and 3.15 and the 700 μm bridge, Fig. 3.16 and 3.17. The switch design and material parameters were taken from Tables 3.1 and 3.2 respectively. Results of these simulations show that the Sonnet-em simulations generated higher insertion loss and lower isolation values than the analytical results.

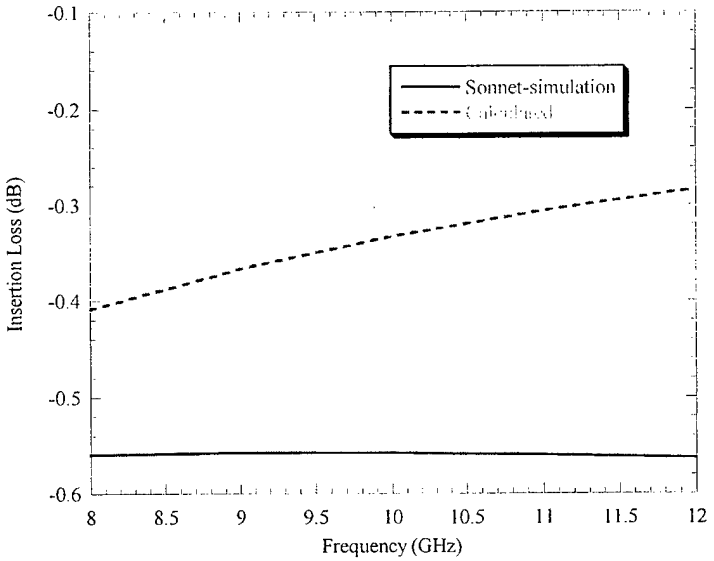

Fig. 3.14. Comparison of calculated and simulated insertion loss for 300 μm cantilever.

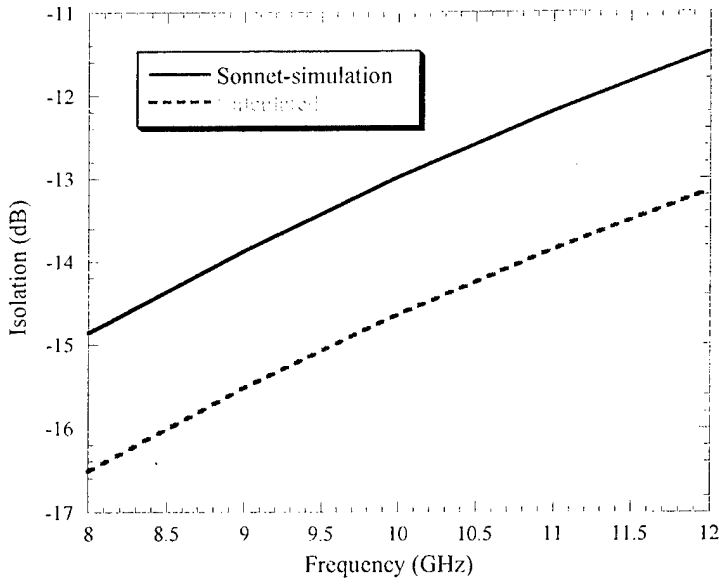

Fig. 3.15. Comparison of calculated and simulated isolation for 300 μm cantilever.

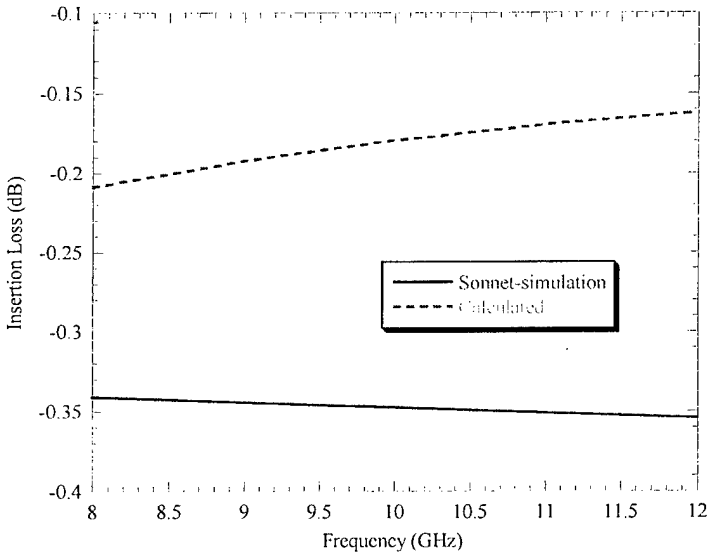

Fig. 3.16. Comparison of calculated and simulated insertion loss for 700 μm bridge.

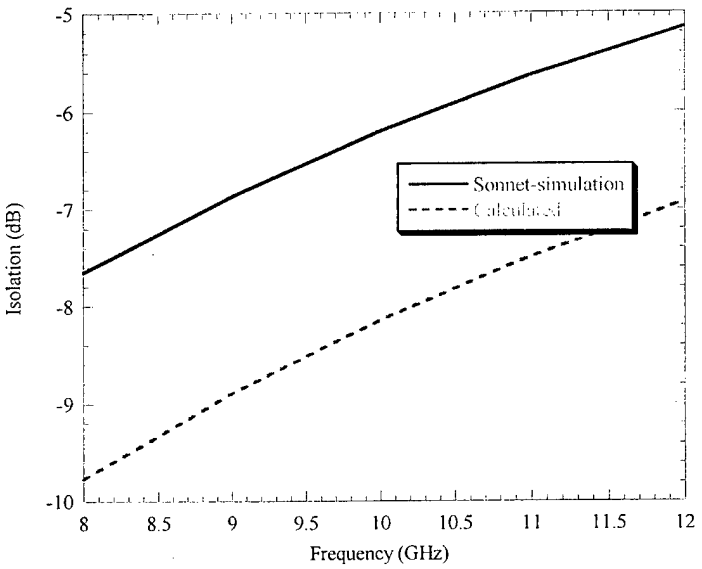

Fig. 3.17. Comparison of calculated and simulated isolation for 700 μm bridge.

These analytical and simulation results were then compared with actual data. As will be discussed in later chapters, switch results were dependent upon material considerations and device yield. To make accurate comparisons between the analytical, simulated, and actual results, material values from actual tested wafers were used in the simulations and are listed in Table 3.5. The transmission line data was from Table 3.2.

Table 3.5
SWITCH MATERIAL PARAMETERS FOR SIMULATIONS.

Parameter	**Cantilevers**	**Bridges**
Bottom Metal	t_L = 0.15 μm	t_L = 0.25 μm
	$2.0995e^7$ S/m	$3.8023e^7$ S/m
Dielectric	t_D= 0.1 μm	t_D=0.25 μm
Post	h= 5.0 μm	h= 5.0 μm
Top Metal	t_U = 1.0 μm Ti / 0.5 μm Au	t_U = 200 Å Ti / 1.5 μm Au
	$1.7476e^7$ S/m	$6.1013e^7$ S/m

Comparison of the insertion losses and isolations for the various switches, Fig. 3.18 to 3.21 were very reasonable. The insertion loss deviates by less than 0.2 dB and the isolation by less than 2 dB over the entire frequency range of 1 – 25 GHz.

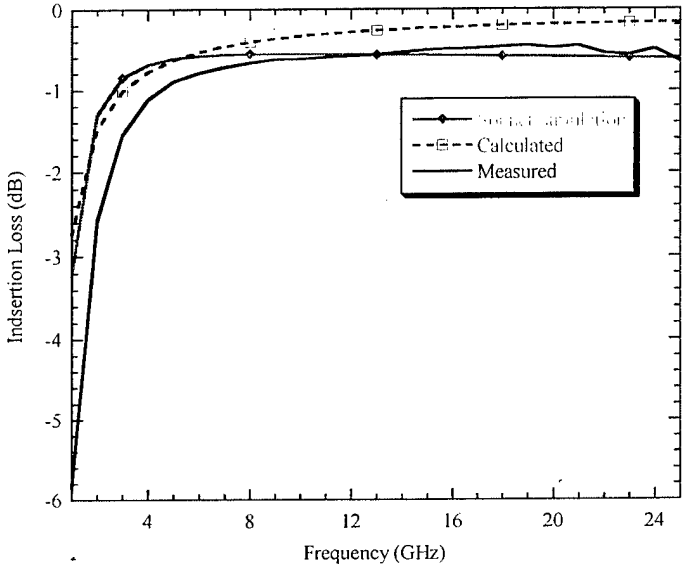

Fig. 3.18. Comparison of insertion loss for 300 μm cantilever.

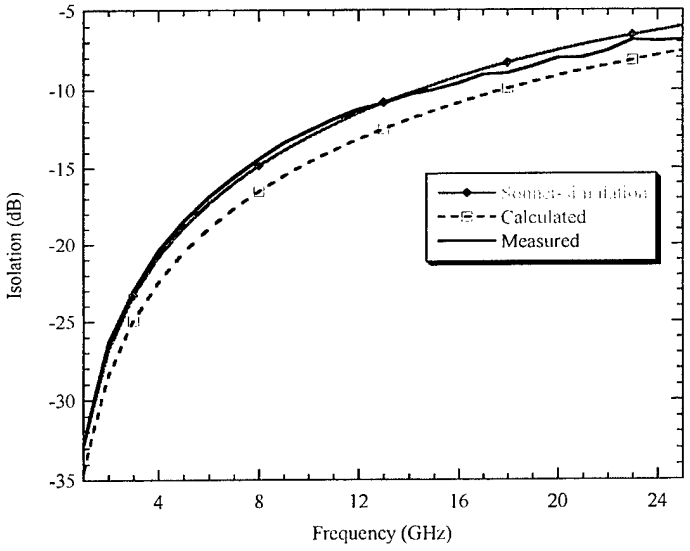

Fig. 3.19. Comparison of isolation for 300 μm cantilever.

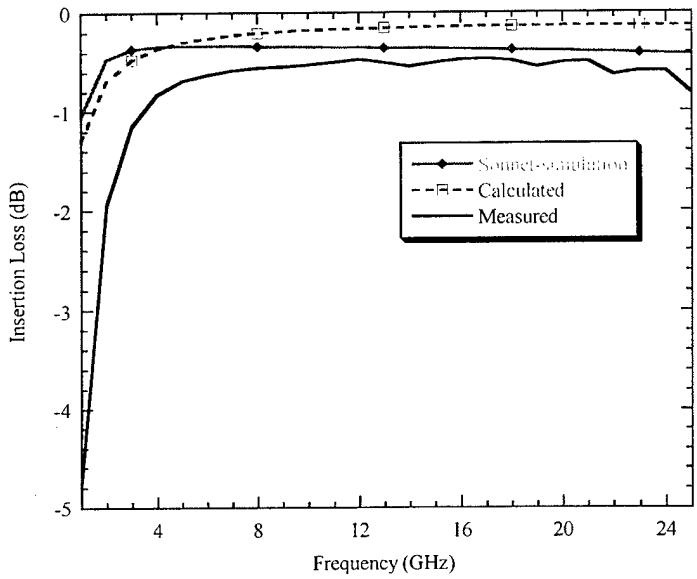

Figure 3.20 Comparison of insertion loss for 700 μm microbridge.

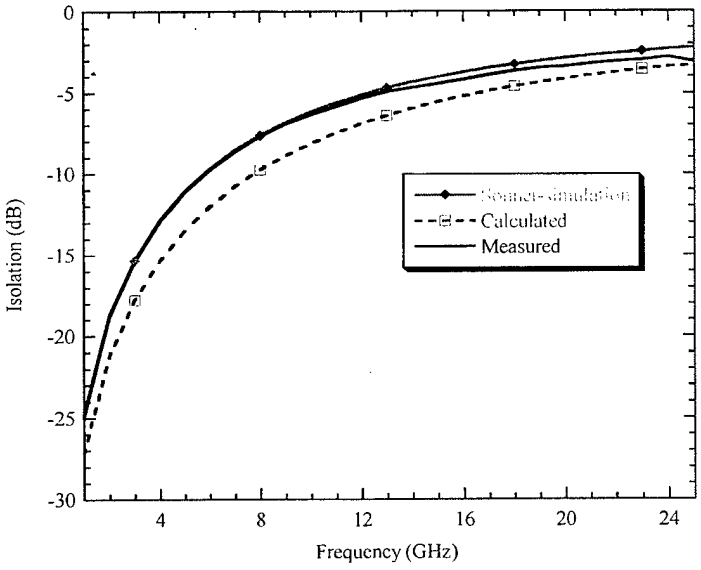

Figure 3.21 Comparison of isolation for 700 μm microbridge.

3.5 Summary

The results of the simulations were in close agreement with the measured results, as shown in Figs. 3.18 to 3.21. The analytical model consistently provided insertion

losses 0.2 dB better than measured value and isolations 2 dB better than the measured values over the entire frequency range of 1 – 25 GHz. The primary contributor to the loss was the capacitance. In the up-state, the theoretical capacitance values were low and indicated more parasitic effects than were taken into consideration. In the down-state, the theoretical capacitance values were approximately three to four times too large. The most obvious reasons for the higher capacitance value would be that the contact area was less than expected, the dielectric constant was less, and the dielectric film thickness was larger than expected. Both the dielectric constant and thickness could be measured fairly accurately, leaving the contact area subject to question. Assuming a lower dielectric constant ($\varepsilon_R = 6$), a thicker dielectric ($t_D = 0.3$ μm), and a contact area of 200 μm by 50 μm still resulted in a theoretical capacitance value approximately twice as large as expected. Additional research is necessary to profile the switches during deflection, particularly while in the contact mode.

Results of the electromagnetic simulations using Sonnet-em®, provided excellent agreement for the off-state, with a variation of 0.1 to 0.2 dB over the frequency range of 1 – 25 GHz. The on-state, insertion loss results were slightly better than the measured values (approximately 0.1 to 0.2 dB) which also indicated that the assumptions concerning contact area were questionable. Overall, both the analytical model and electromagnetic simulations provided accurate results for a first design iteration.

3.6 References

[1]. D.M. Pozar, "*Microwave Engineering*", Addison-Wesley Publishing Company, Reading, MA, (1990): 67 – 200.

[2]. K.C. Gupta, R. Garg, and I.J. Bahl, "*Microstrip Lines and Slotlines*", Artech House, Dedham, MA, (1979): 1 – 3.

[3]. D.M. Pozar, op. cit., 26 – 27.

[4]. D.M. Pozar, op. cit., 714.

[5]. R. Williams, "*Modern GaAs Processing Methods*", Artech House, Norwood, MA, (1990): 320 - 331.

[6]. C.P. Wen, "Coplanar Waveguide: A Surface Strip Transmission Line Suitable for Non-Reciprocal Gyromagnetic Device Applicaion", *IEEE Trans. Microwave Theory and Techniques*, Vol, MTTT-21, 1969: 1087 – 1090.

[7]. K.C. Gupta, et all, "*Microstrip Lines and Slotlines*": 257 – 301.

[8]. D.M. Pozar, "*Microwave Engineering*": 715.

[9]. Z.J. Yao, S. Chèn, S. Eshelman, D. Denniston, and C. Goldsmith, "*Micromachined Low-Loss Microwave Switches*", IEEE Journal of Microelectromechanical Systems, Vol. 8, No. 2, (June 1999): 129 – 134.

[10]. R.Williams, op. cit., 4.

[11]. W.H. Hayt, Jr., "Engineering Electromagnetics", McGraw Hill Book Company, New York, NY, (1981): 435 - 439.

[12]. J.B. Muldavin and G.M. Rebeiz, "High Isolation MEMS Shunt Switches Part 1: Modeling", IEEE Trans. on Microwave Theory and Techniques, Vol 42, (Dec 1999): 1045-1052.

[13]. D.M. Pozar, op. cit., 714.

[14]. S.M. Sze, "*Semiconductor Devices, Physics and Technology*", John Wiley & Sons, New York, NY, (1985): 472.

[15]. J. Helszajn, "*Microwave Engineering: Passive, Active and Non-reciprocal Circuits*", McGraw Hill Book Co., London, England, (1992): pp. 362 – 365.

[16]. Sonnet User's Manual, Volume 1, Release 6.0, Sonnet Software Inc., Liverpool, NY, April 1999.

CHAPTER 4

FABRICATION PROCESS

The fabrication process for the RF MEMS switches was constrained to be fully compatible with standard Gallium Arsenide (GaAs) processes. Although other RF MEMS switch efforts have produced excellent results on high resistivity silicon or quartz substrates [1, 2], these switches cannot be monolithically integrated with active microwave electronics, such as tuning circuits in amplifiers and filters. The intent of this research was to investigate the effect of material systems on the performance of the switches operating over the frequency range of 1 – 26 GHz, and in particular X-band (8 – 12 GHz). The material systems utilized in this research were titanium and gold metallization, silicon nitride dielectric, and photoresist as a sacrificial material. The fabrication process was based upon an air-bridge process routinely used in GaAs circuits for interconnections [3].

4.1 Fabrication Process

The fabrication sequence for the switches consisted of four mask levels and is shown in Fig. 4.1. Process followers and mask layers for all steps are included in Appendix D. A two level photoresist process was used throughout the fabrication to provide precise pattern definition and repeatability. The bottom layer resist was a polymethylglutarimide (PMGI) positive resist sensitive to deep ultra-violet (DUV) radiation and developed with a SAL 101 developer. The top layer resist was a Microposit S1800 series positive resist exposed at 405 nm and developed with a diluted Microposit

351 developer. Alignment was performed using a Karl Suss MJB-3 Mask Aligner and the DUV exposure was conducted using a JBA Flood Deep UV source.

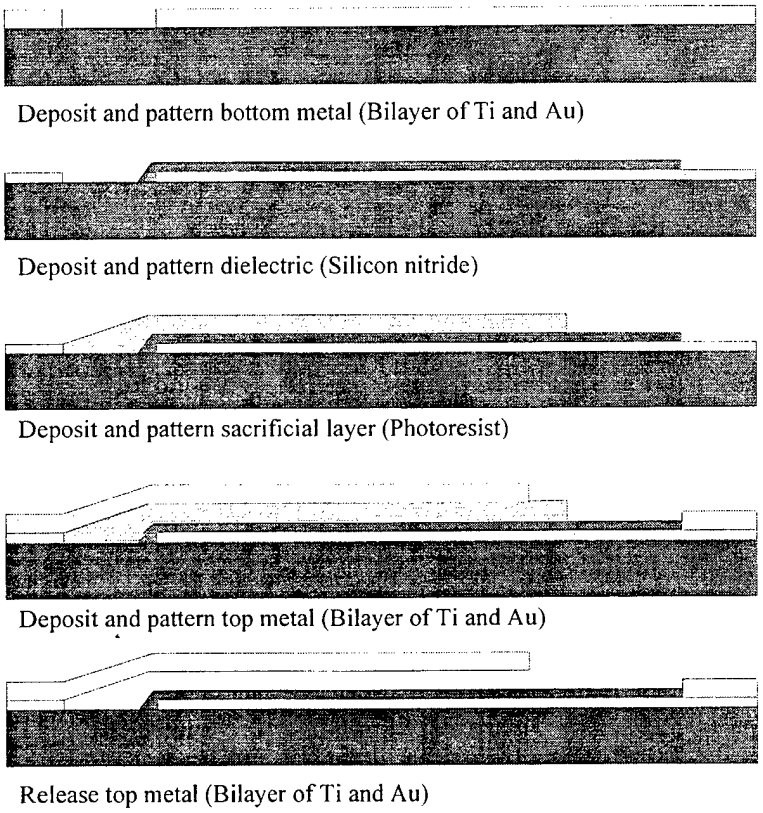

Fig. 4.1. Fabrication sequence for the cantilever beam switch.

The process began with wafer cleaning and lithography to form the pattern for the bottom level metal. A 200 Å titanium (Ti) adhesion layer was evaporated followed by 2300 Å evaporated gold (Au). Metal evaporation was done using a Temescal BJD or FC-1800 E-beam evaporator operating in the mid 10^{-7} torr range. The purity of the Ti was MARZ grade (99.97) with a deposition rate of 7 Å/sec for thick deposits (> 1000 Å) and 5 Å/sec for thin deposits. The purity of Au was 99.99, with a deposition rate of

10 – 12 Å/sec. Excess metal was removed using tape lift-off and residue was removed using an Acetone spray. Bottom metal thickness was measured with a Tencor profilometer.

The next processing sequence consisted of a blanket deposition of 2500 Å silicon nitride. Silicon nitride was deposited using either a Semi Group Plasma Enhanced Chemical Vapor Deposition (PECVD) system or reactively sputtered using a Denton Discovery Sputter system. After nitride deposition, the nitride was patterned and the unwanted nitride was etched. A wet etch was used for the PECVD nitride and a dry etch was used for the sputtered nitride. The wet etch consisted of a diluted Buffered Oxide Etch (BOE) consisting of (1:7, HF:water) and had an etch rate of 70 Å/sec. The sputtered nitride was impervious to the wet etch and was removed in a PlasmaTherm Dual Chamber Reactive Ion Etching (RIE) system using Freon 14 gas with an etch rate of 330 Å/min. The deposition conditions for the PECVD system are listed in Table 4.1. Deposition conditions for the reactively sputtered silicon nitride are listed in Table 4.2.

Table 4.1
PECVD SILICON NITRIDE DEPOSITION CONDITIONS.

Parameter	**Value**
Gas 1 (5% silane and 95% nitrogen)	168 sccm
Gas 2 (nitrogen)	1250 sccm
Gas 3 (ammonia)	10 sccm
Forward RF power	21 Watts
RF frequency	13.56 MHz
Chamber pressure	850 mTorr
Chamber temperature	250°C or 300°C
Index of refraction	1.903
Deposition rate	100 Å/min

Sccm – Standard Cubic Centimeters per Minute

Table 4.2
SPUTTERED SILICON NITRIDE DEPOSITION CONDITIONS.

Parameter	**Value**
Gas 1 (argon)	71.1 sccm
Gas 2 (nitrogen)	70.6 sccm
Forward RF power	400W
Target bias	604 V
Base chamber pressure	8×10^{-9} Torr
Sputter pressure	5.2 mTorr
Temperature	21 °C
Deposition rate	105 Å/min

The third process sequence consisted of depositing the sacrificial layer or post which defined the gap spacing of the switch. A thick, high temperature photoresist (SF-19 PMGI) was used to form the post. After resist exposure and development, the post was reflowed in a 250 °C hot air oven for 90 seconds. Reflow was critical to form the smooth edge profile required when using evaporated metal. Examples of good and bad reflow are shown in the next section. After reflow, the wafer was subjected to a hard bake for over an hour in a 90 °C hot air oven.

The fourth sequence involved the deposition, patterning, and release of the evaporated top-level metal. The top-level metal was defined using a poly(methylmethacrylate) (PMMA) positive resist that was developed with chlorobenzene. Top-level metal was maintained at a constant thickness of 1.5 μm, but the relative thicknesses of Ti and Au was varied to control residual stress. Results of these experiments will be discussed in Chapter 5. A scanning electron micrograph of the top-level metal before lift-off is shown in Fig. 4.2. In this picture, the circular caps are the perforations on the top-level metal that are removed in the acetone lift-off. A scanning electron micrograph of the top-level metal after lift-off is shown in Fig. 4.3.

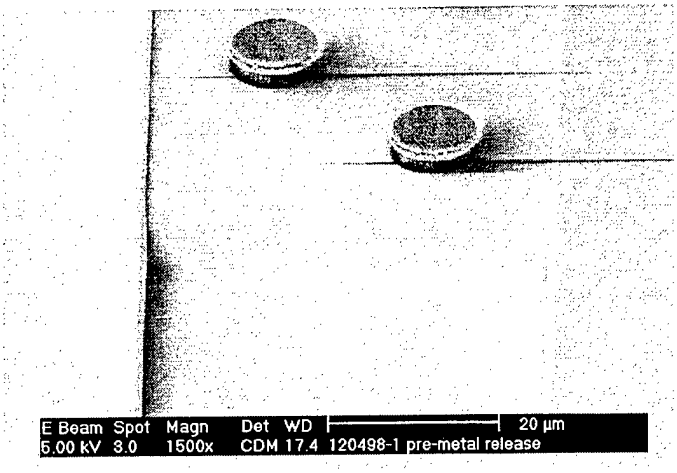

Fig. 4.2. Scanning electron micrograph of top-level metal before lift-off.

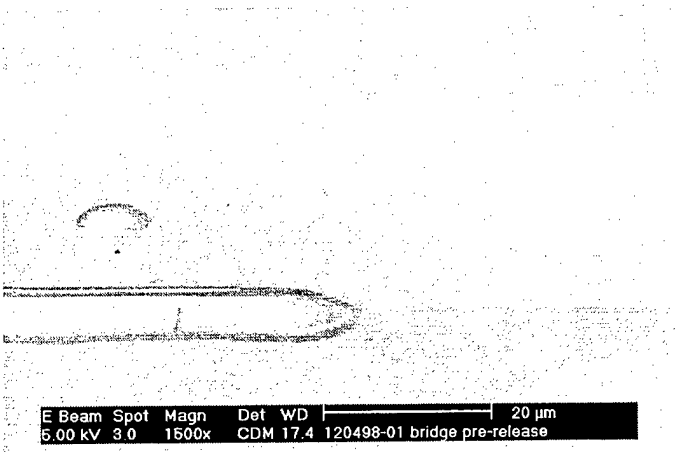

Fig. 4.3. Scanning electron micrograph of top-level metal after lift-off.

The release step consisted of dissolving the photoresist in hot (90 °C) Microposit 1165 stripper. Removal of residue was done through a petri dish rinse in a solution of DI water and methanol (1:1), followed by a petri dish rinse in methanol, and then a petri dish rinse in isoproply alcohol (IPA). The alcohol was then allowed to air dry, resulting in released switches. Examples of released cantilever beam switches and microbridges are shown in the micrographs of Fig. 4.4

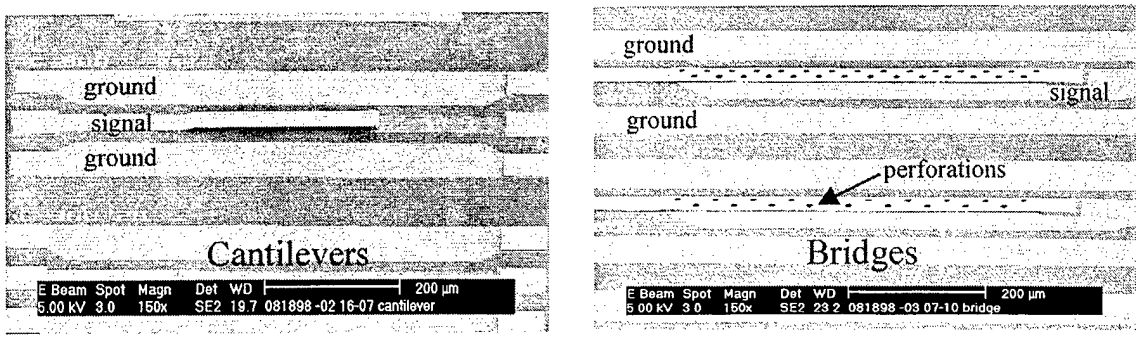

0.5 µm Au on 1.0 µm Ti

Fig. 4.4. Released cantilever and microbridge switches.

4.2 Switch Layout

As discussed previously, two switch designs were investigated, a cantilever beam and a microbridge. Both switch designs used a constant beam width of 50 µm and a 5.0 µm air gap. For the cantilevers, three beam lengths were investigated 300 µm, 400 µm, and 500 µm. For the microbridges, three beam lengths were also investigated 600 µm, 700 µm, and 800 µm. Also, for each cantilever and microbridge beam length, three perforation patterns were included, along with a beam containing no perforations. The perforation patterns and nomenclature are shown in Fig. 4.5. In all cases, the perforations were 10 µm in diameter. The four mask level steps for both cantilever beam and microbridge switches are shown in Fig. 4.6.

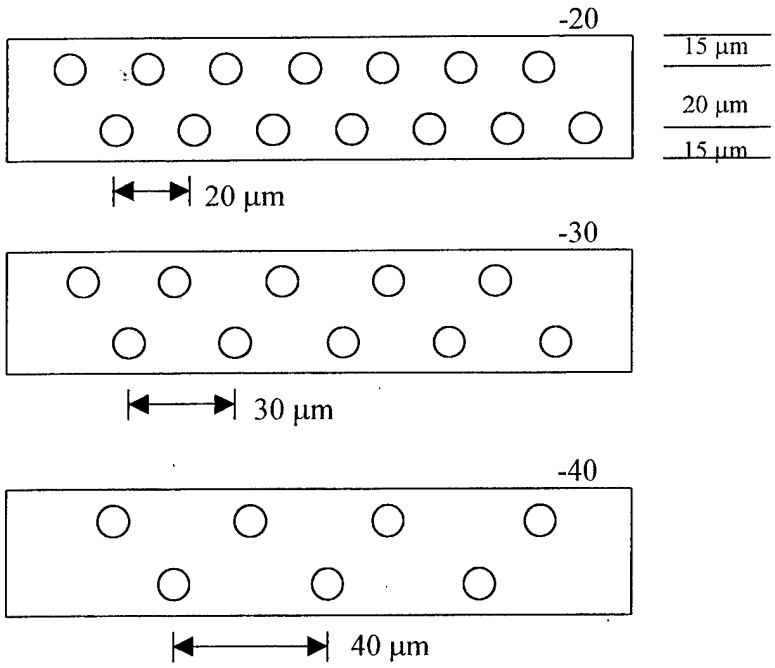

Fig. 4.5. Beam perforation patterns and nomenclature.

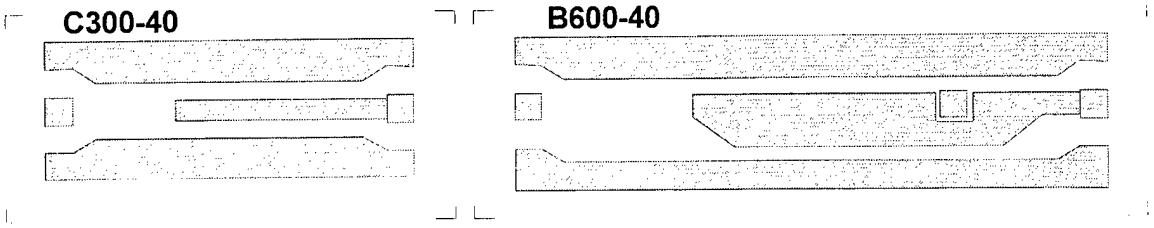

Bottom metal (200 Å Ti / 2300 Å Au)

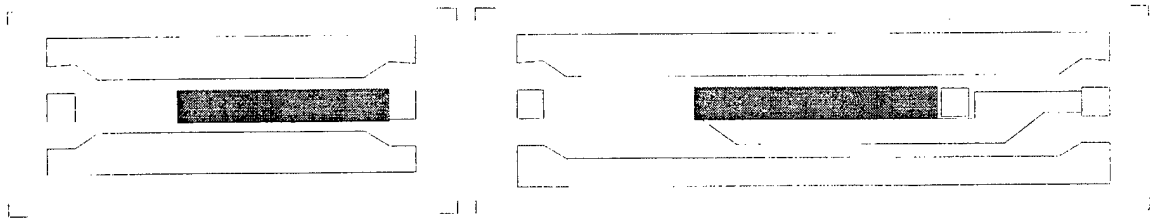

Silicon nitride (2500 Å)

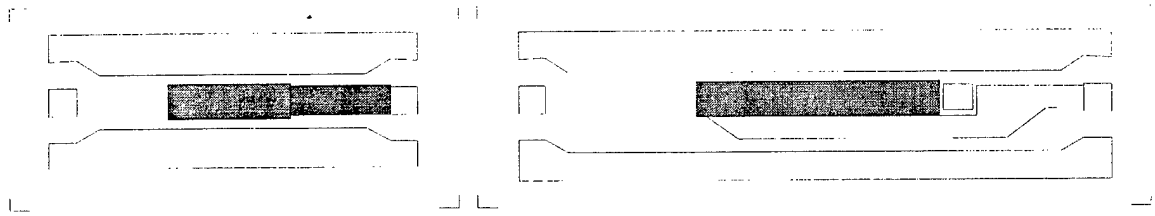

Post (5.0 μm PMGI photoresist)

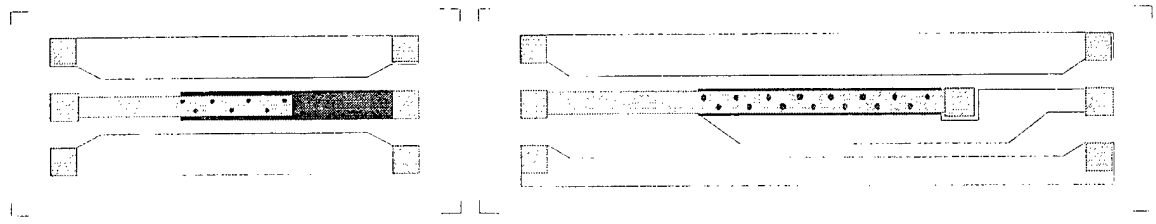

Top metal (1.5 μm Ti/Au)

Fig. 4.6. Mask levels for cantilever and microbridge switches.

4.3 Fabrication Issues

The primary fabrication step, which affected device yield, was the reflow of the sacrificial or post resist. Proper reflow, as shown in Fig. 4.3, provided the smooth curved transition necessary when using evaporated metal. Insufficient reflow, as shown in Fig. 4.7 caused an abrupt transition that led to crack formation at the point of flexure. This scanning electron micrograph was taken after ion milling through a section of the beam at the point of flexure, prior to lift-off. Ion milling was performed using a FEI Inc. dual beam (focused ion beam/scanning electron) microscope system. The lift-off and release processes caused the crack in Figure 4.7 to propagate, resulting in the broken switch, Fig. 4.8. On wafers fabricated with insufficient post reflow, the majority of switches sheared off at the point of flexure and were rinsed away in the acetone lift-off step.

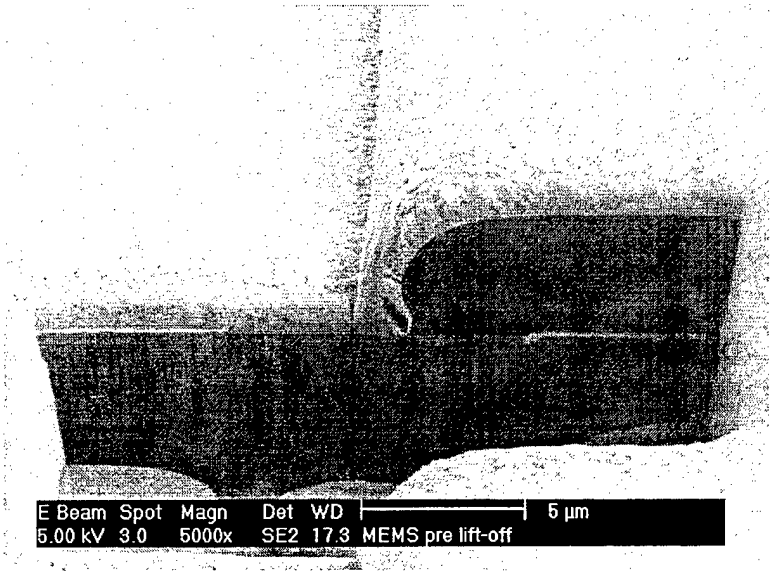

Fig. 4.7. Cross-section of the switch structure prior to lift-off.

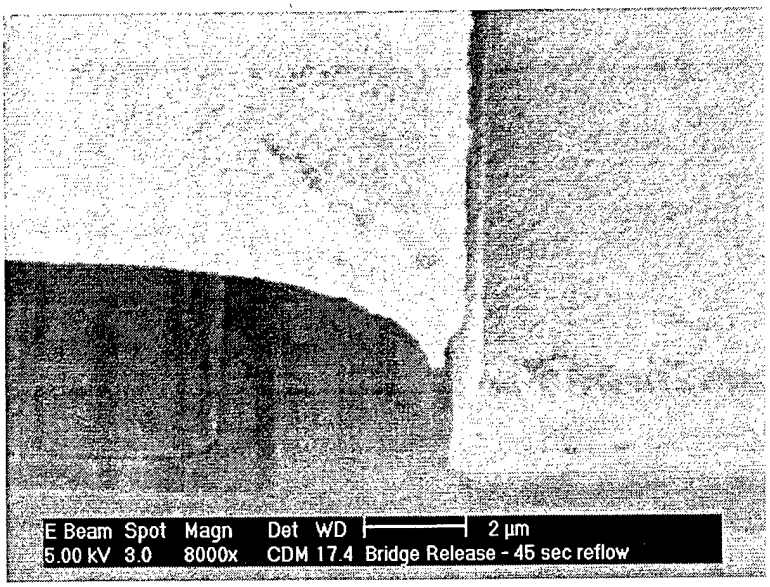

Fig. 4.8. Bridge structure after release indicating sheared beam.

As the reflow time was increased, the abrupt junction at the point of flexure was minimized, but the beams exhibited a slight bow across the width, as shown in Figs. 4.9 and 4.10. These images were also taken after ion beam milling through the beam. The circular cap in the upper left hand corner of Fig. 4.9 was a remnant of a perforation that was not removed during the lift-off process and was subsequently redeposited on the substrate. The surface roughness surrounding the cut was due to redeposition of material from the milling process. Fig. 4.11 shows the extent of cupping that occurred at the tip of the cantilever for this reflow condition.

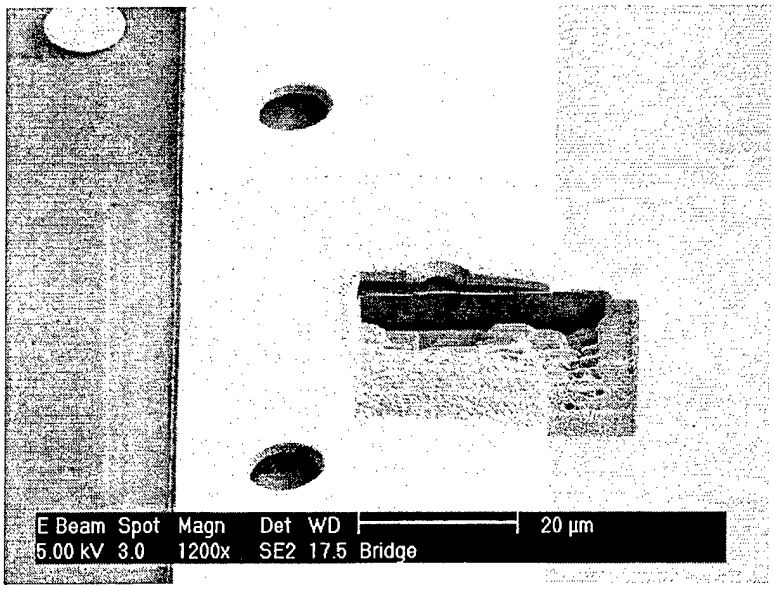

Fig. 4.9. Cross-section of cupped beam resulting from insufficient reflow time.

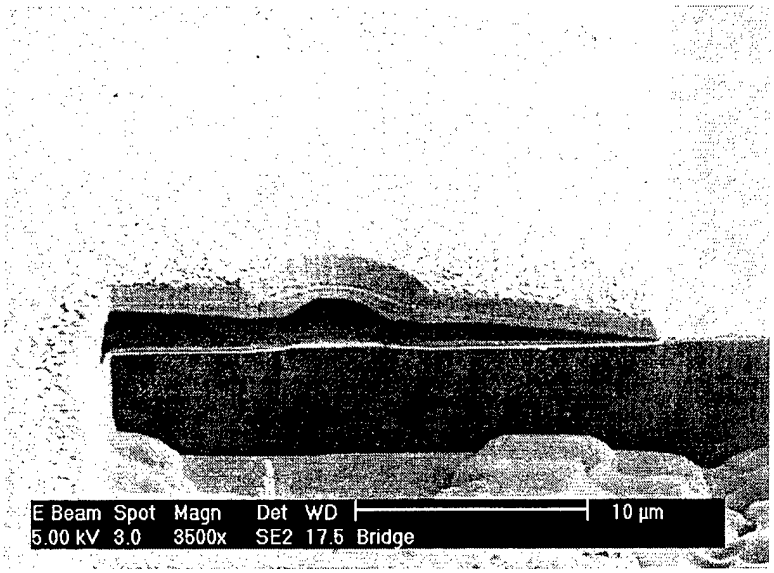

Fig. 4.10. Close-up of milled section of cupped beam.

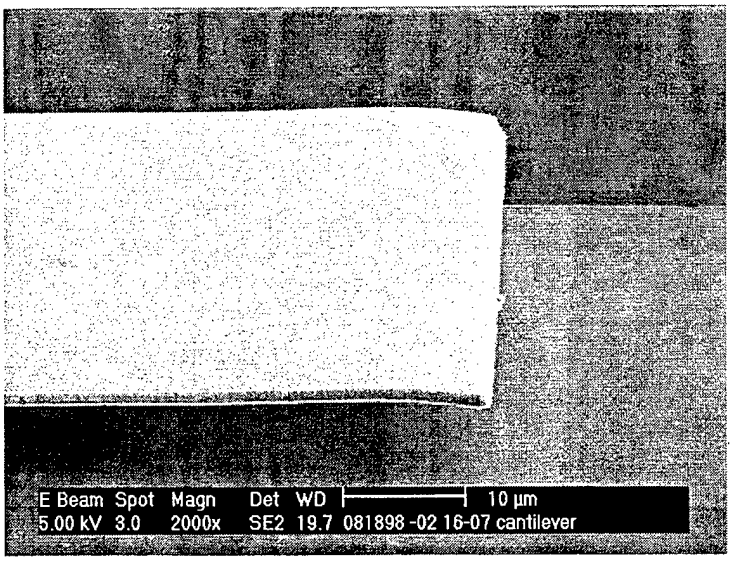

Fig. 4.11. Close-up of curling at beam tip due to insufficient reflow time.

When the reflow time was adjusted to the proper time of 90 seconds, a smooth transition was obtained, as shown in Fig. 4.12. This image shows a smooth transition at the point of flexure and good step coverage of the silicon nitride over the bottom level metal. Scanning electron micrographs of functional cantilever and microbridge switches are shown in Figs. 4.13 and 4.14.

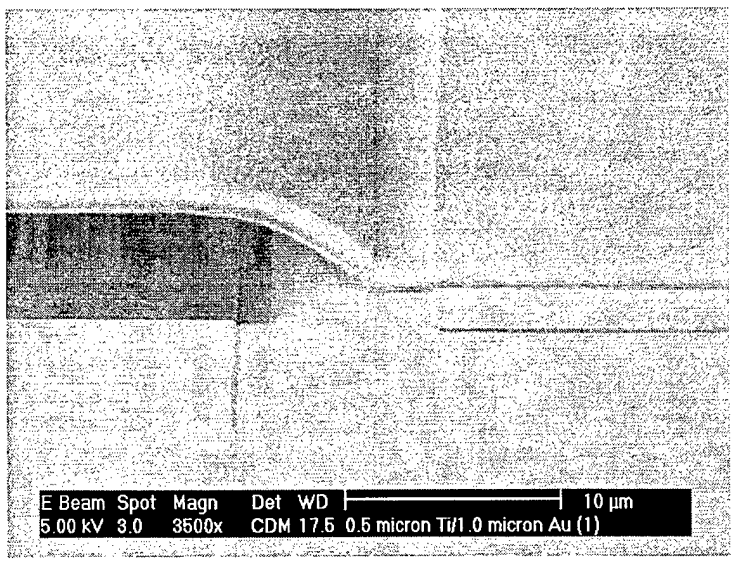

Fig. 4.12. Smooth transition at point of flexure due to proper reflow time.

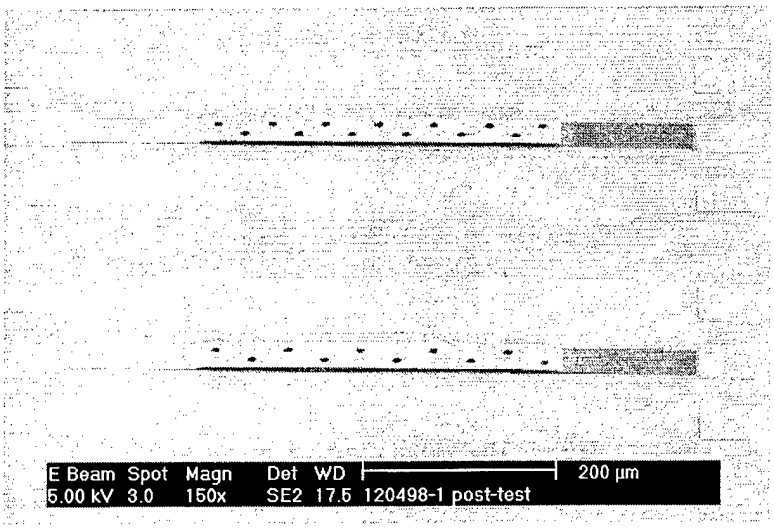

Fig. 4.13. Scanning electron micrograph of 400 µm long cantilever switches.

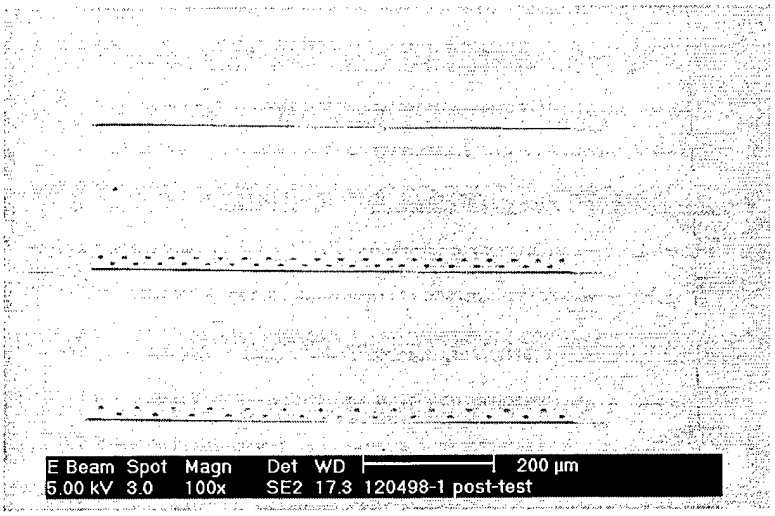

Fig. 4.14. Scanning electron micrographs of 800 µm long microbridge switches.

4.4 Summary

In total, 25 GaAs wafers were processed, of which 20 were used for switch processing variations. Functional devices were obtained from five wafers. A listing of the process parameters for the functional wafers is provided in Table 4.3. Comparisons between switch performance and material characteristics will be presented in Chapter 5.

Table 4.3

FUNCTIONAL WAFER PROCESS PARAMETERS.

Run condition	**R120498-1**	**MEMS-1C**	**MEMS-3A**	**MEMS-3C**	**MEMS-4**
Bottom metal	200 Å Ti 1300 Å Au	200 Å Ti / 2300 Å Au			
Dielectric	1000 Å PECVD Si_3N_4		2500 Å sputtered Si_3N_4 20% N_2 flow	2500 Å sputtered Si_3N_4 50% N_2 flow	
Post	5.0 μm (SF-19 PMGI)				
Top metal	1.0 μm Ti 0.5 μm Au	0.5 μm Ti 1.0 μm Au	200 Å Ti / 1.5 μm Au		500 Å Ti 6500 Å Au 500 Å Ti
Cantilevers: Visible Yield / Tested Yield	67% / 35%	0			
Bridges: Visible Yield / Tested Yield	87% / 35%	39% / 38%	53% / 2%	13% / 10%	74% / 43%

4.5 References

[1]. Z.J. Yao, S. Chen, S. Eshelman, D. Denniston, and C. Goldsmith, "Micromachined Low-Loss Microwave Switches", *IEEE Journal of Microelectromechanical Systems*, Vol. 8, No. 2, (June 1999): 129-134.

[2]. J.B. Muldavin and G.M. Rebeiz, "High Isolation MEMS Shunt Switches Part 1: Modeling:, *IEEE. Trans. on Microwave Theory and Techniques*, Vol. 48, No., 6 (June 2000): 1045-1052.

[3]. R. Williams, "*Modern GaAs Processing Methods*", Artech House, Norwood MA (1990): 320-321.

CHAPTER 5

MATERIALS INFLUENCE

The performance of MEMS switches is highly dependent on the switches' constituent materials [1]. The switch material must be able to provide both structural integrity and high electrical conductivity. In this study, cantilever and spring bridge microswitches were fabricated on GaAs substrates using evaporated bilayers of titanium and gold metallization. The beam width was fixed at 50 μm and the total thickness was held constant at 1.5 μm while the thickness of gold varied from 0.5 μm to 1.5 μm. The lengths of the cantilevers varied from 300 to 500 μm and the spring bridge lengths varied from 600 to 800 μm. The material properties of film stress and resistivity were made using laser reflectometry and four-point probing, respectively. This chapter will present the results of the observed microswitch structure within the context of the measured film stresses. Comparisons of the average film stress, insertion loss, isolation, and actuation voltages were made based on the various beam metal thickness ratios.

5.1 Average Stress Characteristics

Average stress measurements of the various thin film metals were made using a Tencor® FLX-2900 Thin Film Stress Measurement System. This system calculates the average intrinsic stress, σ, using the radius of curvature and Stoney's equation [2, 3]

$$\sigma = \frac{Et_w^2}{(1-\nu)6Rt_f}, \tag{5.1}$$

where E is the Modulus of Elasticity, ν is Poisson's ratio, t_w is the thickness of the wafer, t_f is the thickness of the film, and R is radius of curvature of the wafer. Differences in the intrinsic stress measurements on Si and GaAs substrates were negligible and the film stress measurements reported are from Si substrates.

The residual stress of evaporated Au films (with a 200 Å Ti adhesion layer) varying from 0.7 μm to 2.0 μm thickness was nominally stress free (1 MPa compressive to 16 MPa tensile). Bilayer films of Ti/Au were evaporated with a fixed total thickness of 1.5 μm and varying gold thickness. A comparison of the measured average intrinsic stress between the dominant gold films and the Ti/Au bilayer films is provided in Fig. 5.1. Since the Au films were found to be relatively stress free, the Ti layer dominated the stress of the Ti/Au bilayer films.

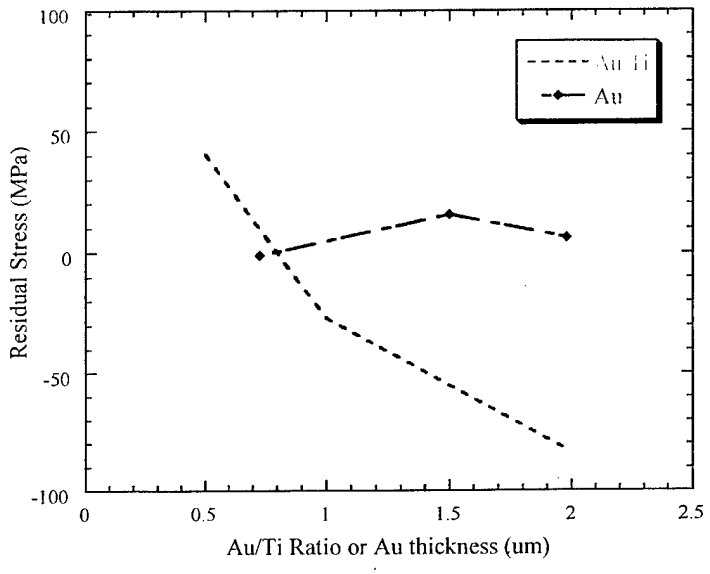

Fig. 5.1. Average residual stress versus either ratio of gold to titanium thickness in TiAu bilayer films or gold thickness.

Fabricated switches exhibited noticeable variations in stiffness due to the top-layer metallization. The switches shown in Fig. 5.2 and 5.3 consisted of 0.5 μm Au on

1.0 μm Ti. This metal combination resulted in a low stress film as indicated by the cantilever of Fig. 5.2 and the bridge switches of Fig. 5.3.

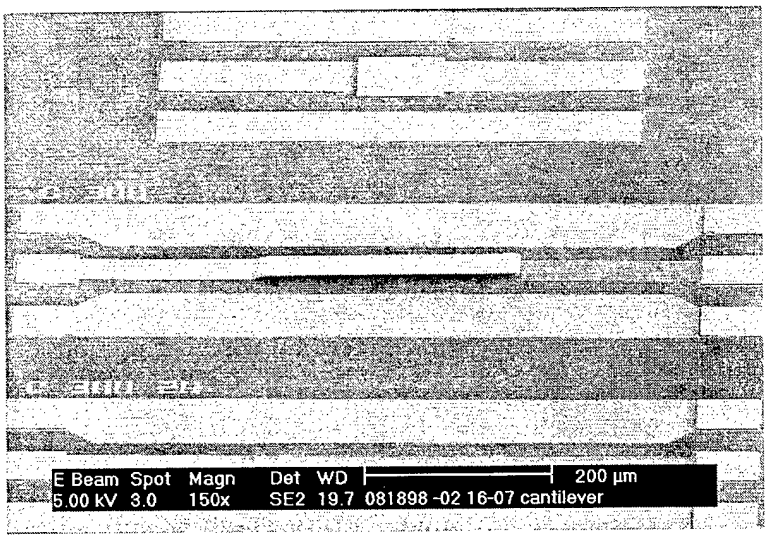

Fig. 5.2. Released cantilever beam switches composed of 0.5 μm Au on 1.0 μm Ti.

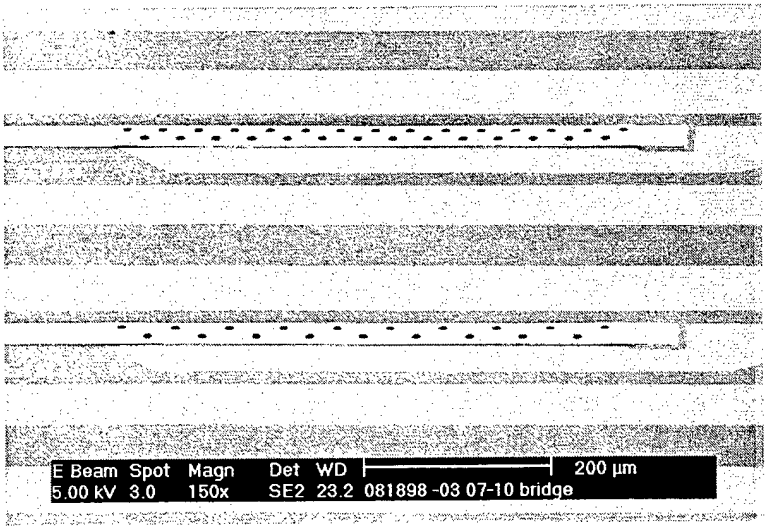

Fig. 5.3. Released bridge switches composed of 0.5 μm Au on 1.0 μm Ti.

As the bilayer combination of Ti/Au was varied, a pronounced stress gradient in the top metal film was evident from the curling of the cantilevers. The bilayer combination of 1.0 μm Au on 0.5 μm Ti resulted in a stress gradient of the released

beams as shown by the curled cantilevers of Fig. 5.4. These cantilevers curled out the plane, required actuation voltages in excess of 60 V, and were considered non-functional.

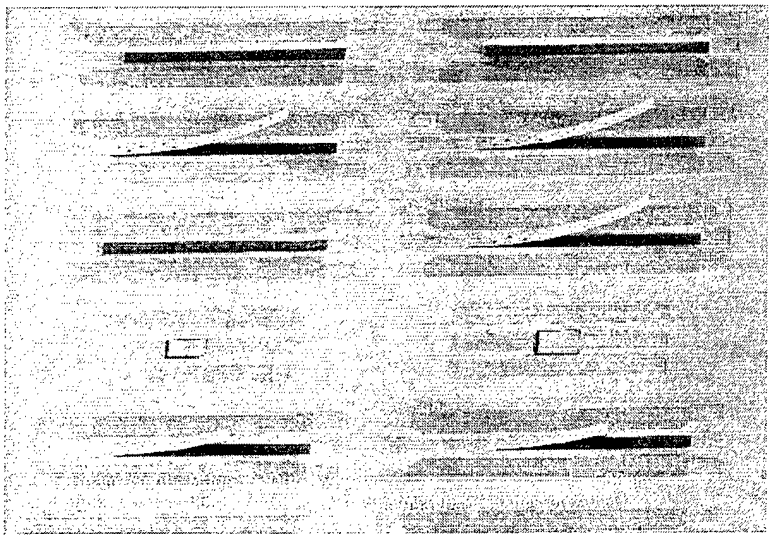

Fig. 5.4. Released cantilever beams composed of 1.0 μm Au on 0.5 μm Ti.

Although a stress gradient existed within the top metal, many of the spring bridges were susceptible to stiction resulting from the wet release process. In this release process, the surface tension of the deionized water used to rinse the wafer was sufficient to overcome the spring tension of the structure and cause stiction. In this study, circular perforations or cut outs were included on some beams to reduce contact surface area and investigate stiction effects of the wet release process. The top bridge switch in Fig. 5.5 had no perforations and was stuck to the substrate, while the lower bridges, containing perforations were functional.

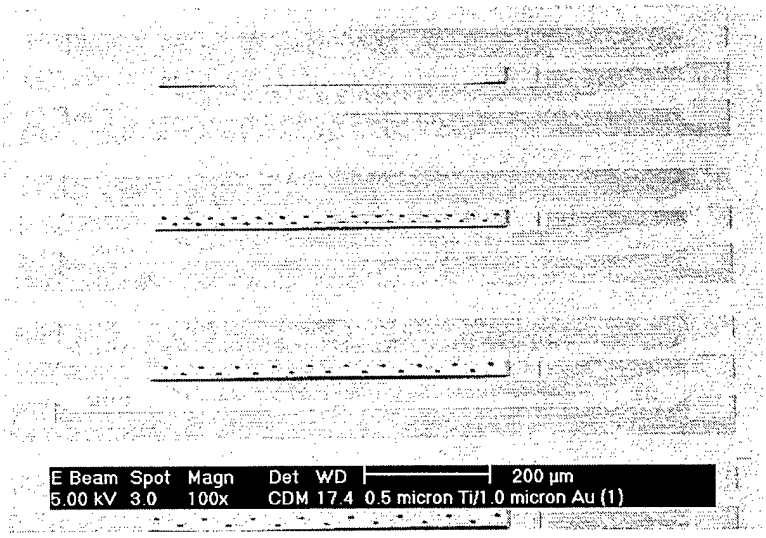

Fig. 5.5. Released bridge switches composed of 1.0 µm Au on 0.5 µm Ti.

For the extreme case of 1.5 µm Au on a 200 Å Ti adhesion layer, the released stress gradient caused the cantilevers to curl and the bridges to bow upwards as shown in Fig. 5.6 and 5.7. The bridges exhibited an upward bow of approximately 8 µm at the beam center. Under all conditions, the bridges with the highest density of perforations, i.e. less surface area along its length were least susceptible to stiction. The mottling of the substrates was due to a residue from the release process.

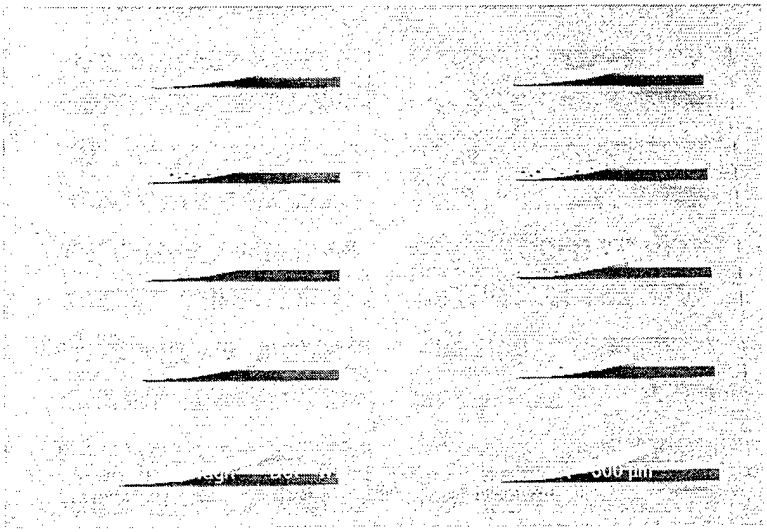

Fig. 5.6. Released cantilever beam switches composed of 1.5 µm Au on 200 Å Ti.

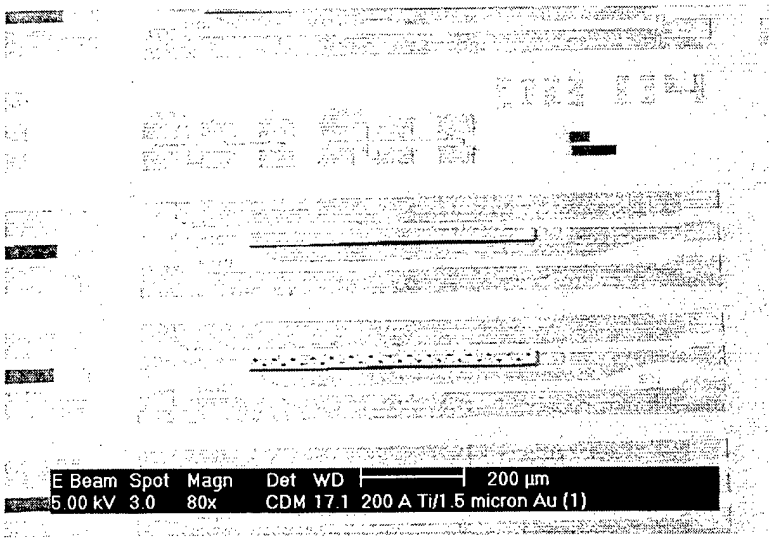

Fig. 5.7. Released bridge switches composed of 1.5 µm Au on 200 Å Ti.

Based upon these results, the structural integrity of the switches was dominated by the thickness of the Ti layer. The bilayer combination of 0.5 µm Au on 1.0 µm Ti resulted in a low stress film and functional cantilever and bridge switches. The other bilayer combinations produced stress gradients that caused the cantilevers to curl upward. The impact of the bilayer films on microwave performance will be discussed in the next section, followed by a discussion of yield.

5.2 Microwave Performance

To determine the impact of bilayer film composition on microwave performance, the switches were tested using a 10 GHz signal. Details of the RF testing are discussed Chapter 6, but in principal an RF signal (10 GHz) riding on a pulsed DC voltage was applied to the switches and the output RF signal was measured. The pulsed DC signal was limited to 60 V by the test equipment. The microwave performance was clearly influenced by the released stress gradient and bilayer composition. Cantilevers curled as

shown in Figs. 5.4 and 5.6 required actuation voltages in excess of 60 V and were not tested.

Functional cantilevers were only available on the wafers using the 0.5 μm Au on 1.0 μm Ti bilayer composition, Fig. 5.2. Average S-parameter and actuation voltages of these cantilevers, taken from several die sites are shown in Table 5.1. This data demonstrates the conflicting issues of switch size and performance. Short cantilevers provide higher isolation at the expense of higher insertion loss and actuation voltage.

Table 5.1
CANTILEVER BEAM MICROWAVE PERFORMANCE FOR
0.5 μm Au ON 1.0 μm Ti.

Cantilever Switch Length (μm)	**Insertion Loss (dB @ 10 GHz)**	**Isolation (dB @ 10 GHz)**	**Actuation Voltage (V)**
300	0.6 – 0.7	11.7 – 13.6	20.5 – 23.2
400	0.5 – 0.6	11.0 – 13.0	16.7 – 19.7
500	0.5	10.7 – 12.1	15.0 – 23.5

Functional bridges were tested for all bilayer compositions. Switches with the highest concentration of perforations, the –20 variants, (Fig. 4.5) offered the highest yield and were used for comparison. The insertion loss for the 600 μm, 700 μm, and 800 μm bridges, shown in Fig. 5.8 decreased as the thickness of gold increased. Switch isolation, shown in Fig. 5.9 increased as the gold thickness increased, as a result of a slight upward bow of the beams. The most pronounced effect of beam curvature appeared in the actuation voltage, Fig. 5.10. Nearly twice the voltage was required to activate switches composed of 1.5 μm thick gold. As discussed in Chapter 1, published results for RF MEMS switches operating at 10 GHz give insertion losses of 0.1 – 0.2 dB, isolations of 15 – 30 dB, and actuation voltages of 50 V. However, these devices were in the shunt configuration and no data on series configured switches using capacitive coupling has

been published, to the author's knowledge. Direct comparisons with these values are inappropriate as these results represent a variety of switch designs including contact switches and shunt configurations in which actuation causes the switch to ground the signal line. Insertion losses of 0.6 and 0.7 dB, isolations of 12 and 6 dB, and actuation voltages of 19 and 30 V for cantilevers and bridges, respectively, are reasonable and can be optimized after the material characteristics are understood. To the authors' knowledge, data on thick Ti/Au beams has not been reported in the open literature.

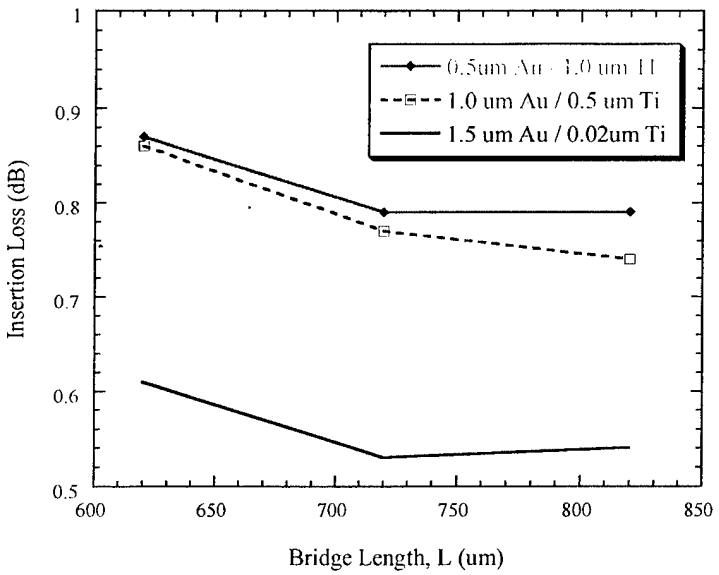

Fig. 5.8. Insertion loss for various Ti/Au bilayer film compositions.

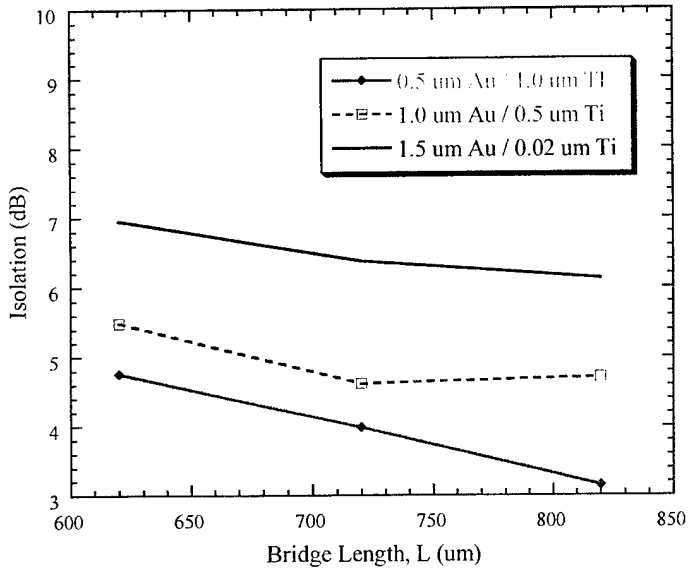

Fig. 5.9. Isolation for various Ti/Au bilayer film compositions.

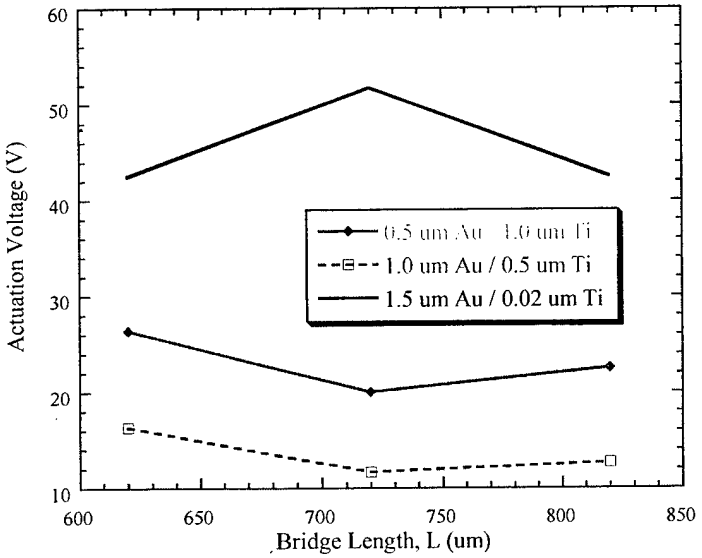

Fig. 5.10. Actuation voltage for various Ti/Au bilayer film compositions.

A tri-layer film composition consisting of 500 Å Ti / 6500 Å Au / 500 Å Ti was also processed, yielding functional bridges. Cantilevers, shown in Fig. 5.11 were generally curled and non-functional. Bridges, shown in Fig. 5.12 were functional and

characterized at 1 – 26 GHz. Results of the 600 μm, 700 μm, and 800 μm long bridges tested at 10 GHz are shown in Figs. 5.13 and 5.14 for the insertion loss and isolation respectively. The actuation voltage was 20 V for all bridge lengths.

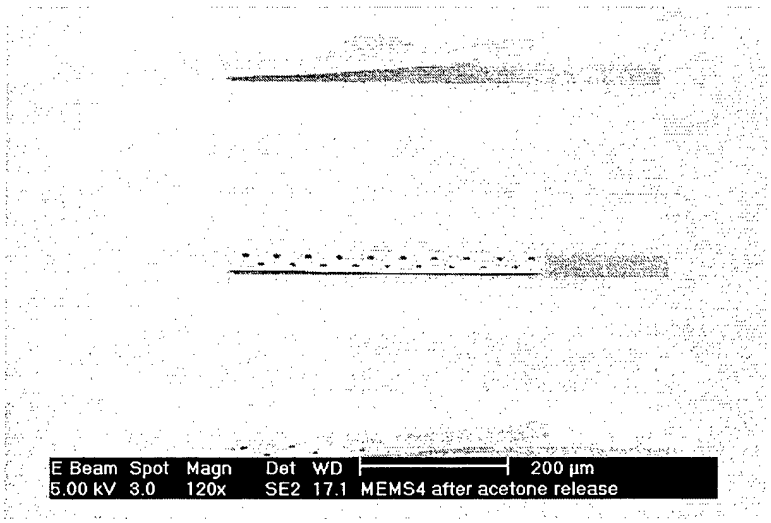

Fig. 5.11. Released cantilever switches composed of 500 Å Ti / 6500 Å Au /500 Å Ti.

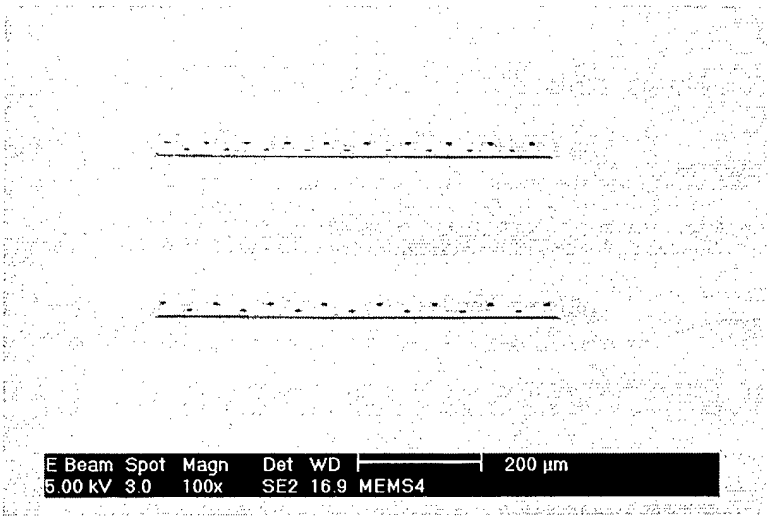

Fig. 5.12. Released bridge switches composed of 500 Å Ti / 6500 Å Au /500 Å Ti.

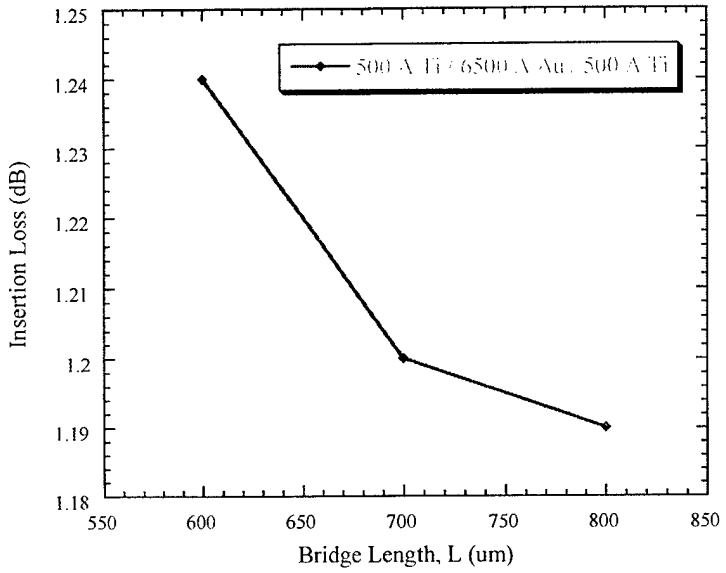

Fig. 5.13. Bridge insertion loss for TiAuTi trilayer film composition.

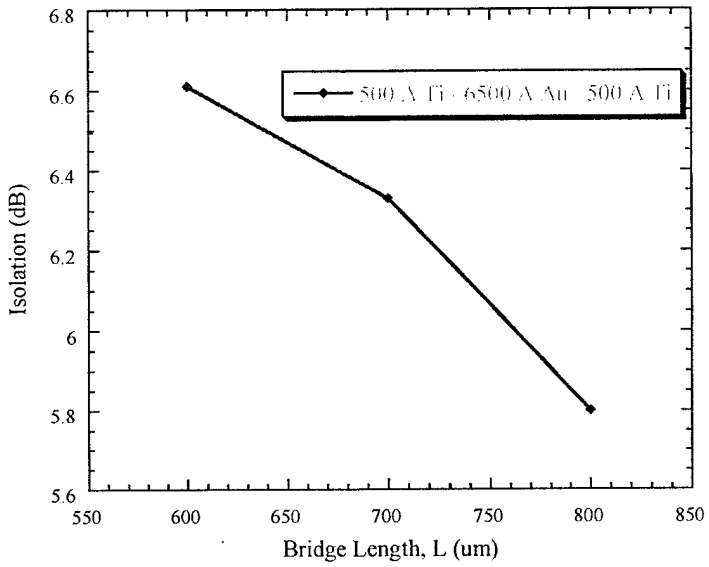

Fig. 5.14. Bridge isolation for TiAuTi trilayer film composition.

Resistivity of the metallization was also measured using an Alessi CPS-06 Contact Probe Station with a C4S four-point probe head, a Fluke 8842A multimeter, and

a HP 6181B DC Current Source. The bilayer and trilayer film resistivity values are listed in Table 5.2.

Table 5.2
METAL RESISTIVITY MEASUREMENTS.

Film Thickness (μm)	Film Composition	Resistivity (μΩ•cm)
0.15	200 Å Ti / 1300 Å Au	4.76
0.25	200 Å Ti / 2300 Å Au	2.63
0.75	200 Å Ti / 7300 Å Au	2.41
0.75	500 Å Ti / 6500 Å Au / 500 Å Au	3.13
1.50	0.50 μm Ti / 1.00 μm Au	3.11
1.50	0.75 μm Ti / 0.75 μm Au	4.46
1.50	1.00 μm Ti / 0.50 μm Au	5.72
1.50	2 layers of 500 Å Ti / 6500 Å Au / 500 Å Au	2.84
1.52	200 Å Ti / 1.50 μm Au	1.64
2.05	500 Å Ti / 2.00 μm Au	2.71

5.3 Yield

The yield of the switches was measured using both visual examination and tested results. After processing, wafers were visually inspected under a microscope and potentially good switches were recorded. Visual inspection was adequate to detect curled cantilevers and missing devices, but was often inadequate to detect switches that were stuck down. Potentially good devices were then tested on an automated RF testing system and the yield recorded. Yield results are based upon limited sample sizes and listed only to indicate overall trends. For the tables that follow, cantilevers are indicated by the C-xxx notation and the bridges by the B-xxx notation.

Wafer R12049801 consisted of a 1500 Å TiAu bottom metal, 1000 Å PECVD Si_3N_4, and a top metal of 0.5 μm Au on 1.0 μm Ti. This combination resulted in both cantilever and bridge switches. Cantilever results indicated yield decreased with

increasing perforation density (-40 to –20), but bridge yield increased with increasing perforation density.

Table 5.3
WAFER R12049801 YIELD RESULTS

Switch	Visual Yield (%)	Tested Yield (%)	Combined Visual and Tested Yield (%)
C-300	78	63	49
C-300-20	46	38	17
C-300-30	74	56	42
C-300-40	77	75	58
C-400	79	38	30
C-400-20	42	19	8
C-400-30	74	44	32
C-400-40	74	44	32
C-500	80	19	15
C-500-20	44	0	0
C-500-30	59	19	11
C-500-40	73	6	5
B-600	86	56	48
B-600-20	86	63	54
B-600-30	85	63	53
B-600-40	85	69	59
B-700	89	0	0
B-700-20	90	0	0
B-700-30	89	0	0
B-700-40	89	0	0
B-800	87	44	38
B-800-20	88	56	49
B-800-30	85	31	26
B-800-40	85	44	37

Wafer MEMS-1C consisted of a 2500 Å TiAu bottom metal, 1000 Å PECVD Si_3N_4, and a top metal of 1.0 μm Au on 0.5 μm Ti. This material combination resulted in no functional cantilevers. Results of the bridge yield are listed in Table 5.4. The bridge results also indicated that yield was dependent upon perforations. Beams with no perforations (B-600, B-700, and B-800) produced the lowest combined yield.

Table 5.4
WAFER MEMS-1C YIELD RESULTS

Switch	Visual Yield (%)	Tested Yield (%)	Combined Visual and Tested Yield (%)
B-600	38	25	10
B-600-20	38	63	24
B-600-30	37	43	16
B-600-40	38	50	19
B-700	38	13	5
B-700-20	39	44	17
B-700-30	3	38	15
B-700-40	940	60	24
B-800	40	0	0
B-800-20	38	44	17
B-800-30	40	50	20
B-800-40	37	25	9

Wafer MEMS-3A consisted of a 2500 Å TiAu bottom metal, 2500 Å sputtered Si_3N_4 (20% N_2 flow), and a top metal of 1.5 μm Au on 200 Å Ti. This material combination resulted in no functional cantilevers. Results of the bridge yield are listed in Table 5.5. These results show that the sputtered silicon nitride with a 20% N2 flow was not suitable for functional devices.

Table 5.5
WAFER MEMS-3A YIELD RESULTS

Switch	Visual Yield (%)	Tested Yield (%)	Combined Visual and Tested Yield (%)
B-600	50	0	0
B-600-20	67	0	0
B-600-30	67	0	0
B-600-40	67	25	17
B-700	42	0	0
B-700-20	50	0	0
B-700-30	50	0	0
B-700-40	50	0	0
B-800	50	0	0
B-800-20	50	0	0
B-800-30	50	0	0
B-800-40	53	0	0

Wafer MEMS-3C consisted of a 2500 Å TiAu bottom metal, 2500 Å sputtered Si_3N_4 (50% N_2 flow), and a top metal of 1.5 μm Au on 200 Å Ti. This material combination resulted in no functional cantilevers. Results of the bridge yield are listed in Table 5.6. These results show poor structural stability of the bridges (low visual yield) and functional devices limited to only two variations (B600-20 and B700-20).

Table 5.6
WAFER MEMS-3C YIELD RESULTS

Switch	Visual Yield (%)	Tested Yield (%)	Combined Visual and Tested Yield (%)
B-600	6	0	0
B-600-20	39	50	19
B-600-30	20	0	0
B-600-40	9	0	0
B-700	7	0	0
B-700-20	35	75	26
B-700-30	4	0	0
B-700-40	0	0	0
B-800	0	0	0
B-800-20	24	0	0
B-800-30	9	0	0
B-800-40	6	0	0

Wafer MEMS-4 consisted of a 2500 Å TiAu bottom metal, 2500 Å sputtered Si_3N_4 (50% N_2 flow), and a top metal of 500 Å Ti / 6500 Å Au / 500 Å Ti. This material combination resulted in no functional cantilevers. Results of the bridge yield are listed in Table 5.7. These results show high structural integrity of the bridges (high visual yield) and generally higher yield for the perforated bridges (-20, -30, and –40).

Table 5.7
WAFER MEMS-4 YIELD RESULTS

Switch	**Visual Yield (%)**	**Tested Yield (%)**	**Combined Visual and Tested Yield (%)**
B-600	72	36	50
B-600-20	79	26	33
B-600-30	79	13	17
B-600-40	78	52	67
B-700	67	0	0
B-700-20	79	39	50
B-700-30	77	52	67
B-700-40	76	25	33
B-800	63	0	0
B-800-20	73	48	67
B-800-30	76	51	67
B-800-40	72	48	67

5.4 Summary

Incorporating both cantilevers and doubly clamped beams (bridges) on a single die provided a suitable medium to investigate the material and design influences on MEMS switch performance. The structural integrity of the switches was dominated by the thickness of the Ti layer. The bilayer combination of 0.5 μm Au on 1.0 μm Ti resulted in a low stress film and functional cantilever and bridge switches. The other bilayer combinations produced stress gradients that caused the cantilevers to curl upward. Increasing the Au contribution in the bilayer bridges resulted in a greater released tensile stress gradient that improved bridge switch isolation by bowing the beam upward, but

greatly increased the actuation voltage. The incorporation of a Ti layer (> 200 Å) reduced the released stress gradient at the expense of higher insertion loss. Perforations significantly reduced stiction effects of the long bridges switches during release and had no adverse impact on microwave performance at 10 GHz. Increased beam length resulted in lower insertion losses and higher isolation with little effect on actuation voltage.

5.5 References

[1]. R. Strawser, R. Cortez, M.O'Keefe, K. Leedy, J. Ebel, and H. Henderson, "Film Stress Influence of Bilayer Metallization on the Structure of RF MEMS Switches", *Thin Films – Stresses and Mechanical Properties VIII*, Vol. 594, Materials Research Society, Pittsburgh, PA, (September 2000): 213-218.

[2]. Tencor® FLX-2900 Thin Film Stress Measurement User Manual, # 274500, Rev. A, (November 1994): 9.1-9.3.

[3]. G. Moulard, G. Contoux. G. Motyl, G. Gardet, and M. Courbon, "Improvement of the Cantilever Beam Technique for Stress Measurement During the Physical Vapor Deposition Process", *J. Vac. Sci. Technology A*, Vol. 16, No. 2, (March/April 1998): 736-742.

CHAPTER 6

SWITCH RESULTS

Electrical testing of the RF MEMS devices was performed to characterize the electrical performance of the switches and compare these results with modeled values. These tests, conducted at the wafer level included the actuation voltage, RF performance (e.g. S_{11}, S_{21}, and S_{22}), and switching speed. Cantilevers and microbridges were tested and mean values were listed to indicate the general trend of a particular device and fabrication process. Testing configurations, calibration sequences, and deficiencies have been described.

6.1 Switching Voltage

The switching voltage was characterized using three test configurations, preliminary screening, switching speed, and RF characterization. Preliminary screening was made on an Alessi REL-4100A manual probe station connected to a Tektronix 370A Programmable Curve Tracer. This configuration allowed for quick visual confirmation of mechanical switching, but provided no indication of switch performance. This arrangement relied upon visual detection of switch motion and in general provided a rough estimate of the actual switching voltage measured using RF characterization. Switching speed testing, which will be discussed in more detail in section 6.4 was made using a 1 GHz RF signal and also provided limited data on switch performance. The most accurate RF results were obtained using a dedicated RF probing system, shown in Fig. 6.1. This system, based upon an Electroglas 2001X Prober, Cascade microprobes,

and an HP 8510C Network Analyzer, provided calibrated RF performance at each switching voltage. This system was calibrated prior to each test sequence using the SOLT (Short-Open-Line-Through) calibration sequence and had an accuracy of 0.1 dB.

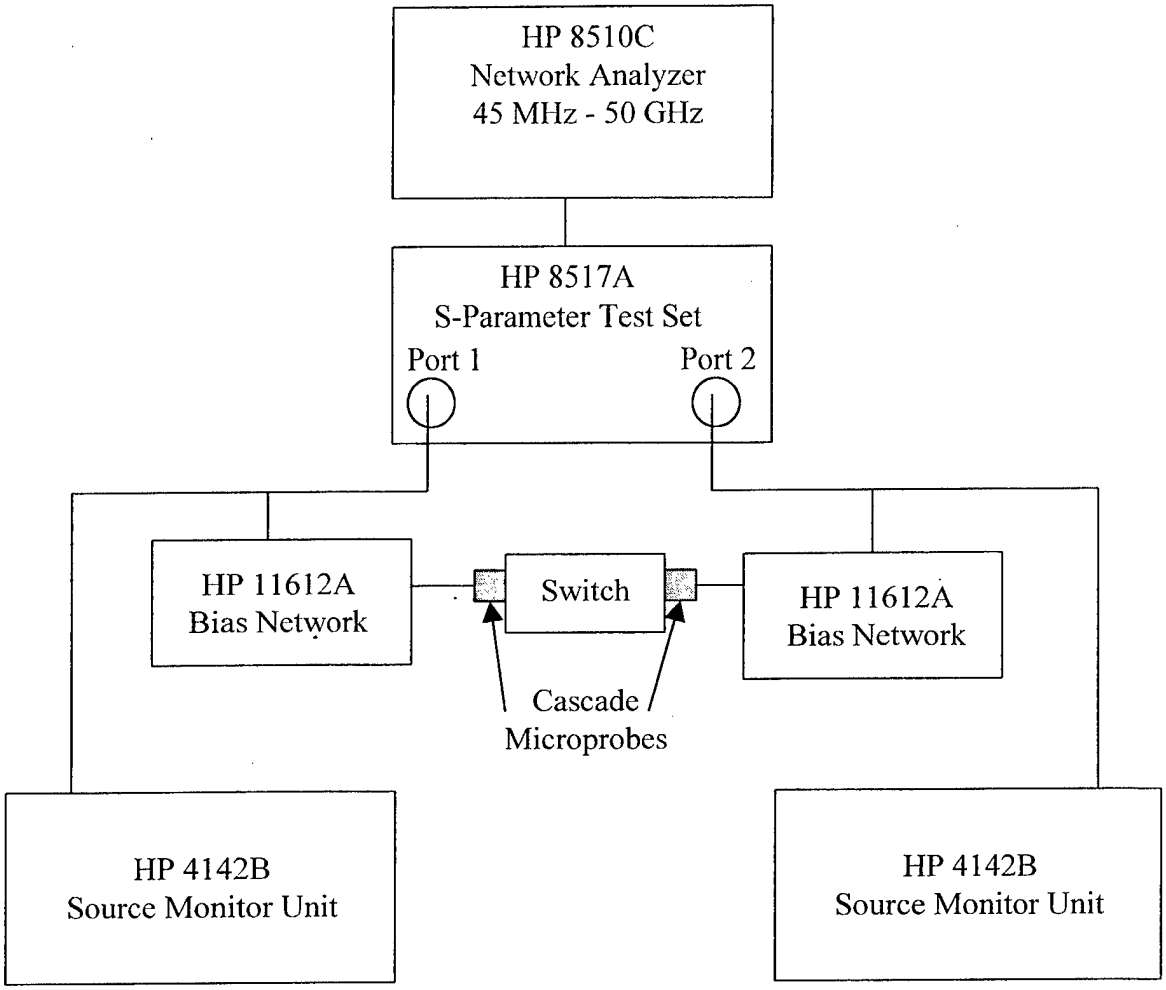

Fig. 6.1. RF probe test set-up.

Switching voltage data was analyzed using a 10 GHz RF signal to verify insertion loss (S_{21}). As discussed previously, cantilever data was limited due to fabrication yield; however, excellent results were obtained on wafer R120498-1 consisting of a bilayer film of 1.0 μm Ti and 0.5 μm Au. Eight die sites were probed resulting in a total of sixteen switches for each configuration tested. Table 6.1 lists an example of a typical sequence for a 300 μm cantilever (C-300). This sequence illustrated a common problem with

capacitively coupled RF switches, namely, the charging of the dielectric and the resulting operational stiction.

Table 6.1
CANTILEVER SWITCHING VOLTAGE TEST SEQUENCE FOR WAFER R120498-1.

C-300	**Die: 11-02-1**	**Die: 12-03-1**	**Die: 11-05-13**	**Die: 11-04-13**
Voltage (V)	**S-21 (dB)**	**S-21 (dB)**	**S-21 (dB)**	**S-21 (dB)**
0	-12.0	-13.2	-12.6	-13.1
15	-7.4	-12.8	-8.8	-12.1
18	-7.0	-12.3	-8.6	-6.8
20	-0.7	-0.6	-8.5	-0.7
22	-0.7	-0.6	-8.3	-0.6
25	-0.6	-0.6	-7.9	-0.7
28	-0.6	-0.6	-0.6	-0.6
30	-0.6	-0.6	-0.7	-0.6
0	-0.9	-0.8	-1.4	-2.6
0	-0.9	-0.8	-1.4	-2.6
0	-7.5	-0.8	-1.4	-2.6

In this testing sequence, the switch of Die: 11-02-1 closed at 20 V, but remained stuck down until the end of the sequence. The switch of Die: 11-05-13 closed at 28 V and only partially opened at 0V. As discussed previously, several variations of dielectric material were tested, with no significant differences in the charging problem. The data also indicated that increasing the switching voltage beyond the pull-in voltage did not significantly improve the insertion loss.

Table 6.2 lists the mean switching voltage and standard deviation for each cantilever configuration tested on wafer R120498-1. Although the switching voltage decreased with increasing length the results were less than expected based upon analytical results. The material configuration for this wafer also produced consistent results as shown by the standard deviation. On one hand, perforations would be expected to decrease the parallel plate capacitance requiring higher actuation voltages, but on the

other hand they would reduce damping effects and the beam mass requiring less actuation voltage.

Table 6.2
CANTILEVER SWITCHING VOLTAGES FOR WAFER R120498-1.

Cantilever	Mean Voltage (V)	Standard Deviation
C-300	22.2	3.9
C-300-20	20.8	2.7
C-300-30	21.2	2.0
C-300-40	21.4	3.3
C-400	18.3	2.9
C-400-20	19.3	1.2
C-400-30	17.1	2.7
C-400-40	16.7	1.6
C-500	25.3	4.6
C-500-20	No functional devices	
C-500-30	18.7	1.2
C-500-40	15.0	0.0

Fig. 6.2 shows a direct comparison of the switching voltage with the analytical model, Eqn. (2.31) and pull-in model, Eqn. (2.55). For this figure, the measured results consist of the average of the perforated and non-perforated beams. Results of the non-perforated cantilever, C-500 was discarded due to the high mean and standard deviation, shown in Table 6.2. The measured results indicated that as the beam length increased, the actuation voltage leveled out, rather than decreased as predicted by the models.

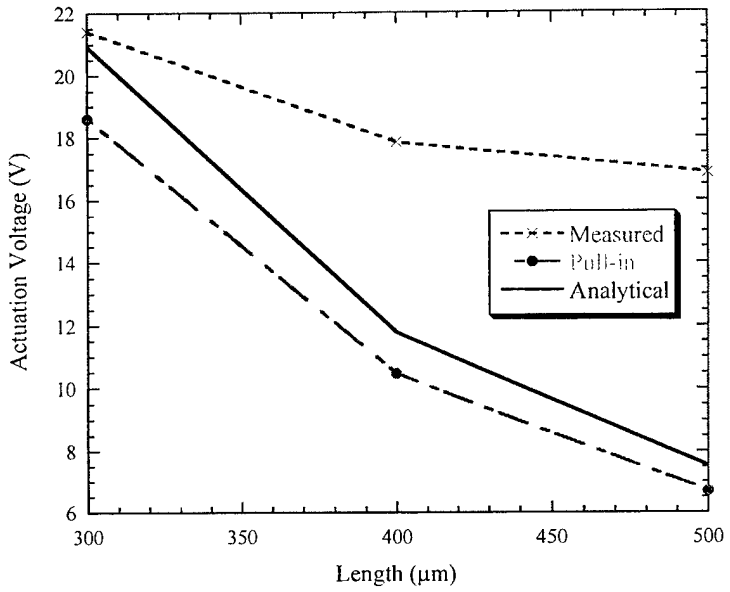

Fig. 6.2. Comparison of cantilever beam actuation voltages.

Functional bridge switches were obtained on four top level metal combinations; however, the actuation voltages varied considerably due to the curvature of the released structures. Table 6.3 lists the testing sequence for bridges from wafer R120498-1 consisting of 1.0 μm Ti and 0.5 μm Au. This is the same wafer reported earlier for the cantilevers. Actuation occurred between 20 V and 30 V. The results also demonstrate that higher actuation voltages did not result in lower insertion loss. These devices also did not fully release after the actuation voltage returned to zero and this was considered to be due to dielectric charging.

Table 6.3
BRIDGE SWITCHING VOLTAGE TEST SEQUENCE FOR WAFER R120498-1.

B-600	**Die: 11-02-1**	**Die: 12-02-1**	**Die: 12-05-13**	**Die: 11-05-13**
Voltage (V)	**S-21 (dB)**	**S-21 (dB)**	**S-21 (dB)**	**S-21 (dB)**
0	-4.8	-4.6	-4.9	-5.1
20	-4.0	-1.1	-4.2	-4.6
30	-0.8	-0.8	-0.8	-0.7
35	-0.7	-0.9	-0.8	-0.7
40	-0.7	-0.8	-0.8	-0.7
45	-0.7	-0.8	-0.8	-0.7
0	-0.7	-1.2	-0.9	-0.8
0	-0.8	-1.2	-0.9	-0.8
0	-0.8	-1.2	-0.9	-0.8

Table 6.4 lists the mean switching voltage and standard deviation (σ) for four wafers yielding functional bridges. The results showed significant variability in pull-in voltage due to top level metallization. The lowest bridge actuation voltages (12.8 V – 18 V) were obtained from wafer MEMS-1C (0.5 μm Ti and 1.0 μm Au). The most consistent results (20 V) were obtained from wafer MEMS-4 (500 Å Ti / 6500 Å Au / 500 Å Ti).

Table 6.4
BRIDGE SWITCHING VOLTAGES DUE TO TOP METAL.

	R120498-1 1.0 μm Ti 1.5 μm Au		**MEMS-1C** 0.5 μm Ti 1.0 μm Au		**MEMS-3C** 200 Å Ti 1.5 μm Au		**MEMS-4** 500 Å Ti 6500 Å Au 500 Å Ti	
Bridge	**Voltage**	σ	**Voltage**	σ	**Voltage**	σ	**Voltage**	σ
B-600	26.7	5.0	17.0	1.4			20.0	0.0
B-600-20	26.0	8.1	17.0	2.6	42.5	3.5	20.0	0.0
B-600-30	26.0	5.2	13.0	2.0			20.0	0.0
B-600-40	23.6	5.1	17.3	1.2			20.0	0.0
B-700			14.0	0.0			20.0	0.0
B-700-20			12.8	2.5	51.7	7.6	20.0	0.0
B-700-30			13.0	1.0			20.0	0.0
B-700-40			15.5	2.0			20.0	0.0
B-800	20.0	0.0					20.0	0.0
B-800-20	22.2	4.4	14.8	2.2			20.0	0.0
B-800-30	24.0	8.9	18.0	0.0			20.0	0.0
B-800-40	20.0	0.0	13.0	0.0			20.0	0.0

6.2 Cantilever Beam Switch RF Performance

The RF performance of the cantilever beam switches was obtained using the test set-up shown in Fig. 6.1. In this RF testing, the frequency was swept from 1 – 26 GHz, while the actuation voltage was varied over the same intervals listed in the previous section. The definition of the Scattering parameters (S-parameters) used for these tests is shown in Fig. 6.3.

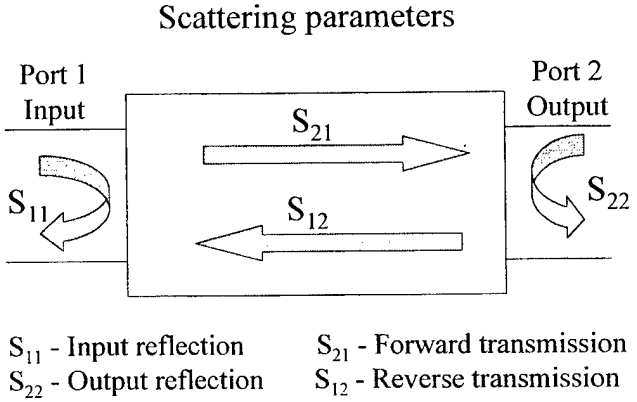

Fig. 6.3. Scattering parameters.

Results for the input reflection (S_{11}), forward transmission (S_{21}), and output reflection (S_{22}) for both the off-state and on-state will be presented, with the statistical data listed in Appendix E. The S_{12} data was not listed, as it was nearly identical to S_{21}.

Cantilevers from wafer R120498-1 (1.0 μm Ti and 0.5 μm Au) were tested and the input reflection results in the off-state (i.e. when the switch is up) are shown in Figs. 6.4 and 6.5. Ideally, in the off-state, the switch is open and all incident power should be reflected (i.e. S_{11} = 0 dB). For these cantilevers, all incident power was not reflected. As the frequency increased, less signal was reflected back to the input, indicating a load mismatch at the input. The mismatch would be due to either loss or transmission through the switch and is dependent upon the forward transmission (S_{21}). The phase plot, Fig. 6.5 was linear, as would be expected for a transmission line.

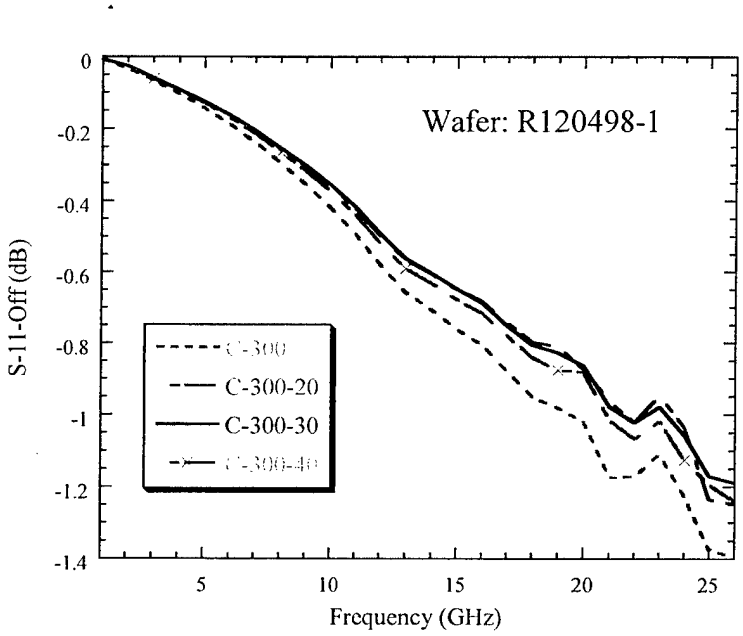

Fig. 6.4. Measured off-state input reflection for 300 μm cantilevers.

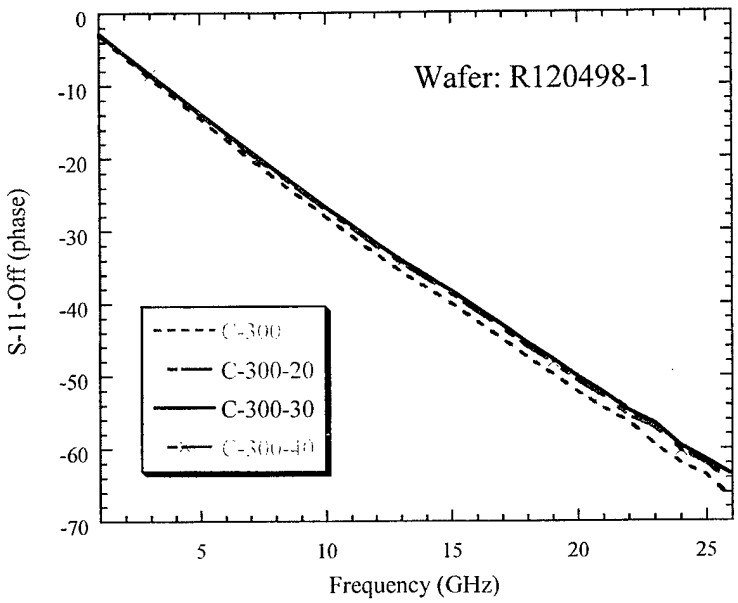

Fig. 6.5. Measured off-state input reflection phase for 300 μm cantilevers.

In the off-state, the forward transmission (S_{21}) becomes the switch isolation. The isolation results are shown in Figs. 6.6 and 6.7. Ideally, the switch is open and the isolation (S_{21}) should be high. These cantilevers were not ideal and the isolation decreased as the frequency increased. This indicated that the signal was either reflected back to the input or transmitted through the switch. For a network, the sum of the input reflection and forward transmission magnitudes is equal to or less than zero [1], as shown by Eq. (6.1)

$$|S_{11}|^2 + |S_{21}|^2 \leq 1 \tag{6.1}$$

$$|S_{11}|^2 = 10^{0.1 S_{11}\, in\, dB}$$

$$|S_{21}|^2 = 10^{0.1\, S_{21}\, in\, dB}.$$

When the sum equals zero, the network is lossless. When the sum is less than zero, the difference represents the power absorbed by the network. Using cantilever (C-300) data

at 10 GHz from Appendix E, the switches were not lossless, but had an absorption magnitude of 0.04.

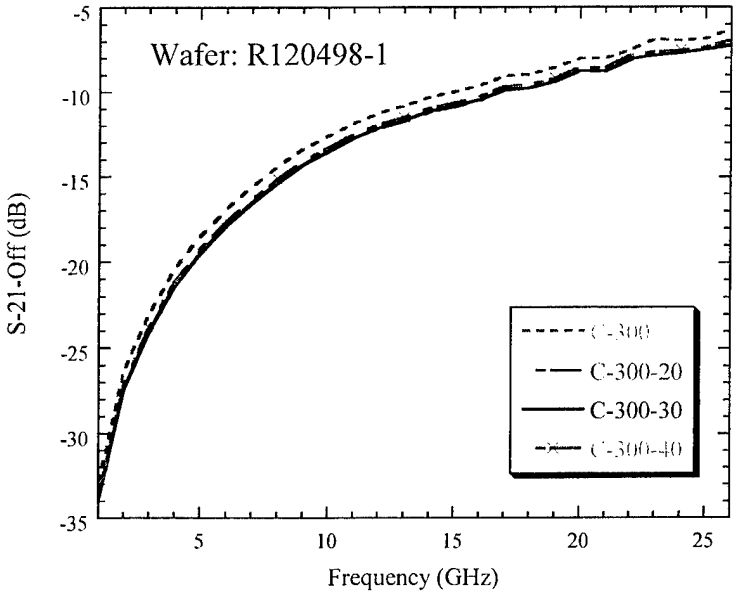

Fig. 6.6. Measured off-state isolation for 300 μm cantilevers.

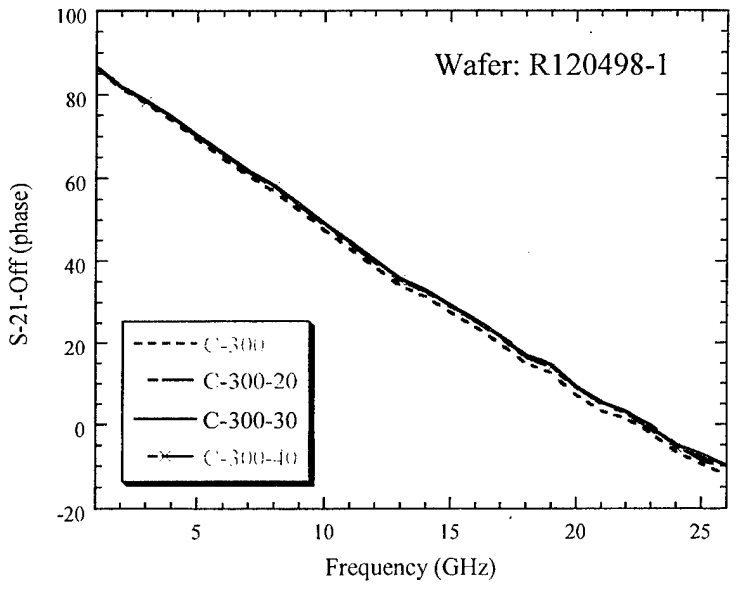

Fig. 6.7. Measured off-state isolation phase for 300 μm cantilevers.

The output reflection in the off-state is plotted in Figs. 6.8 and 6.9. The output reflection, Fig. 6.8 provides a measure of the output impedance matching of the switch. This plot, although similar to the input reflection, Fig. 6.4 indicated that the switch was not entirely symmetric (i.e. matched input and output impedance).

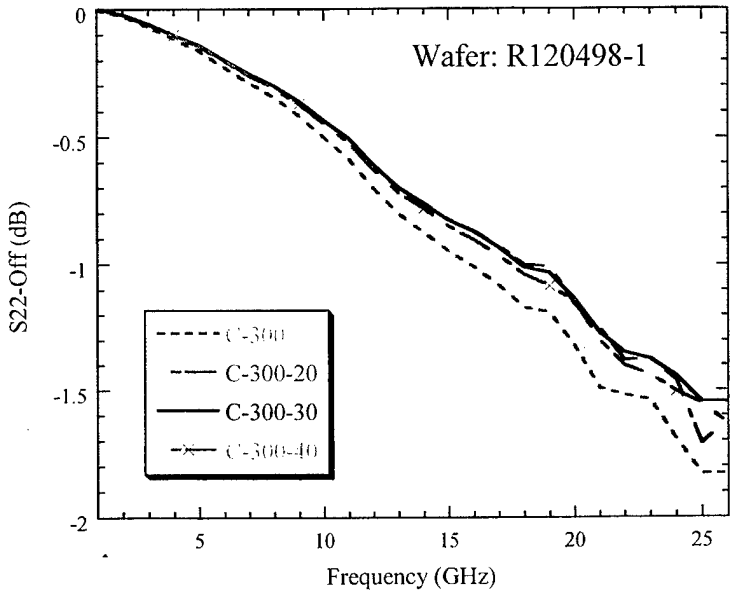

Fig. 6.8. Measured off-state output reflection for 300 μm cantilevers.

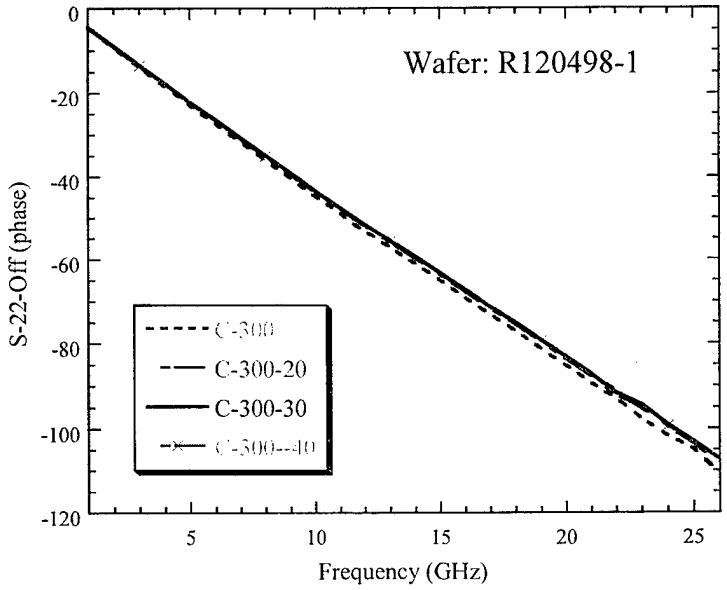

Fig. 6.9. Measured off-state output reflection phase for 300 μm cantilevers.

Switch results in the on-state (i.e. when the switch is down) are shown in Figs. 6.10 - 6.15. In the on-state, the switches are parallel plate capacitors and the impedance varied with frequency. At low frequencies, the input reflection, Fig. 6.10 was high due to the high impedance of the capacitance and resulted in a high reflection ($S_{11} \sim 0$). As the frequency increased, the impedance decreased and more signal was transmitted through the switch and less was reflected back to the input. The variation in phase, Fig. 6.11 also tracked the impedance and became linear above 5 GHz.

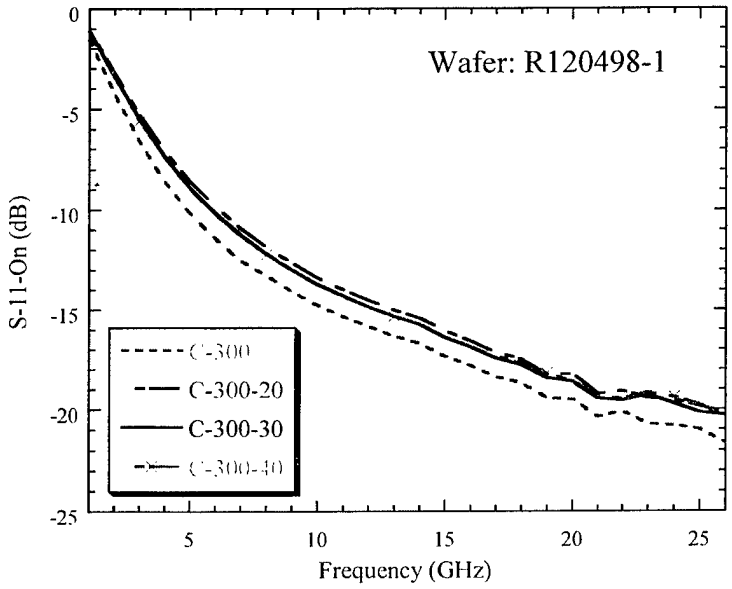

Fig. 6.10. Measured on-state input reflection for 300 μm cantilevers.

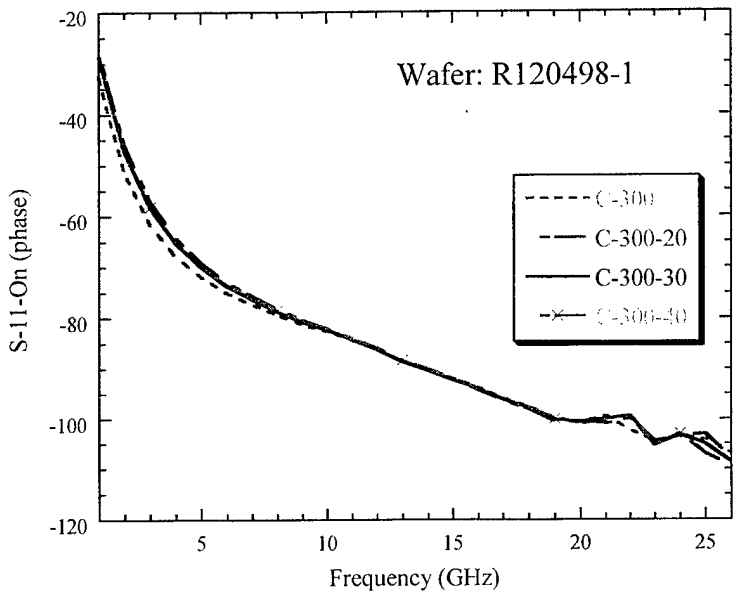

Fig. 6.11. Measured on-state input reflection phase for 300 μm cantilevers.

In the on-state, the forward transmission (S_{21}) becomes the insertion loss and is shown in Figs. 6.12 and 6.13. The insertion loss was also high at low frequencies due to the high impedance of the parallel plate capacitor. Above 5 GHz, the insertion loss leveled to a minimum value (0.6 dB). Comparing the magnitudes of S_{11} and S_{21}, the lossless nature of the switches can be determined. Using S-parameter data at 10 GHz from Appendix E and Eq. (6.1), the switches were not lossless, but had an absorption magnitude of 0.1.

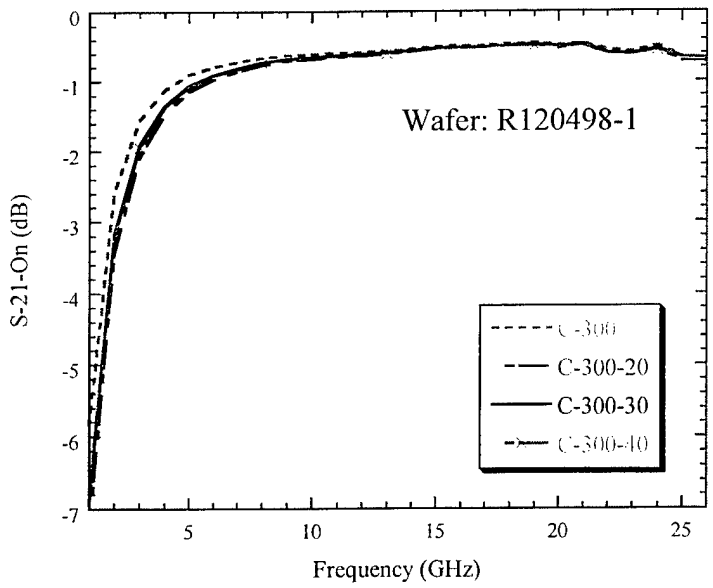

Fig. 6.12. Measured on-state insertion loss for 300 μm cantilevers.

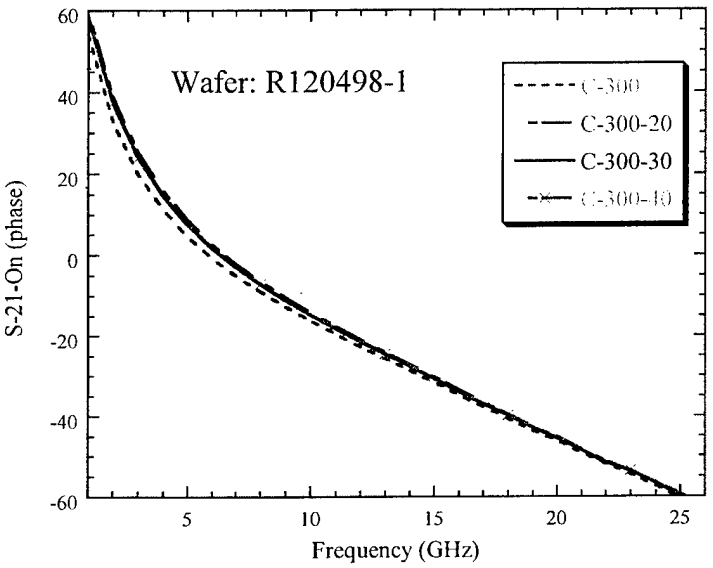

Fig. 6.13. Measured on-state insertion loss phase for 300 μm cantilevers.

The output reflection (S_{22}) results for the 300 μm cantilevers are shown in

Figs. 6.14 and 6.15. These results vary slightly with the input reflection plot, Fig. 6.10 at the high frequencies (i.e. ~ 3 dB lower at 26 GHz) and indicate that the impedance matching between the input and output was slightly off. In all cases, the results do not show a large variation between the beams with and without perforations.

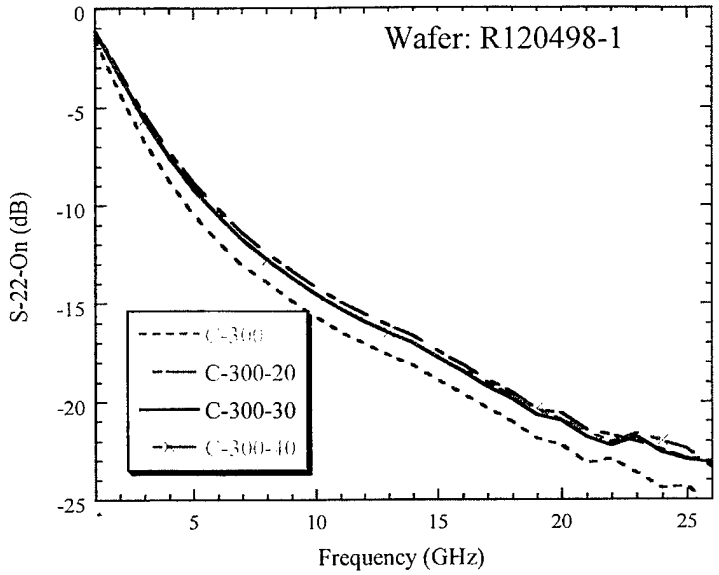

Fig. 6.14. Measured on-state output reflection for 300 μm cantilevers.

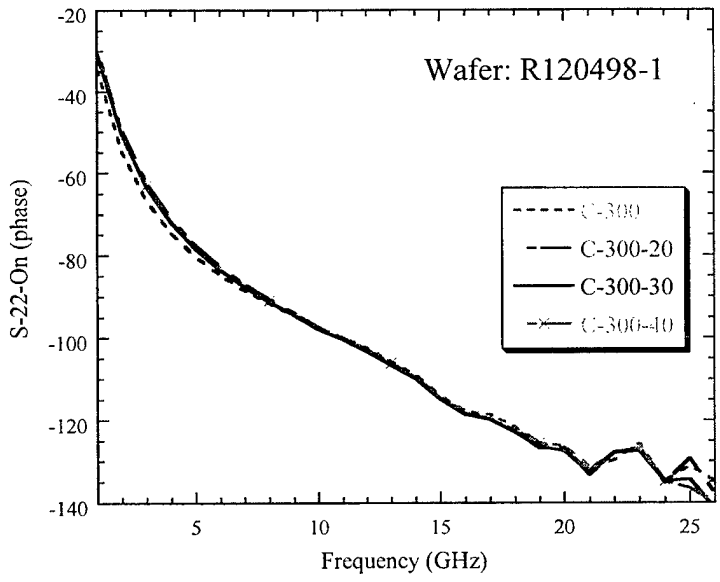

Fig. 6.15. Measured on-state output reflection phase for 300 μm cantilevers.

Results for both the 400 μm and 500 μm cantilevers follow the same trends as the 300 μm cantilevers. Using tabulated values listed in Appendix E at 10 GHz, the magnitude of the absorption of both 400 μm and 500 μm cantilevers was 0.04 in the off-state and 0.09 in the on-state. The off-state absorption did not vary based upon cantilever length (0.04 for all lengths) and the on-state absorption was only slightly higher for the 300 μm cantilever (0.1).

The cantilever results are summarized for X-band (8 – 12 GHz) in Table 6.5. For the off-state, the input reflection, (S_{11} off-state) decreased for both increasing frequency and beam length. This demonstrated that less signal was being reflected back to the input and more was coupled through the open switch due to both the higher frequencies and longer beam lengths. The decreasing isolation, (S_{21} off-state) corroborated his conclusion. For the on-state, the input reflection (S_{11} on-state) increased with both frequency and beam length. This indicated that less signal was reflected back to the input and more was transmitted through the switch. This was corroborated by the decreasing insertion loss (S_{21} on-state).

Table 6.5
CANTILEVER S-PARAMETER RESULTS.

	C-300	C-400	C-500		C-300	C-400	C-500
Frequency (GHz)	**S_{11} dB (Off-state)**				**S_{11} dB (On-state)**		
8	-0.25	-0.27	-0.31		-11.86	-14.54	-15.80
10	-0.36	-0.38	-0.44		-13.38	-15.97	-17.12
12	-0.50	-0.53	-0.61		-14.52	-17.02	-18.09
	S_{21} dB (Off-state)				**S_{21} dB (On-state)**		
8	-15.40	-14.78	-13.84		-0.77	-0.59	-0.56
10	-13.56	-12.97	-12.06		-0.69	-0.56	-0.53
12	-12.18	-11.60	-10.73		-0.64	-0.53	-0.52
	S_{22} dB (Off-state)				**S_{22} dB (On-state)**		
8	-0.30	-0.34	-0.42		-12.42	-15.39	-16.97
10	-0.44	-0.50	-0.61		-14.46	-17.15	-18.72
12	-0.61	-0.69	-0.85		-15.52	-18.49	-20.05

6.3 Microbridge Switch RF Performance

RF performance of the microbridge switches was obtained for several metal combinations. Representative data from wafer R120498-1 (1.0 μm Ti and 0.5 μm Au) are listed in Tables 6.5 – 6.6. The results at 10 GHz show low isolation (S_{21}-dB) in the off-state and high insertion loss (S_{21}-dB) in the on-state.

Table 6.6

MEASURED BRIDGE RF RESULTS (OFF-STATE) FROM WAFER R120498-1.

Switch	Yield	S_{11}-dB	S_{11}-phase	S_{21}-dB	S_{21}-phase	S_{22}-dB	S_{22}-phase
B600	0.56	-2.4	-49	-4.7	11	-3.1	-94
B600-20	0.63	-2.3	-49	-4.7	11	-.31	-93.4
B600-30	0.63	-2.1	-46	-5.5	14	-2.9	-92
B600-40	0.69	-2.3	-49	-4.8	11	-3.0	-93
B700	0.56	-2.9	-51	-4.0	6	-3.8	-101
B700-20	0.44	-2.9	-51	-4.0	6	-3.8	-100
B700-30	0.41	-2.9	-51	-4.0	6	-3.8	-101
B700-40	0.81	-2.9	-51	-4.0	6	-3.8	-101
B800	0.44	-3.5	-54	-3.4	1	-4.5	-107
B800-20	0.56	-3.0	-50	-4.7	6	-3.9	-104
B800-30	0.31	-3.0	-58	-6	10	-3.6	-86
B800-40	0.44	-3.5	-54	-3.4	2	-4.5	-107

Table 6.7

MEASURED BRIDGE RF RESULTS (ON-STATE) FROM WAFER R120498-1.

Switch	Yield	S_{11}-dB	S_{11}-phase	S_{21}-dB	S_{21}-phase	S_{22}-dB	S_{22}-phase
B600	0.56	-16.1	-87	-0.8	-30	-18.0	-107
B600-20	0.63	-14.5	-85	-0.8	-28	-16.4	-111
B600-30	0.63	-15.2	-86	-0.8	-29	-17.1	-110
B600-40	0.69	-15.3	-86	-0.8	-29	-17.3	-109
B700	0.56	-15.5	-87	-0.8	-30	-17.3	-111
B700-20	0.44	-15.5	-87	-0.8	-30	-17.5	-110
B700-30	0.41	-15.2	-87	-0.8	-29	-17.2	-111
B700-40	0.81	-15.3	-86	-0.8	-30	-17.3	-109
B800	0.44	-15.7	-90	-0.8	-31	-17.3	-111
B800-20	0.56	-15.7	-89	-0.8	-30	-17.4	-113
B800-30	0.31	-16.1	-90	-0.8	-31	-17.9	-110
B800-40	0.44	-15.1	-89	-0.8	-30	-16.7	-112

The results for wafer MEMS-1C (200 Å Ti and 1.5 μm Au) are listed in Tables 6.7 and 6.8. These results, also at 10 GHz show a higher isolation (S_{21} dB) in the off-state and a lower insertion loss (S_{21} dB) in the on-state as compared with the previous results. As mentioned in Chapter 5, this was due to the high stress gradient in the gold

dominated film, which caused the bridges to bow upwards. The high resistivity of the gold film also allowed for lower insertion loss.

Table 6.8
MEASURED BRIDGE RF RESULTS (OFF-STATE) FROM WAFER MEMS-1C.

Switch	Yield	S_{11}-dB	S_{11}-phase	S_{21}-dB	S_{21}-phase	S_{22}-dB	S_{22}-phase
B600	0.25	-1.3	-41	-6.4	23	-1.6	-85
B600-20	0.63	-1.3	-41	-6.4	23	-1.6	-85
B600-30	0.43	-1.6	-44	-5.6	20	-1.9	-88
B600-40	0.50	-1.3	-42	-6.2	22	-1.7	-86
B700	0.13	-1.6	-43	-5.45	19	-2.0	-92
B700-20	0.40	-1.8	-44	-5.3	17	-2.2	-94
B700-30	0.33	-1.6	-42	-5.7	19	-2.0	-92
B700-40	0.60	-1.4	-41	-6.1	19	-1.8	-91
B800	0						
B800-20	0.44	-1.7	-42	-5.8	17	-2.0	-95
B800-30	0.50	-1.4	-23	-6.0	16	-1.8	-60
B800-40	0.25	-1.9	-42	-5.2	14	-2.5	-99

Table 6.9
MEASURED BRIDGE RF RESULTS (ON-STATE) FROM WAFER MEMS-1C.

Switch	Yield	S_{11}-dB	S_{11}-phase	S_{21}-dB	S_{21}-phase	S_{22}-dB	S_{22}-phase
B600	0.25	-10.5	-85	-0.8	-19	-11.3	-118
B600-20	0.63	-9.8	-81	-0.9	-18	-10.3	-118
B600-30	0.43	-10.1	-83	-0.9	-19	-10.8	-118
B600-40	0.50	-10.9	-84	-0.8	-20	-11.5	-119
B700	0.13	-11.9	-88	-0.6	-23	-12.6	-123
B700-20	0.40	-11.5	-86	-0.7	-22	-12.2	-123
B700-30	0.33	-11.3	-86	-0.8	-22	-11.9	-124
B700-40	0.60	-11.6	-87	-0.7	-23	-12.3	-123
B800	0						
B800-20	0.44	-12.0	-89	-0.8	-25	-12.5	-126
B800-30	0.50	-12.4	-55	-0.7	-14	-13	-79
B800-40	0.25	-11.8	-87	-0.7	-24	-12	-130

Results of microbridge switches swept over a 1 – 26 GHz frequency range were made on wafer MEMS-3A. As discussed in Chapter 4, this wafer was quartered and quarter "A" was fabricated using sputtered silicon nitride with a 20% N_2 gas flow. The

purpose of this experiment was to make the dielectric more conductive and allow the charging voltage to bleed off. However, the dielectric produced poor results and low yield. The poor behavior of this dielectric material was shown most noticeably by the fluctuation of the insertion loss (S_{21}) of Fig. 6.16. In this figure, the phase signal is linear, but the insertion loss fluctuated widely.

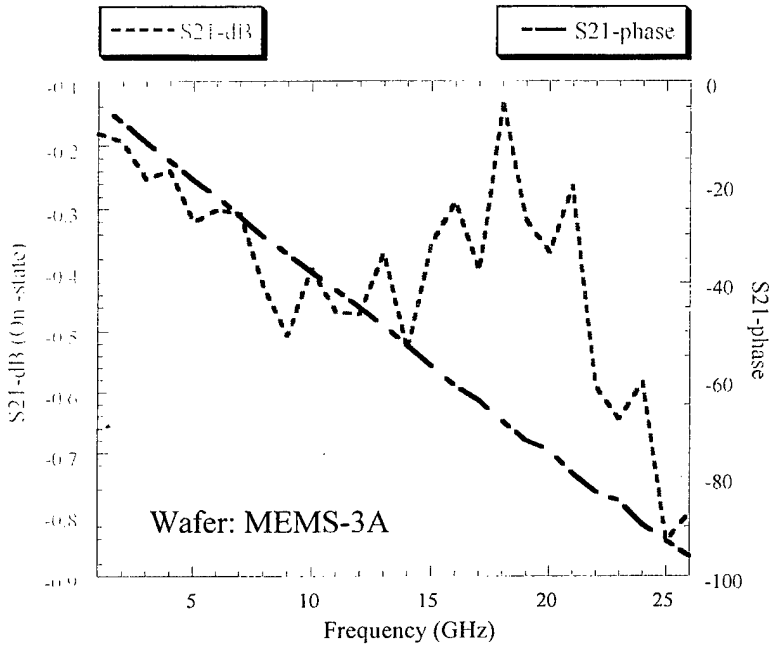

Fig. 6.16. Measured on-state insertion loss and phase for B-600-40 bridge.

Wafer MEMS-3C was also probed over the frequency range of 1 – 26 GHz. This wafer used sputtered silicon nitride with a 50% N_2 gas flow. The input reflection of the B600-20 switches in the off-state is shown in Fig. 6.17. The input reflection decreased as the frequency increased, indicating more signal was transmitting through the switch. The on-state input reflection, shown in Fig. 6.18 steadily decreased and leveled out at 13 GHz.

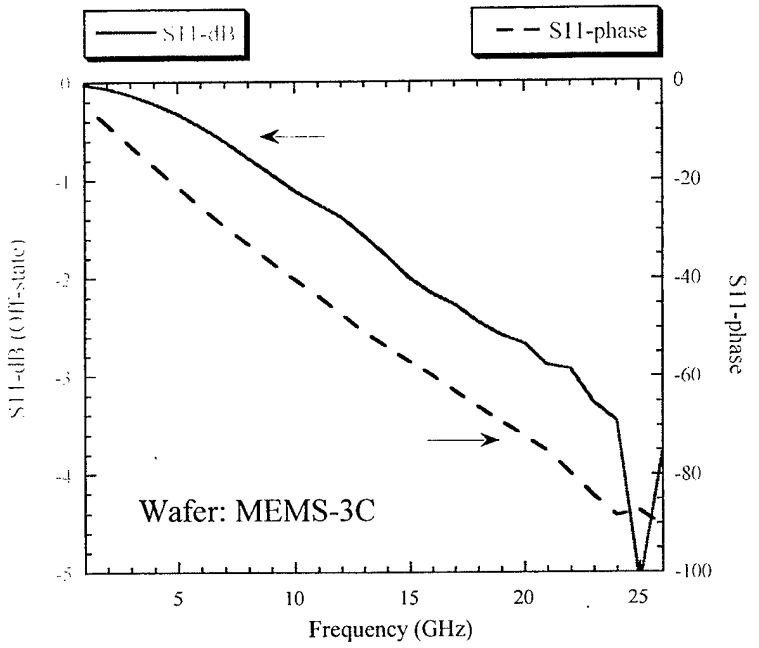

Fig. 6.17. Measured off-state input reflection and phase for B600-20 microbridge.

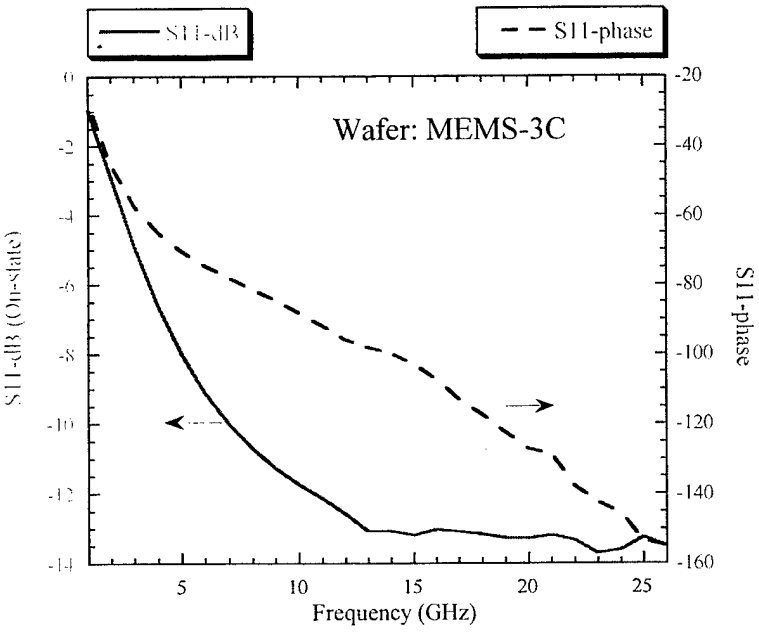

Fig. 6.18. Measured on-state input reflection and phase for B600-20 microbridge.

The off-state isolation results are shown in Fig. 6.19. The isolation of the switch was low, due to an error in the layout, resulting in coupling through the switch. The on-

state insertion loss magnitude and phase is shown in Fig. 6.20. Based upon Figs. 6.17 and 6.19, a resonance occurred at 25 GHz. The switch loss increased at this point, with an absorption magnitude increasing from 0.05 to 0.29.

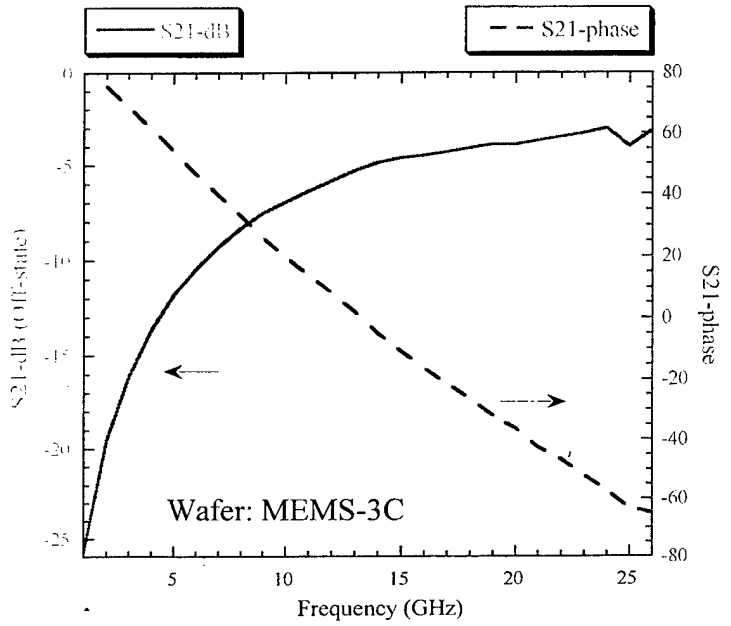

Fig. 6.19. Measured off-state isolation and phase for B600-20 microbridge.

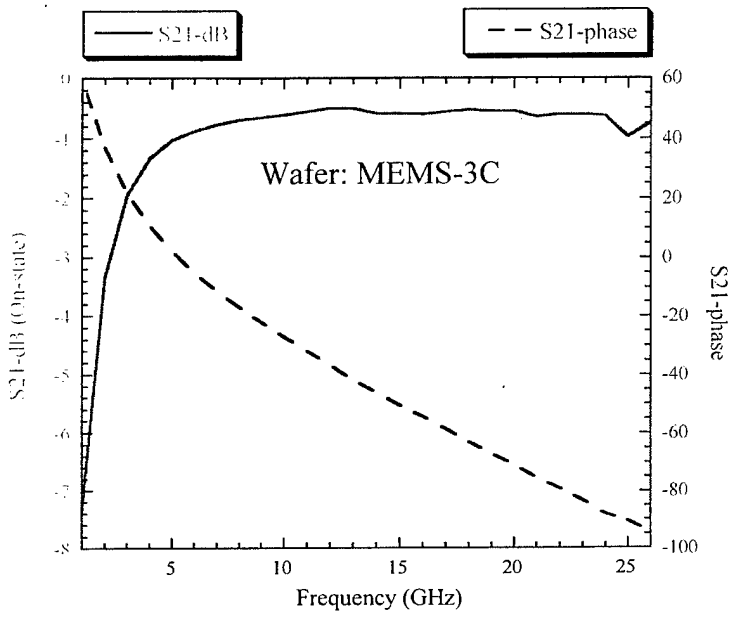

Fig. 6.20. Measured on-state insertion loss and phase for B600-20 microbridge.

The output reflection and phase plots shown in Fig. 6.21 for the off-state and Fig. 6.22 for the on-state follow the same pattern as the cantilevers.

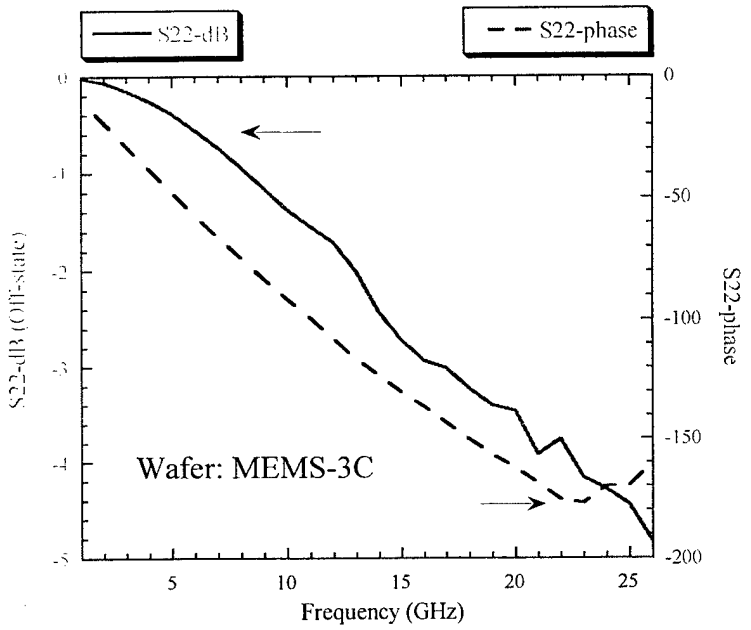

Fig. 6.21. Measured off-state output reflection and phase for B600-20 microbridge.

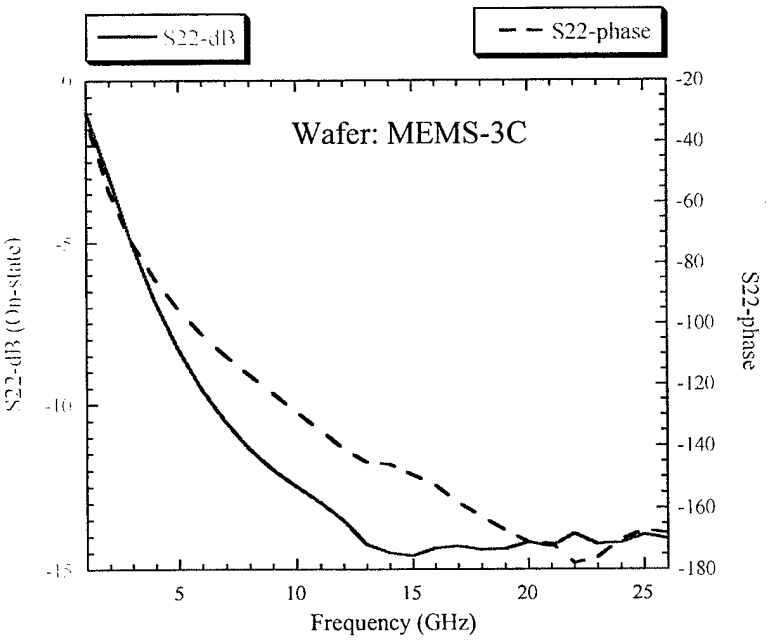

Fig. 6.22. Measured on-state output reflection and phase for B600-20 microbridge.

Results of the B700-20 switches follow the same pattern as the B-600-20 microbridges. These results were consistent with the results for the B-600-20 microbridge. In both cases, the isolation leveled out at ~ 5 dB at 10 GHz and the insertion loss decreased to ~ 0.6 dB at 5 GHz and leveled out.

In an attempt to compensate for the unbalanced stress gradient of bilayer films, a trilayer top metal combination was processed. This wafer MEMS-4 consisted of a top layer metallization of 500 Å Ti – 6500 Å Au – 500 Å Ti. Cantilever beam switches generally were curled out of the plane and required a minimum of 60 V for actuation. The microbridges yielded working devices for the perforated beams. The results followed the same pattern as the results of wafer MEMS-3C, with an insertion loss of - 1.0 dB and an isolation of –6.55 dB at 10 GHz. These results showed that the input reflection in the off-state increased slightly as the beam length increased and was reasonably constant for changing beam length in the on-state. The isolation decreased with increasing beam length, while the insertion loss remained constant with changing beam length. The output reflection increased with increasing beam length in the off-state, but remained constant with changing beam length in the on-state. These results can be attributed to the poor impedance matching in the off-state. When the switch was up (off-state), the beam was suspended at least 5 μm above the substrate and the coupling distance to the ground planes was changed. In the on-state, the increasing beam length contact area allowed for increased coupling to the signal line.

6.4 Switching Speed

The final performance parameter of the research was the determination of the switching speed of the devices. As discussed in Chapter 1, device switching speeds on the order of 10's of μsec were acceptable to meet the system requirements of many radar systems. The switching speed of RF MEMS switches consisted of the turn-on time, which was a function of the actuation voltage and the turn-off time, which was dependent on the spring constant of the structure. A high spring constant provided fast turn-off times, but resulted in a slower turn-on time due to the high stiffness of the switch. Increasing the actuation voltage to compensate for the turn-on time stressed the dielectric material and often led to device failure, defined as operational stiction.

The switching speed of both cantilever beam and microbridge switches was investigated by probing unpackaged wafers using the setup shown in Fig. 6.23. Since the switch contacts were dielectrically isolated, the switching speed was determined by measuring the electrical response of the switch to a high frequency RF signal riding on a pulsed direct current (DC) voltage square wave. The HP 214C pulse generator provided a DC pulse with variable pulse width and voltage and the HP 8350B RF generator provided the RF signal. These signals were combined in a HP 11612A bias network that also provided isolation between the two generators. The electrical response was then detected by a Schottky diode detector and recorded on a Tektronix oscilloscope. Impedance matching was a primary consideration in setting up the test fixture to ensure isolation between the two generators and prevent overloading.

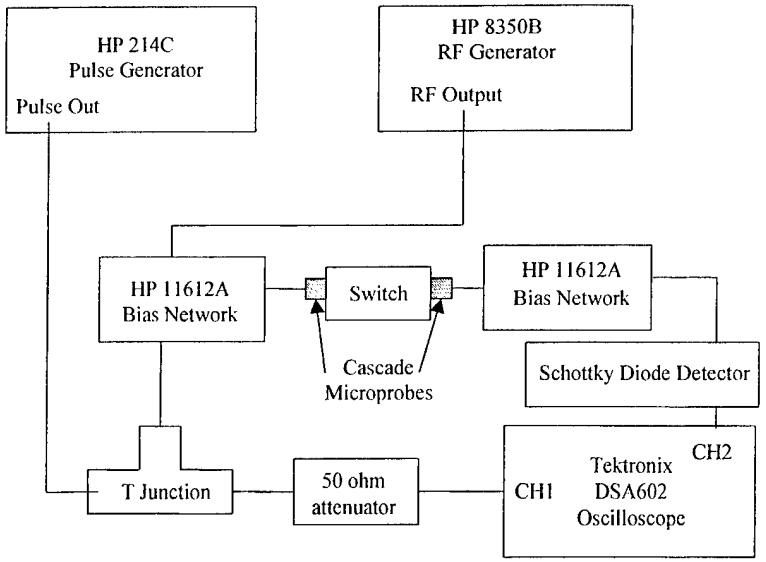

Fig. 6.23. Test setup used to measure device switching speed.

An example of the signal input and electrical response of the switches is shown in Fig. 6.24. The top trace consisted of a 1 GHz signal riding upon a pulsed DC voltage. The DC pulse width was approximately 280 μsec with rise and fall times on the order of a few nsec. The bottom trace was the electrical response of the switch to the RF signal. Due to a software glitch in the oscilloscope, the bottom signal trace was inverted, but the waveform remained valid.

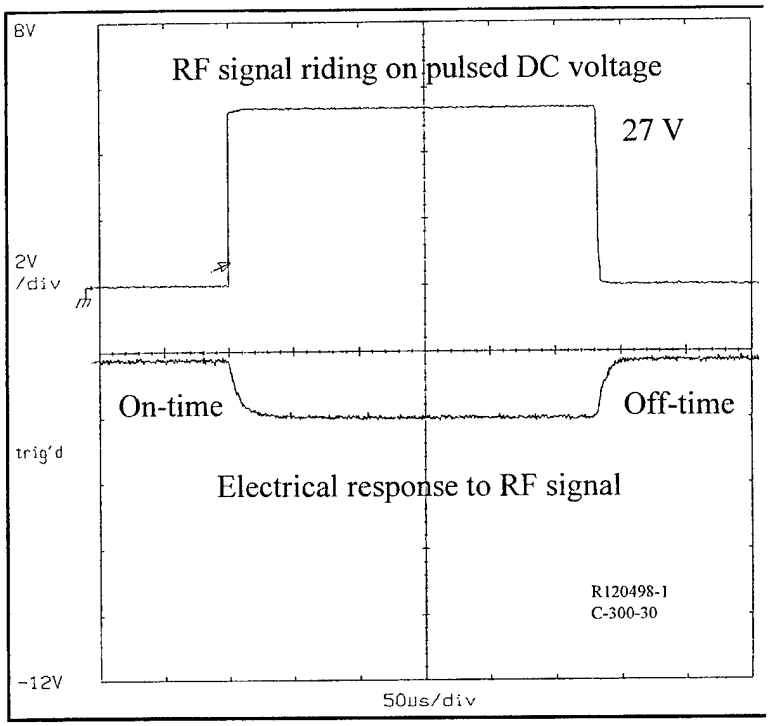

Fig. 6.24. Electrical switching response waveforms.

Device testing was conducted by increasing the magnitude of the DC pulse until the maximum RF response through the switch was observed. The rise time (turn-on) and fall time (turn-off) of the switches was then recorded and averaged for several samples. A number of drawbacks to the setup must be mentioned. First, the RF signal was limited to 1 GHz, due the particular signal generator available at the time of testing. From previous sections, the switches were optimized for operation at 8 – 12 GHz and the insertion loss at 1 GHz varied by as much as 4 dB. The variation in insertion loss and the lack of a calibration standard made the determination of the switch actuation difficult. The second drawback was the poor response of the pulse generator, which also had no overload protection.

Results of the switching speed experiment for wafer 120498-1 are listed in Table 6.10 along with the critical wafer processing conditions. This wafer yielded both cantilever and microbridge switches. The results are listed for the overall beam length as no significant variations between the perforated and non-perforated beams were observed with this test configuration. Although the numerical results may be questionable, the general trend indicated that the on-time increased with increasing beam length. This was most likely due to the squeeze film damping effect that increased for longer beams. The off-time also increased with increasing beam length, potentially due to the decreasing spring constant of the longer beams.

Table 6.10
SWITCHING SPEED EXPERIMENT FOR WAFER R120498-1.

Switch	**On-time (μsec)**	**Off-time (μsec)**	**Voltage (V)**	**Processing Conditions**
C-300	28	10	30	**Bottom Metal:** 200 Å Ti / 1000 Å Au **Dielectric:** 1000 Å PECVD silicon nitride **Top Metal:** 1.0 μm Ti / 0.5μ Au **Initial Air Gap:** 5.0 μm
C-400	25	15	19	
C-500	42	50	13	
B-600	40	46	14	
B-700	50	42	12	
B-800	70	70	7	

Switching speed results for wafer MEMS-1C are listed in Table 6.11. The top metal for this wafer produced only microbridges and had the highest insertion loss and lowest isolation of all the top metal compositions. These results were highly suspect, as the actuation voltages for this test were much higher than the 12-16 V results taken from the calibrated RF probing system.

Table 6.11
SWITCHING SPEED EXPERIMENT FOR WAFER MEMS-1C.

Switch	**On-time (μsec)**	**Off-time (μsec)**	**Voltage (V)**	**Processing Conditions**
B-600	12 – 15	15 – 20	30	**Bottom Metal:** 200 Å Ti / 2300 Å Au **Dielectric:** 2500 Å PECVD nitride **Top Metal:** 0.5 μm Ti / 1.0 μm Au **Initial Air Gap:** 5.0 μm
B-700	12 – 15	15 – 20	30	
B-800	12 - 15	15 - 20	30	

Switching speed results for wafer MEMS-3A are listed in Table 6.12. The top metal composition for this wafer produced only working microbridges. The sputtered silicon nitride for this wafer provided poor RF results and generally low device yield. The only meaningful observation from this test was that the off-time decreased with increasing beam length. This was due to the decreased spring constant.

Table 6.12
SWITCHING SPEED EXPERIMENT FOR WAFER MEMS-3A.

Switch	**On-time (μsec)**	**Off-time (μsec)**	**Voltage (V)**	**Processing Conditions**
B-600	40	30	10	**Bottom Metal:** 200 Å Ti / 2300 Å Au **Dielectric:** 2500 Å sputtered nitride (20% N_2) **Top Metal:** 200 Å Ti / 1.5 μm Au **Initial Air Gap:** 5.0 μm
B-700	40	50	9	
B-800	40	70	9	

Switching speed results for wafer MEMS-3C are listed in Table 6.13. The top metal composition for this wafer also resulted in only working microbridges. This wafer

produced the highest RF performance results, with the lowest insertion loss and the highest isolation.

Table 6.13
SWITCHING SPEED EXPERIMENT FOR WAFER MEMS-3C.

Switch	**On-time (μsec)**	**Off-time (μsec)**	**Voltage (V)**	**Processing Conditions**
B-600	20	15	30	**Bottom Metal:** 200 Å Ti / 2300 Å Au **Dielectric:** 2500 Å sputtered nitride (50% N_2) **Top Metal:** 200 Å Ti / 1.5 μm Au **Initial Air Gap:** 5.0 μm
B-700	30	20	40	
B-800	20	15	40	

Experiments to monitor the turn-on time with increasing actuation voltage were largely inconclusive. In many instances, the poor response of the pulse generator resulted in voltage spikes that produced pin holes within the silicon nitride. As the dielectric began to breakdown, the devices shorted and were fused. However, results from wafer R-120498-1 did indicate that the on-time decreased with increasing actuation voltage as expected. The drawback of this approach was that when the actuation voltage exceeded the pull-in voltage, additional charging of the dielectric led to premature device failure.

Based upon these results, the optimum switch metallization for switching speed would appear to be the 0.5 μm Ti and 1.0 μm Au combination of wafer MEMS-1C. This combination provided the lowest on-time (12-15 μsec), but the highest insertion loss and lowest isolation. The on-time results of wafer R-120498-1 were approximately 40 – 50 μsec, which compares reasonably well with devices reported in the literature

(10 – 50 μsec) [2]. As discussed previously, these on-time results were sufficient in many microwave applications, such as the phase shifter circuits of phased array radar. The trade-offs impacting switching speed included the spring constant of the beam structure, residual stress in the beam, and air-damping. The devices in this study were tested in an electronics lab with no special fixtures to control the humidity or packaging.

6.5 Summary

The insertion loss of the devices demonstrated in this research varied from 0.5 – 0.9 dB. Cantilever beam isolation was 17 dB. The switching speed results require additional calibration due to the low RF signal, but the on-times of 40 – 50 μsec compared reasonable well with the literature values of 10 – 50 μsec [2]. The main advantage of the current devices was the low switching voltage (10 – 25 V). The actuation voltage of devices reported in the literature vary from 30 – 50 V [2].

This research also demonstrated the trade-off issues between the actuation voltage, RF performance, switching time, and fabrication process. Higher initial gap spacing offered higher isolation at the expense of high actuation voltage. Thin dielectrics offered lower insertion loss, but decreased reliability due to dielectric charging and lower breakdown voltages. Metal compositions that produce low switch on-times provided poor RF performance. Each performance criteria required prioritization to meet the overall application goals.

6.6 References

[1]. D.M. Pozer, "*Microwave Engineering*", Addison-Wesley Publishing Company, Reading, MA, (1990):226-227.

[2]. E.R. Brown, "RF-MEMS Switches for Reconfigurable Integrated Circuits", *IEEE Trans. On Microwave Theory and Techniques*, Vol. 46, No. 11, (November 1998): 1868-1880.

CHAPTER 7

CONCLUSIONS AND RECOMMENDATIONS

7.1 Summary

One increasingly important insertion area for MEMS technology is the switching of tuning circuits in RF systems, particularly microwave systems. The objective of this research was to investigate electrostatically actuated MEMS switches, fabricated on GaAs substrates for use at X-band (8 – 12 GHz) frequencies. Electrostatically actuated RF MEMS cantilever and microbridge switches based upon capacitive coupling were successfully designed, fabricated, and tested. The switches, relying on capacitive coupling were configured in series with the RF signal to investigate the effects of switch length and materials on performance. The performance parameters investigated included: insertion loss, isolation, actuation voltage, and switching speed.

Standard GaAs fabrication procedures were utilized, making the switch process integratable with active GaAs electronics. Depending upon the metallization composition used, actuation voltages from 10 – 20 V were achieved with switching times ranging from 10 to 40 μsec. The insertion losses of the fabricated cantilevers and bridges were -0.5 and -0.6 dB at 12 GHz, respectively. The series resistance of the thin Au bottom level metal (0.25 μm) dominated these losses. Simulations using the Sonnett $_{em}$ tool showed that insertion loss could be decreased to -0.2 dB using thicker metal (0.5 μm). Measured switch isolation was typically -15 dB for the cantilevers and -6 dB for the bridges at 12 GHz. The lower isolation for the bridges was due to increased coupling resulting from compromises in the switch layout.

Analytical models of the MEMS structures were developed for the spring-like switches and compared with the classical clamped models reported in most texts. Analysis of the spring models indicated that the more simple classical clamped beam models were sufficiently accurate for initial mechanical designs and were also sufficient to predict the actuation voltage of the switch. The spring models were more accurate as the gap spacing increased beyond the 5 μm goal of the fabrication process. Finite element modeling of the tip deflection of both switches closely matched both analytical models.

Lumped element electrical models were developed along with design procedures to allow first order designs. These lumped element models were compared with both 2 ½ dimensional electromagnetic simulations and measured values of insertion loss and isolation. For a 300 μm long cantilever, the insertion loss of the lumped element model, 2 ½ simulation, and measured results were –0.3 dB, -0.6 dB, and –0.6 dB at 12 GHz respectively. The isolation for the lumped model, simulation, and measured results were –13 dB, -11 dB, and –11 dB at 12 GHz, respectively. For a 700 μm long bridge, the insertion loss for the lumped model, simulation, and measured results were –0.2 dB, -0.4 dB, and –0.5 dB at 12 GHz, respectively. Finally, the isolation for the lumped model, simulation, and measured results were –7 dB, -5 dB, and –5 dB. The discrepancy between the lumped models and simulations was primarily due to the difficulty in accounting for all the parasitic coupling effects of the switches.

An additional goal of the research was to correlate switch length and metal properties to RF performance. The impact of switch length was most significant on the actuation voltage of the cantilevers. In this case, the actuation voltage decreased with

increasing switch length, while insertion loss and isolation decreased only slightly. Metal composition was significant in controlling stress for both the cantilevers and bridges. Only one metal composition (1.0 μm Ti and 0.5 μm Au) resulted in working cantilevers. For bridges, switch length had a negligible impact on actuation voltage, insertion loss, and isolation. Bridge results were more dependent upon metal composition. The film composition of 0.5 μm Ti / 1.0 μm Au produced an actuation voltage of 12 – 16 V, an insertion loss of -0.7 to -0.8 dB, and an isolation of -5 dB for the bridges. The metal combination most suitable for cantilevers (1.0 μm Ti / 0.5 μm Au) produced bridges with actuation voltages of 22 – 27 V, insertion losses of -0.8 dB, and the isolations of -3 to -5 dB. The high insertion loss was due to metal resistivity and the low isolation was due to sagging of the released structure. Perforations included to investigate damping effects offered no significant affect on RF performance or switching speed, but did influence processing yield. Beams with the highest density of perforations were less susceptible to stiction, induced by the wet release process.

7.2 Unique Developments of this Research

This research produced a number of unique aspects and significant contributions. A design methodology was developed for series configured capacitively coupled RF MEMS switches, which included both mechanical and electrical modeling. To date, no design approaches for series configured switches had been published. Stress control using bilayer and trilayers of evaporated metal was demonstrated and correlated with electrical performance. A test configuration for switching speed testing was developed and major limitations of the configuration were described. The material conditions

necessary to fabricate long cantilever beam and microbridge switches were demonstrated along with the performance impact of the material composition. Through the development of the design procedures and analysis, this research served as a documentation of the deficiencies of the series configuration for capacitively coupled switches.

7.3 Recommendations for Future Research

Several areas for future research are evident from this effort. First, detailed studies of electrostatically actuated MEMS switch reliability have not been published. In operation, after repeated switching cycles, the dielectric material appears to become charged and the switches stick down and fail to open. This failure can be called operational stiction. The precise failure mechanism has not been defined and can potentially be due to dielectric charging, residual moisture accumulation, or fatigue (for example). Factors that would contribute to the dielectric charging include the thickness of the dielectric film, the quality of the dielectric, and the actuation voltage. Increases in the actuation voltage, required for high spring constant designs also results in operational stiction. In an effort to study charge accumulation in the dielectric, Plasma Enhanced Chemical Vapor Deposition (PECVD) and sputtered silicon nitrides were investigated. Changing the deposition temperature of the PECVD process and changing the nitrogen flow rate of the sputtered process tested variations in the quality of the dielectrics. The variations in quality of the PECVD silicon nitride produced no noticeable impact on charging. The quality of the sputtered films varied from both extremes and the results were not conclusive.

In addition, the actual deflection and contact area of the switches have not been fully investigated. Detailed analysis of the switches in contact would aid in calculating the device capacitance and determining points of flexure. Contact area investigations in this effort were inconclusive due to insufficient equipment, namely an electrical feed through port in the scanning electron microscope chamber or an optical profiler or interferometric microscope. An initial attempt to study the shape of a collapsed microswitch subject to electrical actuation involved examining the surface area of stuck "released" structures. The scanning electron micrograph of Fig. 7.1 indicated that switch contact begins approximately 100 μm from the fixed end of the beam. The scanning electron micrograph of Fig. 7.2 further indicated that the switch contact area was flat which validates the use of parallel plate capacitors for lumped element modeling. These results are somewhat corroborated using visual inspection of the switches during actuation. Using a microscope with 40X magnification, the light reflection of the switches changed during actuation. The contrast change indicated that the switch contact was flat and did not begin at the fixed end of the beam, but approximately 100 μm from the fixed end as shown by the arrow in Fig. 7.1. The point of contact was determined by monitoring the ~20 perforated beams, which had the highest perforation density, also shown in Fig. 7.1.

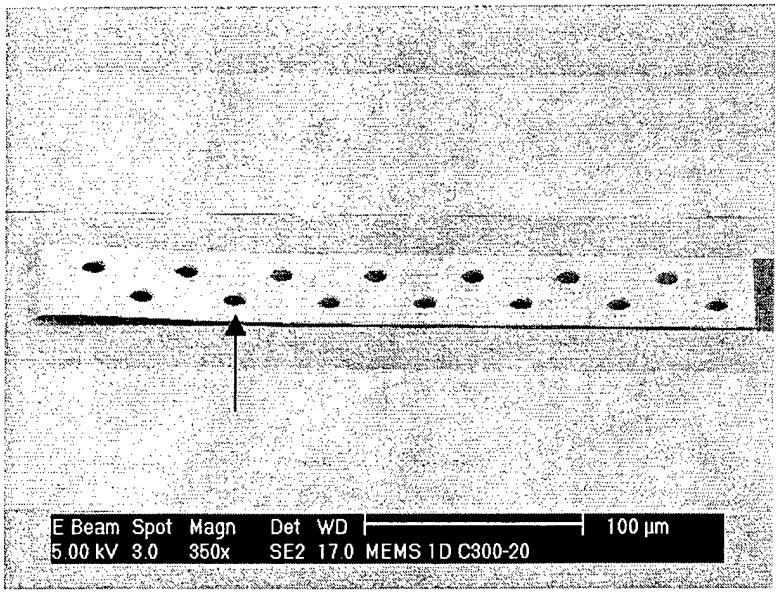

Fig. 7.1. Scanning electron micrograph of 300 µm long cantilever in contact with substrate surface due to liquid induced stiction.

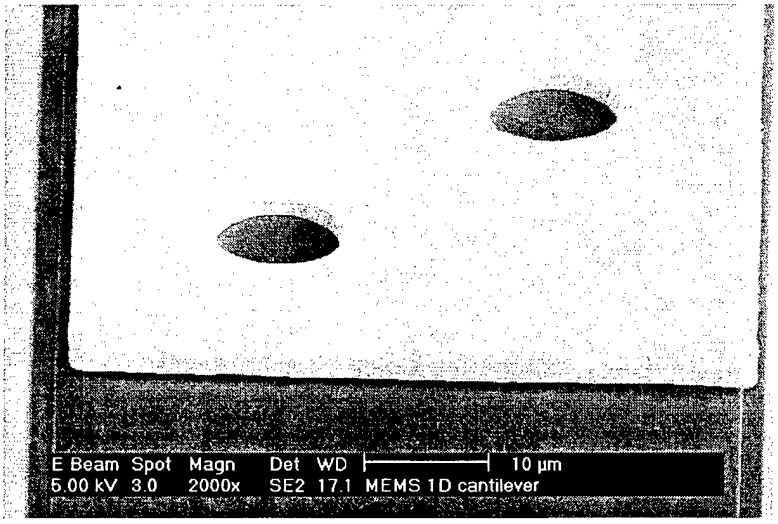

Fig. 7.2. Scanning electron micrograph of cantilever tip in contact with substrate due to liquid induced stiction.

Packaging of RF MEMS switches is a major issue with little documented research and requires numerous considerations. To optimize performance, RF MEMS switches require integration with other circuit elements, i.e. phase delay lines, tuning circuits, etc. Therefore, packaging will be at a higher functional level and parasitic effects of the

package need to be incorporated into the design to the extent possible. One consideration is hermeticity. Hermetic packages are desired to minimize damping, humidity effects, and provide protection from the external environment. However, the major drawback to hermetic packaging is cost. A low cost packaging approach, providing the same protection would greatly improve commercial and military insertion efforts. An additional consideration is the interconnect approach. Typical interconnects consist of wire bonding, which can be lossy and has poor reproducibility at RF frequencies. A soldered approach such as flip chip bonding is very reproducible and has low loss, but requires careful layout and design. The implementation of a flip chip technology with RF MEMS switches is a bottom up process and must consider the switch design and processing.

Finally, the results show that capacitively coupled switches in the series configuration are not ideal for low loss devices. The switch is extremely sensitive to parasitic effects and impedance matching is difficult to achieve. Lower loss capacitively coupled switches can be developed using a shunt configuration. The use of a series switch is more appropriate when relying upon a metal-to-metal contact approach. In this approach, parasitic effects would be minimized.

In conclusion, this research investigated the design and material influences on the performance of RF MEMS switches. The analysis and design guidelines provided accurate results for the dimensions, materials, processes, and test procedures used. The limitations of the fabrication processes and test procedures have been identified where applicable. Finally, a fundamental understanding of the design trade-off issues and

material influences for series configured RF MEMS switches should assist others in the development of other switch designs and configurations.

Appendix A ANSYS Simulation Files

A.1 Spring Cantilever

```
!*
/BATCH
/COM,ANSYS RELEASE  5.4    UP19971021         14:10:33    03/21/2000
/input,menust,tmp     ,,,,,,,,,,,,,,,,1
/GRA,POWER
/GST,ON
!*
/NOPR
/PMETH,OFF
KEYW,PR_SET,1
KEYW,PR_STRUC,1
KEYW,PR_THERM,0
KEYW,PR_FLUID,0
KEYW,PR_ELMAG,0
KEYW,MAGNOD,0
KEYW,MAGEDG,0
KEYW,MAGHFE,0
KEYW,MAGELC,0
KEYW,PR_MULTI,0
KEYW,PR_CFD,0
/GO
!*
/COM,
/COM,Preferences for GUI filtering have been set to display:
/COM,  Structural            (SET PREFERERENCE TO STRUCTURAL MODELING)
!*
/PREP7                                                  (DEFINE KEYPOINTS)
K,1,0,0,0,
K,2,10,0,0,
K,3,20,5,0,
K,4,60,5,0,
K,5,310,5,0,
LSTR,        1,        2      (CONNECT KEYPOINTS FOR STRAIGHT LINE MODEL)
LSTR,        2,        3
LSTR,        3,        4
LSTR,        4,        5
!*
ET,1,BEAM3                   (DEFINE ELEMENT AS BEAM3 - 2D ELASTIC BEAM)
!*
!*
R,1,75,14.2788,1.5, , , ,                              (SET REAL CONSTANTS)
                                          (Cross-Sectional Area = 75 μm²,
                                        Moment of Inertia = 14.2788 μm⁴,
                                                    Height = 1.5 μm)
!*
!*
UIMP,1,EX, , ,0.091653,                        (SET MATERIAL PROPERTIES)
UIMP,1,DENS, , , ,                       (Young's Modulus = 0.091653 N/μm²)
UIMP,1,ALPX, , , ,
UIMP,1,REFT, , , ,
```

```
UIMP,1,NUXY, , , ,                                   (EI_eff = 1.3087 N/μm²)
UIMP,1,PRXY, , , ,
UIMP,1,GXY, , , ,
UIMP,1,MU, , , ,
UIMP,1,DAMP, , , ,
UIMP,1,KXX, , , ,
UIMP,1,C, , , ,
UIMP,1,ENTH, , , ,
UIMP,1,HF, , , ,
UIMP,1,EMIS, , , ,
UIMP,1,QRATE, , , ,
UIMP,1,MURX, , , ,
UIMP,1,MGXX, , , ,
UIMP,1,RSVX, , , ,
UIMP,1,PERX, , , ,
UIMP,1,VISC, , , ,
UIMP,1,SONC, , , ,
!*
FLST,2,4,4,ORDE,2
FITEM,2,1
FITEM,2,-4
LMESH,P51X                                  (MESH USING THE MESHTOOL)
/UI,MESH,OFF
/SOLU
FINISH
/SOLU
FLST,2,2,3,ORDE,2
FITEM,2,1
FITEM,2,-2
DK,P51X, , , ,0,ALL                  (APPLY STRUCTURAL DISPLACEMENTS FOR
LPLOT                               ALL DEGREES OF FREEDOM AT END POINTS)
FLST,2,6,2,ORDE,2
FITEM,2,12
FITEM,2,-17
SFBEAM,P51X,1,PRES,6.4071e-9, , , , , ,  (APPLY PRESSURE OF 6.4071 nPa)
/STAT,SOLU                                                    (SOLVE)
SOLVE
/POST1
FINISH
/POST1
SET,FIRST                                        (READ FIRST DATA SET)
PLDISP,0                                  (DISPLAY DEFLECTION PLOT)
FINISH
! /EXIT,NOSAV
```

A.2 Spring Bridge

```
 /BATCH
! /COM,ANSYS RELEASE  5.4    UP19971021          14:37:57    03/21/2000
/input,menust,tmp     ,,,,,,,,,,,,,,,,,1
!*
/NOPR
/PMETH,OFF
KEYW,PR_SET,1
KEYW,PR_STRUC,1
KEYW,PR_THERM,0
KEYW,PR_FLUID,0
KEYW,PR_ELMAG,0
KEYW,MAGNOD,0
KEYW,MAGEDG,0
KEYW,MAGHFE,0
KEYW,MAGELC,0
KEYW,PR_MULTI,0
KEYW,PR_CFD,0
/GO
!*
! /COM,
! /COM,Preferences for GUI filtering have been set to display:
! /COM,  Structural            (SET PREFERENCE TO STRUCTURAL MODELING)
!*
/PREP7                                                  (DEFINE KEYPOINTS)
K,1,0,0,0,
K,2,10,0,0,
K,3,20,5,0,
K,4,60,5,0,
K,5,560,5,0,
K,6,600,5,0,
K,7,610,0,0,
K,8,620,0,0,
LSTR,       1,       2      (CONNECT KEYPOINTS FOR STRAIGHT LINE MODEL)
LSTR,       2,       3
LSTR,       3,       4
LSTR,       4,       5
LSTR,       5,       6
LSTR,       6,       7
LSTR,       7,       8
!*
ET,1,BEAM3                   (DEFINE ELEMENT A BEAM3 - 2D ELASTIC BEAM)
!*
!*
R,1,75,14.2788,1.5, , , ,                          (SET REAL CONSTANTS)
                                        (Cross-Sectional Area = 75 μm²,
                                      Moment of Inertia = 14.2788 μm⁴,
                                                    Height = 1.5 μm)
!*
!*
UIMP,1,EX, , ,0.091653,                   (SET MATERIAL PROPERTIES)
UIMP,1,DENS, , , ,                    (Young's Modulus = 0.019653 N/μm²)
UIMP,1,ALPX, , , ,
UIMP,1,REFT, , , ,                                  (EI_eff = 1.3087 nPa)
UIMP,1,NUXY, , , ,
```

```
UIMP,1,PRXY, , , ,
UIMP,1,GXY, , , ,
UIMP,1,MU, , , ,
UIMP,1,DAMP, , , ,
UIMP,1,KXX, , , ,
UIMP,1,C, , , ,
UIMP,1,ENTH, , , ,
UIMP,1,HF, , , ,
UIMP,1,EMIS, , , ,
UIMP,1,QRATE, , , ,
UIMP,1,MURX, , , ,
UIMP,1,MGXX, , , ,
UIMP,1,RSVX, , , ,
UIMP,1,PERX, , , ,
UIMP,1,VISC, , , ,
UIMP,1,SONC, , , ,
!*
FLST,2,7,4,ORDE,2
FITEM,2,1
FITEM,2,-7
LMESH,P51X                                          (MESH USING MESHTOOL)
/UI,MESH,OFF
FINISH
/SOLU
FLST,2,4,3,ORDE,4
FITEM,2,1
FITEM,2,-2
FITEM,2,7
FITEM,2,-8
DK,P51X, , , ,0,ALL                  (APPLY STRUCTURAL DISPLACEMENTS FOR
! LPLOT                            ALL DEGREES OF FREEDOM AT END POINTS)
FLST,2,15,2,ORDE,2
FITEM,2,12
FITEM,2,-26
SFBEAM,P51X,1,PRES,20.722e-9, , , , , ,  (APPLY PRESSURE OF 20.722 nPa)
! /STAT,SOLU                                                  (SOLVE)
SOLVE
FINISH
/POST1
SET,FIRST                                          (READ FIRST DATA SET)
! PLDISP,0                                      (DISPLAY DEFLECTION PLOT)
! LGWRITE,bridge,lgw,c:\TEMP\,COMMENT
FINISH
! /EXIT,NOSAV
```

Appendix B Built-in Beam Model

Analysis of the built-in beam model (Figure B.1) also utilized the method of successive integration, which relates deflection in terms of the bending moment. The bending moment of the beam is given by

$$EI\upsilon'' = -M, \tag{B.1}$$

where M is the bending moment. Integrating this equation twice results in the deflection equation for the beam.

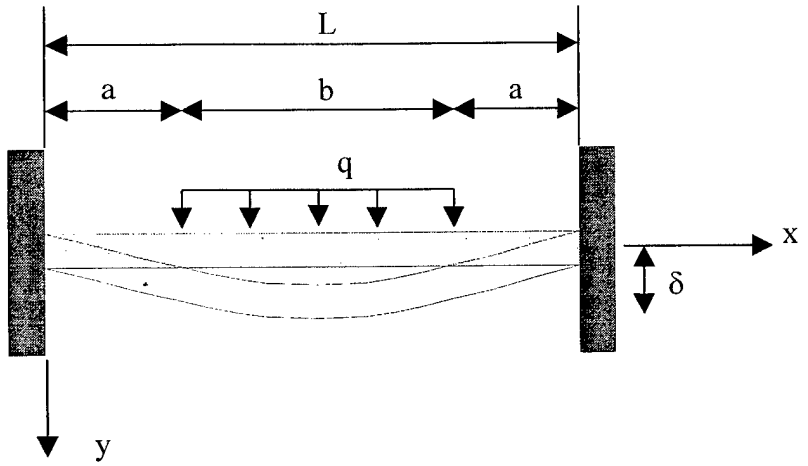

Figure B.1 Built-in beam model.

Using the free-body diagram (Figure B.2) and the dimensions of the model (Figure B.1), an examination of the external reactions results in $M_A = M_B$ and $R_A = R_B = qb/2$. The model was then subdivided into two sections and the deflection equation for each section was derived.

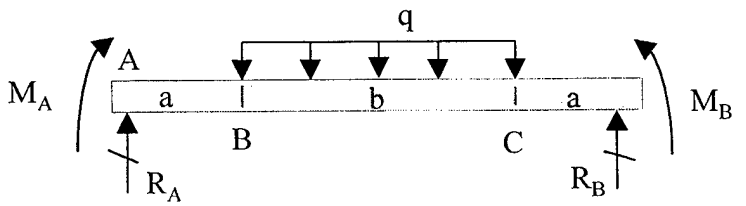

Figure B.2 Free-body diagram.

The deflection equation for the segment *A-B (0 < x < a)* was derived from Figure B.3, with the bending moment M_1 given by

$$M_1 = M_A + R_A x \ . \tag{B.2}$$

The deflection equation was determined by two successive integrations of Equation B.1.

$$EI\upsilon'' = -M_A - \frac{qbx}{2} \tag{B.3}$$

$$EI\upsilon' = -M_A x - \frac{qbx^2}{4} + C_1 \tag{B.4}$$

$$EI\upsilon = -\frac{M_A x^2}{2} - \frac{qbx^3}{12} + C_1 x + C_2 \ . \tag{B.5}$$

From the boundary conditions $EI\upsilon'_{(x=0)} = 0$ and $EI\upsilon_{(x=0)} = 0$, the constants of integration were determined to be $C_1 = 0$ and $C_2 = 0$. The end point conditions at $x = a$ then gives

$$EI\upsilon'_{(x=a)} = -M_A a - \frac{qa^2 b}{4}. \tag{B.6}$$

$$EI\upsilon_{(x=a)} = -\frac{M_A a^2}{2} - \frac{qa^3 b}{12}. \tag{B.7}$$

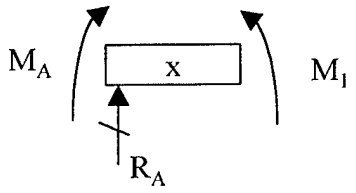

Figure B.3 Beam segment A-B *(0 < x < a)*.

The derivation for the segment A-C *(0 < x < L)* follows the same procedure and was derived using Figure B.4. The bending moment M_2 was given by

$$M_2 = M_A + R_A x - \frac{q(x-a)^2}{2} \tag{B.8}$$

The deflection equation was then determined by

$$EI\upsilon'' = -M_A - \frac{qbx}{2} + \frac{q(x-a)^2}{2} \tag{B.9}$$

$$EI\upsilon' = -M_A x - \frac{qbx^2}{4} + \frac{q(x-a)^3}{6} + C_3 \tag{B.10}$$

$$EI\upsilon = -\frac{M_A x^2}{2} - \frac{qbx^3}{12} + \frac{q(x-a)^4}{24} + C_3 x + C_4 . \tag{B.11}$$

Solving Equations B.10 and B.11 for $x = a$ and equating them with the end point conditions of Equations B.6 and B.7, the constants of integration were determined to be $C_3 = 0$ and $C_4 = 0$. Since the slope of the deflection curve is zero at the center of the beam $(EI\upsilon'_{(x=L/2)} = 0)$, the bending moment M_A can be obtain by substituting $x=L/2$ into Equation B.10 and solving for M_A giving

$$EI\upsilon'_{(x=L/2)} = 0 = -M_A \frac{L}{2} - \frac{qbL^2}{16} + \frac{q}{6}\left(\frac{L}{2} - a\right)^3 \tag{B.12}$$

$$\frac{b}{2} = \frac{L}{2} - a \tag{B.13}$$

$$M_A = -\frac{qbL}{8} + \frac{qb^3}{24L}. \tag{B.14}$$

Substituting this result into Equation B.11 and solving for maximum beam deflection at the center of the beam $(x = L/2)$ results in

$$\delta_{max} = \frac{qb}{384EI}\left(2L^3 - 2b^2L + b^3\right) \tag{B.15}$$

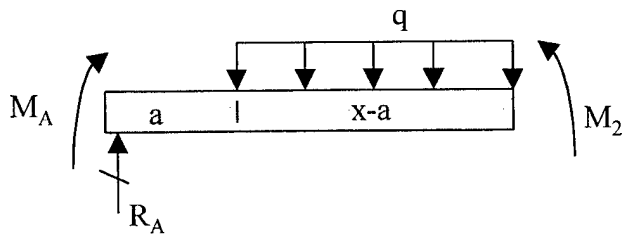

Figure B.4 Beam segment A-C $(0< x < L)$.

Appendix C Spring Bridge Model

Analysis of the spring bridge model (Figure C.1) also utilized the method of successive integration, which relates deflection in terms of the bending moment. The bending moment of the beam was given by

$$EI\upsilon'' = -M, \tag{C.1}$$

where M is the bending moment. Integrating this equation twice results in the deflection equation for the beam.

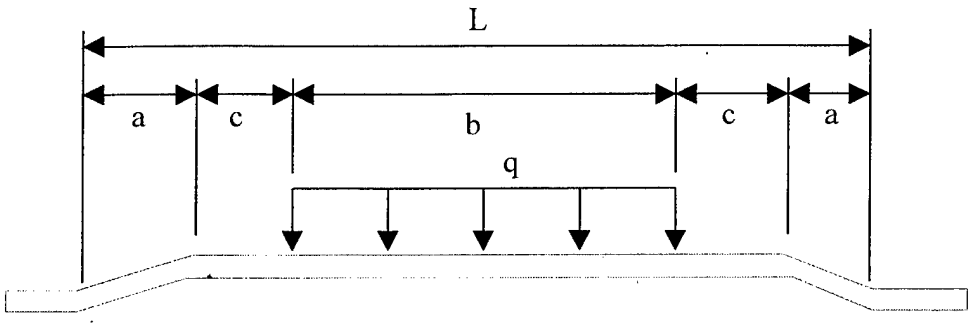

Figure C.1 Spring bridge model.

Using the free-body diagram (Figure C.2) and the dimensions of the model (Figure C.1), examination of the external reactions results in $M_A = M_B$ and $R_A = R_B = qb/2$. The model was then subdivided into three sections and the deflection equation for each section was derived.

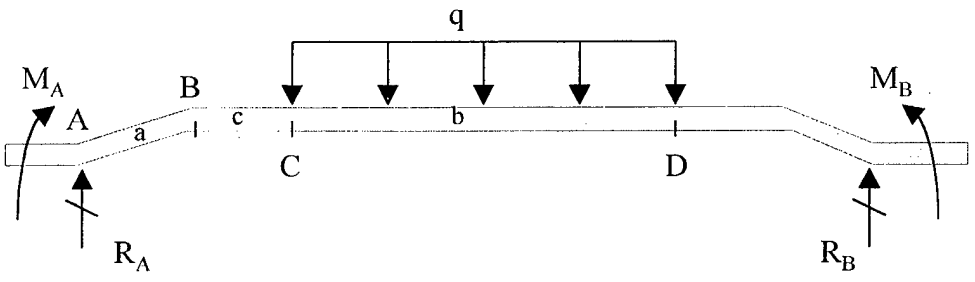

Figure C.2 Free-body diagram.

The deflection equation for the segment *A-B (0 < x < a)* was derived from Figure C.3, with the bending moment M_1 given by

$$M_1 = M_A + \frac{R_A x}{\cos\theta} \,. \tag{C.2}$$

The deflection equation was determined by two successive integrations of Equation C.1.

$$EI\upsilon'' = -M_A - \frac{qbx}{2\cos\theta} \tag{C.3}$$

$$EI\upsilon' = -M_A x - \frac{qbx^2}{4\cos\theta} + C_1 \tag{C.4}$$

$$EI\upsilon = -\frac{M_A x^2}{2} - \frac{qbx^3}{12\cos\theta} + C_1 x + C_2 \,. \tag{C.5}$$

From the boundary conditions $EI\upsilon'_{(x=0)} = 0$ and $EI\upsilon_{(x=0)} = 0$, the constants of integration are determined to be $C_1 = 0$ and $C_2 = 0$. The end point conditions at $x = a$ then gives

$$EI\upsilon'_{(x=a)} = -M_A a - \frac{qa^2 b}{4\cos\theta}. \tag{C.6}$$

$$EI\upsilon_{(x=a)} = -\frac{M_A a^2}{2} - \frac{qa^3 b}{12\cos\theta}. \tag{C.7}$$

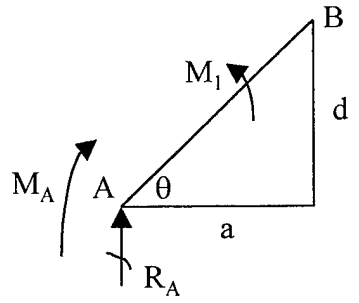

Figure C.3 Beam segment A-B *(0 < x < a)*.

The derivation for the segment A-C *(0 < x < a+c)* follows the same procedure and was derived using Figure C.4. The bending moment M_2 was given by

$$M_2 = M_A + R_A x . \tag{C.8}$$

The deflection equation was then determined by

$$EI\upsilon'' = -M_A - \frac{qbx}{2} \tag{C.9}$$

$$EI\upsilon' = -M_A x - \frac{qbx^2}{4} + C_3 \tag{C.10}$$

$$EI\upsilon = -\frac{M_A x^2}{2} - \frac{qbx^3}{12} + C_3 x + C_4 . \tag{C.11}$$

Solving Equations C.10 and C.11 for $x = a$ and equating them with the end point conditions of C.6 and C.7, results in the constants of integration

$$C_3 = \frac{qa^2 b}{4}\left(1 - \frac{1}{\cos\theta}\right) \tag{C.12}$$

$$C_4 = -\frac{qa^3 b}{6}\left(1 - \frac{1}{\cos\theta}\right) \tag{C.13}$$

Substituting these results into Equations C.10 and C.11 and solving for the end point at $x = a+c$ gave

$$EI\upsilon'_{(x=a+c)} = -M_A(a+c) - \frac{qb}{4}(a+c)^2 + \frac{qa^2 b}{4}\left(1 - \frac{1}{\cos\theta}\right) \tag{C.14}$$

$$EI\upsilon_{(x=a+c)} = -\frac{M_A}{2}(a+c)^2 - \frac{qb}{12}(a+c)^3 + \frac{qa^2 b}{4}(a+c)\left(1 - \frac{1}{\cos\theta}\right) - \frac{qa^3 b}{6}\left(1 - \frac{1}{\cos\theta}\right). \tag{C.15}$$

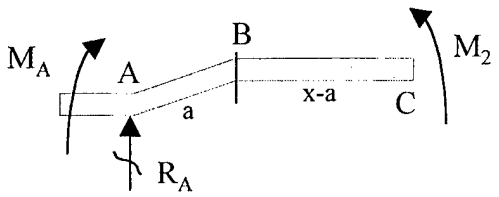

Figure C.4 Beam segment A-C *(0 < x < a+c)*.

The derivation of the deflection equation for the beam segment A-*D* *(0 < x < a+c+b)* was derived from Figure C.5, with the moment M_3 given by

$$M_3 = M_A + \frac{qbx}{2} - \frac{q(x-a-c)^2}{2}. \tag{C.16}$$

The deflection equation was then determined from

$$EI\upsilon'' = -M_A - \frac{qbx}{2} + \frac{q(x-a-c)^2}{2} \tag{C.17}$$

$$EI\upsilon' = -M_A x - \frac{qbx^2}{4} + \frac{q(x-a-c)^3}{6} + C_5 \tag{C.18}$$

$$EI\upsilon = -\frac{M_A x^2}{2} - \frac{qbx^3}{12} + \frac{q(x-a-c)^4}{24} + C_5 x + C_6 . \tag{C.19}$$

Solving Equations C.18 and C.19 for $x = a+c$ and equating them with the end point conditions of Equations C.14 and C.15, results in the constants C_5 and C_6

$$C_5 = \frac{qa^2 b}{4}\left(1 - \frac{1}{\cos\theta}\right) \tag{C.20}$$

$$C_6 = -\frac{qa^3 b}{6}\left(1 - \frac{1}{\cos\theta}\right). \tag{C.21}$$

Since the slope of the deflection curve is zero at the center of the beam $EI\upsilon'_{(x=L/2)} = 0$, the bending moment M_A can be obtain by substituting $x=L/2$ into Equation C.18 and solving for M_A giving

$$EI\upsilon'_{(x=L/2)} = 0 = -M_A\left(\frac{L}{2}\right) - \frac{qbL^2}{16} + \frac{q}{6}\left(\frac{L}{2} - a - c\right)^3 + \frac{qa^2 b}{4}\left(1 - \frac{1}{\cos\theta}\right) \tag{C.22}$$

$$M_A = -\frac{qbL}{8} + \frac{qb^3}{24L} + \frac{qa^2 b}{2L}\left(1 - \frac{1}{\cos\theta}\right), \tag{C.23}$$

$$\frac{b}{2} = \frac{L}{2} - a - c . \tag{C.24}$$

Finally, substituting C_5, C_6, and M_A into Equation C.19 results in the spring bridge deflection equation in terms of x.

$$EI\upsilon = \frac{q}{48}\left[\begin{array}{l} 3bLx^2 - \frac{b^3x^2}{L} - 4bx^3 + 2(x-a-c)^4 + 12a^2bx\left(1-\frac{1}{\cos\theta}\right) + 8a^3b\left(1-\frac{1}{\cos\theta}\right) \\ -\frac{12a^2bx^2}{L}\left(1-\frac{1}{\cos\theta}\right) \end{array}\right]. \quad \text{(C.24)}$$

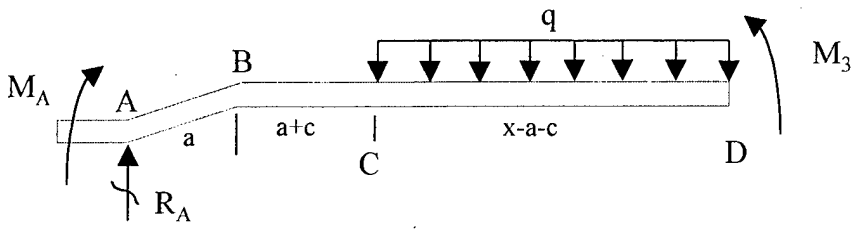

Figure C.5 Beam segment A-D *(0 < x < a+c+b)*.

Solving for maximum beam deflection at the beam center *(x = L/2)* and using

$$\cos\theta = \frac{a}{\sqrt{a^2+d^2}}, \quad \text{(C.25)}$$

Equation C.24 can be rearranged to give

$$\delta_{max} = \frac{qb}{384EI}\left[2L^3 - 2b^2L + b^3 + 24a^2L\left(1-\frac{\sqrt{a^2+d^2}}{a}\right) - 84a^3\left(1-\frac{\sqrt{a^2+d^2}}{a}\right)\right]. \quad \text{(C.26)}$$

For the case when $d = 0$ (no incline), then $\cos\theta = 1$ and this equation resorts to the built-in beam equation B.15.

Appendix D Process Followers and Masks **BOTTOM METAL** ver 2.0

Wafer ID:

Init.	Process Step	Notes	Date Time
	BOE CLEAN: ❑ Mix (1:10) BOE:DI; mix 25 ml of BOE with 250 ml of H_2O in Teflon bucket ❑ 30 sec dip (1:10) BOE:DI ❑ 3 X DI water rinse ❑ Dry wafer on clean texwipes with Nitrogen	**Start Date** **Start Time**	
	SOLVENT CLEAN: ❑ 20 sec Acetone rinse ❑ 20 sec Isopropyl alcohol rinse ❑ Dry with Nitrogen (spinning at 500 rpm) ❑ Dry wafer on texwipes with Nitrogen **INSPECT WAFER:** ❑ Note any defects		
	PMGI COAT #1: ❑ Flood wafer with SF-11 PMGI ❑ 30 sec Spin at 4,000 RPM, Ramp = 200 ❑ Use edge bead remover (EBR) to remove PMGI on backside ❑ 1 min Air Bake ❑ 5 min 270 °C Hot plate bake		
	1813 COAT: ❑ Flood wafer with 1813 ❑ 30 sec Spin at 4,000 RPM, Ramp = 200 ❑ Use Acetone to remove 1813 on backside ❑ 75 sec 110°C Hot plate bake		
	EXPOSE 1813 TO BOTTOM METAL MASK: ❑ 40 sec Exposure @ 2.0 mW/cm^2 of 405 nm Light on **MJB3**		
	1813 DEVELOP: ❑ 30 sec 351 Develop with (1:5) 351:DI water (while spinning wafer at 500 RPM). ❑ 30 sec Rinse with DI water stream (Spinning at 500 RPM) ❑ Dry with Nitrogen (spinning at 500 RPM) ❑ Dry wafer on clean texwipes with Nitrogen		
	INSPECT RESIST: ❑ Inspect photoresist using yellow filter		
	DUV ❑ 200 sec Deep UV exposure @ 16 mW/cm^2, 254 nm		
	PMGI DEVELOP ❑ 60 sec SAL 101 Develop in petri dish ❑ 3 X DI water rinse ❑ Dry with Nitrogen ❑ Dry wafer on clean texwipes with Nitrogen		
	INSPECT RESIST: ❑ Inspect photoresist		
	ASHER (JUST PRIOR TO DIP): ❑ 4 min, 200 W, 400 sccm O_2, LFE		
	PRE-METAL DIP: ❑ Mix (1:10) BOE:DI, mix 25 ml of BOE with 250 ml of H_2O in Teflon bucket ❑ 30 sec Dip (1:10) BOE:DI ❑ 3 X DI water rinse ❑ Dry wafer on clean texwipes with Nitrogen		
	BOTTOM METAL DEPOSITION: ❑ Evaporate _____ Å _____ / _____ Å ____		

Appendix D
Wafer ID:

BOTTOM METAL ver 2.0

	LIFT-OFF BOTTOM METAL: ❑ Use tape to remove excess metal ❑ Inspect for metal removal ❑ 15 sec spray with acetone gun (spinning at 500 RPM) ❑ 15 sec spray with acetone bottle (spinning at 500 RPM) ❑ 30 sec Isopropyl alcohol (spinning at 500 RPM) ❑ Dry with Nitrogen (spinning at 500 RPM)) ❑ Dry wafer on clean texwipes with Nitrogen		
	1165 STRIP PMGI: ❑ 2 min 90 °C 1165 remover ❑ 3 X DI water rinse ❑ Dry wafer on 3 clean texwipes with Nitrogen		
	INSPECT WAFER: ❑ Inspect for resist removal and measure metal layer height with profilometer Feature measured: _____		

	Die #	Total metal thickness, Å	Finish Date Finish Time	
	02-06			
	08-02			
	08-06			
	08-11			
	15-06			

NITRIDE ver 2.0

Wafer ID:

Init.	Process Step	Notes	Date Time
	SOLVENT CLEAN: ❑ 20 sec Acetone rinse ❑ 20 sec Isopropyl alcohol rinse ❑ Dry with Nitrogen (spinning at 500 RPM) ❑ Dry wafer on clean texwipes with Nitrogen	Start Date Start Time	
	DEHYDRATION BAKE: ❑ 1 min 110 °C Hot plate bake		
	NITRIDE DEPOSITION: ❑ Deposit nitride ❑ CVD (250°C or 300°C) or ❑ Sputtered ❑ Measure index of refraction and actual height using ellipsometer N_f = _____ **Thickness** _____ Å		
	PMGI COAT #1: ❑ Flood wafer with SF-11 PMGI ❑ 30 sec Spin at 4,000 RPM, Ramp = 200 ❑ Use edge bead remover (EBR) to remove PMGI on backside ❑ 1 min Air Bake ❑ 5 min 270 °C Hot plate bake		
	1813 COAT: ❑ Flood wafer with 1813 ❑ 30 sec Spin at 4,000 RPM, Ramp = 200 ❑ Use Acetone to remove 1813 on backside ❑ 75 sec 110°C Hot plate bake		
	EXPOSE 1813 TO MEMS NITRIDE MASK: ❑ 40 sec Exposure @ 2.0 mW/cm^2 of 405 nm Light on **MJB3**		
	1813 DEVELOP: ❑ 30 sec 351 Develop with (1:5) 351:DI (while spinning wafer at 500 RPM) ❑ 30 sec Rinse with DI water stream (Spinning at 500 RPM) ❑ Dry with Nitrogen (spinning at 500 RPM) ❑ Dry wafer on clean texwipes with Nitrogen		
	INSPECT RESIST: ❑ Inspect photoresist using yellow filter		
	DUV ❑ 200 sec Deep UV exposure @ 16 mW/cm^2, 254 nm		
	PMGI DEVELOP ❑ 60 sec SAL 101 Develop in petri dish ❑ 3 X DI water rinse ❑ Dry with Nitrogen ❑ Dry wafer on clean texwipes with Nitrogen		
	INSPECT RESIST: ❑ Inspect photoresist		
	ASHER: ❑ 4 min, 200 W, 400 sccm O_2, LFE		
	ETCH NITRIDE: ❑ Use RIE operating at the following conditions: Gas: Freon 23 & O_2 Time: ~7 ½ minutes (time typical for 2500 Å CVD nitride)		
	INSPECT WAFER: ❑ Inspect for nitride removal		

Wafer ID:

	1165 STRIP PMGI: ❑ 2 min 90 °C 1165 remover ❑ 3 X DI water rinse ❑ Dry wafer on clean texwipes with Nitrogen			
	INSPECT WAFER: ❑ Inspect for resist removal ❑ Measure nitride step height using Tencor profilometer Feature measured _____			
	Die #	**Capacitor Height, Å**	**Finish Date** **Finish Time**	
	02-06			
	08-02			
	08-06			
	08-11			
	15-06			

Wafer ID:

Init.	Process Step	Notes	Date Time
	SOLVENT CLEAN: ❑ 20 sec Acetone rinse ❑ 20 sec Isopropyl alcohol rinse ❑ Dry with Nitrogen (spinning at 500 RPM) ❑ Dry wafer on clean texwipes with Nitrogen	Start Date Start Time	
	DEHYDRATION BAKE: ❑ 60 sec 110°C Hot plate bake		
	PMGI COAT: ❑ Flood wafer with SF-19 PMGI (cut pipet end or pour on) ❑ 5 sec Spread at 2,000 rpm, Ramp = 200 ❑ 30 sec Spin at 4,000 rpm, Ramp = 200 ❑ Use edge bead remover (EBR) to remove PMGI on backside Dispense on edge with pipet spinning at 4,000 rpm ❑ 1 min Air Bake ❑ 5 min 270 °C Hot plate bake		
	1813 COAT: ❑ Flood wafer with 1813 ❑ 30 sec Spin at 4000 rpm, Ramp = 200 ❑ Use Acetone to remove 1813 on backside ❑ 75 sec 110 °C Hot plate bake		
	EXPOSE 1813 TO MEMS POST MASK: ❑ 4.0 sec Exposure @ 20 mW/cm^2 of 405 nm Light on **MJB3**		
	1813 DEVELOP: ❑ 30 sec Develop with (1:5) 351:DI (while spinning wafer at 500 rpm) ❑ 30 sec Rinse with DI water stream (Spinning at 500 rpm) ❑ Dry with Nitrogen (spinning at 500 rpm) ❑ Dry wafer on clean texwipes with Nitrogen		
	INSPECT RESIST: ❑ Inspect photoresist using yellow filter		
	ASHER: ❑ 4 min, 200 W, 400 sccm O_2, LFE		
	1ST DUV CYCLE: ❑ 200 sec Deep UV exposure @ 16 mW/cm^2, 254 nm		
	PMGI DEVELOP: ❑ 60 sec SAL 101 Develop in petri dish ❑ 3 X DI water rinse ❑ Dry with Nitrogen ❑ Dry wafer on clean texwipes with Nitrogen		
	INSPECT RESIST: ❑ Inspect photoresist using yellow filter		
	2ND DUV CYCLE: ❑ 200 sec Deep UV exposure @ 16 mW/cm^2, 254 nm		
	PMGI DEVELOP: ❑ 60 sec SAL 101 Develop in petri dish ❑ 3 X DI water rinse ❑ Dry wafer on clean texwipes with Nitrogen		
	INSPECT RESIST: ❑ Inspect photoresist using yellow filter		
	3RD DUV CYCLE ❑ 200 sec Deep UV exposure @ 16 mW/cm^2, 254 nm		
	PMGI DEVELOP ❑ 60 sec SAL 101 Develop in petri dish ❑ 3 X DI water rinse ❑ Dry with Nitrogen ❑ Dry wafer on clean texwipes with Nitrogen		

Wafer ID:

	INSPECT RESIST: ❑ Inspect photoresist using yellow filter ❑ Measure thickness using Tencor profilometer **REPEAT DUV CYCLE and PMGI DEVELOP as needed**		
	ASHER: ❑ 4 min, 200 W, 400 sccm O_2, LFE		
	STRIP 1813: ❑ 5 min room temperature Acetone soak (DO NOT LET THE WAFER DRY) ❑ 30 sec Acetone **Spray** (spinning at 500 rpm) ❑ 20 sec Acetone bottle (spinning at 500 rpm) ❑ 20 sec Isopropyl alcohol rinse (spinning at 500 rpm) ❑ 10 sec DI H_20 rinse(spinning at 500 rpm) ❑ Dry with Nitrogen (spinning at 500 rpm) ❑ Dry wafer on clean texwipes with Nitrogen		
	INSPECT RESIST: ❑ Inspect photoresist for 1813 removal		
	POST REFLOW: ❑ 75 sec 250 °C hot air oven bake (up to 90 sec reflow time have been previously used) **USE OVEN TRAY** Start timer after door is closed		
	INSPECT WAFER: ❑ Inspect for SF-19 resist reflow		
	HARD BAKE: ❑ > 1 hour 90 °C hot air oven bake (Overnight Bake Acceptable) ❑ Measure bridge height using Tencor profilometer after cool down. **Die #** **Height, Å**	**Finish Date** **Finish Time**	

TOP METAL ver 2.0

Wafer ID:

Init.	Process Step	Notes	Date Time
	PREPARATIONS: ❑ Set oven (blue) to 190 °C	Start Date Start Time	
	SOLVENT CLEAN: ❑ 20 sec Acetone rinse ❑ 20 sec Isopropyl alcohol rinse ❑ Dry with Nitrogen (spinning at 500 RPM) ❑ Dry wafer on clean texwipes with Nitrogen		
	DEHYDRATION BAKE: ❑ 60 sec 110°C Hot plate bake		
	PMMA COAT #1: 950K ❑ Flood wafer with PMMA 950K ❑ 60 sec spin @ 3000 rpm, ramp = 200 ❑ Use Acetone to remove PMMA on backside ❑ 30 min 190°C Hot air oven ❑ Cool Wafer on Wafer Chuck		
	PMMA COAT #2: 950K ❑ Flood wafer with PMMA 950K ❑ 60 sec spin @ 3000 rpm, ramp = 200 ❑ Use Acetone to remove PMMA on backside ❑ 30 min 190°C Hot air oven ❑ Cool Wafer on chuck		
	1813 COAT : ❑ Flood wafer with 1813 ❑ 30 sec spin @ 4000 rpm, ramp=200 ❑ Use Acetone to remove 1813 on backside ❑ 75 sec 110°C Hot plate bake ❑ Cool Wafer on Wafer Chuck		
	EXPOSE 1813 TO MEMS TOP METAL MASK: ❑ 50 sec Exposure @ 2.0 mW/cm^2 of 405 nm Light on **MJB3**		
	1813 DEVELOP: ❑ 45 sec 351 Develop with (1:5) 351:DI @ 500 rpm ❑ 30 sec Rinse with DI water stream @ 500 rpm ❑ Dry with Nitrogen @ 500 rpm ❑ Dry wafer on clean texwipes with Nitrogen		
	INSPECT RESIST: ❑ Inspect photoresist using yellow filter		
	ASHER: ❑ 6 min, 200 W, 400 sccm O_2, LFE		
	1ST DUV CYCLE ❑ 200 sec Deep UV exposure @ 16 mW/cm^2, 254 nm		
	PMMA DEVELOP: ❑ 60 sec chlorobenzene @ 500 rpm **Use lift-off or cleaning hood** ❑ Dry with Nitrogen @ 500 rpm ❑ Dry wafer on clean texwipes with Nitrogen **Note:** Pour Isopropyl alcohol in spinner pan to flush chlorobenzene		
	INSPECT RESIST: ❑ Inspect photoresist using yellow filter		
	2ND DUV CYCLE ❑ 200 sec Deep UV exposure @ 16 mW/cm^2, 254 nm		

Wafer ID:

	PMMA DEVELOP: ❑ 60 sec chlorobenzene @ 500 rpm **Use lift-off or cleaning hood** ❑ Dry with Nitrogen @ 500 rpm ❑ Dry wafer on clean texwipes with Nitrogen **Note:** Pour Isopropyl alcohol in spinner pan to flush chlorobenzene		
	INSPECT RESIST: ❑ Inspect photoresist using yellow filter		
	PRE-METAL DIP: ❑ Mix (1:10) BOE:DI, mix 25 ml of BOE with 250 ml of H_2O in Teflon bucket **Use clean solution** ❑ 30 sec BOE:DI H_2O (1:10) ❑ 3 X DI water rinse ❑ Dry wafer on clean texwipes with Nitrogen		
	BRIDGE METAL DEPOSITION: ❑ Evaporate _____ Å _____/_____ Å _____		
	LIFT-OFF BRIDGE METAL: ❑ ~30 min room temperature acetone soak (covered) ❑ **Take care not to allow acetone to dry** on wafer transfer to spinner chuck ❑ 15 sec spray with acetone spray gun @ 500 rpm ❑ 30 sec spray with acetone bottle @ 500 rpm ❑ 30 sec spray with Isopropyl alcohol @ 500 rpm ❑ Dry wafer with nitrogen @ 500 rpm ❑ Dry wafer on clean texwipes		
	INSPECT WAFER: ❑ Inspect for metal lift-off		
	REMOVE PMGI: ❑ Heat 1165 remover to 90°C ❑ 10 min 90°C 1165 soak ❑ Remove beaker from heat, let 1165 cool 15 min ❑ Put wafer in petri dish with room temperature 1165 ❑ Examine wafer (in dish) under microscope for PMGI removal ❑ 2 min soak (in petri dish) in 50 vol % DI water/methanol solution (15 mL of each) ❑ Replace 15 mL of original solution with 15 mL methanol ❑ Examine wafer (In dish) for release ❑ 60 sec soak in petri dish containing Isopropyl alcohol **Do not use spray bottle** ❑ Dry wafer over 110°C hot plate after most of isopropyl alcohol has evaporated		
	INSPECT WAFER: ❑ Inspect for resist removal	**Finish Date** **Finish Time**	

Bottom Metal - Mask 1

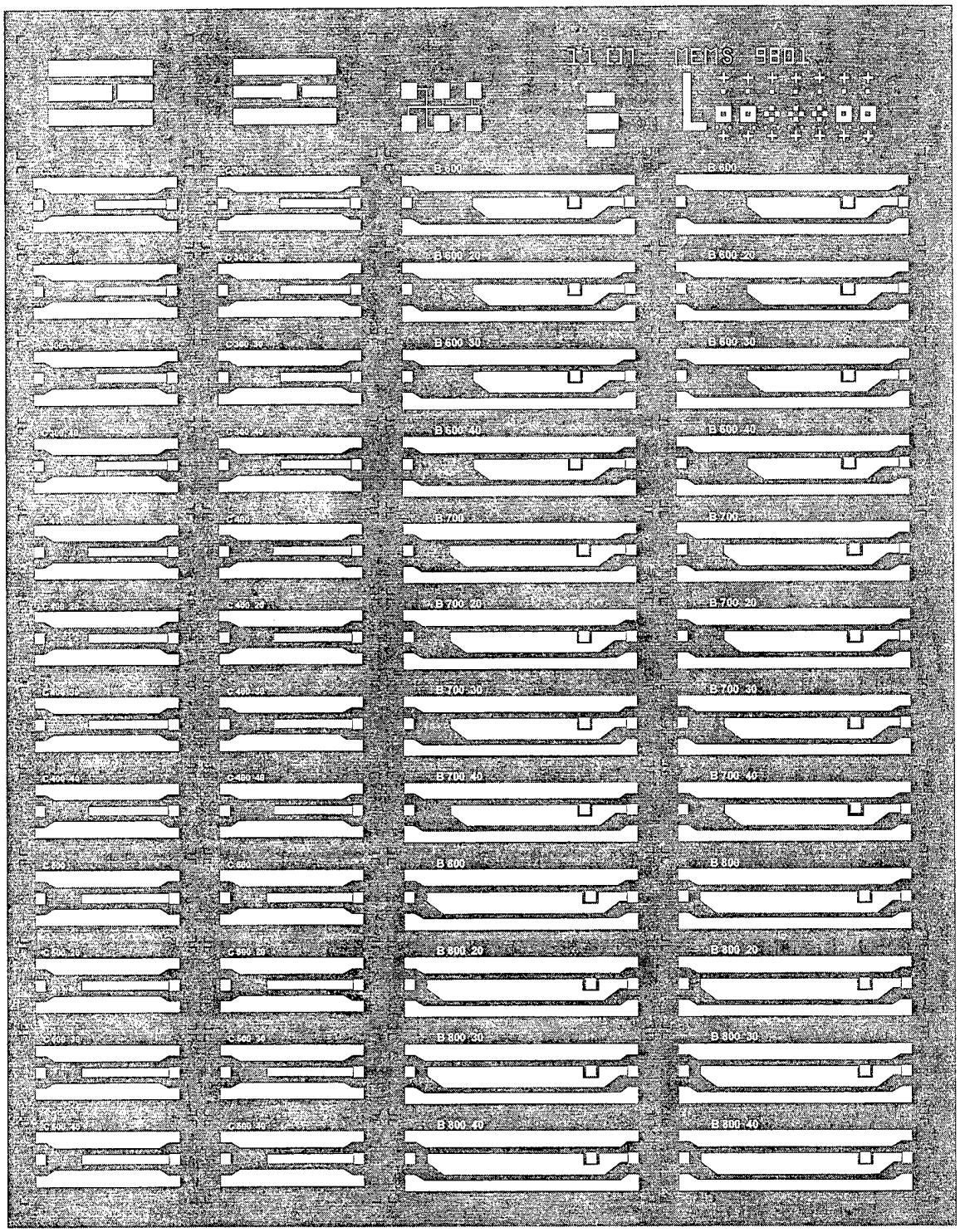

Nitride Layer - Mask 2

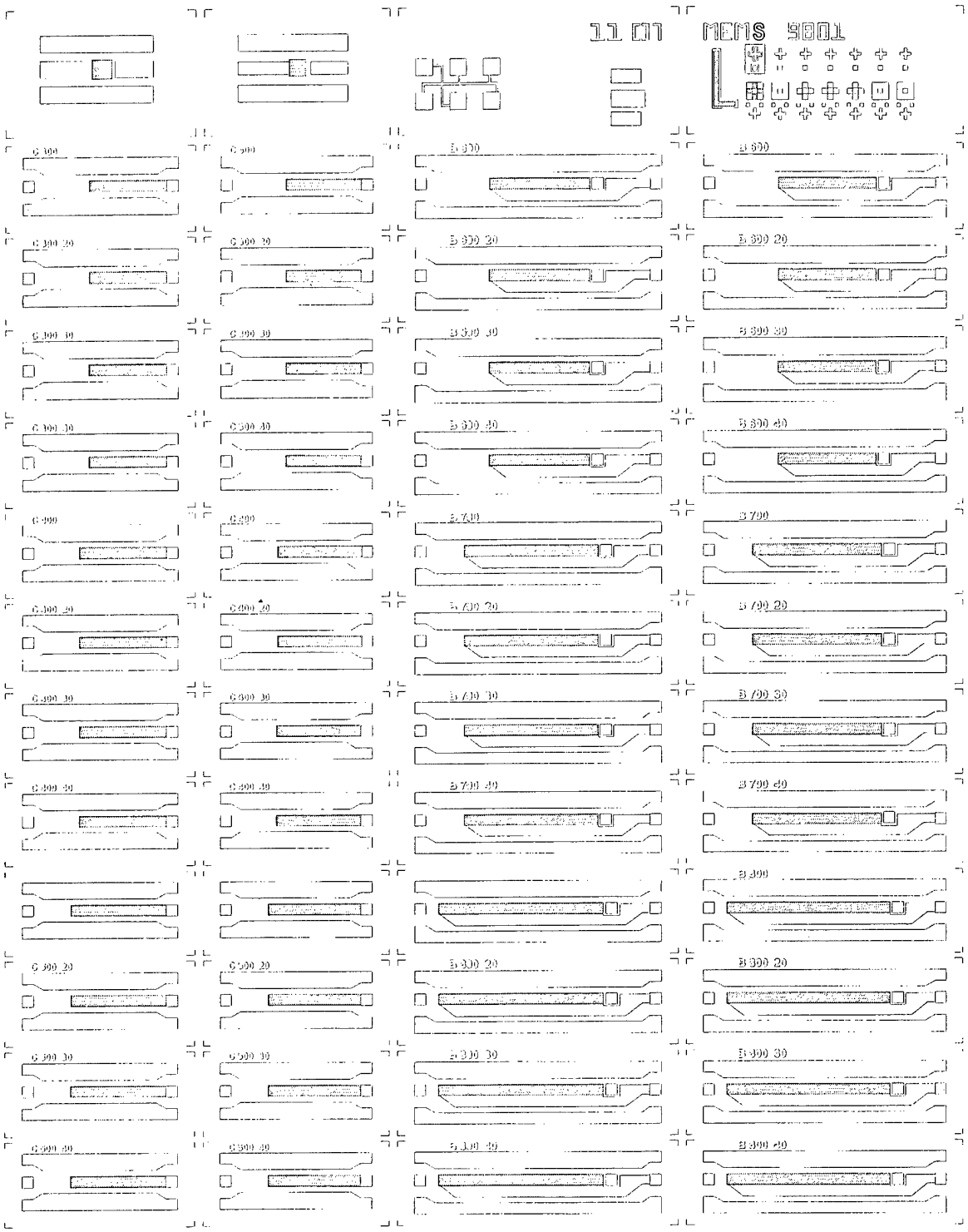

Post - Mask 3

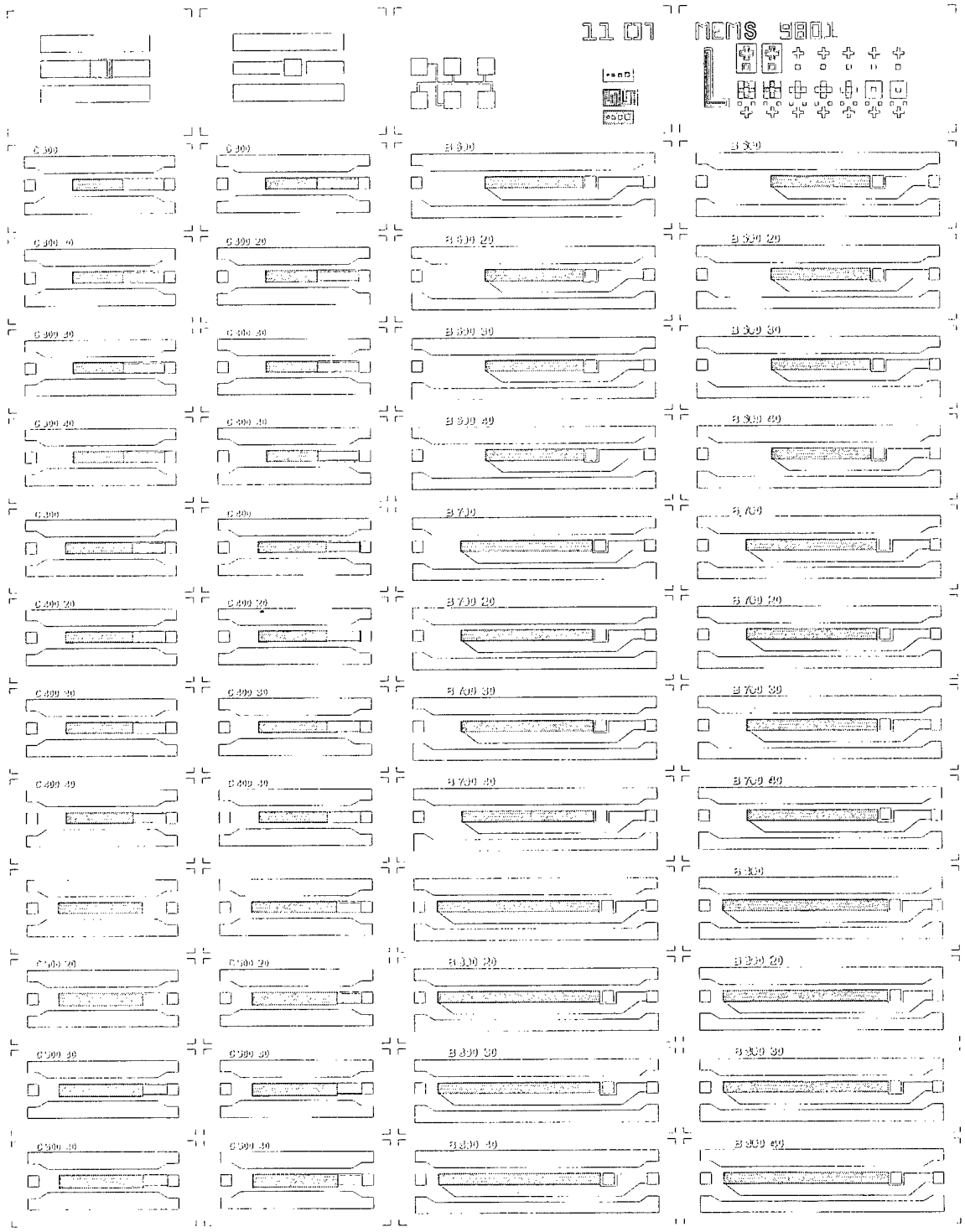

Top Metal - Mask 4

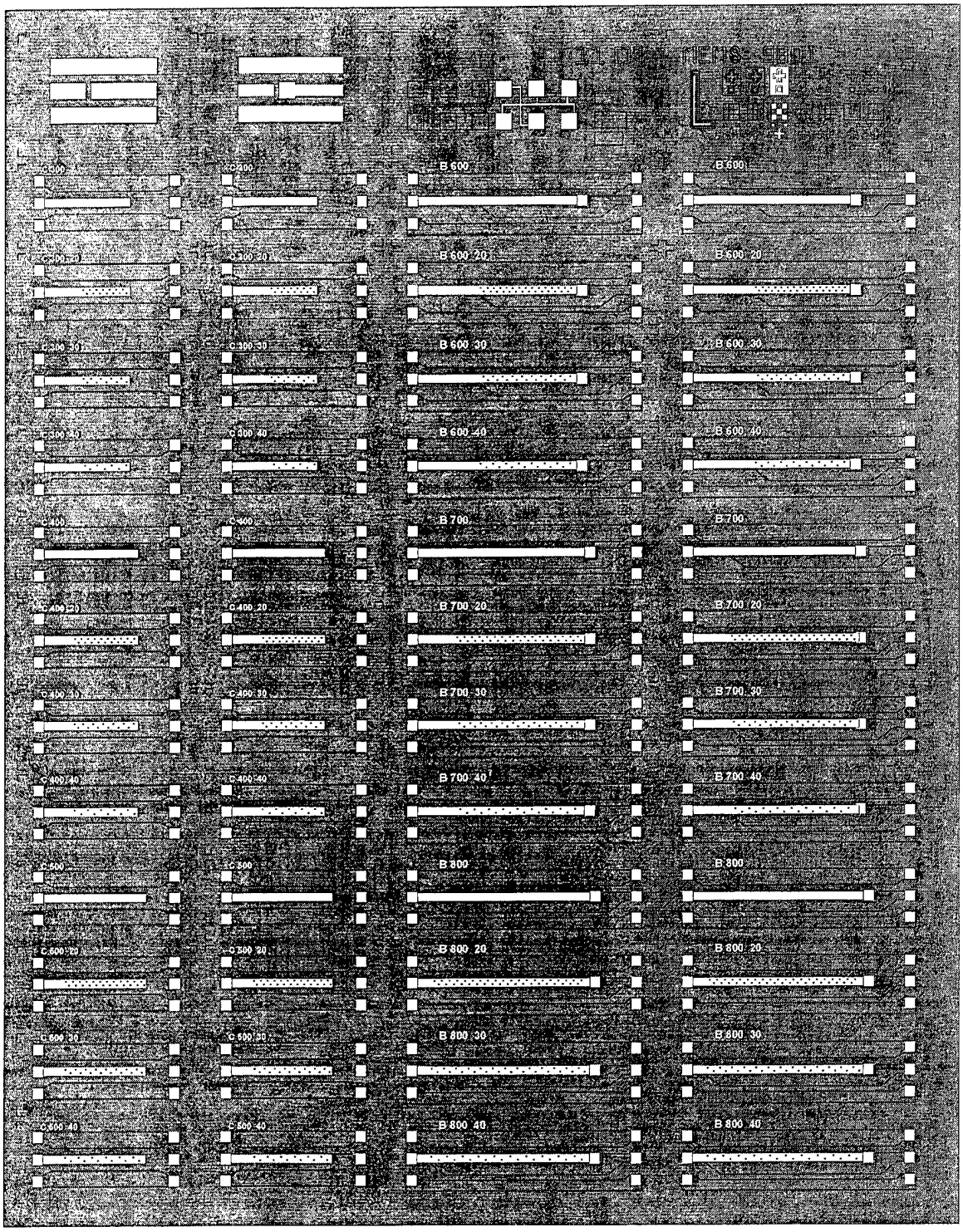

Appendix E Measured Results (# of working switches / # of switches tested)

Off - 0 V Wafer: R120498-1 **C-300** (10 / 16)

Freq-GHz	S11-dB	St. Dev.	S11-pha	St. Dev.
1	-0.01	0.00	-3.03	0.14
2	-0.03	0.00	-5.98	0.27
3	-0.07	0.01	-8.87	0.42
4	-0.10	0.01	-11.69	0.54
5	-0.14	0.02	-14.50	0.67
6	-0.19	0.02	-17.32	0.79
7	-0.24	0.03	-20.04	0.91
8	-0.29	0.04	-22.74	1.02
9	-0.35	0.05	-25.42	1.12
10	-0.42	0.06	-28.11	1.22
11	-0.49	0.07	-30.69	1.32
12	-0.58	0.08	-33.25	1.39
13	-0.66	0.09	-35.67	1.46
14	-0.71	0.10	-37.89	1.52
15	-0.76	0.11	-40.10	1.61
16	-0.81	0.11	-42.63	1.71
17	-0.88	0.13	-44.99	1.81
18	-0.95	0.14	-47.52	1.88
19	-0.98	0.16	-49.82	1.88
20	-1.02	0.15	-52.24	2.11
21	-1.17	0.21	-54.49	2.13
22	-1.17	0.19	-56.31	2.08
23	-1.11	0.19	-59.48	2.09
24	-1.23	0.23	-62.03	2.44
25	-1.37	0.18	-63.63	2.40
26	-1.40	0.24	-67.03	2.39

On

S11-dB	St. Dev.	S11-pha	St. Dev.
-1.57	0.54	-32.79	4.98
-4.26	1.09	-51.50	4.91
-6.64	1.33	-61.74	3.82
-8.59	1.44	-67.82	2.82
-10.14	1.48	-71.89	2.02
-11.44	1.48	-75.05	1.44
-12.53	1.47	-77.29	0.96
-13.28	1.31	-79.40	0.66
-14.07	1.28	-81.20	0.46
-14.77	1.25	-82.56	0.37
-15.35	1.21	-84.30	0.41
-15.85	1.18	-86.21	0.51
-16.34	1.17	-88.59	0.59
-16.71	1.14	-90.16	0.85
-17.36	1.13	-91.92	0.92
-17.83	1.08	-93.80	1.04
-18.38	1.06	-95.88	1.12
-18.70	1.02	-97.63	0.90
-19.44	1.07	-99.96	0.80
-19.52	1.17	-100.74	1.45
-20.39	1.07	-99.41	2.83
-20.11	1.18	-102.36	1.97
-20.71	1.02	-104.46	1.77
-20.79	1.22	-103.42	2.32
-21.00	1.41	-104.13	3.60
-21.63	1.11	-106.90	1.77
Actuation Voltage		22.20	3.91

Off - 0 V

Freq-GHz	S21-dB	St. Dev.	S21-pha	St. Dev.
1	-32.77	1.03	86.32	0.45
2	-26.41	0.96	81.41	0.38
3	-23.05	0.98	77.91	0.71
4	-20.41	0.95	73.75	0.79
5	-18.50	0.94	69.31	0.90
6	-16.90	0.92	64.72	1.02
7	-15.61	0.91	60.48	1.16
8	-14.44	0.89	56.81	1.23
9	-13.40	0.88	52.28	1.35
10	-12.64	0.87	47.58	1.40
11	-11.86	0.85	43.08	1.48
12	-11.27	0.84	38.53	1.51
13	-10.86	0.84	34.06	1.54
14	-10.32	0.84	31.29	1.67
15	-10.01	0.83	27.52	1.81
16	-9.63	0.81	23.87	1.93
17	-9.07	0.79	19.85	2.06
18	-8.97	0.77	15.02	1.96
19	-8.55	0.75	12.63	2.07
20	-8.01	0.78	7.14	1.86
21	-8.01	0.75	3.25	2.27
22	-7.55	0.73	1.49	2.04
23	-6.89	0.65	-2.12	2.09
24	-6.96	0.76	-6.74	2.14
25	-6.83	0.78	-9.52	1.76
26	-6.30	0.71	-12.22	2.33

On

S21-dB	St. Dev.	S21-pha	St. Dev.
-5.85	1.23	54.20	5.27
-2.58	0.66	32.69	5.45
-1.56	0.38	19.83	4.59
-1.12	0.25	11.24	3.81
-0.90	0.17	4.65	3.19
-0.79	0.13	-0.68	2.72
-0.72	0.10	-5.14	2.38
-0.67	0.07	-8.92	1.93
-0.63	0.06	-12.71	1.71
-0.62	0.05	-16.16	1.56
-0.60	0.04	-19.48	1.41
-0.59	0.04	-22.61	1.31
-0.57	0.03	-25.64	1.22
-0.54	0.02	-28.60	1.12
-0.51	0.02	-31.70	1.04
-0.49	0.02	-34.82	0.98
-0.49	0.02	-37.75	0.90
-0.47	0.03	-40.74	0.87
-0.45	0.02	-43.73	0.79
-0.49	0.04	-46.22	0.76
-0.46	0.04	-49.25	0.73
-0.55	0.03	-51.87	0.78
-0.58	0.03	-54.52	0.56
-0.50	0.04	-57.40	0.62
-0.65	0.05	-60.40	0.69
-0.67	0.04	-62.82	0.57
Actuation Voltage		22.20	3.91

Wafer: R120498-1 C-300 S-22 (10 / 16)

	Off - 0 V				On			
Freq-GHz	S22-dB	St. Dev.	S22-pha	St. Dev.	S22-dB	St. Dev.	S22-pha	St. Dev.
1	0.00	0.01	-4.69	0.14	-1.57	0.54	-34.46	4.97
2	-0.02	0.00	-9.32	0.28	-4.29	1.09	-54.85	4.90
3	-0.07	0.01	-13.88	0.42	-6.72	1.35	-66.73	3.81
4	-0.11	0.01	-18.36	0.54	-8.74	1.48	-74.53	2.81
5	-0.16	0.02	-22.82	0.67	-10.42	1.54	-80.14	1.99
6	-0.23	0.03	-27.24	0.80	-11.83	1.56	-84.65	1.37
7	-0.29	0.03	-31.57	0.91	-13.09	1.59	-88.43	0.89
8	-0.34	0.04	-35.97	1.03	-13.93	1.44	-91.63	0.53
9	-0.42	0.05	-40.33	1.13	-14.86	1.43	-94.36	0.48
10	-0.50	0.06	-44.69	1.23	-15.68	1.41	-97.75	0.59
11	-0.59	0.07	-48.95	1.32	-16.43	1.41	-99.89	0.86
12	-0.70	0.08	-53.17	1.41	-17.03	1.39	-102.43	1.08
13	-0.80	0.09	-57.02	1.49	-17.61	1.37	-105.72	1.25
14	-0.88	0.11	-61.02	1.56	-18.13	1.34	-109.07	1.29
15	-0.95	0.12	-65.02	1.64	-18.87	1.33	-114.08	1.23
16	-1.01	0.13	-69.27	1.70	-19.59	1.31	-117.96	1.00
17	-1.08	0.15	-73.24	1.72	-20.34	1.36	-118.70	1.43
18	-1.17	0.15	-77.15	1.77	-21.00	1.46	-121.65	1.55
19	-1.19	0.16	-81.31	1.85	-21.86	1.43	-125.65	2.38
20	-1.32	0.15	-85.24	2.14	-22.21	1.55	-126.34	2.58
21	-1.49	0.23	-89.42	2.19	-23.12	1.61	-131.35	4.29
22	-1.52	0.19	-92.90	2.00	-22.91	1.65	-129.77	3.79
23	-1.54	0.20	-97.72	2.01	-23.64	1.15	-125.71	4.65
24	-1.69	0.28	-101.76	2.55	-24.40	1.48	-134.86	4.11
25	-1.83	0.26	-104.81	2.26	-24.31	1.39	-131.03	5.58
26	-1.83	0.27	-110.80	2.12	-25.34	1.36	-134.91	7.35
					Actuation Voltage		22.20	3.91

Wafer: 120498-1 **C-300-20** S-11 (6 /16)

	Off - 0 V				On			
Freq-GHz	S11-dB	St. Dev.	S11-pha	St. Dev.	S11-dB	St. Dev.	S11-pha	St. Dev.
1	-0.01	0.00	-2.89	0.04	-1.09	0.38	-27.80	4.73
2	-0.03	0.00	-5.69	0.09	-3.22	0.93	-46.06	5.75
3	-0.06	0.00	-8.43	0.13	-5.30	1.27	-57.18	5.15
4	-0.09	0.00	-11.11	0.15	-7.09	1.46	-64.22	4.23
5	-0.12	0.01	-13.78	0.19	-8.58	1.56	-69.14	3.39
6	-0.16	0.01	-16.47	0.21	-9.85	1.62	-72.96	2.69
7	-0.21	0.01	-19.06	0.25	-10.93	1.64	-75.76	2.08
8	-0.25	0.01	-21.65	0.30	-11.86	1.65	-78.31	1.64
9	-0.30	0.01	-24.21	0.32	-12.66	1.64	-80.45	1.20
10	-0.36	0.02	-26.80	0.35	-13.38	1.63	-82.06	0.88
11	-0.42	0.02	-29.27	0.37	-13.99	1.62	-84.05	0.65
12	-0.50	0.02	-31.74	0.40	-14.52	1.60	-86.08	0.53
13	-0.57	0.02	-34.08	0.42	-15.02	1.60	-88.55	0.54
14	-0.61	0.03	-36.23	0.45	-15.43	1.59	-90.38	0.35
15	-0.65	0.04	-38.35	0.45	-16.07	1.61	-92.22	0.37
16	-0.68	0.04	-40.77	0.47	-16.60	1.61	-94.16	0.47
17	-0.74	0.04	-43.04	0.46	-17.16	1.60	-96.32	0.87
18	-0.80	0.03	-45.52	0.49	-17.50	1.54	-98.00	0.60
19	-0.81	0.03	-47.78	0.50	-18.27	1.68	-100.46	0.73
20	-0.87	0.06	-50.13	0.52	-18.25	1.60	-100.50	2.36
21	-0.96	0.05	-52.30	0.50	-19.23	1.68	-100.89	2.57
22	-1.02	0.08	-54.62	0.63	-19.09	1.65	-99.94	3.16
23	-0.95	0.05	-57.20	0.73	-19.46	1.53	-104.49	3.15
24	-1.04	0.06	-59.79	0.95	-19.53	1.57	-103.57	2.08
25	-1.24	0.10	-62.00	1.44	-19.86	1.71	-103.05	3.96
26	-1.25	0.08	-64.38	1.48	-20.18	1.49	-107.84	2.80
					Actuation Voltage		20.83	2.71

	Off - 0 V				On			
Freq-GHz	S21-dB	St. Dev.	S21-pha	St. Dev.	S21-dB	St. Dev.	S21-pha	St. Dev.
1	-33.83	0.24	86.49	0.38	-7.27	1.57	59.45	5.01
2	-27.45	0.23	81.90	0.24	-3.43	1.01	38.64	6.22
3	-24.09	0.24	78.48	0.16	-2.08	0.65	25.14	5.85
4	-21.41	0.25	74.61	0.20	-1.47	0.44	15.80	5.15
5	-19.50	0.25	70.26	0.18	-1.14	0.31	8.54	4.48
6	-17.88	0.23	65.77	0.16	-0.98	0.23	2.67	3.91
7	-16.58	0.23	61.70	0.25	-0.86	0.18	-2.17	3.47
8	-15.40	0.23	58.11	0.23	-0.77	0.14	-6.50	3.12
9	-14.33	0.23	53.63	0.32	-0.71	0.11	-10.55	2.79
10	-13.56	0.23	49.01	0.32	-0.69	0.10	-14.19	2.56
11	-12.76	0.22	44.55	0.37	-0.66	0.08	-17.69	2.34
12	-12.18	0.22	40.06	0.40	-0.64	0.08	-20.96	2.18
13	-11.75	0.23	35.68	0.41	-0.62	0.07	-24.10	2.06
14	-11.21	0.23	33.00	0.54	-0.57	0.05	-27.18	1.92
15	-10.89	0.22	29.37	0.67	-0.54	0.05	-30.33	1.82
16	-10.50	0.20	25.75	0.69	-0.52	0.05	-33.56	1.73
17	-9.91	0.19	21.94	0.67	-0.52	0.04	-36.62	1.60
18	-9.80	0.18	16.99	0.45	-0.50	0.04	-39.67	1.53
19	-9.35	0.18	14.88	0.50	-0.48	0.03	-42.77	1.45
20	-8.80	0.18	8.95	1.04	-0.53	0.07	-45.28	1.32
21	-8.79	0.19	5.55	0.64	-0.48	0.04	-48.35	1.28
22	-8.14	0.20	2.89	1.51	-0.61	0.05	-51.27	1.21
23	-7.61	0.20	-0.35	0.74	-0.62	0.04	-53.79	1.03
24	-7.69	0.27	-4.92	0.94	-0.55	0.05	-56.57	1.05
25	-7.42	0.37	-8.60	2.20	-0.72	0.07	-59.83	1.15
26	-7.18	0.36	-10.75	0.96	-0.73	0.06	-61.92	0.98
					Actuation Voltage		20.83	2.71

Wafer: 120498-1 C-300-20 S-22 (6/16)

	Off - 0 V				On			
Freq-GHz	S22-dB	St. Dev.	S22-pha	St. Dev.	S22-dB	St. Dev.	S22-pha	St. Dev.
1	0.00	0.00	-4.55	0.06	-1.09	0.38	-29.46	4.73
2	-0.02	0.01	-9.02	0.10	-3.24	0.93	-49.42	5.75
3	-0.06	0.01	-13.43	0.12	-5.37	1.29	-62.19	5.15
4	-0.10	0.01	-17.77	0.16	-7.22	1.49	-70.96	4.25
5	-0.14	0.01	-22.10	0.19	-8.81	1.61	-77.44	3.39
6	-0.20	0.01	-26.37	0.23	-10.17	1.68	-82.63	2.68
7	-0.25	0.01	-30.57	0.25	-11.40	1.73	-87.01	2.07
8	-0.30	0.02	-34.86	0.29	-12.42	1.76	-90.70	1.50
9	-0.36	0.02	-39.10	0.32	-13.35	1.78	-93.87	1.04
10	-0.44	0.02	-43.33	0.35	-14.16	1.78	-97.49	0.79
11	-0.51	0.03	-47.50	0.39	-14.91	1.79	-100.02	0.48
12	-0.61	0.03	-51.60	0.43	-15.52	1.77	-102.87	0.44
13	-0.70	0.03	-55.36	0.43	-16.12	1.77	-106.30	0.50
14	-0.76	0.04	-59.29	0.47	-16.64	1.77	-109.84	0.65
15	-0.83	0.05	-63.20	0.44	-17.39	1.78	-114.63	0.67
16	-0.87	0.05	-67.34	0.43	-18.11	1.83	-118.60	0.88
17	-0.93	0.05	-71.24	0.48	-18.87	1.87	-119.87	1.04
18	-1.00	0.04	-75.10	0.40	-19.51	1.95	-122.76	1.47
19	-1.01	0.05	-79.22	0.40	-20.39	1.99	-126.84	1.83
20	-1.15	0.08	-83.02	0.45	-20.57	2.00	-126.62	3.32
21	-1.25	0.06	-87.12	0.48	-21.42	2.04	-133.31	2.43
22	-1.38	0.14	-91.33	0.59	-21.71	1.81	-127.84	4.81
23	-1.37	0.10	-95.33	0.56	-22.04	1.64	-126.98	5.30
24	-1.46	0.11	-99.18	0.68	-22.45	1.77	-135.16	4.05
25	-1.71	0.29	-103.14	1.31	-22.90	1.97	-129.35	7.34
26	-1.62	0.13	-107.58	0.97	-22.89	1.74	-137.74	4.03
					Actuation Voltage		20.83	2.71

Wafer: 120498-1 C-300-30 S-11 (9/16)

Off - 0 V					On			
Freq-GHz	S11-dB	St. Dev.	S11-pha	St. Dev.	S11-dB	St. Dev.	S11-pha	St. Dev.
1	-0.01	0.00	-2.88	0.04	-1.15	0.27	-28.67	3.29
2	-0.03	0.00	-5.68	0.08	-3.38	0.65	-47.23	3.90
3	-0.06	0.00	-8.42	0.11	-5.53	0.88	-58.29	3.41
4	-0.09	0.00	-11.09	0.14	-7.37	1.01	-65.21	2.78
5	-0.12	0.00	-13.77	0.18	-8.88	1.07	-69.95	2.19
6	-0.16	0.01	-16.46	0.22	-10.16	1.10	-73.64	1.73
7	-0.20	0.01	-19.04	0.26	-11.25	1.11	-76.29	1.34
8	-0.25	0.01	-21.61	0.29	-12.19	1.12	-78.76	1.07
9	-0.30	0.01	-24.18	0.32	-12.99	1.12	-80.79	0.79
10	-0.35	0.02	-26.75	0.34	-13.71	1.10	-82.38	0.54
11	-0.42	0.02	-29.24	0.37	-14.32	1.09	-84.26	0.47
12	-0.49	0.02	-31.73	0.38	-14.84	1.08	-86.27	0.47
13	-0.56	0.02	-34.08	0.38	-15.34	1.07	-88.64	0.53
14	-0.60	0.02	-36.24	0.39	-15.74	1.08	-90.36	0.70
15	-0.65	0.02	-38.36	0.42	-16.40	1.13	-92.20	0.63
16	-0.69	0.02	-40.77	0.50	-16.90	1.15	-93.94	0.73
17	-0.75	0.02	-43.02	0.59	-17.44	1.19	-96.10	0.89
18	-0.81	0.03	-45.50	0.69	-17.79	1.14	-97.80	0.61
19	-0.83	0.04	-47.69	0.68	-18.45	1.23	-100.18	0.96
20	-0.86	0.09	-50.14	0.57	-18.60	1.04	-100.55	2.21
21	-0.98	0.07	-52.30	0.71	-19.46	1.23	-100.04	3.07
22	-1.02	0.08	-54.78	0.82	-19.58	1.14	-99.30	3.27
23	-0.98	0.11	-56.49	0.65	-19.29	0.93	-105.21	3.04
24	-1.06	0.05	-59.63	1.01	-19.72	1.03	-103.17	2.19
25	-1.17	0.13	-61.49	1.14	-20.16	1.00	-105.12	3.16
26	-1.19	0.11	-63.63	1.21	-20.32	0.93	-108.68	2.16
					Actuation Voltage		21.22	1.99

Off - 0 V					On			
Freq-GHz	S21-dB	St. Dev.	S21-pha	St. Dev.	S21-dB	St. Dev.	S21-pha	St. Dev.
1	-33.83	0.28	86.41	0.40	-6.93	1.04	58.56	3.45
2	-27.45	0.26	81.75	0.17	-3.20	0.65	37.41	4.22
3	-24.07	0.27	78.49	0.20	-1.92	0.41	23.92	3.88
4	-21.41	0.26	74.58	0.22	-1.36	0.28	14.68	3.38
5	-19.48	0.25	70.25	0.23	-1.06	0.19	7.56	2.91
6	-17.87	0.25	65.80	0.27	-0.91	0.15	1.81	2.53
7	-16.57	0.24	61.72	0.31	-0.81	0.12	-2.94	2.25
8	-15.39	0.24	58.19	0.34	-0.73	0.09	-7.18	2.02
9	-14.33	0.23	53.75	0.38	-0.68	0.07	-11.16	1.80
10	-13.55	0.23	49.09	0.43	-0.66	0.06	-14.75	1.65
11	-12.75	0.22	44.69	0.44	-0.63	0.06	-18.20	1.50
12	-12.16	0.21	40.18	0.48	-0.62	0.05	-21.44	1.40
13	-11.72	0.20	35.73	0.39	-0.59	0.05	-24.55	1.31
14	-11.17	0.20	33.00	0.32	-0.56	0.04	-27.58	1.25
15	-10.86	0.21	29.26	0.31	-0.53	0.04	-30.73	1.22
16	-10.48	0.23	25.67	0.31	-0.51	0.04	-33.92	1.19
17	-9.90	0.25	21.76	0.34	-0.51	0.03	-36.93	1.13
18	-9.78	0.26	16.87	0.38	-0.49	0.03	-39.97	1.07
19	-9.37	0.28	14.58	0.47	-0.48	0.03	-42.96	1.07
20	-8.76	0.21	9.19	1.34	-0.50	0.04	-45.54	0.91
21	-8.76	0.26	5.32	0.93	-0.47	0.03	-48.59	1.00
22	-8.07	0.31	3.13	1.21	-0.59	0.03	-51.60	0.92
23	-7.84	0.18	-0.82	1.61	-0.61	0.04	-53.66	0.75
24	-7.72	0.26	-4.99	0.85	-0.55	0.04	-56.69	0.82
25	-7.51	0.26	-7.26	2.25	-0.67	0.06	-59.83	0.71
26	-7.25	0.27	-10.06	1.32	-0.68	0.05	-61.85	0.60
					Actuation Voltage		21.22	1.99

Wafer: 120498-1 C-300-30 S-22 (9/16)

	Off - 0 V				On			
Freq-GHz	S22-dB	St. Dev.	S22-pha	St. Dev.	S22-dB	St. Dev.	S22-pha	St. Dev.
1	0.00	0.01	-4.53	0.04	-1.15	0.27	-30.32	3.28
2	-0.02	0.00	-9.01	0.08	-3.40	0.66	-50.58	3.89
3	-0.06	0.01	-13.43	0.11	-5.60	0.89	-63.30	3.40
4	-0.10	0.00	-17.76	0.14	-7.49	1.03	-71.95	2.77
5	-0.14	0.01	-22.09	0.17	-9.11	1.10	-78.27	2.16
6	-0.20	0.01	-26.37	0.20	-10.49	1.15	-83.38	1.67
7	-0.25	0.01	-30.57	0.23	-11.73	1.18	-87.63	1.25
8	-0.30	0.01	-34.85	0.26	-12.76	1.19	-91.24	0.87
9	-0.36	0.01	-39.10	0.28	-13.70	1.20	-94.36	0.55
10	-0.43	0.01	-43.34	0.30	-14.52	1.20	-97.91	0.33
11	-0.51	0.02	-47.51	0.32	-15.28	1.20	-100.31	0.28
12	-0.61	0.02	-51.63	0.33	-15.91	1.19	-103.16	0.32
13	-0.70	0.02	-55.43	0.36	-16.49	1.19	-106.48	0.28
14	-0.76	0.02	-59.35	0.38	-17.00	1.19	-109.85	0.37
15	-0.83	0.03	-63.25	0.41	-17.73	1.24	-114.73	0.35
16	-0.87	0.03	-67.39	0.43	-18.45	1.32	-118.66	0.55
17	-0.93	0.03	-71.32	0.47	-19.22	1.40	-119.91	1.09
18	-1.01	0.03	-75.17	0.52	-19.86	1.42	-122.95	1.48
19	-1.03	0.04	-79.18	0.69	-20.65	1.53	-126.52	1.36
20	-1.14	0.12	-83.16	0.48	-20.97	1.35	-127.43	3.77
21	-1.27	0.10	-87.26	0.71	-21.79	1.63	-132.78	3.47
22	-1.35	0.15	-91.64	1.03	-22.23	1.63	-127.98	4.61
23	-1.38	0.16	-94.41	0.45	-21.79	1.19	-127.59	5.14
24	-1.45	0.12	-99.10	0.80	-22.58	1.51	-134.75	4.39
25	-1.55	0.26	-103.05	0.62	-22.95	1.31	-134.36	6.64
26	-1.55	0.12	-107.38	0.69	-23.15	1.49	-141.43	3.23
					Actuation Voltage		21.22	1.99

Wafer: 120498-1 C-300-40 S-11 (12/16)

Off - 0 V					On			
Freq-GHz	S11-dB	St. Dev.	S11-pha	St. Dev.	S11-dB	St. Dev.	S11-pha	St. Dev.
1	-0.01	0.00	-2.92	0.06	-1.18	0.42	-28.84	4.70
2	-0.03	0.00	-5.76	0.12	-3.43	0.95	-47.23	5.38
3	-0.06	0.00	-8.54	0.18	-5.57	1.26	-58.18	4.63
4	-0.09	0.01	-11.25	0.23	-7.41	1.42	-65.05	3.71
5	-0.13	0.01	-13.95	0.29	-8.91	1.50	-69.76	2.92
6	-0.17	0.01	-16.68	0.35	-10.19	1.53	-73.43	2.29
7	-0.21	0.01	-19.30	0.40	-11.27	1.55	-76.09	1.75
8	-0.26	0.02	-21.91	0.46	-12.21	1.55	-78.53	1.36
9	-0.32	0.02	-24.50	0.51	-13.00	1.53	-80.56	1.03
10	-0.37	0.03	-27.11	0.54	-13.72	1.51	-82.10	0.71
11	-0.44	0.04	-29.61	0.58	-14.32	1.48	-84.01	0.57
12	-0.52	0.04	-32.11	0.59	-14.84	1.47	-85.97	0.45
13	-0.59	0.04	-34.47	0.60	-15.33	1.45	-88.36	0.40
14	-0.63	0.04	-36.64	0.61	-15.72	1.43	-90.15	0.35
15	-0.68	0.04	-38.78	0.63	-16.38	1.44	-91.99	0.48
16	-0.72	0.04	-41.24	0.74	-16.87	1.44	-93.94	0.59
17	-0.78	0.04	-43.53	0.85	-17.36	1.40	-96.32	0.84
18	-0.84	0.06	-46.06	0.97	-17.69	1.42	-97.75	0.58
19	-0.88	0.07	-48.19	0.93	-18.20	1.43	-100.00	0.73
20	-0.88	0.07	-50.76	0.92	-18.62	1.26	-101.00	1.22
21	-1.02	0.08	-52.90	1.00	-19.28	1.38	-100.14	2.70
22	-1.07	0.11	-55.51	1.22	-19.52	1.50	-99.56	2.16
23	-1.02	0.11	-57.15	1.08	-19.18	1.34	-105.39	2.42
24	-1.12	0.09	-60.27	1.53	-19.40	1.13	-103.04	2.08
25	-1.20	0.15	-62.05	1.24	-19.78	1.40	-106.94	2.06
26	-1.24	0.15	-64.93	1.26	-20.39	1.38	-109.69	1.50
					Actuation Voltage		21.42	3.32

Off - 0 V					On			
Freq-GHz	S21-dB	St. Dev.	S21-pha	St. Dev.	S21-dB	St. Dev.	S21-pha	St. Dev.
1	-33.58	0.38	86.47	0.20	-6.95	1.42	58.37	4.93
2	-27.19	0.38	81.81	0.20	-3.23	0.87	37.35	5.82
3	-23.82	0.38	78.32	0.18	-1.95	0.54	23.94	5.27
4	-21.18	0.38	74.43	0.33	-1.39	0.36	14.76	4.56
5	-19.25	0.38	70.05	0.36	-1.08	0.26	7.64	3.92
6	-17.63	0.37	65.56	0.42	-0.93	0.20	1.90	3.39
7	-16.35	0.36	61.42	0.48	-0.83	0.16	-2.85	3.03
8	-15.16	0.36	57.85	0.54	-0.74	0.12	-7.11	2.71
9	-14.11	0.35	53.36	0.62	-0.69	0.10	-11.09	2.41
10	-13.34	0.34	48.72	0.70	-0.67	0.09	-14.68	2.21
11	-12.54	0.33	44.29	0.78	-0.64	0.08	-18.14	2.01
12	-11.94	0.31	39.74	0.80	-0.63	0.07	-21.37	1.87
13	-11.52	0.29	35.30	0.72	-0.61	0.06	-24.48	1.76
14	-10.98	0.29	32.58	0.66	-0.57	0.05	-27.51	1.64
15	-10.67	0.29	28.89	0.52	-0.54	0.05	-30.67	1.57
16	-10.29	0.31	25.26	0.47	-0.52	0.04	-33.87	1.47
17	-9.70	0.32	21.35	0.51	-0.51	0.03	-36.76	1.36
18	-9.57	0.34	16.52	0.64	-0.50	0.04	-39.86	1.31
19	-9.20	0.34	13.85	0.83	-0.49	0.04	-42.76	1.24
20	-8.57	0.31	9.11	0.86	-0.50	0.03	-45.51	1.02
21	-8.57	0.33	4.98	0.78	-0.49	0.04	-48.47	1.04
22	-7.84	0.43	2.71	1.46	-0.60	0.05	-51.55	0.95
23	-7.66	0.30	-1.32	1.74	-0.62	0.05	-53.56	0.93
24	-7.55	0.39	-5.68	1.11	-0.56	0.05	-56.47	0.76
25	-7.37	0.28	-7.38	1.89	-0.65	0.05	-59.50	0.89
26	-6.92	0.28	-10.74	1.74	-0.67	0.05	-62.03	0.72
					Actuation Voltage		21.42	3.32

Wafer: 120498-1 C-300-40 S-22 (12/16)

	Off - 0 V				On			
Freq-GHz	S22-dB	St. Dev.	S22-pha	St. Dev.	S22-dB	St. Dev.	S22-pha	St. Dev.
1	0.00	0.01	-4.58	0.07	-1.18	0.42	-30.48	4.68
2	-0.02	0.00	-9.08	0.12	-3.45	0.96	-50.58	5.37
3	-0.06	0.01	-13.54	0.18	-5.64	1.27	-63.19	4.61
4	-0.10	0.01	-17.89	0.22	-7.53	1.45	-71.77	3.73
5	-0.14	0.01	-22.26	0.27	-9.15	1.55	-78.04	2.90
6	-0.20	0.01	-26.57	0.32	-10.51	1.61	-83.10	2.28
7	-0.26	0.02	-30.80	0.36	-11.75	1.66	-87.35	1.73
8	-0.31	0.02	-35.11	0.40	-12.77	1.67	-90.94	1.26
9	-0.37	0.02	-39.38	0.45	-13.69	1.68	-94.01	0.86
10	-0.45	0.03	-43.65	0.48	-14.51	1.68	-97.53	0.65
11	-0.52	0.03	-47.84	0.52	-15.26	1.69	-99.99	0.48
12	-0.63	0.04	-51.99	0.52	-15.88	1.67	-102.77	0.48
13	-0.72	0.04	-55.79	0.53	-16.46	1.68	-106.12	0.56
14	-0.78	0.04	-59.73	0.55	-16.98	1.66	-109.59	0.67
15	-0.85	0.04	-63.66	0.58	-17.71	1.69	-114.43	0.64
16	-0.90	0.05	-67.83	0.63	-18.42	1.72	-118.31	0.87
17	-0.96	0.05	-71.72	0.64	-19.00	1.77	-119.73	1.32
18	-1.04	0.05	-75.66	0.72	-19.72	1.89	-122.58	1.39
19	-1.09	0.06	-79.57	0.81	-20.34	1.92	-125.56	2.21
20	-1.14	0.07	-83.67	0.84	-20.92	1.77	-127.67	3.45
21	-1.30	0.08	-87.78	0.98	-21.52	1.85	-132.12	3.49
22	-1.40	0.17	-92.32	1.47	-22.06	1.73	-127.90	3.68
23	-1.44	0.20	-94.90	0.87	-21.62	1.60	-126.82	5.65
24	-1.51	0.14	-99.53	1.07	-21.99	1.46	-134.78	4.15
25	-1.55	0.18	-103.44	0.65	-22.40	1.89	-136.50	4.16
26	-1.64	0.19	-108.63	1.12	-23.38	1.46	-139.90	4.10
					Actuation Voltage		21.42	3.32

Wafer: 120498-1 C-400 S-11 (6/16)

Off - 0 V					On			
Freq-GHz	S11-dB	St. Dev.	S11-pha	St. Dev.	S11-dB	St. Dev.	S11-pha	St. Dev.
1	-0.01	0.00	-3.08	0.16	-2.57	0.46	-40.97	3.12
2	-0.03	0.00	-6.09	0.32	-6.06	0.57	-58.56	1.90
3	-0.08	0.01	-9.04	0.47	-8.80	0.65	-66.79	1.30
4	-0.13	0.02	-11.91	0.62	-10.92	0.67	-71.12	0.87
5	-0.18	0.02	-14.76	0.76	-12.53	0.67	-73.80	0.56
6	-0.24	0.03	-17.62	0.89	-13.84	0.67	-75.98	0.38
7	-0.30	0.04	-20.35	1.03	-14.93	0.66	-77.25	0.19
8	-0.38	0.05	-23.07	1.16	-15.84	0.65	-78.77	0.06
9	-0.46	0.06	-25.75	1.27	-16.58	0.62	-79.97	0.13
10	-0.55	0.07	-28.42	1.38	-17.22	0.61	-80.72	0.21
11	-0.65	0.08	-30.94	1.48	-17.77	0.59	-82.22	0.18
12	-0.76	0.10	-33.42	1.57	-18.22	0.57	-84.10	0.22
13	-0.86	0.11	-35.78	1.65	-18.68	0.57	-86.93	0.31
14	-0.92	0.12	-37.92	1.71	-19.07	0.53	-88.46	0.38
15	-0.99	0.13	-40.11	1.80	-19.86	0.55	-89.97	0.36
16	-1.06	0.14	-42.65	1.84	-20.40	0.57	-91.49	0.37
17	-1.16	0.16	-45.01	1.88	-21.12	0.58	-93.30	0.86
18	-1.27	0.17	-47.61	1.96	-21.47	0.68	-93.97	0.55
19	-1.38	0.16	-49.67	1.99	-21.80	0.62	-94.82	1.68
20	-1.41	0.16	-52.09	2.28	-22.38	0.44	-96.71	0.54
21	-1.63	0.11	-53.86	2.27	-22.69	0.47	-92.02	3.09
22	-1.68	0.20	-56.29	2.43	-22.72	0.61	-92.79	1.60
23	-1.60	0.24	-58.72	2.63	-22.76	0.57	-98.04	1.98
24	-1.75	0.27	-60.95	3.04	-22.47	0.55	-97.51	2.28
25	-1.91	0.23	-63.26	2.78	-22.93	0.95	-99.75	2.70
26	-2.05	0.30	-65.73	3.08	-23.74	0.76	-99.23	3.12
					Actation Voltage		18.33	2.89

Off - 0 V					On			
Freq-GHz	S21-dB	St. Dev.	S21-pha	St. Dev.	S21-dB	St. Dev.	S21-pha	St. Dev.
1	-30.79	0.85	85.90	0.37	-4.01	0.43	45.08	2.20
2	-24.50	0.82	80.64	0.57	-1.63	0.20	23.71	1.92
3	-21.14	0.84	76.77	0.83	-1.01	0.10	12.42	1.48
4	-18.57	0.82	72.37	1.01	-0.77	0.06	5.15	1.17
5	-16.66	0.81	67.63	1.10	-0.65	0.04	-0.44	0.96
6	-15.10	0.80	62.76	1.30	-0.60	0.03	-5.03	0.81
7	-13.86	0.78	58.29	1.41	-0.57	0.03	-8.94	0.70
8	-12.72	0.77	54.41	1.58	-0.54	0.02	-12.53	0.62
9	-11.71	0.75	49.66	1.69	-0.52	0.02	-15.93	0.55
10	-10.99	0.73	44.83	1.75	-0.52	0.01	-19.10	0.50
11	-10.25	0.72	40.22	1.78	-0.51	0.01	-22.15	0.45
12	-9.71	0.71	35.69	1.91	-0.50	0.01	-25.08	0.42
13	-9.31	0.70	31.31	1.96	-0.48	0.01	-27.96	0.38
14	-8.77	0.69	28.42	2.09	-0.47	0.01	-30.81	0.37
15	-8.45	0.69	24.75	2.24	-0.44	0.01	-33.85	0.35
16	-8.07	0.67	21.09	2.36	-0.43	0.01	-36.91	0.34
17	-7.52	0.63	16.83	2.32	-0.43	0.01	-39.74	0.31
18	-7.39	0.62	12.16	2.32	-0.41	0.01	-42.72	0.30
19	-7.04	0.58	8.38	2.11	-0.44	0.02	-45.41	0.30
20	-6.59	0.64	3.59	2.02	-0.43	0.01	-47.90	0.21
21	-6.58	0.59	-1.14	0.56	-0.45	0.04	-50.83	0.25
22	-5.97	0.62	-3.57	2.12	-0.57	0.02	-53.73	0.27
23	-5.62	0.61	-6.79	3.01	-0.57	0.02	-55.91	0.18
24	-5.76	0.75	-10.95	2.94	-0.51	0.02	-58.54	0.14
25	-5.43	0.63	-13.70	2.60	-0.66	0.04	-61.52	0.33
26	-5.08	0.59	-17.26	3.50	-0.67	0.02	-64.07	0.17
					Actuation Voltage		18.33	2.89

Wafer: 120498-1 C-400 S-22 (6/16)

	Off- 0 V				On			
Freq-GHz	S22-dB	St. Dev.	S22-pha	St. Dev.	S22-dB	St. Dev.	S22-pha	St. Dev.
1	0.00	0.00	-5.34	0.16	-2.51	0.34	-42.83	2.38
2	-0.03	0.00	-10.59	0.31	-6.11	0.58	-63.08	1.89
3	-0.09	0.01	-15.80	0.46	-8.95	0.67	-73.45	1.27
4	-0.15	0.01	-20.85	0.61	-11.16	0.70	-79.92	0.80
5	-0.22	0.02	-25.93	0.75	-12.95	0.72	-84.47	0.42
6	-0.30	0.03	-30.91	0.88	-14.42	0.72	-88.18	0.19
7	-0.39	0.04	-35.82	1.01	-15.73	0.73	-91.37	0.29
8	-0.47	0.05	-40.77	1.14	-16.77	0.71	-93.93	0.47
9	-0.57	0.06	-45.66	1.26	-17.70	0.71	-96.01	0.70
10	-0.68	0.07	-50.52	1.36	-18.49	0.70	-99.37	0.76
11	-0.80	0.09	-55.28	1.47	-19.24	0.69	-100.97	0.90
12	-0.95	0.10	-59.93	1.57	-19.82	0.69	-103.45	1.03
13	-1.08	0.11	-64.25	1.65	-20.41	0.72	-107.22	1.02
14	-1.17	0.13	-68.69	1.74	-21.01	0.74	-110.58	1.09
15	-1.27	0.14	-73.26	1.82	-21.98	0.79	-116.23	1.26
16	-1.37	0.16	-78.07	1.93	-22.88	0.85	-119.60	1.95
17	-1.49	0.16	-82.47	1.92	-23.82	0.81	-118.44	3.09
18	-1.61	0.19	-86.97	2.01	-24.66	0.87	-120.68	2.73
19	-1.75	0.18	-91.35	1.90	-25.03	0.80	-121.71	4.33
20	-1.83	0.18	-95.84	2.30	-26.08	0.68	-126.62	3.45
21	-2.12	0.08	-100.20	2.29	-26.65	0.74	-127.56	8.79
22	-2.30	0.23	-105.16	2.29	-27.27	1.06	-119.35	5.28
23	-2.33	0.30	-109.23	2.27	-27.26	0.70	-115.47	4.59
24	-2.47	0.31	-113.02	3.00	-27.30	0.45	-126.47	6.88
25	-2.60	0.24	-117.73	2.34	-26.62	0.60	-125.45	11.19
26	-2.77	0.32	-123.90	2.31	-30.01	2.10	-128.99	8.81
					Actuation Voltage		18.33	2.89

Wafer: 120498-1 C-400-20 S-11 (3/16)

Off - 0 V					On			
Freq-GHz	S11-dB	St. Dev.	S11-pha	St. Dev.	S11-dB	St. Dev.	S11-pha	St. Dev.
1	0.00	0.00	-2.67	0.01	-2.02	0.85	-36.28	7.47
2	-0.02	0.00	-5.27	0.04	-5.11	1.67	-54.39	7.18
3	-0.06	0.00	-7.85	0.05	-7.65	2.04	-63.49	5.49
4	-0.09	0.00	-10.35	0.08	-9.67	2.20	-68.62	3.93
5	-0.13	0.00	-12.84	0.09	-11.25	2.26	-71.88	2.70
6	-0.17	0.00	-15.34	0.13	-12.55	2.28	-74.45	1.77
7	-0.21	0.01	-17.74	0.15	-13.63	2.26	-76.14	1.02
8	-0.27	0.01	-20.14	0.15	-14.54	2.24	-77.86	0.56
9	-0.32	0.01	-22.50	0.18	-15.30	2.20	-79.25	0.57
10	-0.38	0.01	-24.91	0.20	-15.97	2.15	-80.31	0.77
11	-0.45	0.02	-27.18	0.21	-16.55	2.11	-81.90	0.98
12	-0.53	0.01	-29.45	0.20	-17.02	2.08	-83.62	1.02
13	-0.60	0.02	-31.61	0.20	-17.50	2.06	-86.27	0.99
14	-0.64	0.01	-33.54	0.21	-17.91	2.02	-87.67	1.36
15	-0.70	0.01	-35.50	0.24	-18.62	2.03	-89.06	1.68
16	-0.74	0.00	-37.74	0.34	-19.10	1.99	-90.82	1.79
17	-0.81	0.01	-39.78	0.49	-19.76	1.99	-92.51	2.26
18	-0.88	0.03	-42.17	0.59	-20.09	1.90	-93.46	2.82
19	-0.94	0.08	-43.91	0.56	-20.24	1.89	-95.57	1.21
20	-0.92	0.05	-46.47	0.35	-21.14	1.99	-97.18	2.73
21	-1.12	0.10	-48.15	0.32	-21.35	2.10	-93.80	3.26
22	-1.09	0.09	-50.10	0.15	-21.68	2.13	-97.17	3.02
23	-1.07	0.08	-52.76	0.56	-22.14	2.02	-98.14	4.78
24	-1.10	0.06	-54.92	0.28	-21.94	1.94	-98.45	4.94
25	-1.34	0.10	-57.15	0.82	-22.09	2.21	-97.46	4.61
26	-1.45	0.16	-58.74	0.55	-22.71	2.22	-102.19	3.91
					Actuation Voltage		19.33	1.15

Off - 0 V					On			
Freq-GHz	S21-dB	St. Dev.	S21-pha	St. Dev.	S21-dB	St. Dev.	S21-pha	St. Dev.
1	-33.10	0.17	86.29	0.21	-5.01	1.78	50.26	7.94
2	-26.76	0.18	81.60	0.14	-2.16	0.93	28.88	8.10
3	-23.38	0.13	77.98	0.05	-1.31	0.53	16.72	6.75
4	-20.77	0.14	73.95	0.04	-0.96	0.34	8.70	5.58
5	-18.84	0.14	69.50	0.11	-0.78	0.23	2.53	4.68
6	-17.23	0.14	64.97	0.11	-0.70	0.17	-2.49	4.00
7	-15.96	0.14	60.78	0.14	-0.64	0.13	-6.71	3.52
8	-14.78	0.13	57.20	0.13	-0.59	0.10	-10.55	3.12
9	-13.73	0.13	52.60	0.20	-0.57	0.08	-14.16	2.77
10	-12.97	0.12	47.92	0.23	-0.56	0.07	-17.48	2.53
11	-12.18	0.12	43.46	0.27	-0.54	0.06	-20.69	2.30
12	-11.60	0.10	39.02	0.26	-0.53	0.05	-23.71	2.13
13	-11.18	0.10	34.61	0.18	-0.51	0.05	-26.68	2.01
14	-10.62	0.10	31.84	0.10	-0.49	0.03	-29.60	1.87
15	-10.31	0.11	28.15	0.07	-0.46	0.03	-32.66	1.76
16	-9.91	0.15	24.55	0.18	-0.45	0.03	-35.76	1.67
17	-9.33	0.18	20.58	0.13	-0.45	0.03	-38.69	1.51
18	-9.18	0.21	15.86	0.36	-0.44	0.04	-41.70	1.45
19	-8.87	0.19	12.52	1.09	-0.46	0.04	-44.30	1.41
20	-8.24	0.11	8.16	0.67	-0.44	0.01	-47.09	1.25
21	-8.28	0.15	3.45	1.42	-0.46	0.06	-49.85	1.14
22	-7.72	0.08	2.10	1.34	-0.53	0.03	-52.69	1.13
23	-7.11	0.23	-2.01	1.16	-0.57	0.04	-55.26	0.89
24	-7.26	0.10	-5.44	0.87	-0.48	0.03	-58.07	0.89
25	-6.83	0.18	-9.12	1.32	-0.68	0.09	-60.99	0.84
26	-6.70	0.13	-12.58	1.18	-0.69	0.07	-63.04	1.14
					Actuation Voltage		19.33	1.15

Wafer: 120498-1 C-400-20 S-22 (3/16)

	Off - 0 V				On			
Freq-GHz	S22-dB	St. Dev.	S22-pha	St. Dev.	S22-dB	St. Dev.	S22-pha	St. Dev.
1	0.00	0.00	-4.92	0.04	-2.03	0.85	-38.52	7.48
2	-0.02	0.00	-9.79	0.06	-5.16	1.68	-58.91	7.18
3	-0.06	0.00	-14.59	0.09	-7.78	2.08	-70.19	5.42
4	-0.11	0.01	-19.31	0.10	-9.88	2.26	-77.57	3.87
5	-0.16	0.01	-24.02	0.14	-11.62	2.37	-82.79	2.54
6	-0.22	0.01	-28.67	0.15	-13.06	2.41	-87.12	1.57
7	-0.29	0.01	-33.25	0.15	-14.34	2.45	-90.86	0.90
8	-0.34	0.01	-37.89	0.18	-15.39	2.45	-93.85	0.60
9	-0.42	0.01	-42.49	0.18	-16.34	2.46	-96.40	1.01
10	-0.50	0.02	-47.10	0.21	-17.15	2.45	-99.85	1.44
11	-0.58	0.02	-51.59	0.20	-17.91	2.45	-101.85	2.03
12	-0.69	0.02	-56.06	0.21	-18.49	2.42	-104.48	2.37
13	-0.79	0.02	-60.18	0.18	-19.05	2.39	-108.20	2.44
14	-0.86	0.02	-64.45	0.21	-19.60	2.39	-111.39	2.72
15	-0.93	0.02	-68.76	0.22	-20.40	2.39	-117.33	2.38
16	-0.99	0.02	-73.35	0.27	-21.22	2.45	-121.28	2.40
17	-1.07	0.03	-77.64	0.28	-22.18	2.55	-122.00	2.85
18	-1.17	0.04	-82.00	0.39	-23.05	2.75	-124.40	3.27
19	-1.29	0.07	-85.99	0.33	-23.43	2.97	-125.50	4.34
20	-1.31	0.04	-90.62	0.31	-24.42	2.89	-129.59	6.99
21	-1.55	0.12	-94.82	0.42	-24.63	2.69	-133.20	4.79
22	-1.55	0.12	-98.98	0.24	-25.01	2.57	-130.29	6.97
23	-1.61	0.15	-103.95	1.02	-25.63	1.78	-124.44	11.33
24	-1.66	0.09	-108.01	0.25	-26.28	2.34	-136.91	9.21
25	-1.92	0.22	-112.98	0.72	-25.93	1.85	-129.83	7.18
26	-1.96	0.13	-117.26	0.41	-26.53	2.45	-139.88	12.82
					Actuation Voltage		19.33	1.15

Wafer: 120498-1 C-400-30 S-11 (7/16)

	Off - 0 V				On			
Freq-GHz	S11-dB	St. Dev.	S11-pha	St. Dev.	S11-dB	St. Dev.	S11-pha	St. Dev.
1	-0.01	0.00	-2.86	0.16	-2.06	0.57	-36.99	4.68
2	-0.03	0.01	-5.64	0.30	-5.24	1.07	-55.32	4.21
3	-0.07	0.01	-8.37	0.44	-7.84	1.27	-64.37	3.11
4	-0.11	0.01	-11.02	0.58	-9.89	1.36	-69.38	2.19
5	-0.15	0.02	-13.66	0.72	-11.48	1.37	-72.55	1.49
6	-0.20	0.03	-16.31	0.84	-12.80	1.37	-75.03	1.02
7	-0.25	0.04	-18.86	0.98	-13.89	1.36	-76.67	0.60
8	-0.31	0.05	-21.40	1.11	-14.77	1.37	-78.42	0.39
9	-0.38	0.05	-23.91	1.21	-15.53	1.35	-79.75	0.24
10	-0.45	0.07	-26.41	1.31	-16.21	1.31	-80.68	0.29
11	-0.53	0.08	-28.80	1.41	-16.77	1.29	-82.29	0.36
12	-0.62	0.09	-31.17	1.49	-17.25	1.25	-84.21	0.42
13	-0.70	0.09	-33.40	1.55	-17.74	1.23	-86.72	0.37
14	-0.76	0.10	-35.46	1.63	-18.14	1.20	-88.29	0.59
15	-0.82	0.11	-37.52	1.72	-18.89	1.22	-89.81	0.87
16	-0.87	0.12	-39.89	1.87	-19.43	1.21	-91.38	0.92
17	-0.95	0.13	-42.11	2.03	-20.04	1.20	-92.90	0.92
18	-1.03	0.14	-44.53	2.13	-20.55	1.24	-93.97	0.99
19	-1.14	0.20	-46.41	2.19	-20.50	1.18	-95.07	1.24
20	-1.12	0.18	-48.94	2.09	-21.49	1.32	-97.11	0.96
21	-1.31	0.19	-50.62	2.08	-21.75	1.32	-93.66	3.06
22	-1.29	0.19	-52.37	2.25	-21.56	1.08	-99.75	1.42
23	-1.27	0.19	-55.73	2.52	-22.40	1.03	-97.76	1.92
24	-1.36	0.20	-57.76	2.55	-22.14	1.30	-98.98	2.49
25	-1.61	0.24	-60.26	2.80	-22.49	1.13	-98.14	2.10
26	-1.76	0.31	-61.40	3.05	-22.66	1.20	-102.70	3.33
					Actuation Voltage		17.14	2.67

	Off - 0 V				On			
Freq-GHz	S21-dB	St. Dev.	S21-pha	St. Dev.	S21-dB	St. Dev.	S21-pha	St. Dev.
1	-32.12	0.84	85.90	0.30	-5.27	1.83	51.22	7.54
2	-25.80	0.81	81.13	0.36	-2.31	1.03	29.91	8.01
3	-22.43	0.82	77.27	0.45	-1.41	0.62	17.62	6.92
4	-19.82	0.80	73.14	0.72	-1.03	0.41	9.46	5.84
5	-17.91	0.79	68.57	0.77	-0.83	0.28	3.16	4.95
6	-16.33	0.78	63.83	0.92	-0.74	0.21	-1.95	4.27
7	-15.06	0.77	59.54	1.04	-0.68	0.17	-6.26	3.76
8	-13.90	0.75	55.78	1.20	-0.62	0.13	-10.16	3.36
9	-12.88	0.74	51.14	1.25	-0.59	0.10	-13.82	2.99
10	-12.13	0.72	46.38	1.33	-0.58	0.09	-17.19	2.75
11	-11.37	0.71	41.86	1.40	-0.56	0.08	-20.43	2.51
12	-10.79	0.69	37.34	1.43	-0.55	0.07	-23.50	2.32
13	-10.38	0.68	32.98	1.42	-0.53	0.06	-26.49	2.19
14	-9.83	0.68	30.15	1.47	-0.51	0.05	-29.45	2.04
15	-9.51	0.68	26.46	1.52	-0.48	0.04	-32.55	1.93
16	-9.12	0.68	22.78	1.60	-0.46	0.04	-35.68	1.81
17	-8.55	0.67	18.62	1.69	-0.47	0.04	-38.61	1.67
18	-8.41	0.67	14.06	1.69	-0.44	0.05	-41.68	1.61
19	-8.10	0.67	10.15	2.15	-0.49	0.05	-44.27	1.53
20	-7.52	0.60	5.99	1.92	-0.46	0.04	-47.07	1.47
21	-7.55	0.60	1.69	1.92	-0.47	0.08	-49.91	1.30
22	-7.15	0.59	-0.28	2.08	-0.54	0.02	-52.48	1.37
23	-6.38	0.62	-4.37	2.08	-0.59	0.03	-55.37	1.16
24	-6.56	0.62	-8.20	2.10	-0.51	0.04	-58.02	1.32
25	-6.15	0.60	-11.90	2.59	-0.71	0.07	-61.13	1.05
26	-6.17	0.55	-15.63	3.11	-0.71	0.05	-62.96	1.20
					Actuation Voltage		17.14	2.67

Wafer: 120498-1 C-400-30 S-22 (7/16)

	Off - 0 V				On			
Freq-GHz	S22-dB	St. Dev.	S22-pha	St. Dev.	S22-dB	St. Dev.	S22-pha	St. Dev.
1	0.00	0.01	-5.11	0.15	-1.93	0.77	-37.62	7.15
2	-0.03	0.01	-10.15	0.30	-4.96	1.57	-57.99	7.26
3	-0.08	0.01	-15.11	0.44	-7.53	1.97	-69.46	5.81
4	-0.13	0.02	-19.96	0.56	-9.60	2.17	-76.99	4.41
5	-0.18	0.02	-24.84	0.70	-11.32	2.28	-82.41	3.20
6	-0.26	0.03	-29.62	0.80	-12.76	2.35	-86.83	2.26
7	-0.33	0.04	-34.33	0.92	-14.04	2.39	-90.62	1.51
8	-0.40	0.05	-39.12	1.04	-15.07	2.41	-93.74	0.96
9	-0.48	0.06	-43.84	1.14	-16.01	2.41	-96.36	0.90
10	-0.58	0.07	-48.55	1.24	-16.82	2.40	-99.94	1.02
11	-0.67	0.08	-53.18	1.34	-17.56	2.40	-102.00	1.49
12	-0.80	0.09	-57.72	1.42	-18.17	2.37	-104.82	1.81
13	-0.91	0.10	-61.92	1.48	-18.77	2.38	-108.49	1.92
14	-0.99	0.11	-66.29	1.56	-19.32	2.37	-112.00	2.34
15	-1.07	0.13	-70.68	1.62	-20.16	2.45	-117.62	2.14
16	-1.15	0.15	-75.36	1.67	-21.03	2.53	-121.48	2.51
17	-1.25	0.16	-79.73	1.70	-21.89	2.55	-121.41	3.88
18	-1.34	0.16	-84.14	1.71	-22.84	2.73	-124.36	3.88
19	-1.51	0.19	-88.18	1.77	-22.89	2.57	-124.14	4.57
20	-1.52	0.18	-92.85	1.83	-24.16	2.99	-129.18	4.35
21	-1.76	0.22	-97.11	1.88	-24.54	2.83	-132.80	3.84
22	-1.79	0.23	-100.77	1.96	-24.11	2.62	-131.57	7.09
23	-1.89	0.26	-106.67	2.42	-25.46	2.56	-121.33	12.03
24	-2.00	0.29	-110.34	2.20	-26.03	3.32	-133.31	9.30
25	-2.27	0.38	-115.27	2.09	-25.33	2.14	-126.74	10.63
26	-2.30	0.35	-118.79	1.56	-25.14	2.71	-138.58	10.70
					Actuation Voltage		17.14	2.67

Wafer: 120498-1 C-400-40 S-11 (7/16)

Off - 0 V					On			
Freq-GHz	S11-dB	St. Dev.	S11-pha	St. Dev.	S11-dB	St. Dev.	S11-pha	St. Dev.
1	-0.01	0.00	-2.88	0.17	-2.16	0.44	-37.91	3.53
2	-0.03	0.00	-5.71	0.33	-5.44	0.82	-56.25	3.10
3	-0.07	0.01	-8.46	0.48	-8.09	0.97	-65.09	2.19
4	-0.11	0.01	-11.15	0.62	-10.16	1.02	-69.90	1.47
5	-0.15	0.02	-13.82	0.78	-11.77	1.04	-72.91	0.92
6	-0.20	0.03	-16.51	0.92	-13.08	1.03	-75.30	0.52
7	-0.26	0.04	-19.07	1.06	-14.17	1.02	-76.85	0.28
8	-0.32	0.05	-21.63	1.20	-15.08	1.00	-78.52	0.33
9	-0.39	0.06	-24.17	1.32	-15.84	0.97	-79.82	0.48
10	-0.46	0.07	-26.70	1.43	-16.51	0.95	-80.70	0.59
11	-0.54	0.08	-29.10	1.52	-17.08	0.93	-82.34	0.66
12	-0.64	0.10	-31.49	1.59	-17.55	0.91	-84.12	0.75
13	-0.72	0.10	-33.76	1.69	-18.03	0.89	-86.79	0.83
14	-0.78	0.11	-35.82	1.76	-18.43	0.87	-88.30	1.07
15	-0.84	0.12	-37.90	1.86	-19.19	0.86	-89.69	1.33
16	-0.89	0.13	-40.31	2.02	-19.73	0.82	-91.19	1.75
17	-0.98	0.15	-42.54	2.16	-20.39	0.77	-93.08	1.90
18	-1.07	0.16	-45.03	2.24	-20.85	0.75	-93.86	1.98
19	-1.16	0.20	-46.92	2.24	-20.90	0.74	-95.10	1.88
20	-1.19	0.20	-49.35	2.28	-21.44	0.88	-96.23	2.15
21	-1.35	0.20	-51.20	2.30	-22.06	0.93	-93.77	3.87
22	-1.37	0.20	-53.04	2.48	-21.66	1.01	-97.48	2.12
23	-1.33	0.20	-55.71	2.87	-22.28	0.95	-100.46	1.81
24	-1.47	0.26	-58.09	2.87	-22.06	0.91	-98.19	2.30
25	-1.59	0.28	-60.14	2.95	-22.78	1.35	-101.15	3.17
26	-1.65	0.30	-62.52	2.63	-23.36	1.09	-102.18	2.74
					Actuation Voltage		16.71	1.60

Off - 0 V					On			
Freq-GHz	S21-dB	St. Dev.	S21-pha	St. Dev.	S21-dB	St. Dev.	S21-pha	St. Dev.
1	-31.87	0.91	85.93	0.30	-4.55	0.75	48.55	3.75
2	-25.57	0.86	81.16	0.49	-1.89	0.36	26.87	3.54
3	-22.20	0.87	77.18	0.55	-1.15	0.20	14.94	2.84
4	-19.60	0.85	72.93	0.75	-0.85	0.12	7.18	2.30
5	-17.69	0.84	68.34	0.88	-0.71	0.08	1.23	1.91
6	-16.11	0.83	63.59	1.01	-0.64	0.06	-3.61	1.62
7	-14.85	0.81	59.28	1.16	-0.60	0.05	-7.72	1.41
8	-13.69	0.80	55.48	1.25	-0.56	0.04	-11.46	1.25
9	-12.67	0.79	50.85	1.36	-0.54	0.03	-14.98	1.10
10	-11.93	0.77	46.09	1.42	-0.54	0.03	-18.24	1.00
11	-11.17	0.75	41.55	1.49	-0.53	0.02	-21.38	0.91
12	-10.60	0.73	37.03	1.54	-0.52	0.02	-24.38	0.85
13	-10.19	0.72	32.67	1.52	-0.50	0.02	-27.31	0.79
14	-9.63	0.72	29.86	1.59	-0.48	0.01	-30.21	0.70
15	-9.31	0.72	26.12	1.62	-0.45	0.01	-33.28	0.65
16	-8.93	0.72	22.45	1.74	-0.44	0.01	-36.37	0.62
17	-8.36	0.71	18.30	1.84	-0.45	0.01	-39.24	0.54
18	-8.21	0.70	13.74	1.77	-0.42	0.02	-42.27	0.50
19	-7.89	0.68	10.07	2.08	-0.46	0.03	-44.88	0.45
20	-7.37	0.64	5.05	2.00	-0.46	0.03	-47.44	0.49
21	-7.36	0.65	1.37	1.88	-0.45	0.05	-50.38	0.36
22	-6.90	0.64	-1.28	2.15	-0.56	0.03	-52.90	0.52
23	-6.40	0.68	-4.95	2.20	-0.57	0.03	-55.46	0.38
24	-6.44	0.68	-9.19	2.40	-0.51	0.04	-58.22	0.34
25	-6.15	0.64	-11.64	2.66	-0.64	0.05	-61.29	0.41
26	-5.82	0.55	-14.96	2.83	-0.66	0.04	-63.65	0.26
					Actuation Voltage		16.71	1.60

Wafer: 120498-1 C-400-40 S-22 (7/16)

	Off - 0 V				On			
Freq-GHz	S22-dB	St. Dev.	S22-pha	St. Dev.	S22-dB	St. Dev.	S22-pha	St. Dev.
1	0.00	0.00	-5.13	0.16	-2.17	0.44	-40.17	3.52
2	-0.03	0.01	-10.20	0.32	-5.49	0.83	-60.78	3.09
3	-0.07	0.01	-15.21	0.47	-8.22	0.98	-71.77	2.16
4	-0.13	0.02	-20.09	0.60	-10.39	1.05	-78.78	1.44
5	-0.18	0.02	-25.00	0.75	-12.16	1.09	-83.77	0.83
6	-0.26	0.03	-29.82	0.87	-13.61	1.10	-87.84	0.43
7	-0.33	0.04	-34.57	1.00	-14.91	1.12	-91.31	0.22
8	-0.40	0.05	-39.36	1.12	-15.96	1.12	-94.17	0.43
9	-0.49	0.06	-44.12	1.21	-16.90	1.11	-96.54	0.73
10	-0.59	0.07	-48.85	1.34	-17.71	1.11	-99.95	0.83
11	-0.69	0.09	-53.49	1.43	-18.46	1.11	-101.76	1.13
12	-0.82	0.10	-58.04	1.51	-19.06	1.10	-104.40	1.38
13	-0.93	0.11	-62.29	1.59	-19.65	1.08	-108.06	1.63
14	-1.01	0.13	-66.68	1.66	-20.22	1.05	-111.58	1.97
15	-1.10	0.14	-71.10	1.75	-21.06	0.99	-116.97	1.69
16	-1.17	0.16	-75.79	1.80	-21.90	0.95	-120.85	1.63
17	-1.28	0.18	-80.15	1.83	-22.87	0.98	-120.59	2.23
18	-1.38	0.18	-84.62	1.87	-23.79	1.01	-123.40	2.49
19	-1.52	0.19	-88.76	1.87	-24.02	1.17	-123.28	2.52
20	-1.61	0.20	-93.19	2.00	-24.71	1.27	-126.32	3.47
21	-1.80	0.22	-97.72	2.13	-25.49	0.96	-131.69	5.14
22	-1.92	0.27	-101.47	2.10	-24.97	1.24	-126.96	4.44
23	-1.95	0.30	-106.14	2.40	-25.75	0.88	-121.89	6.51
24	-2.11	0.34	-110.56	2.31	-26.22	1.15	-132.75	7.08
25	-2.23	0.36	-114.94	1.97	-26.14	1.10	-130.60	7.24
26	-2.32	0.37	-120.51	1.95	-27.83	0.67	-136.63	7.75
					Actuation Voltage		16.71	1.60

Wafer: 120498-1 C-500 S-11 (3/16)

Off - 0 V					On			
Freq-GHz	S11-dB	St. Dev.	S11-pha	St. Dev.	S11-dB	St. Dev.	S11-pha	St. Dev.
1	-0.01	0.00	-2.64	1.63	-4.13	1.09	-49.39	24.08
2	-0.03	0.01	-5.20	3.06	-8.48	1.50	-64.13	30.76
3	-0.07	0.01	-7.69	4.47	-11.43	1.59	-69.59	33.18
4	-0.11	0.03	-10.13	5.85	-13.59	1.61	-71.86	34.20
5	-0.15	0.04	-12.57	7.24	-15.15	1.57	-73.10	34.81
6	-0.20	0.06	-15.01	8.62	-16.38	1.53	-74.19	35.40
7	-0.26	0.08	-17.33	9.95	-17.12	1.60	-75.00	35.92
8	-0.32	0.10	-19.63	11.27	-17.95	1.56	-76.00	36.51
9	-0.39	0.12	-21.91	12.58	-18.60	1.50	-76.80	37.03
10	-0.46	0.14	-24.22	13.90	-19.14	1.43	-77.20	37.38
11	-0.55	0.17	-26.36	15.13	-19.63	1.40	-78.76	38.28
12	-0.65	0.19	-28.50	16.37	-20.00	1.32	-80.61	39.33
13	-0.74	0.21	-30.50	17.54	-20.45	1.33	-83.68	40.96
14	-0.79	0.24	-32.31	18.63	-20.79	1.29	-85.08	41.80
15	-0.85	0.27	-34.11	19.71	-21.59	1.35	-86.33	42.55
16	-0.91	0.30	-36.24	20.94	-22.11	1.39	-87.88	43.46
17	-0.99	0.33	-38.17	22.08	-22.93	1.34	-90.06	44.65
18	-1.07	0.36	-40.41	23.36	-23.37	1.52	-90.41	45.01
19	-1.16	0.33	-42.06	24.36	-23.51	1.41	-92.22	46.06
20	-1.17	0.36	-44.34	25.68	-24.14	1.42	-91.86	46.07
21	-1.35	0.41	-46.17	26.76	-24.94	1.63	-86.37	43.72
22	-1.39	0.42	-48.07	27.89	-24.12	1.17	-87.24	44.41
23	-1.36	0.48	-49.41	28.78	-23.51	0.59	-95.95	48.66
24	-1.51	0.51	-52.06	30.22	-23.64	0.89	-93.57	47.79
25	-1.58	0.50	-53.37	31.08	-24.26	0.74	-99.38	50.69
26	-1.67	0.53	-56.10	32.60	-24.95	0.95	-98.64	50.55
					Actuation Voltage		25.33	4.62

Off - 0 V					On			
Freq-GHz	S21-dB	St. Dev.	S21-pha	St. Dev.	S21-dB	St. Dev.	S21-pha	St. Dev.
1	-31.89	1.96	85.86	49.53	-2.57	0.71	35.85	18.13
2	-25.58	1.93	80.98	45.39	-1.05	0.27	16.64	8.30
3	-22.19	1.89	77.08	42.53	-0.71	0.14	7.18	3.67
4	-19.57	1.83	72.81	39.72	-0.59	0.09	1.03	1.91
5	-17.67	1.82	68.20	36.92	-0.53	0.07	-3.80	3.32
6	-16.09	1.78	63.37	34.11	-0.51	0.05	-7.85	5.27
7	-14.83	1.75	59.04	31.64	-0.50	0.05	-11.13	7.00
8	-13.67	1.72	55.11	29.39	-0.49	0.04	-14.42	8.76
9	-12.65	1.68	50.42	26.83	-0.48	0.03	-17.62	10.48
10	-11.91	1.65	45.64	24.33	-0.49	0.03	-20.62	12.13
11	-11.16	1.61	41.06	21.95	-0.48	0.03	-23.55	13.74
12	-10.60	1.59	36.45	19.66	-0.48	0.03	-26.35	15.29
13	-10.20	1.59	32.11	17.60	-0.46	0.03	-29.15	16.85
14	-9.64	1.57	29.25	16.22	-0.45	0.02	-31.91	18.38
15	-9.34	1.56	25.56	14.63	-0.43	0.02	-34.88	20.02
16	-8.96	1.54	21.98	13.19	-0.41	0.02	-37.87	21.67
17	-8.42	1.49	17.92	11.69	-0.41	0.02	-40.64	23.21
18	-8.27	1.46	13.59	10.51	-0.38	0.03	-43.62	24.86
19	-7.95	1.44	9.98	9.81	-0.41	0.03	-46.25	26.33
20	-7.45	1.42	5.44	9.39	-0.42	0.02	-48.76	27.75
21	-7.31	1.37	1.75	9.63	-0.42	0.04	-51.76	29.40
22	-6.74	1.40	-1.64	10.16	-0.56	0.01	-54.36	30.85
23	-6.65	1.43	-5.94	11.33	-0.59	0.00	-56.19	31.94
24	-6.53	1.32	-9.73	12.58	-0.51	0.01	-59.07	33.54
25	-6.35	1.39	-12.03	13.58	-0.60	0.01	-62.11	35.20
26	-5.87	1.29	-15.41	14.99	-0.66	0.02	-64.60	36.60
					Actuation Voltage		25.33	4.62

Wafer: 120498-1 C-500 S-22 (3/16)

	Off - 0 V				On			
Freq-GHz	S22-dB	St. Dev.	S22-pha	St. Dev.	S22-dB	St. Dev.	S22-pha	St. Dev.
1	0.00	0.00	-5.49	3.01	-4.15	1.10	-52.23	25.47
2	-0.04	0.01	-10.88	5.81	-8.58	1.53	-69.76	33.49
3	-0.09	0.02	-16.22	8.59	-11.69	1.64	-77.85	37.17
4	-0.15	0.03	-21.41	11.30	-14.00	1.68	-82.61	39.37
5	-0.21	0.05	-26.64	14.03	-15.83	1.68	-85.99	40.98
6	-0.29	0.06	-31.74	16.69	-17.29	1.68	-88.74	42.33
7	-0.37	0.09	-36.80	19.33	-18.31	1.81	-91.48	43.74
8	-0.44	0.11	-41.90	22.00	-19.32	1.77	-93.58	44.84
9	-0.54	0.14	-46.95	24.64	-20.23	1.73	-94.89	45.58
10	-0.65	0.16	-52.00	27.27	-20.97	1.70	-98.07	47.23
11	-0.76	0.19	-56.91	29.83	-21.69	1.63	-98.98	47.80
12	-0.90	0.22	-61.74	32.35	-22.24	1.59	-101.33	49.07
13	-1.02	0.25	-66.23	34.71	-22.79	1.62	-105.18	51.05
14	-1.11	0.27	-70.85	37.14	-23.37	1.60	-108.61	52.84
15	-1.20	0.29	-75.53	39.59	-24.42	1.78	-115.23	56.11
16	-1.28	0.31	-80.53	42.20	-25.39	1.92	-118.29	57.72
17	-1.37	0.34	-85.18	44.64	-26.56	1.91	-116.41	56.99
18	-1.47	0.37	-89.96	47.15	-27.84	2.48	-118.84	58.28
19	-1.61	0.42	-94.45	49.50	-28.03	2.06	-119.93	58.93
20	-1.67	0.44	-99.31	52.05	-29.40	2.54	-121.27	59.74
21	-1.90	0.43	-104.51	54.73	-30.83	2.93	-124.08	61.18
22	-2.10	0.43	-109.31	57.23	-29.45	1.99	-108.69	54.63
23	-2.22	0.53	-112.09	58.77	-27.43	0.72	-106.47	53.56
24	-2.35	0.53	-117.38	61.50	-29.00	1.70	-120.81	60.35
25	-2.40	0.53	-121.93	63.90	-29.89	1.85	-126.53	63.18
26	-2.58	0.57	-128.74	67.37	-33.12	4.86	-105.79	55.61
					Actuation Voltage		25.33	4.62

Wafer: 120498-1 C-500-30 S-11 (3/16)

Off - 0 V					On			
Freq-GHz	S11-dB	St. Dev.	S11-pha	St. Dev.	S11-dB	St. Dev.	S11-pha	St. Dev.
1	-0.01	0.00	-2.59	0.14	-2.82	1.52	-40.92	11.66
2	-0.03	0.00	-5.12	0.26	-6.36	2.72	-57.45	10.25
3	-0.06	0.01	-7.55	0.39	-9.02	3.20	-65.05	7.51
4	-0.10	0.01	-9.95	0.52	-11.08	3.40	-69.08	5.20
5	-0.14	0.02	-12.34	0.64	-12.62	3.45	-71.51	3.52
6	-0.19	0.02	-14.73	0.75	-13.90	3.44	-73.44	2.22
7	-0.25	0.03	-17.03	0.87	-14.93	3.40	-74.68	1.25
8	-0.31	0.04	-19.30	0.98	-15.80	3.36	-76.12	0.64
9	-0.37	0.05	-21.55	1.09	-16.50	3.28	-77.25	0.11
10	-0.44	0.06	-23.81	1.19	-17.12	3.19	-78.09	0.34
11	-0.51	0.07	-25.96	1.26	-17.65	3.15	-79.50	0.61
12	-0.61	0.08	-28.11	1.34	-18.09	3.08	-81.31	0.60
13	-0.69	0.09	-30.09	1.36	-18.55	3.05	-83.80	0.59
14	-0.74	0.09	-31.90	1.41	-18.90	3.01	-85.23	0.83
15	-0.81	0.09	-33.71	1.49	-19.59	3.01	-86.58	1.24
16	-0.87	0.09	-35.79	1.62	-20.06	2.93	-87.94	2.07
17	-0.94	0.09	-37.70	1.80	-20.67	2.88	-89.97	2.38
18	-1.02	0.10	-39.87	1.96	-21.14	2.87	-91.41	1.23
19	-1.08	0.15	-41.69	1.99	-21.73	3.01	-94.13	0.84
20	-1.10	0.14	-43.71	2.22	-21.69	2.47	-95.20	1.56
21	-1.27	0.23	-45.53	2.42	-23.04	2.96	-93.00	2.99
22	-1.33	0.25	-47.44	2.00	-22.51	3.22	-91.40	2.68
23	-1.26	0.19	-49.55	1.91	-22.92	3.27	-96.36	2.82
24	-1.39	0.17	-51.61	2.37	-22.87	2.93	-95.51	3.02
25	-1.55	0.24	-53.24	2.17	-23.26	3.57	-93.18	7.10
26	-1.56	0.20	-55.25	2.30	-23.39	3.55	-97.57	5.09
					Actuation Voltage		18.67	1.15

Off - 0 V					On			
Freq-GHz	S21-dB	St. Dev.	S21-pha	St. Dev.	S21-dB	St. Dev.	S21-pha	St. Dev.
1	-32.06	0.71	86.13	0.24	-4.20	2.47	45.01	12.33
2	-25.71	0.67	81.13	0.38	-1.82	1.23	24.65	11.58
3	-22.34	0.71	77.05	0.39	-1.13	0.70	13.51	9.37
4	-19.74	0.69	72.95	0.63	-0.85	0.44	6.13	7.65
5	-17.84	0.70	68.41	0.70	-0.71	0.31	0.42	6.35
6	-16.26	0.68	63.66	0.83	-0.64	0.24	-4.27	5.39
7	-14.99	0.68	59.33	0.98	-0.60	0.18	-8.28	4.70
8	-13.84	0.67	55.50	0.98	-0.56	0.14	-11.96	4.17
9	-12.81	0.64	50.88	1.24	-0.54	0.12	-15.41	3.66
10	-12.06	0.62	46.13	1.23	-0.53	0.11	-18.64	3.32
11	-11.31	0.61	41.56	1.35	-0.52	0.09	-21.75	3.01
12	-10.73	0.59	37.08	1.41	-0.52	0.09	-24.72	2.79
13	-10.31	0.57	32.65	1.34	-0.50	0.08	-27.61	2.61
14	-9.75	0.56	29.72	1.32	-0.48	0.06	-30.49	2.40
15	-9.45	0.56	25.98	1.22	-0.45	0.05	-33.51	2.27
16	-9.08	0.57	22.34	1.12	-0.43	0.05	-36.56	2.09
17	-8.54	0.58	18.26	1.01	-0.44	0.04	-39.40	1.86
18	-8.39	0.61	13.85	1.18	-0.41	0.05	-42.39	1.77
19	-8.02	0.58	10.82	1.58	-0.41	0.04	-45.17	1.70
20	-7.58	0.65	5.69	1.17	-0.43	0.04	-47.63	1.26
21	-7.48	0.73	2.35	2.19	-0.40	0.09	-50.75	1.22
22	-6.88	0.57	-1.13	2.99	-0.56	0.09	-53.46	1.27
23	-6.48	0.48	-4.72	2.20	-0.56	0.06	-55.78	1.22
24	-6.54	0.64	-8.59	1.85	-0.47	0.07	-58.60	0.94
25	-6.21	0.52	-11.95	3.63	-0.65	0.11	-61.78	0.95
26	-6.01	0.33	-14.93	2.56	-0.67	0.08	-63.73	1.08
					Actuation Voltage		18.67	1.15

Wafer: 120498-1 C-500-30 S-22 (3/16)

	Off - 0 V				On			
Freq-GHz	S22-dB	St. Dev.	S22-pha	St. Dev.	S22-dB	St. Dev.	S22-pha	St. Dev.
1	0.00	0.01	-5.43	0.15	-2.83	1.53	-43.78	11.64
2	-0.03	0.00	-10.77	0.30	-6.43	2.75	-63.12	10.22
3	-0.08	0.01	-16.06	0.42	-9.21	3.27	-73.40	7.33
4	-0.14	0.01	-21.21	0.54	-11.39	3.51	-80.14	5.06
5	-0.19	0.02	-26.40	0.67	-13.16	3.63	-84.97	3.17
6	-0.28	0.03	-31.48	0.77	-14.62	3.67	-88.98	1.76
7	-0.35	0.03	-36.51	0.89	-15.93	3.73	-92.52	0.56
8	-0.42	0.04	-41.57	0.99	-16.97	3.72	-95.42	0.59
9	-0.51	0.05	-46.62	1.08	-17.93	3.73	-97.72	1.64
10	-0.61	0.06	-51.64	1.18	-18.72	3.69	-101.31	2.13
11	-0.72	0.07	-56.56	1.26	-19.48	3.69	-103.00	3.25
12	-0.85	0.08	-61.40	1.28	-20.05	3.63	-105.43	4.04
13	-0.97	0.09	-65.92	1.33	-20.61	3.57	-109.50	4.16
14	-1.06	0.10	-70.55	1.40	-21.09	3.55	-112.95	4.69
15	-1.15	0.10	-75.26	1.47	-21.93	3.58	-119.50	4.08
16	-1.22	0.11	-80.25	1.51	-22.80	3.62	-124.49	3.82
17	-1.32	0.10	-84.89	1.57	-23.78	3.63	-124.74	5.57
18	-1.43	0.11	-89.55	1.72	-24.70	3.80	-128.06	5.15
19	-1.50	0.14	-94.20	1.81	-25.43	4.05	-131.31	7.02
20	-1.63	0.11	-98.80	2.32	-25.94	3.50	-133.91	8.05
21	-1.81	0.27	-103.80	2.65	-27.28	3.66	-142.16	3.18
22	-1.98	0.37	-108.67	2.17	-26.93	3.58	-129.80	6.89
23	-2.02	0.26	-113.24	2.08	-27.01	3.26	-123.56	14.22
24	-2.15	0.30	-117.86	2.99	-27.94	2.76	-141.44	7.11
25	-2.41	0.64	-123.00	2.23	-28.34	2.51	-136.00	11.33
26	-2.42	0.40	-127.81	1.10	-28.65	4.37	-141.63	11.38
					Actuation Voltage		18.67	1.15

Wafer: 120498-1 C-500-40 S-11 (1 / 16)

	Off - 0 V		On	
Freq-GHz	S11-dB	S11-pha	S11-dB	S11-pha
1	0.00	-2.72	-2.94	-43.43
2	-0.03	-5.35	-6.80	-60.65
3	-0.07	-7.92	-9.64	-67.86
4	-0.11	-10.45	-11.79	-71.44
5	-0.16	-12.93	-13.38	-73.53
6	-0.21	-15.42	-14.67	-75.17
7	-0.27	-17.83	-15.72	-76.24
8	-0.34	-20.21	-16.62	-77.57
9	-0.41	-22.53	-17.31	-78.51
10	-0.48	-24.89	-17.94	-79.02
11	-0.57	-27.12	-18.46	-80.49
12	-0.67	-29.35	-18.90	-82.02
13	-0.77	-31.43	-19.29	-84.59
14	-0.84	-33.34	-19.59	-85.70
15	-0.92	-35.19	-20.20	-87.35
16	-0.98	-37.22	-20.64	-89.64
17	-1.07	-39.13	-21.23	-92.57
18	-1.15	-41.32	-21.63	-93.85
19	-1.23	-43.30	-22.25	-96.07
20	-1.24	-45.04	-21.92	-98.50
21	-1.38	-46.71	-23.36	-97.91
22	-1.39	-49.18	-23.47	-98.35
23	-1.42	-51.54	-23.78	-101.21
24	-1.54	-53.47	-23.87	-102.90
25	-1.57	-54.75	-24.51	-103.93
26	-1.66	-57.31	-25.10	-101.98
			Voltage	15 V

Wafer: 120498-1 C-500-40 S-21 (1 / 16)

	Off - 0 V		On	
Freq-GHz	S21-dB	S21-pha	S21-dB	S21-pha
1	-31.19	85.79	-3.43	42.54
2	-24.89	80.67	-1.36	21.55
3	-21.59	76.77	-0.85	10.78
4	-18.99	72.33	-0.65	3.83
5	-17.08	67.62	-0.56	-1.55
6	-15.52	62.70	-0.53	-5.94
7	-14.27	58.36	-0.50	-9.74
8	-13.13	54.57	-0.48	-13.23
9	-12.11	49.86	-0.47	-16.52
10	-11.37	45.11	-0.47	-19.62
11	-10.61	40.53	-0.47	-22.66
12	-10.04	36.00	-0.47	-25.56
13	-9.61	31.54	-0.45	-28.39
14	-9.05	28.38	-0.44	-31.17
15	-8.76	24.48	-0.42	-34.06
16	-8.42	20.72	-0.41	-37.00
17	-7.92	16.67	-0.41	-39.73
18	-7.79	12.41	-0.37	-42.63
19	-7.37	9.17	-0.37	-45.45
20	-7.10	3.91	-0.40	-47.74
21	-7.04	1.11	-0.34	-50.75
22	-6.34	-1.52	-0.46	-53.64
23	-5.91	-6.23	-0.50	-55.94
24	-6.02	-9.53	-0.39	-58.69
25	-5.74	-11.39	-0.51	-61.78
26	-5.34	-15.40	-0.56	-64.09
			Voltage	15 V

Wafer: 120498-1 C-500-40 S-22 (1 / 16)

	Off - 0 V		On	
Freq-GHz	S22-dB	S22-pha	S22-dB	S22-pha
1	0.01	-5.51	-2.95	-46.24
2	-0.03	-11.01	-6.88	-66.26
3	-0.07	-16.40	-9.82	-76.14
4	-0.14	-21.67	-12.10	-82.50
5	-0.20	-26.96	-13.92	-86.93
6	-0.29	-32.16	-15.41	-90.92
7	-0.37	-37.31	-16.72	-94.19
8	-0.45	-42.49	-17.81	-96.98
9	-0.55	-47.63	-18.75	-99.03
10	-0.66	-52.72	-19.58	-102.68
11	-0.78	-57.76	-20.32	-104.15
12	-0.92	-62.67	-20.91	-106.62
13	-1.05	-67.36	-21.37	-110.46
14	-1.16	-72.10	-21.86	-113.19
15	-1.27	-76.87	-22.53	-119.72
16	-1.37	-81.81	-23.24	-124.71
17	-1.47	-86.40	-24.16	-126.06
18	-1.58	-91.13	-25.01	-130.84
19	-1.68	-96.11	-25.82	-134.18
20	-1.86	-100.00	-26.00	-134.70
21	-1.95	-104.79	-26.97	-147.74
22	-2.05	-110.18	-27.58	-138.15
23	-2.20	-114.87	-27.69	-127.54
24	-2.26	-119.19	-28.17	-147.31
25	-2.28	-124.37	-29.29	-152.22
26	-2.49	-130.35	-30.98	-148.92
			Voltage	15 V

Wafer: R120498-1 B-600 (9 / 16)

Off - 0V					On			
Freq-GHz	S11-dB	St. Dev.	S11-pha	St. Dev.	S11-dB	St. Dev.	S11-pha	St. Dev.
10	-2.35	0.12	-49.19	1.00	-16.07	1.06	-86.62	0.97
					Actuation Voltage		26.67	5.00

Off - 0V					On			
Freq-GHz	S21-dB	St. Dev.	S21-pha	St. Dev.	S21-dB	St. Dev.	S21-pha	St. Dev.
10	-4.68	0.20	10.97	1.03	-0.78	0.04	-29.61	1.10
					Actuation Voltage		26.67	5.00

Off - 0V					On			
Freq-GHz	S22-dB	St. Dev.	S22-pha	St. Dev.	S22-dB	St. Dev.	S22-pha	St. Dev.
10	-3.12	0.14	-93.68	1.05	-18.02	1.10	-107.38	3.14
					Actuation Voltage		26.67	5.00

Wafer: R120498-1 B-600-20 (10 / 16)

Off - 0V					On			
Freq-GHz	S11-dB	St. Dev.	S11-pha	St. Dev.	S11-dB	St. Dev.	S11-pha	St. Dev.
10	-2.31	0.12	-48.79	1.05	-14.52	1.32	-85.19	1.59
					Actuation Voltage		26.00	8.10

Off - 0V					On			
Freq-GHz	S21-dB	St. Dev.	S21-pha	St. Dev.	S21-dB	St. Dev.	S21-pha	St. Dev.
10	-4.75	0.19	11.33	1.04	-0.84	0.07	-27.80	1.73
					Actuation Voltage		26.00	8.10

Off - 0V					On			
Freq-GHz	S22-dB	St. Dev.	S22-pha	St. Dev.	S22-dB	St. Dev.	S22-pha	St. Dev.
10	-3.07	0.14	-93.45	0.81	-16.36	1.47	-111.07	2.64
					Actuation Voltage		26.00	8.10

Wafer: R120498-1 B-600-30 (10 / 16)

Off - 0V

Freq-GHz	S11-dB	St. Dev.	S11-pha	St. Dev.
10	-2.14	0.64	-46.37	8.75

On

S11-dB	St. Dev.	S11-pha	St. Dev.
-15.19	1.21	-85.74	1.44
Actuation Voltage		26.00	5.16

Off - 0V

Freq-GHz	S21-dB	St. Dev.	S21-pha	St. Dev.
10	-5.54	2.67	13.59	8.10

On

S21-dB	St. Dev.	S21-pha	St. Dev.
-0.81	0.05	-28.63	1.43
Actuation Voltage		26.00	5.16

Off - 0V

Freq-GHz	S22-dB	St. Dev.	S22-pha	St. Dev.
10	-2.88	0.70	-91.60	6.38

On

S22-dB	St. Dev.	S22-pha	St. Dev.
-17.14	1.29	-109.67	2.94
Actuation Voltage		26.00	5.16

Wafer: R120498-1 B-600-40 (11 / 16)

Off - 0V

Freq-GHz	S11-dB	St. Dev.	S11-pha	St. Dev.
10	-2.29	0.13	-48.72	1.01

On

S11-dB	St. Dev.	S11-pha	St. Dev.
-15.30	1.69	-86.16	1.42
Actuation Voltage		23.64	5.05

Off - 0V

Freq-GHz	S21-dB	St. Dev.	S21-pha	St. Dev.
10	-4.77	0.20	11.50	1.06

On

S21-dB	St. Dev.	S21-pha	St. Dev.
-0.80	0.07	-28.75	1.94
Actuation Voltage		23.64	5.05

Off - 0V

Freq-GHz	S22-dB	St. Dev.	S22-pha	St. Dev.
10	-3.04	0.14	-93.23	0.98

On

S22-dB	St. Dev.	S22-pha	St. Dev.
-17.27	1.71	-108.73	3.69
Actuation Voltage		23.64	5.05

Wafer: R120498-1 B-800 (7 / 16)

Off - 0V

Freq-GHz	S11-dB	St. Dev.	S11-pha	St. Dev.
10	-3.50	0.23	-54.00	1.54

On

S11-dB	St. Dev.	S11-pha	St. Dev.
-15.66	1.63	-89.60	3.09
Actuation Voltage		20.00	0.00

Off - 0V

Freq-GHz	S21-dB	St. Dev.	S21-pha	St. Dev.
10	-3.35	0.21	1.50	1.39

On

S21-dB	St. Dev.	S21-pha	St. Dev.
-0.78	0.07	-30.59	1.98
Actuation Voltage		20.00	0.00

Off - 0V

Freq-GHz	S22-dB	St. Dev.	S22-pha	St. Dev.
10	-4.48	0.25	-107.22	1.09

On

S22-dB	St. Dev.	S22-pha	St. Dev.
-17.27	1.61	-110.60	4.39
Actuation Voltage		20.00	0.00

Wafer: R120498-1 B0800-20 (9 / 16)

Off - 0V

Freq-GHz	S11-dB	St. Dev.	S11-pha	St. Dev.
10	-2.99	1.15	-49.52	11.05

On

S11-dB	St. Dev.	S11-pha	St. Dev.
-15.67	0.82	-88.68	2.94
Actuation Voltage		22.22	4.41

Off - 0V

Freq-GHz	S21-dB	St. Dev.	S21-pha	St. Dev.
10	-4.66	3.29	5.56	10.16

On

S21-dB	St. Dev.	S21-pha	St. Dev.
-0.77	0.04	-30.05	1.67
Actuation Voltage		22.22	4.41

Off - 0V

Freq-GHz	S22-dB	St. Dev.	S22-pha	St. Dev.
10	-3.92	1.25	-103.93	8.36

On

S22-dB	St. Dev.	S22-pha	St. Dev.
-17.35	0.68	-112.61	3.68
Actuation Voltage		22.22	4.41

Wafer: R120498-1 B-800-30 (5 / 16)

Off - 0V

Freq-GHz	S11-dB	St. Dev.	S11-pha	St. Dev.
10	-2.99	1.13	-58.05	9.03

On

S11-dB	St. Dev.	S11-pha	St. Dev.
-16.07	0.78	-90.12	1.84
Actuation Voltage		24.00	8.94

Off - 0V

Freq-GHz	S21-dB	St. Dev.	S21-pha	St. Dev.
10	-6.22	6.42	10.06	19.20

On

S21-dB	St. Dev.	S21-pha	St. Dev.
-0.77	0.05	-31.31	0.88
Actuation Voltage		24.00	8.94

Off - 0V

Freq-GHz	S22-dB	St. Dev.	S22-pha	St. Dev.
10	-3.59	1.96	-86.42	46.46

On

S22-dB	St. Dev.	S22-pha	St. Dev.
-17.90	0.78	-109.58	1.72
Actuation Voltage		24.00	8.94

Wafer: R120498-1 B-800-40 (7 / 16)

Off - 0V

Freq-GHz	S11-dB	St. Dev.	S11-pha	St. Dev.
10	-3.47	0.20	-53.79	1.14

On

S11-dB	St. Dev.	S11-pha	St. Dev.
-15.07	1.48	-88.51	2.66
Actuation Voltage		20.00	0.00

Off - 0V

Freq-GHz	S21-dB	St. Dev.	S21-pha	St. Dev.
10	-3.38	0.16	1.61	1.19

On

S21-dB	St. Dev.	S21-pha	St. Dev.
-0.81	0.07	-29.97	1.78
Actuation Voltage		20.00	0.00

Off - 0V

Freq-GHz	S22-dB	St. Dev.	S22-pha	St. Dev.
10	-4.46	0.22	-107.10	1.08

On

S22-dB	St. Dev.	S22-pha	St. Dev.
-16.70	1.49	-112.23	3.61
Actuation Voltage		20.00	0.00

Wafer: MEMS-1C B-600 (2 / 8)

S11 **Off - 0V**

Freq-GHz	S11-dB	St. Dev.	S11-pha	St. Dev
9	-1.28	0.03	-40.97	0.16
10	-1.51	0.03	-44.71	0.17

On

S11-dB	St. Dev.	S11-pha	St. Dev
-10.54	1.95	-84.62	6.25
-11.01	1.89	-87.83	6.18
Actuation Voltage		17.00	1.41

S21 **Off - 0V**

Freq-GHz	S21-dB	St. Dev.	S21-pha	St. Dev
9	-6.39	0.03	22.81	0.18
10	-5.86	0.03	16.46	0.13

On

S21-dB	St. Dev.	S21-pha	St. Dev
-0.84	0.24	-19.43	4.17
-0.80	0.21	-24.30	3.88
Actuation Voltage		17.00	1.41

S22 **Off - 0V**

Freq-GHz	S22-dB	St. Dev.	S22-pha	St. Dev
9	-1.63	0.02	-84.76	0.21
10	-1.94	0.03	-92.87	0.26

On

S22-dB	St. Dev.	S22-pha	St. Dev
-11.25	2.10	-117.67	1.35
-11.86	2.04	-123.36	0.54
Actuation Voltage		17.00	1.41

Wafer: MEMS-1C B-600-20 (5 / 8)

S11 **Off - 0V**

Freq-GHz	S11-dB	St. Dev.	S11-pha	St. Dev
9	-1.29	0.13	-40.51	1.38
10	-1.52	0.15	-44.22	1.45

On

S11-dB	St. Dev.	S11-pha	St. Dev
-9.80	0.19	-80.92	1.37
-10.30	0.22	-84.22	1.42
Actuation Voltage		17.00	2.58

S21 **Off - 0V**

Freq-GHz	S21-dB	St. Dev.	S21-pha	St. Dev
9	-6.41	0.37	22.84	1.40
10	-5.88	0.35	16.53	1.41

On

S21-dB	St. Dev.	S21-pha	St. Dev
-0.93	0.03	-17.92	0.42
-0.87	0.02	-22.92	0.44
17.00	2.58	17.00	2.58

S22 **Off - 0V**

Freq-GHz	S22-dB	St. Dev.	S22-pha	St. Dev
9	-1.61	0.12	-85.08	1.52
10	-1.91	0.13	-93.30	1.57

On

S22-dB	St. Dev.	S22-pha	St. Dev
-10.32	0.24	-118.02	0.93
-10.98	0.26	-124.34	1.12
Actuation Voltage		17.00	2.58

Wafer: MEMS-1C B-600-30 (3 / 7)

S11 **Off - 0V**

Freq-GHz	S11-dB	St. Dev.	S11-pha	St. Dev
9	-1.56	0.18	-43.96	2.19
10	-1.84	0.20	-47.81	2.25

On

S11-dB	St. Dev.	S11-pha	St. Dev
-10.12	0.65	-83.26	1.95
-10.64	0.63	-86.59	1.96
Actuation Voltage		13.00	2.00

S21 **Off - 0V**

Freq-GHz	S21-dB	St. Dev.	S21-pha	St. Dev
9	-5.64	0.45	19.87	1.92
10	-5.14	0.41	13.48	1.99

On

S21-dB	St. Dev.	S21-pha	St. Dev
-0.86	0.08	-18.65	1.52
-0.81	0.07	-23.61	1.40
Actuation Voltage		13.00	2.00

S22 **Off - 0V**

Freq-GHz	S22-dB	St. Dev.	S22-pha	St. Dev
9	-1.93	0.20	-87.58	1.67
10	-2.27	0.23	-95.79	1.63

On

S22-dB	St. Dev.	S22-pha	St. Dev
-10.76	0.72	-117.97	0.88
-11.40	0.70	-123.95	0.73
Actuation Voltage		13.00	2.00

Wafer: MEMS-1C B-600-40 (3 / 6)

S11 **Off - 0V**

Freq-GHz	S11-dB	St. Dev.	S11-pha	St. Dev
9	-1.34	0.05	-41.76	0.44
10	-1.58	0.06	-45.54	0.47

On

S11-dB	St. Dev.	S11-pha	St. Dev
-10.89	1.00	-84.36	3.22
-11.35	0.98	-87.62	3.26
Actuation Voltage		17.33	1.15

S21 **Off - 0V**

Freq-GHz	S21-dB	St. Dev.	S21-pha	St. Dev
9	-6.19	0.16	22.05	0.56
10	-5.67	0.15	15.72	0.56

On

S21-dB	St. Dev.	S21-pha	St. Dev
-0.79	0.11	-20.28	2.10
-0.76	0.10	-25.09	1.96
Actuation Voltage		14.00	5.29

S22 **Off - 0V**

Freq-GHz	S22-dB	St. Dev.	S22-pha	St. Dev
9	-1.67	0.07	-85.62	0.90
10	-1.99	0.09	-93.81	1.00

On

S22-dB	St. Dev.	S22-pha	St. Dev
-11.46	0.98	-119.06	1.45
-12.10	0.97	-124.90	1.42
Actuation Voltage		17.33	1.15

Wafer: MEMS-1C B-700 (1 / 8)

Off

Freq-GHz	S11-dB	S11pha	S21-dB	S21pha	S22-dB	S22pha
9	-1.59	-43.03	-5.45	18.67	-2.00	-91.72
10	-1.87	-46.77	-4.97	12.29	-2.35	-100.11

On

Freq-GHz	S11-dB	S11pha	S21-dB	S21pha	S22-dB	S22pha
9	-11.86	-87.83	-0.65	-22.81	-12.61	-122.76
10	-12.25	-91.17	-0.63	-27.46	-13.15	-128.11
Actuation Voltage		14				

Wafer: MEMS-1C B-700-20 (4 / 9)

S11 Off - 0V

Freq-GHz	S11-dB	St. Dev	S11-pha	St. Dev
9	-1.82	0.39	-44.12	3.24
10	-2.11	0.44	-47.79	3.31

On

S11-dB	St. Dev	S11-pha	St. Dev
-11.52	0.63	-85.76	1.91
-11.91	0.62	-89.10	1.93
Actuation Voltage		12.75	2.50

S21 Off - 0V

Freq-GHz	S21-dB	St. Dev	S21-pha	St. Dev
9	-5.26	0.66	16.59	3.80
10	-4.81	0.61	10.24	3.76

On

S21-dB	St. Dev	S21-pha	St. Dev
-0.74	0.05	-22.44	1.39
-0.72	0.04	-27.14	1.28
Actuation Voltage		12.75	2.50

S22 Off - 0V

Freq-GHz	S22-dB	St. Dev	S22-pha	St. Dev
9	-2.24	0.43	-93.60	3.34
10	-2.59	0.45	-102.03	3.26

On

S22-dB	St. Dev	S22-pha	St. Dev
-12.17	0.52	-123.40	2.31
-12.67	0.43	-129.11	2.46
Actuation Voltage		12.75	2.50

Wafer: MEMS-1C B-700-30 (3 / 8)

S11 Off - 0V

Freq-GHz	S11-dB	St. Dev.	S11-pha	St. Dev
9	-1.58	0.17	-42.04	0.34
10	-1.84	0.17	-45.67	0.31

On

S11-dB	St. Dev.	S11-pha	St. Dev
-11.29	0.78	-85.70	0.86
-11.69	0.73	-89.08	1.01
Actuation Voltage		13.00	1.00

S21 Off - 0V

Freq-GHz	S21-dB	St. Dev.	S21-pha	St. Dev
9	-5.73	0.12	18.66	1.80
10	-5.25	0.10	12.36	1.71

On

S21-dB	St. Dev.	S21-pha	St. Dev
-0.75	0.03	-22.12	1.60
-0.72	0.02	-26.81	1.45
Actuation Voltage		13.00	1.00

S22 Off - 0V

Freq-GHz	S22-dB	St. Dev.	S22-pha	St. Dev
9	-1.99	0.24	-91.79	2.29
10	-2.31	0.23	-100.19	2.36

On

S22-dB	St. Dev.	S22-pha	St. Dev
-11.88	0.68	-123.87	4.39
-12.37	0.60	-129.61	4.72
Actuation Voltage		13.00	1.00

Wafer: MEMS-1C B-700-40 (6 / 10)

S11 Off - 0V

Freq-GHz	S11-dB	St. Dev.	S11-pha	St. Dev
9	-1.41	0.03	-40.93	1.11
10	-1.66	0.04	-44.51	1.11

On

S11-dB	St. Dev.	S11-pha	St. Dev
-11.64	0.82	-86.63	2.45
-12.07	0.78	-90.09	2.67
Actuation Voltage		15.50	1.97

S21 Off - 0V

Freq-GHz	S21-dB	St. Dev.	S21-pha	St. Dev
9	-6.06	0.09	19.35	2.03
10	-5.56	0.08	13.09	1.98

On

S21-dB	St. Dev.	S21-pha	St. Dev
-0.72	0.05	-23.08	1.81
-0.70	0.05	-27.72	1.66
Actuation Voltage		15.50	1.97

S22 Off - 0V

Freq-GHz	S22-dB	St. Dev.	S22-pha	St. Dev
9	-1.78	0.04	-90.89	2.32
10	-2.09	0.04	-99.30	2.33

On

S22-dB	St. Dev.	S22-pha	St. Dev
-12.28	0.82	-123.26	3.81
-12.80	0.75	-128.97	3.87
Actuation Voltage		15.50	1.97

Wafer: MEMS-1C B-800 (0 / 10)

Wafer: MEMS-1C B-800-20 (4 / 9)

S11 **Off - 0V**

Freq-GHz	S11-dB	St. Dev.	S11-pha	St. Dev.
9	-1.74	0.34	-42.26	4.12
10	-2.01	0.38	-45.69	4.12

On

S11-dB	St. Dev.	S11-pha	St. Dev.
-11.96	0.18	-89.44	3.25
-12.19	0.33	-92.97	2.85
Actuation Voltage		14.75	2.22

S21 **Off - 0V**

Freq-GHz	S21-dB	St. Dev.	S21-pha	St. Dev.
9	-5.77	0.26	17.18	2.40
10	-5.32	0.26	11.01	2.33

On

S21-dB	St. Dev.	S21-pha	St. Dev.
-0.75	0.11	-24.79	1.43
-0.74	0.12	-29.21	1.22
Actuation Voltage		14.75	2.22

S22 **Off - 0V**

Freq-GHz	S22-dB	St. Dev.	S22-pha	St. Dev.
9	-1.99	0.25	-94.95	2.35
10	-2.30	0.25	-103.43	2.38

On

S22-dB	St. Dev.	S22-pha	St. Dev.
-12.51	0.17	-126.17	4.62
-12.89	0.16	-131.81	5.26
Actuation Voltage		14.75	2.22

Wafer: MEMS-1C B-800-30 (2 / 4)

S11 **Off- 0V**

Freq-GHz	S11-dB	St. Dev.	S11-pha	St. Dev.
9	-1.42	0.15	-23.07	1.07
10	-1.65	0.17	-25.00	1.03

On

S11-dB	St. Dev.	S11-pha	St. Dev.
-12.45	1.01	-55.34	1.45
-12.65	0.92	-57.32	1.45
Actuation Voltage		18.00	0.00

S21 **Off- 0V**

Freq-GHz	S21-dB	St. Dev.	S21-pha	St. Dev.
9	-5.99	0.44	15.69	2.02
10	-5.52	0.41	11.84	2.01

On

S21-dB	St. Dev.	S21-pha	St. Dev.
-0.67	0.08	-13.75	1.94
-0.66	0.07	-16.37	1.77
Actuation Voltage		18.00	0.00

S22 **Off- 0V**

Freq-GHz	S22-dB	St. Dev.	S22-pha	St. Dev.
9	-1.85	0.26	-59.60	2.69
10	-2.16	0.29	-64.95	2.74

On

S22-dB	St. Dev.	S22-pha	St. Dev.
-13.25	1.45	-79.44	1.88
-13.58	1.38	-82.59	1.44
Actuation Voltage		18.00	0.00

Wafer: MEMS-1C B-800-40 (1 / 4)

Off

Freq-GHz	S11-dB	S11pha	S21-dB	S21pha	S22-dB	S22pha
9	-1.94	-42.54	-5.20	14.07	-2.47	-99.46
10	-2.23	-45.98	-4.78	7.92	-2.78	-108.01

On - 13V

Freq-GHz	S11-dB	S11pha	S21-dB	S21pha	S22-dB	S22pha
9	-11.80	-87.04	-0.74	-24.27	-12.31	-130.01
10	-12.12	-90.86	-0.72	-28.81	-12.61	-135.58

Wafer: MEMS-3A C-600-40 (1 / 4)

Off - 0V

Freq-GHz	S11-dB	S11pha	S21-dB	S21pha	S22-dB	S22pha
1	-0.02	-4.53	-25.67	83.25	-0.07	-13.24
2	-0.06	-8.96	-19.39	74.98	-0.16	-25.67
3	-0.14	-13.39	-16.08	68.04	-0.38	-38.01
4	-0.24	-17.61	-13.48	60.98	-0.59	-49.10
5	-0.35	-21.85	-11.81	53.93	-0.83	-60.19
6	-0.49	-26.14	-10.22	47.17	-1.10	-70.24
7	-0.66	-29.99	-9.16	39.58	-1.33	-79.73
8	-0.80	-33.64	-8.42	32.94	-1.58	-88.58
9	-0.95	-37.49	-7.65	26.99	-1.84	-96.56
10	-1.20	-41.00	-6.96	19.47	-1.90	-103.60
11	-1.37	-44.40	-6.48	13.30	-2.06	-110.16
12	-1.55	-47.48	-6.10	7.14	-2.24	-116.47
13	-1.72	-50.40	-5.76	1.41	-2.33	-121.96
14	-1.77	-53.78	-5.48	-3.18	-2.36	-127.37
15	-1.94	-56.77	-5.09	-8.34	-2.30	-133.73
16	-2.06	-59.95	-4.74	-13.46	-2.37	-139.94
17	-2.21	-63.66	-4.42	-18.46	-2.46	-145.78
18	-2.38	-66.60	-4.08	-23.55	-2.43	-152.04
19	-2.56	-69.87	-3.89	-29.26	-2.58	-157.84
20	-2.75	-73.54	-3.71	-33.14	-2.57	-163.68
21	-2.86	-76.60	-3.43	-38.87	-2.68	-169.01
22	-3.04	-81.22	-3.38	-44.02	-2.77	-174.80
23	-3.49	-85.49	-3.34	-48.82	-2.98	-178.27
24	-3.75	-85.46	-3.58	-54.97	-3.14	-178.05
25	-3.64	-89.39	-3.23	-56.91	-3.35	-171.02
26	-3.97	-92.01	-3.21	-62.09	-3.55	-165.72

Wafer: MEMS-3A C-600-40 (1 / 4)

	On - 60V					
Freq-GHz	S11-dB	S11pha	S21-dB	S21pha	S22-dB	S22pha
1	-34.06	-29.92	-0.18	-4.21	-30.90	-68.16
2	-31.90	-45.79	-0.19	-8.10	-26.14	-83.35
3	-30.08	-66.65	-0.25	-11.96	-22.80	-93.65
4	-29.00	-74.52	-0.24	-15.51	-20.87	-101.44
5	-27.21	-86.07	-0.32	-19.21	-19.08	-106.72
6	-26.25	-92.45	-0.30	-22.37	-17.56	-111.73
7	-24.90	-99.42	-0.31	-26.36	-16.56	-116.97
8	-23.72	-105.77	-0.42	-30.53	-15.49	-121.40
9	-22.90	-112.90	-0.51	-33.96	-14.61	-125.30
10	-22.26	-115.79	-0.40	-37.69	-14.00	-130.19
11	-21.47	-120.47	-0.47	-41.34	-13.71	-133.14
12	-20.53	-125.10	-0.47	-45.04	-13.21	-136.47
13	-19.79	-130.63	-0.37	-48.73	-12.56	-141.40
14	-19.10	-138.78	-0.53	-52.81	-12.45	-144.91
15	-18.93	-143.03	-0.36	-56.99	-12.20	-149.00
16	-18.64	-146.72	-0.29	-61.14	-11.84	-152.34
17	-18.46	-151.59	-0.40	-64.15	-11.66	-155.82
18	-17.92	-153.91	-0.13	-68.44	-11.42	-159.99
19	-17.66	-157.80	-0.32	-72.48	-11.21	-163.05
20	-17.69	-160.31	-0.37	-74.43	-11.17	-167.58
21	-16.52	-163.57	-0.26	-79.14	-11.10	-170.36
22	-16.97	-171.04	-0.59	-82.97	-10.95	-175.54
23	-16.43	-174.76	-0.64	-84.80	-10.36	-176.28
24	-15.62	-172.31	-0.58	-89.61	-10.44	-178.56
25	-15.11	-175.56	-0.84	-92.82	-10.68	-178.53
26	-15.39	-175.64	-0.80	-96.02	-10.56	-174.26

Wafer: MEMS-3C B-600-20 S11 (2 / 4)

OFF					On			
Freq-GHz	S11-dB	St. Dev.	S11-pha	St. Dev.	S11-dB	St. Dev.	S11-pha	St. Dev.
1	-0.03	0.00	-4.44	0.02	-0.95	0.00	-26.88	0.02
2	-0.07	0.00	-8.74	0.03	-2.91	0.01	-45.62	0.02
3	-0.13	0.00	-13.07	0.06	-4.89	0.01	-57.39	0.07
4	-0.22	0.00	-17.23	0.07	-6.61	0.01	-64.99	0.12
5	-0.33	0.00	-21.44	0.09	-7.98	0.00	-70.33	0.19
6	-0.46	0.01	-25.51	0.08	-9.11	0.00	-74.57	0.24
7	-0.61	0.01	-29.41	0.11	-9.99	0.01	-78.01	0.27
8	-0.78	0.01	-33.18	0.13	-10.69	0.01	-81.48	0.24
9	-0.94	0.01	-36.75	0.13	-11.26	0.01	-84.56	0.26
10	-1.11	0.01	-40.21	0.14	-11.73	0.01	-88.10	0.25
11	-1.25	0.01	-43.64	0.09	-12.13	0.03	-91.97	0.30
12	-1.38	0.00	-47.29	0.08	-12.59	0.07	-95.90	0.53
13	-1.57	0.01	-50.96	0.17	-13.08	0.08	-98.18	1.03
14	-1.78	0.01	-54.13	0.30	-13.08	0.03	-99.84	1.41
15	-2.00	0.01	-57.12	0.37	-13.19	0.01	-103.02	1.67
16	-2.16	0.00	-59.92	0.35	-13.03	0.04	-107.23	1.82
17	-2.27	0.01	-63.13	0.36	-13.10	0.06	-112.90	1.65
18	-2.44	0.00	-66.26	0.30	-13.17	0.08	-117.27	1.49
19	-2.58	0.02	-69.28	0.27	-13.28	0.00	-122.35	1.75
20	-2.67	0.05	-72.29	0.72	-13.29	0.16	-127.12	2.77
21	-2.88	0.05	-75.35	1.47	-13.19	0.15	-128.72	2.56
22	-2.93	0.04	-79.87	0.93	-13.34	0.04	-137.92	1.57
23	-3.27	0.01	-84.41	0.39	-13.72	0.05	-142.46	1.21
24	-3.46	0.02	-88.40	0.51	-13.62	0.11	-145.61	0.89
25	-5.10	0.16	-87.37	0.00	-13.25	0.33	-153.59	0.45
26	-3.76	0.08	-90.48	1.19	-13.52	0.26	-155.12	1.92
					Actuation Voltage		42.50	3.54

Wafer: MEMS-3C B-600-20 S21 (2 / 4)

OFF					On			
Freq-GHz	S21-dB	St. Dev.	S21-pha	St. Dev.	S21-dB	St. Dev.	S21-pha	St. Dev.
1	-25.75	0.03	82.98	0.15	-7.36	0.00	59.41	0.02
2	-19.57	0.00	75.54	0.09	-3.34	0.01	37.08	0.04
3	-16.16	0.01	68.55	0.14	-1.95	0.01	21.81	0.03
4	-13.69	0.01	61.52	0.07	-1.34	0.00	10.90	0.02
5	-11.85	0.01	53.92	0.10	-1.03	0.00	2.14	0.04
6	-10.47	0.01	46.46	0.07	-0.88	0.00	-5.01	0.04
7	-9.31	0.01	39.61	0.08	-0.78	0.00	-11.23	0.03
8	-8.31	0.00	32.87	0.06	-0.70	0.00	-16.90	0.03
9	-7.52	0.00	25.86	0.11	-0.65	0.00	-22.15	0.01
10	-6.96	0.00	19.67	0.08	-0.61	0.00	-27.00	0.01
11	-6.39	0.00	13.65	0.06	-0.56	0.01	-31.81	0.04
12	-5.84	0.00	8.12	0.06	-0.50	0.00	-36.69	0.06
13	-5.29	0.00	1.99	0.05	-0.50	0.00	-41.71	0.06
14	-4.86	0.01	-5.17	0.07	-0.59	0.00	-46.08	0.11
15	-4.61	0.02	-10.95	0.06	-0.59	0.00	-50.45	0.11
16	-4.48	0.03	-16.54	0.20	-0.60	0.01	-54.47	0.16
17	-4.29	0.01	-21.68	0.22	-0.56	0.01	-58.53	0.12
18	-4.07	0.02	-26.59	0.36	-0.53	0.02	-63.06	0.10
19	-3.89	0.02	-31.96	0.42	-0.55	0.02	-67.29	0.10
20	-3.91	0.05	-36.39	0.62	-0.55	0.05	-70.93	0.11
21	-3.68	0.17	-42.62	0.61	-0.65	0.03	-75.61	0.26
22	-3.49	0.05	-46.62	0.08	-0.61	0.01	-79.14	0.02
23	-3.27	0.04	-52.14	0.32	-0.61	0.02	-83.46	0.03
24	-3.02	0.01	-57.21	0.08	-0.62	0.00	-88.13	0.08
25	-3.97	0.14	-63.44	0.15	-0.98	0.03	-90.52	0.09
26	-3.12	0.06	-64.99	0.53	-0.74	0.00	-94.58	0.15
					Actuation Voltage		42.50	3.54

Wafer: MEMS-3C B-600-20 S22 (2 / 4)

OFF					On			
Freq-GHz	S22-dB	St. Dev.	S22-pha	St. Dev.	S22-dB	St. Dev.	S22-pha	St. Dev.
1	-0.02	0.00	-9.81	0.02	-0.97	0.01	-32.45	0.04
2	-0.07	0.00	-19.38	0.00	-2.98	0.01	-56.45	0.03
3	-0.15	0.00	-29.05	0.04	-5.04	0.02	-73.33	0.07
4	-0.26	0.00	-38.42	0.06	-6.83	0.02	-85.68	0.05
5	-0.39	0.00	-47.86	0.10	-8.32	0.02	-95.45	0.06
6	-0.56	0.01	-57.04	0.13	-9.54	0.03	-103.53	0.15
7	-0.74	0.01	-66.04	0.15	-10.53	0.02	-110.77	0.19
8	-0.95	0.02	-74.76	0.14	-11.35	0.02	-117.00	0.19
9	-1.16	0.02	-83.25	0.14	-11.98	0.03	-122.80	0.14
10	-1.37	0.01	-91.42	0.13	-12.48	0.01	-129.01	0.17
11	-1.54	0.00	-99.47	0.13	-12.95	0.03	-135.04	0.28
12	-1.71	0.02	-107.89	0.22	-13.51	0.07	-141.01	0.49
13	-2.01	0.05	-116.45	0.37	-14.24	0.13	-145.38	1.00
14	-2.43	0.05	-123.50	0.79	-14.50	0.08	-146.15	1.79
15	-2.72	0.03	-130.56	0.97	-14.60	0.02	-149.40	2.26
16	-2.93	0.03	-136.56	1.17	-14.35	0.09	-152.76	1.68
17	-3.01	0.05	-143.39	0.97	-14.29	0.07	-158.55	1.35
18	-3.23	0.07	-150.33	0.92	-14.41	0.07	-162.89	0.85
19	-3.40	0.08	-156.91	0.88	-14.38	0.07	-167.23	1.03
20	-3.46	0.09	-162.38	0.46	-14.18	0.20	-171.14	0.04
21	-3.92	0.00	-168.74	0.40	-14.31	0.42	-171.84	1.82
22	-3.76	0.07	-175.56	0.85	-13.91	0.10	-178.04	0.34
23	-4.16	0.03	-177.16	0.49	-14.23	0.12	-176.28	1.44
24	-4.29	0.02	-170.05	0.66	-14.19	0.05	-170.30	1.78
25	-4.44	0.08	-169.72	0.93	-13.94	0.15	-167.21	3.78
26	-4.83	0.03	-160.38	0.35	-14.07	0.31	-168.42	1.34
					Actuation Voltage		42.50	3.54

Wafer: MEMS-3C B-700-20 S11 (3 / 4)

	OFF - 0V				On			
Freq-GHz	S11-dB	St. Dev.	S11-pha	St. Dev.	S11-dB	St. Dev.	S11-pha	St. Dev.
1	-0.03	0.00	-4.52	0.07	-1.95	0.53	-36.80	4.66
2	-0.07	0.00	-8.87	0.12	-5.01	1.01	-55.75	4.44
3	-0.15	0.01	-13.26	0.19	-7.44	1.19	-65.49	3.52
4	-0.26	0.01	-17.42	0.23	-9.34	1.25	-71.05	2.75
5	-0.39	0.01	-21.62	0.28	-10.66	1.23	-75.06	2.30
6	-0.54	0.02	-25.64	0.34	-11.70	1.20	-78.42	2.07
7	-0.72	0.02	-29.51	0.38	-12.45	1.15	-81.33	1.98
8	-0.91	0.03	-33.18	0.44	-13.00	1.10	-84.69	2.11
9	-1.09	0.04	-36.72	0.49	-13.42	1.05	-87.57	2.17
10	-1.29	0.05	-40.10	0.56	-13.76	1.05	-91.03	2.43
11	-1.48	0.08	-43.39	0.61	-14.01	1.07	-94.68	2.57
12	-1.66	0.12	-46.71	0.56	-14.28	1.08	-98.04	2.07
13	-1.90	0.12	-49.70	0.28	-14.41	1.02	-99.03	2.01
14	-2.00	0.05	-52.30	0.31	-13.94	0.88	-103.14	1.46
15	-2.15	0.07	-55.20	0.28	-13.95	0.74	-108.38	3.08
16	-2.27	0.07	-58.41	0.59	-13.94	0.53	-113.55	3.08
17	-2.43	0.05	-62.00	0.61	-14.09	0.41	-118.62	3.28
18	-2.65	0.01	-65.06	0.62	-14.04	0.55	-121.61	4.59
19	-2.86	0.10	-68.10	1.03	-14.06	0.75	-126.13	3.46
20	-2.99	0.07	-71.24	1.48	-14.01	0.57	-131.20	3.67
21	-3.09	0.22	-74.45	0.52	-13.83	0.48	-136.35	3.00
22	-3.40	0.18	-78.23	0.25	-14.12	0.61	-140.23	2.86
23	-3.61	0.15	-82.35	0.07	-13.82	0.46	-146.49	4.37
24	-3.76	0.03	-85.66	0.33	-13.69	0.37	-150.37	3.20
25	-4.59	0.60	-85.72	1.83	-13.63	0.28	-155.16	3.29
26	-4.12	0.16	-88.68	1.62	-13.21	0.18	-159.58	3.45
					Actuation Voltage		51.67	7.64

Wafer: MEMS-3C B-700-20 S21 (3 / 4)

	OFF - 0V				On			
Freq-GHz	S21-dB	St. Dev.	S21-pha	St. Dev.	S21-dB	St. Dev.	S21-pha	St. Dev.
1	-24.96	0.10	82.75	0.39	-4.79	1.04	48.75	4.88
2	-18.76	0.11	74.69	0.05	-1.94	0.52	25.58	4.78
3	-15.36	0.10	67.40	0.15	-1.15	0.29	11.96	3.88
4	-12.88	0.12	59.95	0.14	-0.83	0.19	2.69	3.16
5	-11.09	0.11	52.00	0.17	-0.69	0.13	-4.78	2.62
6	-9.75	0.11	44.33	0.14	-0.63	0.11	-10.93	2.23
7	-8.63	0.11	37.27	0.14	-0.59	0.09	-16.43	1.93
8	-7.67	0.11	30.30	0.16	-0.56	0.07	-21.53	1.69
9	-6.91	0.12	23.14	0.19	-0.55	0.07	-26.32	1.49
10	-6.37	0.14	16.76	0.33	-0.53	0.07	-30.85	1.38
11	-5.84	0.16	10.32	0.65	-0.51	0.08	-35.30	1.34
12	-5.37	0.17	4.42	1.06	-0.48	0.06	-39.79	1.36
13	-4.95	0.10	-2.15	1.33	-0.51	0.06	-44.45	1.27
14	-4.70	0.14	-8.13	0.76	-0.55	0.02	-48.22	1.31
15	-4.46	0.12	-13.00	0.70	-0.51	0.03	-52.47	1.23
16	-4.20	0.03	-17.96	0.95	-0.48	0.04	-56.75	0.91
17	-3.92	0.05	-23.47	0.45	-0.47	0.02	-61.05	0.58
18	-3.68	0.03	-28.79	0.50	-0.49	0.07	-65.60	0.70
19	-3.50	0.13	-34.74	0.89	-0.55	0.05	-69.69	1.00
20	-3.43	0.19	-39.15	0.09	-0.51	0.05	-73.30	0.76
21	-3.23	0.04	-43.75	1.20	-0.50	0.05	-77.71	0.75
22	-3.09	0.05	-49.94	0.98	-0.63	0.02	-81.49	0.80
23	-3.00	0.05	-54.27	0.64	-0.60	0.05	-85.12	0.67
24	-2.80	0.03	-59.18	0.66	-0.60	0.03	-89.76	0.56
25	-3.12	0.37	-64.05	0.41	-0.82	0.10	-92.76	1.00
26	-2.93	0.06	-67.73	1.08	-0.74	0.02	-96.20	0.61
					Actuation Voltage		51.67	7.64

Wafer: MEMS-3C B-700-20 S22 (3 / 4)

Freq-GHz	S22-dB	St. Dev.	S22-pha	St. Dev.
1	-0.03	0.01	-10.76	0.14
2	-0.08	0.01	-21.09	0.18
3	-0.20	0.02	-31.60	0.28
4	-0.33	0.02	-41.57	0.23
5	-0.49	0.03	-51.74	0.29
6	-0.70	0.04	-61.46	0.28
7	-0.91	0.04	-70.96	0.28
8	-1.15	0.04	-80.15	0.28
9	-1.39	0.04	-89.01	0.33
10	-1.63	0.06	-97.53	0.40
11	-1.86	0.10	-105.71	0.52
12	-2.04	0.15	-114.09	0.64
13	-2.39	0.16	-122.58	0.62
14	-2.70	0.10	-129.02	1.11
15	-2.87	0.10	-136.21	1.15
16	-3.00	0.17	-143.28	0.43
17	-3.16	0.09	-150.96	0.62
18	-3.48	0.12	-158.16	0.37
19	-3.78	0.14	-164.81	0.53
20	-3.84	0.05	-171.28	0.99
21	-3.87	0.18	-177.51	0.66
22	-4.30	0.16	-175.67	0.28
23	-4.45	0.11	-169.98	0.78
24	-4.51	0.11	-163.37	0.69
25	-4.89	0.22	-158.03	2.04
26	-5.18	0.17	-154.36	0.97

On

S22-dB	St. Dev.	S22-pha	St. Dev.
-2.00	0.54	-43.29	4.65
-5.12	1.03	-68.05	4.42
-7.68	1.22	-83.36	3.37
-9.66	1.28	-93.92	2.46
-11.15	1.27	-102.29	1.73
-12.28	1.23	-109.06	1.03
-13.13	1.17	-115.30	0.56
-13.78	1.09	-120.56	0.14
-14.23	1.02	-125.56	0.20
-14.52	0.94	-130.70	0.42
-14.75	0.89	-135.52	0.90
-14.96	0.91	-140.59	1.58
-15.30	0.83	-144.21	1.27
-15.12	0.91	-147.09	1.80
-15.08	0.80	-151.93	2.34
-15.00	0.64	-156.62	3.25
-15.12	0.34	-160.93	2.79
-15.16	0.32	-163.47	1.11
-15.00	0.52	-166.42	2.58
-14.80	0.41	-172.09	1.03
-14.56	0.37	-176.68	2.89
-14.46	0.34	-177.83	1.27
-14.18	0.29	-176.85	1.08
-14.02	0.28	-170.75	2.07
-14.33	0.30	-167.83	1.17
-13.53	0.38	-166.98	1.80
Actuation Voltage		51.67	7.64

Wafer: MEMS-4 B-600 S11 (3 / 6)

	Off - 0V				On - 20V			
Freq-GHz	S11-dB	Stn. Dev.	S11-pha	Stn. Dev.	S11-dB	Stn. Dev.	S11-pha	Stn. Dev
1	-0.04	0.01	-5.30	0.09	-1.49	0.18	-27.48	9.53
2	-0.09	0.01	-10.35	0.27	-3.40	1.42	-44.94	12.26
3	-0.19	0.00	-15.38	0.47	-5.20	2.26	-55.54	11.98
4	-0.30	0.02	-20.25	0.64	-6.62	2.96	-63.53	9.15
5	-0.44	0.06	-25.08	0.77	-7.81	3.26	-69.76	6.28
6	-0.60	0.11	-29.76	0.82	-8.70	3.57	-75.34	3.20
7	-0.78	0.16	-34.46	0.58	-9.54	3.59	-81.69	1.71
8	-0.99	0.18	-39.01	0.31	-10.44	3.24	-86.75	5.04
9	-1.23	0.19	-43.25	0.08	-11.19	2.89	-90.70	6.96
10	-1.46	0.19	-47.35	0.20	-11.80	2.55	-94.46	8.47
11	-1.72	0.19	-51.25	0.51	-12.30	2.19	-98.22	9.47
12	-1.96	0.17	-54.85	0.85	-12.69	1.79	-101.91	10.16
13	-2.18	0.12	-58.34	1.16	-13.08	1.45	-106.03	10.12
14	-2.38	0.07	-61.82	1.34	-13.41	1.15	-110.28	10.11
15	-2.60	0.04	-65.43	1.34	-13.81	0.96	-114.43	9.95
16	-2.81	0.01	-68.84	1.46	-14.16	0.58	-117.87	10.40
17	-3.00	0.05	-72.28	1.64	-14.39	0.29	-121.56	9.94
18	-3.21	0.10	-75.67	1.71	-14.68	0.00	-124.70	9.28
19	-3.43	0.15	-79.38	1.55	-14.81	0.17	-129.09	8.50
20	-3.66	0.18	-82.67	1.37	-15.05	0.17	-132.54	9.17
21	-3.83	0.25	-86.16	1.74	-15.25	0.92	-137.63	10.56
22	-4.07	0.32	-89.43	1.92	-15.42	1.32	-141.12	8.27
23	-4.35	0.50	-93.71	1.57	-15.60	1.56	-144.37	3.11
24	-4.71	0.30	-96.47	0.29	-15.31	0.74	-149.41	4.77
25	-4.87	0.33	-98.90	3.25	-15.31	1.35	-154.84	7.36
26	-5.13	0.94	-102.29	2.35	-15.97	1.80	-162.02	7.81

Wafer: MEMS-4 B-600 S21 (3 / 6)

	Off - 0V				On - 20V			
Freq-GHz	S21-dB	Stn. Dev.	S21-pha	Stn. Dev.	S21-dB	Stn. Dev.	S21-pha	Stn. Dev
1	-24.92	0.66	78.79	5.33	-7.71	3.18	49.22	3.32
2	-18.85	0.97	72.29	2.71	-4.16	2.61	32.84	6.63
3	-15.65	1.16	65.05	2.06	-2.92	2.12	19.69	8.19
4	-13.24	1.29	58.63	0.34	-2.25	1.70	11.02	9.54
5	-11.53	1.33	51.25	0.85	-1.84	1.35	3.11	9.39
6	-10.22	1.39	44.57	2.29	-1.62	1.15	-3.24	9.45
7	-9.05	1.28	38.54	4.33	-1.36	0.86	-8.79	9.63
8	-8.01	1.09	31.92	5.17	-1.16	0.62	-14.60	8.80
9	-7.19	0.94	24.94	5.59	-1.05	0.49	-20.16	7.95
10	-6.55	0.80	18.35	5.87	-0.99	0.41	-25.19	7.27
11	-5.99	0.69	11.73	6.16	-0.93	0.34	-30.15	6.75
12	-5.55	0.54	5.49	6.28	-0.89	0.28	-34.79	6.27
13	-5.19	0.42	-0.23	5.88	-0.84	0.25	-39.28	5.74
14	-4.80	0.33	-5.85	5.65	-0.77	0.23	-43.87	5.41
15	-4.47	0.31	-11.08	5.37	-0.73	0.23	-48.19	5.14
16	-4.16	0.25	-16.52	5.25	-0.69	0.21	-52.65	5.02
17	-3.91	0.19	-22.36	5.11	-0.70	0.18	-57.31	4.72
18	-3.69	0.15	-27.33	4.86	-0.69	0.16	-61.46	4.53
19	-3.44	0.12	-32.89	4.79	-0.69	0.15	-65.90	4.29
20	-3.33	0.09	-38.43	4.71	-0.74	0.15	-70.39	4.37
21	-3.12	0.04	-43.22	4.53	-0.74	0.07	-74.38	3.99
22	-2.99	0.14	-49.19	4.00	-0.76	0.06	-78.79	3.64
23	-2.88	0.15	-54.59	2.45	-0.80	0.16	-83.05	3.32
24	-2.83	0.05	-59.31	3.46	-0.81	0.06	-86.81	4.26
25	-2.73	0.20	-64.17	3.13	-0.84	0.02	-90.91	3.16
26	-2.66	0.12	-68.58	1.28	-0.83	0.10	-95.14	2.84

Wafer: MEMS-4 B-600 S22 (3 / 6)

	Off - 0V				On - 20V			
Freq-GHz	S22-dB	Stn. Dev.	S22-pha	Stn. Dev.	S22-dB	Stn. Dev.	S22-pha	Stn. Dev
1	-0.12	0.11	-10.25	0.63	-1.71	0.09	-31.14	11.95
2	-0.21	0.14	-19.57	1.83	-3.70	1.16	-51.11	18.03
3	-0.40	0.20	-29.00	3.18	-5.68	1.91	-64.06	21.23
4	-0.59	0.21	-37.54	4.87	-7.25	2.63	-73.34	22.91
5	-0.78	0.19	-46.56	6.16	-8.57	3.06	-81.48	22.87
6	-1.03	0.18	-54.95	7.73	-9.65	3.39	-87.81	23.40
7	-1.22	0.05	-63.04	9.29	-10.48	3.72	-94.19	22.52
8	-1.42	0.08	-71.43	10.03	-11.31	3.77	-100.38	21.19
9	-1.66	0.17	-79.63	10.50	-12.04	3.71	-105.56	20.15
10	-1.94	0.24	-87.58	10.89	-12.70	3.59	-110.40	19.63
11	-2.23	0.31	-95.21	11.14	-13.21	3.46	-114.69	18.71
12	-2.51	0.35	-102.47	11.02	-13.62	3.19	-118.94	17.88
13	-2.75	0.34	-109.62	10.83	-14.02	2.94	-123.63	17.77
14	-2.97	0.27	-116.64	10.81	-14.33	2.60	-128.35	18.20
15	-3.21	0.22	-123.79	11.08	-14.73	2.43	-132.48	18.64
16	-3.43	0.19	-130.89	11.59	-15.07	2.30	-136.36	19.59
17	-3.66	0.19	-138.05	11.64	-15.38	2.18	-140.37	19.39
18	-3.91	0.21	-145.14	11.63	-15.55	2.03	-144.14	18.49
19	-4.20	0.18	-152.12	11.20	-15.67	1.66	-147.39	18.48
20	-4.50	0.11	-159.28	11.52	-16.16	1.67	-151.80	19.39
21	-4.79	0.14	-165.46	10.98	-16.02	1.37	-153.95	17.95
22	-5.08	0.04	-171.69	10.02	-16.02	1.02	-158.11	17.84
23	-5.37	0.40	-172.76	1.57	-16.04	1.05	-163.28	21.64
24	-5.62	0.06	-171.06	6.70	-16.24	1.38	-168.18	16.64
25	-6.00	0.06	-168.86	10.17	-16.38	0.86	-169.07	14.38
26	-6.03	0.58	-162.85	9.89	-15.95	0.25	-167.02	8.64

Wafer: MEMS-4 B-600-20 S11 (2 / 6)

	Off - 0V				On - 20V			
Freq-GHz	S11-dB	St. Dev.	S11-pha	St. Dev.	S11-dB	St. Dev.	S11-pha	St. Dev.
1	-0.04	0.01	-5.46	0.02	-1.70	0.19	-30.52	3.64
2	-0.12	0.02	-10.68	0.15	-4.27	0.71	-45.86	8.43
3	-0.25	0.00	-15.83	0.40	-6.59	1.99	-51.45	5.97
4	-0.44	0.09	-20.53	0.54	-7.56	2.46	-47.52	8.00
5	-0.57	0.13	-24.35	0.55	-6.43	0.28	-52.61	11.98
6	-0.58	0.01	-28.93	0.68	-6.34	0.38	-67.58	4.83
7	-0.69	0.03	-34.04	0.45	-7.29	0.25	-80.87	1.43
8	-0.88	0.04	-38.96	0.29	-8.47	0.13	-89.99	0.03
9	-1.10	0.04	-43.59	0.19	-9.57	0.01	-96.58	0.84
10	-1.35	0.04	-48.04	0.11	-10.51	0.11	-101.89	1.06
11	-1.62	0.03	-52.24	0.06	-11.32	0.18	-106.66	0.92
12	-1.89	0.02	-56.18	0.09	-12.01	0.24	-110.77	0.47
13	-2.15	0.01	-59.81	0.17	-12.63	0.27	-114.96	0.08
14	-2.39	0.01	-63.39	0.34	-13.14	0.26	-118.97	0.86
15	-2.64	0.02	-67.13	0.36	-13.71	0.22	-123.25	1.50
16	-2.89	0.02	-70.56	0.51	-14.21	0.16	-126.41	2.12
17	-3.12	0.03	-74.01	0.60	-14.58	0.05	-129.95	3.02
18	-3.35	0.02	-77.39	0.88	-15.00	0.05	-133.07	3.79
19	-3.59	0.05	-81.10	1.08	-15.21	0.05	-137.06	4.01
20	-3.85	0.08	-84.51	1.22	-15.75	0.18	-140.60	5.57
21	-4.10	0.12	-87.89	1.40	-15.94	0.51	-143.78	6.21
22	-4.40	0.13	-90.78	2.10	-16.11	0.58	-145.84	6.41
23	-4.55	0.23	-93.60	1.83	-15.55	0.81	-149.70	5.48
24	-4.86	0.24	-97.93	3.01	-16.24	0.90	-156.26	9.88
25	-5.18	0.51	-99.98	4.00	-16.00	1.68	-159.25	7.13
26	-5.24	0.92	-102.30	0.95	-15.87	1.62	-165.00	1.22

Wafer: MEMS-4 B-600-20 S21 (2 / 6)

	Off - 0V				On - 20V			
Freq-GHz	S21-dB	St. Dev.	S21-pha	St. Dev.	S21-dB	St. Dev.	S21-pha	St. Dev.
1	-24.24	0.09	80.63	2.46	-6.38	0.96	65.40	19.08
2	-18.08	0.46	70.77	3.01	-3.43	1.51	47.16	30.38
3	-14.82	0.91	61.45	1.86	-2.62	1.39	33.85	37.17
4	-12.55	1.36	50.52	3.09	-2.71	0.90	22.66	42.48
5	-12.06	0.26	39.64	9.89	-3.52	0.65	18.02	40.46
6	-11.52	0.54	40.35	3.55	-3.15	0.68	20.19	32.06
7	-10.06	0.28	38.63	0.66	-2.23	0.22	17.11	31.09
8	-8.75	0.11	33.45	0.03	-1.67	0.03	11.27	31.33
9	-7.72	0.01	27.05	0.20	-1.37	0.06	4.91	31.12
10	-6.93	0.09	20.68	0.11	-1.21	0.11	-1.09	30.68
11	-6.26	0.14	14.14	0.11	-1.08	0.14	-7.00	30.01
12	-5.73	0.16	7.81	0.34	-1.00	0.14	-12.63	29.26
13	-5.29	0.17	1.93	0.55	-0.93	0.15	-17.90	28.61
14	-4.85	0.18	-3.90	0.70	-0.85	0.14	-23.18	27.98
15	-4.49	0.17	-9.33	0.82	-0.81	0.14	-28.10	27.36
16	-4.14	0.18	-14.93	0.93	-0.76	0.14	-33.16	26.71
17	-3.86	0.16	-20.97	1.07	-0.76	0.13	-38.53	25.91
18	-3.63	0.16	-26.09	1.28	-0.75	0.12	-43.14	25.38
19	-3.38	0.12	-31.91	1.54	-0.74	0.13	-48.20	24.57
20	-3.23	0.08	-37.39	1.58	-0.79	0.13	-53.24	23.98
21	-3.00	0.07	-42.55	1.45	-0.79	0.09	-57.93	23.20
22	-2.86	0.03	-49.16	1.58	-0.82	0.10	-63.51	21.87
23	-2.96	0.01	-53.98	1.51	-0.85	0.07	-67.70	20.91
24	-2.62	0.01	-58.96	2.00	-0.84	0.06	-72.59	21.26
25	-2.68	0.21	-65.48	1.91	-0.94	0.00	-77.82	19.36
26	-3.08	0.19	-69.06	0.08	-1.09	0.01	-81.67	17.74

Wafer: MEMS-4 B-600-20 S22 (2 / 6)

	Off - 0V				On - 20V			
Freq-GHz	S22-dB	St. Dev.	S22-pha	St. Dev.	S22-dB	St. Dev.	S22-pha	St. Dev.
1	-0.08	0.05	-10.77	0.10	-1.90	0.39	-24.72	19.82
2	-0.26	0.14	-20.87	1.03	-4.87	0.33	-42.36	31.43
3	-0.60	0.19	-31.39	2.77	-8.06	2.00	-54.47	35.40
4	-1.31	0.17	-41.40	6.73	-12.33	6.30	-51.42	20.90
5	-2.37	1.26	-44.66	1.99	-9.91	2.29	-34.71	12.08
6	-1.98	0.54	-47.59	2.50	-8.60	0.23	-48.93	0.60
7	-1.69	0.18	-55.65	1.42	-8.89	0.10	-62.02	7.60
8	-1.68	0.06	-64.41	0.57	-9.70	0.17	-72.40	10.73
9	-1.81	0.00	-73.06	0.12	-10.55	0.24	-81.11	11.50
10	-2.05	0.05	-81.25	0.74	-11.38	0.32	-88.51	11.00
11	-2.28	0.07	-89.16	1.35	-12.03	0.39	-95.32	10.05
12	-2.53	0.07	-96.83	1.82	-12.61	0.44	-101.93	9.04
13	-2.80	0.07	-104.38	2.21	-13.26	0.48	-108.21	7.63
14	-3.07	0.08	-111.65	2.60	-13.80	0.51	-114.25	6.27
15	-3.35	0.08	-118.71	2.98	-14.29	0.57	-119.59	4.22
16	-3.60	0.07	-125.94	3.41	-14.77	0.63	-125.04	2.13
17	-3.87	0.06	-133.19	3.89	-15.10	0.70	-130.43	0.01
18	-4.16	0.01	-140.45	4.24	-15.33	0.66	-135.70	2.48
19	-4.49	0.01	-147.41	4.02	-15.46	0.52	-141.60	4.19
20	-4.84	0.07	-154.33	4.46	-16.04	0.63	-147.06	5.82
21	-5.11	0.00	-161.49	5.28	-15.94	0.76	-152.09	8.01
22	-5.56	0.04	-168.05	5.30	-15.94	0.85	-157.40	9.76
23	-5.81	0.04	-173.58	5.13	-15.98	0.40	-164.15	8.21
24	-6.27	0.16	-174.84	3.66	-16.64	1.14	-169.43	11.32
25	-7.06	0.55	-172.89	5.47	-16.51	1.16	-170.35	9.08
26	-7.08	0.57	-174.04	1.89	-15.76	1.21	-168.21	10.13

MEMS-4 Swept data B-600-30 (1 / 6)

Off-state 0 V

Die: 07-02-15

Freq-GHz	S11-dB	S11-pha	S21-dB	S21-pha	S22-dB	S22-pha
1	-0.0351	-5.3254	-24.6194	80.9731	-0.0743	-10.6317
2	-0.1092	-10.4192	-18.4525	70.8878	-0.2617	-20.6077
3	-0.2306	-15.3576	-15.2740	61.7578	-0.6027	-30.6150
4	-0.3699	-19.9261	-13.1962	52.6060	-1.1602	-38.9819
5	-0.4866	-24.3390	-12.0431	45.3487	-1.5755	-45.4981
6	-0.5876	-28.8055	-11.0489	40.9434	-1.7602	-51.6087
7	-0.7085	-33.4496	-9.9337	36.8123	-1.8250	-58.6256
8	-0.8699	-38.0872	-8.8724	31.6808	-1.9261	-66.2130
9	-1.0670	-42.5653	-7.9666	25.7149	-2.0723	-74.0647
10	-1.2821	-46.9192	-7.2317	19.7954	-2.3036	-81.7123
11	-1.5218	-51.1297	-6.5933	13.5914	-2.5354	-89.1852
12	-1.7665	-55.0736	-6.0794	7.5316	-2.7719	-96.4178
13	-2.0032	-58.7677	-5.6567	1.9656	-3.0197	-103.6880
14	-2.2173	-62.3922	-5.2060	-3.5652	-3.2749	-110.7315
15	-2.4443	-66.2605	-4.8347	-8.8334	-3.5520	-117.5444
16	-2.6710	-69.7960	-4.4855	-14.2815	-3.7781	-124.5375
17	-2.8831	-73.4564	-4.1956	-20.1059	-4.0368	-131.3501
18	-3.0998	-76.9994	-3.9445	-24.9948	-4.2913	-138.2642
19	-3.3360	-80.9695	-3.6495	-30.7301	-4.6083	-145.2563
20	-3.5784	-84.5137	-3.4971	-35.9226	-4.9633	-152.0944
21	-3.8373	-88.3135	-3.2241	-41.0147	-5.1506	-158.7356
22	-4.1512	-92.0900	-2.9981	-47.5763	-5.6176	-165.4002
23	-4.5827	-95.1040	-3.0847	-53.8120	-6.0841	-169.8187
24	-4.5510	-98.6249	-2.9200	-56.7029	-6.0226	-176.8784
25	-5.0963	-102.8664	-2.6887	-63.5362	-6.6938	-176.1313
26	-5.6066	-104.5983	-3.0008	-69.0678	-6.7363	-175.3507

MEMS-4 Swept data B-600-30 (1 / 6)

On-state 20 V

Die: 07-02-15

Freq-GHz	S11-dB	S11-pha	S21-dB	S21-pha	S22-dB	S22-pha
1	-1.6642	-30.4502	-6.3981	49.8521	-1.8438	-35.7071
2	-4.2169	-44.6434	-3.5123	26.5205	-4.9314	-53.6768
3	-6.0654	-50.6677	-2.7731	12.6705	-7.5824	-62.1872
4	-6.9153	-53.4914	-2.7054	4.0286	-9.5714	-62.0108
5	-7.1498	-59.7527	-2.6699	-0.8346	-10.0046	-62.4230
6	-7.4993	-68.5100	-2.4207	-4.4824	-10.1825	-67.5610
7	-8.2009	-78.0241	-2.0264	-8.8873	-10.5754	-74.7736
8	-9.0038	-85.9564	-1.7081	-13.8375	-11.1448	-81.9016
9	-9.8124	-92.6578	-1.4750	-19.0503	-11.7593	-88.2935
10	-10.5603	-98.5421	-1.3292	-24.0564	-12.4328	-93.6737
11	-11.2376	-103.8855	-1.2093	-28.9988	-12.9739	-98.4542
12	-11.8338	-108.8123	-1.1208	-33.7546	-13.4670	-103.3061
13	-12.3840	-113.7152	-1.0544	-38.3191	-14.0312	-108.2625
14	-12.8517	-118.6103	-0.9720	-42.9766	-14.5342	-112.5451
15	-13.3667	-123.5974	-0.9248	-47.3070	-15.0134	-115.4045
16	-13.8342	-127.7460	-0.8734	-51.7792	-15.4256	-118.4854
17	-14.2261	-132.2498	-0.8629	-56.4524	-15.6777	-121.5859
18	-14.7007	-136.2764	-0.8509	-60.6637	-15.8804	-124.9653
19	-14.9084	-140.6576	-0.8491	-65.1270	-15.9627	-128.1520
20	-15.3275	-145.8476	-0.8921	-69.4886	-16.4926	-130.5039
21	-15.8032	-150.6882	-0.8651	-73.7243	-16.2355	-134.7916
22	-16.1075	-152.9841	-0.9147	-78.2439	-16.0653	-137.6252
23	-16.0159	-153.6055	-1.0120	-81.9819	-15.7861	-142.9240
24	-15.7619	-165.3526	-0.8896	-85.8665	-16.3179	-149.4386
25	-16.4701	-168.9168	-0.9396	-90.5670	-16.3667	-151.1376
26	-16.7239	-171.1513	-1.1011	-94.0087	-15.1958	-157.5921

Wafer: MEMS-4 B-600-40 S11 (4 / 6)

	Off - 0V				On - 20V			
Freq-GHz	S11-dB	St. Dev.	S11-pha	St. Dev.	S11-dB	St. Dev.	S11-pha	St. Dev.
1	-0.04	0.01	-5.51	0.04	-1.21	0.27	-30.16	5.49
2	-0.11	0.01	-10.77	0.20	-3.17	0.04	-45.96	8.22
3	-0.23	0.00	-15.94	0.39	-4.83	0.29	-49.48	0.12
4	-0.36	0.02	-20.22	0.41	-5.94	0.45	-52.72	5.91
5	-0.50	0.04	-25.24	0.10	-6.79	0.43	-66.87	3.76
6	-0.66	0.06	-30.14	0.23	-7.58	0.48	-75.30	6.31
7	-0.84	0.08	-34.87	0.42	-8.29	0.58	-81.78	6.00
8	-1.03	0.10	-39.48	0.47	-8.98	0.65	-87.29	4.67
9	-1.23	0.13	-43.92	0.41	-9.64	0.67	-92.31	2.98
10	-1.46	0.15	-48.23	0.30	-10.25	0.65	-96.96	1.29
11	-1.70	0.16	-52.36	0.08	-10.82	0.60	-101.35	0.26
12	-1.95	0.16	-56.18	0.25	-11.30	0.50	-105.43	1.57
13	-2.18	0.14	-59.84	0.46	-11.77	0.40	-109.74	2.52
14	-2.39	0.12	-63.44	0.62	-12.18	0.32	-114.07	3.16
15	-2.61	0.10	-67.15	0.72	-12.60	0.25	-118.29	3.80
16	-2.83	0.08	-70.72	0.83	-13.02	0.15	-122.13	4.50
17	-3.03	0.08	-74.28	0.99	-13.37	0.11	-125.92	4.87
18	-3.26	0.06	-77.90	1.17	-13.71	0.02	-129.61	5.00
19	-3.50	0.04	-81.79	1.12	-14.01	0.07	-133.55	5.45
20	-3.75	0.00	-84.89	1.21	-14.09	0.24	-137.00	5.47
21	-3.99	0.04	-88.79	0.71	-14.39	0.52	-142.48	4.76
22	-4.15	0.10	-92.11	0.81	-14.73	0.62	-144.32	6.43
23	-4.56	0.08	-96.33	0.13	-14.78	0.57	-146.31	2.66
24	-4.76	0.06	-99.84	0.80	-14.53	0.46	-153.55	2.13
25	-5.18	0.19	-104.07	2.26	-14.87	0.15	-163.70	3.01
26	-5.28	0.23	-105.47	1.19	-15.06	0.75	-168.80	0.56

Wafer: MEMS-4 B-600-40 S21 (4 / 6)

	Off - 0V				On - 20V			
Freq-GHz	S21-dB	St. Dev.	S21-pha	St. Dev.	S21-dB	St. Dev.	S21-pha	St. Dev.
1	-24.12	0.13	80.65	1.79	-7.62	0.09	50.96	0.65
2	-18.06	0.43	71.06	1.77	-4.16	0.60	27.96	5.59
3	-14.93	0.54	60.90	1.46	-3.04	0.54	12.41	10.06
4	-12.75	0.56	51.55	5.02	-2.56	0.41	7.32	5.55
5	-11.21	0.53	49.25	1.58	-2.19	0.31	4.25	0.11
6	-9.98	0.54	43.35	2.11	-1.92	0.30	-2.63	0.92
7	-8.93	0.54	37.06	1.44	-1.69	0.30	-8.79	1.97
8	-8.02	0.53	30.63	0.52	-1.51	0.27	-14.44	2.60
9	-7.25	0.50	24.09	0.32	-1.35	0.22	-19.78	2.95
10	-6.61	0.45	17.84	1.00	-1.24	0.18	-24.78	3.10
11	-6.04	0.39	11.45	1.58	-1.15	0.15	-29.68	3.14
12	-5.58	0.32	5.36	1.95	-1.07	0.12	-34.38	3.06
13	-5.20	0.25	-0.41	2.24	-1.00	0.10	-38.92	2.94
14	-4.79	0.21	-5.98	2.33	-0.91	0.08	-43.53	2.85
15	-4.46	0.18	-11.23	2.30	-0.86	0.08	-47.91	2.76
16	-4.13	0.14	-16.67	2.42	-0.80	0.06	-52.38	2.74
17	-3.86	0.11	-22.51	2.46	-0.80	0.05	-57.10	2.70
18	-3.62	0.07	-27.45	2.38	-0.80	0.06	-61.32	2.61
19	-3.34	0.05	-33.19	2.39	-0.80	0.04	-65.84	2.71
20	-3.31	0.00	-38.69	2.09	-0.87	0.01	-69.81	2.62
21	-3.11	0.04	-43.61	2.22	-0.82	0.02	-74.25	2.92
22	-2.90	0.07	-49.85	3.02	-0.80	0.03	-78.86	2.40
23	-2.83	0.06	-55.71	2.03	-0.99	0.03	-83.14	2.34
24	-2.77	0.11	-59.96	2.49	-0.95	0.07	-86.77	2.67
25	-2.64	0.10	-63.89	0.40	-0.94	0.13	-90.55	1.92
26	-2.68	0.24	-67.74	1.16	-0.92	0.11	-94.21	1.25

Wafer: MEMS-4 B-600-40 S22 (4 / 6)

	Off - 0V				On - 20V			
Freq-GHz	S22-dB	St. Dev.	S22-pha	St. Dev.	S22-dB	St. Dev.	S22-pha	St. Dev.
1	-0.08	0.04	-10.80	0.12	-1.37	0.42	-35.34	6.04
2	-0.25	0.10	-20.92	1.03	-3.67	0.31	-55.57	12.32
3	-0.54	0.12	-31.38	2.60	-5.80	0.03	-63.00	7.99
4	-0.89	0.11	-37.02	0.79	-7.46	0.27	-54.48	13.22
5	-1.15	0.10	-44.95	1.10	-8.52	0.28	-70.15	0.32
6	-1.43	0.13	-53.80	0.50	-9.47	0.23	-80.08	5.82
7	-1.68	0.13	-62.15	1.95	-10.27	0.27	-87.01	8.63
8	-1.92	0.11	-70.24	3.07	-10.98	0.35	-92.95	9.74
9	-2.15	0.08	-78.23	3.95	-11.59	0.41	-98.31	10.01
10	-2.41	0.04	-86.01	4.54	-12.20	0.43	-103.36	9.94
11	-2.67	0.00	-93.57	5.04	-12.71	0.42	-107.96	9.68
12	-2.93	0.03	-100.93	5.31	-13.17	0.37	-112.78	9.53
13	-3.16	0.03	-108.09	5.23	-13.63	0.26	-117.42	8.82
14	-3.39	0.00	-115.18	5.27	-14.07	0.13	-122.24	9.11
15	-3.64	0.04	-122.38	5.42	-14.56	0.04	-126.07	9.18
16	-3.87	0.05	-129.32	5.63	-14.99	0.02	-129.28	9.51
17	-4.13	0.08	-136.43	5.63	-15.34	0.01	-132.68	10.36
18	-4.41	0.12	-143.61	5.56	-15.62	0.07	-136.17	10.47
19	-4.75	0.10	-150.34	6.21	-15.80	0.18	-137.96	10.95
20	-5.01	0.11	-156.49	6.37	-15.62	0.22	-142.87	10.10
21	-5.20	0.01	-163.40	6.67	-15.60	0.04	-148.20	8.25
22	-5.43	0.10	-170.44	4.73	-16.35	0.19	-151.71	6.28
23	-6.24	0.23	-176.08	4.59	-16.20	0.07	-150.76	11.20
24	-6.24	0.20	-176.64	3.48	-16.13	0.11	-159.35	10.75
25	-6.60	0.11	-170.62	5.67	-16.47	0.21	-164.56	10.03
26	-6.28	0.11	-164.46	3.10	-16.61	0.35	-171.06	3.82

Wafer: MEMS-4 B-700

No data

Wafer: MEMS-4 B-700-20 (3/6)

	Off-state				On-state 20 V			
Freq-GHz	S11-dB	Stn. Dev.	S11-pha	Stn. Dev.	S11-dB	Stn. Dev.	S11-pha	Stn. Dev
1	-0.05	4.03	-5.83	0.08	-2.09	19.57	-32.59	4.31
2	-0.14	7.72	-11.35	0.39	-4.76	26.24	-48.07	7.82
3	-0.30	11.25	-16.76	0.77	-7.08	30.53	-53.09	1.75
4	-0.54	14.54	-21.49	0.51	-7.62	36.64	-49.98	15.10
5	-0.62	18.03	-25.51	0.80	-6.83	44.02	-60.02	12.10
6	-0.69	21.39	-30.70	0.35	-7.36	48.77	-73.49	3.13
7	-0.88	24.66	-35.91	0.01	-8.30	53.58	-83.95	0.24
8	-1.12	27.85	-40.81	0.26	-9.27	58.13	-91.89	0.62
9	-1.39	30.93	-45.35	0.48	-10.16	62.13	-98.33	0.25
10	-1.67	33.90	-49.71	0.63	-10.93	65.80	-103.84	0.55
11	-1.97	36.72	-53.84	0.65	-11.61	69.22	-108.71	1.54
12	-2.26	39.37	-57.63	0.59	-12.20	72.33	-113.00	2.56
13	-2.54	41.85	-61.25	0.44	-12.70	75.61	-117.38	3.60
14	-2.80	44.28	-64.74	0.32	-13.10	78.63	-121.55	4.27
15	-3.07	46.80	-68.35	0.25	-13.53	81.75	-125.76	5.13
16	-3.33	49.11	-71.75	0.20	-13.90	84.31	-129.32	5.67
17	-3.58	51.51	-75.09	0.07	-14.22	87.14	-133.01	6.51
18	-3.85	53.87	-78.41	0.06	-14.58	89.62	-136.44	6.99
19	-4.12	56.22	-82.00	0.23	-14.82	91.97	-139.84	7.23
20	-4.31	58.53	-84.90	0.64	-14.75	94.60	-143.03	7.81
21	-4.57	60.79	-88.40	0.58	-15.08	98.21	-147.51	8.92
22	-4.87	63.23	-91.63	0.86	-15.21	99.51	-150.11	7.95
23	-5.10	65.56	-94.80	0.80	-15.00	103.85	-154.90	9.49
24	-5.47	68.15	-98.26	2.20	-15.24	106.95	-158.88	10.01
25	-5.84	70.07	-100.90	2.82	-15.24	109.19	-161.84	10.23
26	-5.83	70.74	-104.51	0.49	-14.98	110.29	-167.65	3.86

Wafer: MEMS-4 B-700-20 (3/6)

Off-state					On-state 20 V			
Freq-GHz	S21-dB	Stn. Dev.	S21-pha	Stn. Dev.	S21-dB	Stn. Dev.	S21-pha	Stn. Dev
1	-22.96	70.61	78.38	4.14	-7.25	32.44	49.55	0.86
2	-17.01	59.64	69.22	2.75	-4.08	19.50	29.52	9.94
3	-13.76	51.54	59.64	0.10	-3.09	11.65	14.85	14.21
4	-11.61	45.42	48.21	7.86	-3.08	7.40	4.46	18.71
5	-11.32	41.23	40.86	9.04	-3.46	3.67	2.65	11.00
6	-10.08	35.82	40.35	1.34	-2.64	1.22	0.90	4.34
7	-8.70	30.69	35.82	0.09	-1.99	5.35	-4.70	3.75
8	-7.57	25.77	29.69	0.00	-1.60	9.25	-10.78	3.94
9	-6.68	20.70	22.99	0.33	-1.37	13.08	-16.66	4.09
10	-5.98	15.94	16.50	0.77	-1.23	16.65	-22.02	4.18
11	-5.39	11.10	9.92	1.10	-1.11	20.19	-27.24	4.20
12	-4.91	6.49	3.69	1.46	-1.02	23.56	-32.16	4.10
13	-4.53	2.16	-2.28	1.59	-0.95	26.83	-36.93	4.00
14	-4.13	2.15	-8.10	1.72	-0.87	30.17	-41.70	3.90
15	-3.80	6.15	-13.51	1.75	-0.81	33.25	-46.17	3.77
16	-3.50	10.29	-19.11	1.83	-0.76	36.43	-50.74	3.73
17	-3.26	14.64	-25.03	1.90	-0.75	39.73	-55.55	3.58
18	-3.04	18.37	-30.23	1.94	-0.74	42.70	-59.82	3.45
19	-2.81	22.70	-36.16	2.23	-0.74	45.90	-64.51	3.35
20	-2.81	26.30	-41.25	2.16	-0.82	48.65	-68.47	3.30
21	-2.55	30.09	-46.23	1.99	-0.73	51.72	-72.86	3.31
22	-2.41	34.51	-52.44	1.77	-0.78	54.88	-77.60	3.07
23	-2.43	37.73	-57.31	1.78	-0.79	57.69	-81.36	3.02
24	-2.22	41.99	-62.94	1.99	-0.82	60.78	-86.06	2.97
25	-2.28	46.18	-69.29	1.57	-0.93	63.68	-90.66	2.80
26	-2.33	48.80	-71.40	0.65	-0.91	65.87	-93.64	2.30

Wafer: MEMS-4 B-700-20 (3/6)

Off-state					On-state 20 V			
Freq-GHz	S22-dB	Stn. Dev.	S22-pha	Stn. Dev.	S22-dB	Stn. Dev.	S22-pha	Stn. Dev
1	-0.12	8.13	-11.70	0.37	-1.78	22.52	-33.91	11.48
2	-0.31	14.94	-22.39	2.08	-4.41	28.83	-53.98	20.05
3	-0.67	21.52	-33.64	4.59	-7.53	31.98	-65.69	21.40
4	-1.53	26.24	-44.15	8.32	-11.04	31.88	-54.27	5.75
5	-2.11	31.68	-45.94	1.42	-8.22	41.18	-52.81	20.41
6	-1.75	38.00	-53.34	2.54	-8.11	45.40	-68.42	9.23
7	-1.76	43.44	-62.46	0.85	-8.82	48.65	-79.84	3.09
8	-1.91	48.83	-71.37	0.48	-9.63	52.09	-88.53	0.34
9	-2.11	54.29	-80.10	1.45	-10.37	55.41	-95.68	0.83
10	-2.39	59.61	-88.48	2.15	-11.08	58.39	-101.96	1.24
11	-2.67	64.81	-96.59	2.70	-11.66	61.22	-107.61	1.18
12	-2.97	69.85	-104.46	2.99	-12.21	64.07	-113.13	0.88
13	-3.25	74.98	-112.09	3.23	-12.72	67.15	-118.49	0.67
14	-3.55	79.91	-119.62	3.40	-13.22	69.67	-123.81	0.59
15	-3.86	84.58	-126.98	3.59	-13.72	71.54	-127.89	0.17
16	-4.15	89.41	-134.21	3.87	-14.14	73.18	-131.80	0.11
17	-4.43	94.22	-141.70	4.15	-14.48	75.49	-135.92	0.47
18	-4.76	99.01	-149.00	4.31	-14.80	77.77	-139.86	1.15
19	-5.20	103.51	-156.09	4.04	-15.02	79.62	-142.66	1.95
20	-5.53	108.03	-161.98	3.10	-15.08	82.34	-147.37	0.54
21	-5.66	112.41	-169.45	4.67	-15.24	85.90	-153.88	0.78
22	-6.19	117.05	-176.56	4.48	-15.51	88.47	-155.98	0.88
23	-6.39	121.68	-176.73	3.55	-15.35	93.32	-163.14	0.60
24	-7.18	128.52	-169.56	5.29	-16.01	94.52	-164.40	0.96
25	-7.93	126.61	-164.49	5.73	-16.36	94.94	-167.37	2.81
26	-7.49	122.80	-160.82	0.54	-15.88	104.56	-173.01	3.88

Wafer: MEMS-4 B-700-30 (4/6)

Off-state

Freq-GHz	S11-dB	Stn. Dev.	S11-pha	Stn. Dev.
1	-0.05	0.01	-5.71	0.04
2	-0.14	0.00	-11.04	0.18
3	-0.28	0.03	-16.19	0.25
4	-0.43	0.07	-21.02	0.09
5	-0.57	0.08	-25.71	0.20
6	-0.71	0.05	-30.39	0.36
7	-0.86	0.03	-35.20	0.38
8	-1.06	0.03	-39.95	0.37
9	-1.29	0.03	-44.48	0.37
10	-1.54	0.03	-48.89	0.43
11	-1.82	0.04	-53.08	0.55
12	-2.10	0.03	-57.00	0.57
13	-2.37	0.03	-60.69	0.68
14	-2.62	0.02	-64.26	0.74
15	-2.88	0.02	-67.94	0.78
16	-3.14	0.03	-71.41	0.93
17	-3.38	0.03	-74.89	0.92
18	-3.66	0.03	-78.30	1.02
19	-3.94	0.06	-81.84	1.38
20	-4.15	0.02	-84.99	1.66
21	-4.43	0.01	-88.03	1.62
22	-4.63	0.04	-91.57	1.92
23	-5.01	0.18	-95.42	1.89
24	-5.29	0.00	-98.72	2.33
25	-5.64	0.16	-101.80	3.12
26	-5.79	0.37	-103.16	2.20

On-state 20 V

S11-dB	Stn. Dev.	S11-pha	Stn. Dev
-2.29	0.14	-31.46	3.14
-4.57	0.68	-44.33	2.66
-6.15	1.00	-51.35	0.96
-6.92	0.84	-57.00	6.09
-7.38	0.21	-64.46	7.46
-7.82	0.15	-73.26	6.13
-8.50	0.23	-82.51	4.81
-9.31	0.20	-90.22	4.09
-10.08	0.14	-96.67	3.84
-10.77	0.11	-102.27	4.02
-11.40	0.09	-107.42	4.21
-11.93	0.09	-112.04	4.47
-12.43	0.09	-116.66	4.55
-12.84	0.11	-121.07	4.85
-13.27	0.08	-125.40	4.90
-13.65	0.09	-129.15	4.99
-14.01	0.11	-132.98	5.11
-14.38	0.11	-136.40	5.40
-14.65	0.10	-140.21	5.26
-14.72	0.07	-143.84	5.36
-15.01	0.02	-146.71	6.20
-15.04	0.36	-150.89	6.29
-15.28	0.13	-153.72	3.77
-15.39	0.06	-159.82	6.66
-15.70	0.18	-163.59	5.90
-15.17	0.17	-166.18	3.68

Off-state

Freq-GHz	S21-dB	Stn. Dev.	S21-pha	Stn. Dev.
1	-23.23	0.17	78.26	2.13
2	-17.40	0.45	68.41	0.63
3	-14.38	0.54	59.58	1.01
4	-12.34	0.41	51.79	3.44
5	-11.02	0.04	44.69	4.00
6	-9.95	0.21	39.47	2.80
7	-8.87	0.24	34.64	1.60
8	-7.86	0.19	29.04	1.07
9	-7.01	0.15	22.76	0.88
10	-6.33	0.14	16.61	0.83
11	-5.73	0.14	10.38	0.73
12	-5.25	0.16	4.39	0.64
13	-4.85	0.16	-1.55	0.74
14	-4.44	0.16	-7.26	0.70
15	-4.10	0.17	-12.50	0.54
16	-3.78	0.17	-17.93	0.36
17	-3.52	0.16	-23.72	0.26
18	-3.29	0.14	-29.07	0.61
19	-3.05	0.16	-34.89	0.53
20	-2.98	0.21	-40.21	0.74
21	-2.82	0.22	-45.32	0.50
22	-2.64	0.29	-50.63	0.23
23	-2.55	0.18	-56.51	0.54
24	-2.36	0.19	-61.02	0.47
25	-2.31	0.25	-66.76	0.81
26	-2.56	0.19	-70.70	0.38

On-state 20 V

S21-dB	Stn. Dev.	S21-pha	Stn. Dev.
-6.01	0.75	42.32	3.37
-3.66	0.75	23.66	2.64
-2.89	0.43	11.97	4.48
-2.64	0.02	4.63	5.45
-2.44	0.39	-0.72	3.70
-2.19	0.44	-4.91	1.60
-1.83	0.33	-9.40	0.52
-1.53	0.25	-14.55	0.18
-1.33	0.19	-19.85	0.16
-1.20	0.16	-24.83	0.18
-1.10	0.15	-29.77	0.19
-1.03	0.14	-34.46	0.21
-0.96	0.14	-39.04	0.17
-0.89	0.13	-43.66	0.21
-0.85	0.13	-48.00	0.17
-0.81	0.13	-52.44	0.16
-0.80	0.14	-57.10	0.12
-0.79	0.15	-61.28	0.11
-0.79	0.13	-65.79	0.12
-0.85	0.09	-69.77	0.11
-0.83	0.14	-73.89	0.32
-0.83	0.16	-78.35	0.35
-0.88	0.05	-82.71	0.10
-0.85	0.15	-86.71	0.13
-0.91	0.12	-91.20	0.29
-1.00	0.10	-94.07	0.09

Wafer: MEMS-4 B-700-30 (4/6)

	Off-state				On-state 20 V			
Freq-GHz	S22-dB	Stn. Dev.	S22-pha	Stn. Dev.	S22-dB	Stn. Dev.	S22-pha	Stn. Dev
1	-0.13	0.05	-11.60	0.20	-2.67	0.31	-36.42	4.46
2	-0.38	0.04	-21.89	1.10	-5.47	0.72	-50.87	6.98
3	-0.75	0.03	-32.05	1.96	-7.74	1.45	-58.59	5.04
4	-1.25	0.28	-40.40	2.49	-9.30	1.94	-60.15	1.50
5	-1.60	0.47	-48.00	1.11	-9.78	1.28	-63.31	7.10
6	-1.84	0.42	-55.01	0.22	-10.10	0.54	-69.12	6.99
7	-1.95	0.29	-62.62	0.63	-10.52	0.18	-76.71	5.06
8	-2.11	0.22	-70.70	0.51	-11.14	0.07	-83.84	3.39
9	-2.31	0.18	-78.95	0.26	-11.77	0.04	-90.11	2.15
10	-2.58	0.17	-86.95	0.07	-12.41	0.06	-95.55	1.40
11	-2.85	0.18	-94.73	0.06	-12.93	0.06	-100.60	0.86
12	-3.13	0.16	-102.39	0.10	-13.43	0.02	-105.70	0.22
13	-3.41	0.18	-109.92	0.29	-13.92	0.11	-110.48	0.47
14	-3.69	0.18	-117.31	0.40	-14.40	0.16	-115.20	0.85
15	-4.01	0.18	-124.55	0.43	-14.88	0.16	-118.60	1.21
16	-4.30	0.20	-131.68	0.60	-15.26	0.23	-121.69	1.60
17	-4.57	0.22	-138.97	0.84	-15.50	0.33	-125.46	1.69
18	-4.89	0.25	-146.14	0.87	-15.68	0.34	-129.03	1.31
19	-5.28	0.23	-153.03	0.22	-15.73	0.15	-131.94	1.91
20	-5.62	0.05	-159.38	0.13	-15.81	0.00	-137.16	5.21
21	-5.80	0.17	-165.68	1.11	-15.61	0.44	-142.79	3.61
22	-6.10	0.11	-173.08	0.06	-15.86	0.16	-147.50	4.72
23	-6.56	0.13	-177.91	1.48	-16.27	1.06	-152.65	7.33
24	-6.94	0.31	-172.52	2.14	-16.36	0.78	-155.06	4.13
25	-7.50	0.18	-166.93	1.45	-16.35	0.91	-157.92	3.99
26	-7.41	0.30	-164.97	1.22	-15.39	0.34	-165.42	0.64

Wafer: MEMS-4 B-700-40 (2/6)

Off-state

Freq-GHz	S11-dB	Stn. Dev.	S11-pha	Stn. Dev.
1	-0.04	0.00	-5.57	0.11
2	-0.13	0.00	-10.91	0.26
3	-0.28	0.03	-16.05	0.41
4	-0.46	0.06	-20.55	0.29
5	-0.56	0.02	-24.89	0.12
6	-0.66	0.00	-29.64	0.45
7	-0.82	0.02	-34.50	0.72
8	-1.02	0.05	-39.20	0.89
9	-1.26	0.08	-43.64	0.96
10	-1.50	0.11	-47.95	0.96
11	-1.78	0.14	-52.02	0.92
12	-2.04	0.17	-55.77	0.85
13	-2.29	0.18	-59.36	0.75
14	-2.52	0.18	-62.87	0.71
15	-2.76	0.20	-66.54	0.69
16	-2.99	0.21	-69.97	0.63
17	-3.22	0.21	-73.46	0.60
18	-3.47	0.20	-76.96	0.63
19	-3.72	0.17	-80.51	0.54
20	-3.94	0.24	-83.85	0.87
21	-4.22	0.24	-86.82	0.93
22	-4.41	0.27	-90.20	0.67
23	-4.66	0.16	-94.16	0.34
24	-4.96	0.23	-97.57	1.51
25	-5.29	0.18	-100.54	2.15
26	-5.38	0.31	-103.45	0.01

On-state 20 V

S11-dB	Stn. Dev.	S11-pha	Stn. Dev
-1.86	0.11	-18.55	18.25
-4.78	0.52	-28.26	24.27
-6.78	0.82	-33.79	24.67
-7.21	0.38	-37.54	23.74
-6.96	0.25	-43.09	25.61
-7.39	0.14	-50.17	28.58
-8.26	0.17	-57.26	31.48
-9.19	0.40	-63.42	33.37
-10.03	0.55	-68.81	34.64
-10.74	0.65	-73.74	35.51
-11.35	0.71	-78.25	36.18
-11.84	0.72	-82.41	36.83
-12.29	0.72	-86.44	37.55
-12.65	0.70	-90.41	38.24
-13.03	0.70	-94.46	38.80
-13.36	0.68	-98.16	39.24
-13.65	0.70	-101.76	39.42
-13.97	0.72	-105.42	39.63
-14.18	0.62	-109.25	40.10
-14.37	0.46	-113.01	40.37
-14.53	0.56	-115.46	39.57
-14.52	0.44	-119.26	40.43
-14.46	0.13	-122.48	39.70
-14.64	0.51	-127.91	41.39
-14.84	0.54	-130.90	40.78
-14.79	0.17	-135.63	45.50

Off-state

Freq-GHz	S21-dB	Stn. Dev.	S21-pha	Stn. Dev.
1	-23.41	0.29	80.56	0.38
2	-17.25	0.39	70.13	0.21
3	-14.06	0.48	59.69	0.73
4	-12.17	0.31	49.06	2.96
5	-11.34	0.14	42.89	1.57
6	-10.20	0.02	39.81	0.77
7	-8.97	0.19	35.14	0.92
8	-7.90	0.29	29.33	0.46
9	-7.03	0.33	22.85	0.03
10	-6.35	0.33	16.52	0.38
11	-5.76	0.33	10.08	0.70
12	-5.30	0.30	3.92	1.02
13	-4.92	0.28	-1.84	1.16
14	-4.52	0.25	-7.50	1.31
15	-4.18	0.23	-12.74	1.42
16	-3.87	0.21	-18.21	1.42
17	-3.63	0.19	-24.07	1.55
18	-3.39	0.16	-29.10	1.53
19	-3.15	0.12	-34.94	1.29
20	-3.05	0.16	-40.22	1.42
21	-2.93	0.15	-45.44	1.53
22	-2.76	0.07	-50.89	1.78
23	-2.70	0.03	-56.15	0.81
24	-2.53	0.15	-60.54	1.62
25	-2.50	0.11	-66.46	1.02
26	-2.55	0.07	-69.96	1.74

On-state 20 V

S21-dB	Stn. Dev.	S21-pha	Stn. Dev.
-5.73	0.47	64.68	22.84
-3.02	0.44	47.80	31.79
-2.47	0.26	35.48	33.52
-2.71	0.14	25.26	30.69
-2.79	0.34	20.43	30.19
-2.28	0.04	17.89	31.77
-1.78	0.12	13.36	31.72
-1.45	0.15	7.71	31.02
-1.25	0.14	1.68	29.97
-1.13	0.13	-4.13	28.82
-1.04	0.11	-9.94	27.60
-0.97	0.09	-15.46	26.39
-0.92	0.07	-20.68	25.49
-0.85	0.06	-25.87	24.68
-0.81	0.06	-30.70	23.98
-0.77	0.05	-35.66	23.24
-0.77	0.04	-40.96	22.34
-0.77	0.03	-45.55	21.74
-0.78	0.02	-50.62	20.88
-0.81	0.02	-55.43	20.10
-0.84	0.01	-60.04	19.11
-0.83	0.05	-65.17	18.41
-0.90	0.04	-69.64	18.26
-0.83	0.01	-73.77	17.10
-0.91	0.02	-78.79	16.41
-0.90	0.06	-82.68	16.25

Wafer: MEMS-4 B-700-40 (2/6)

Off-state

Freq-GHz	S22-dB	Stn. Dev.	S22-pha	Stn. Dev.
1	-0.07	0.01	-11.62	0.11
2	-0.28	0.03	-22.66	0.52
3	-0.70	0.02	-33.78	1.17
4	-1.47	0.27	-42.66	1.30
5	-1.86	0.24	-47.94	1.23
6	-1.85	0.06	-54.86	1.23
7	-1.88	0.17	-63.19	0.28
8	-2.03	0.18	-71.78	0.46
9	-2.23	0.16	-80.33	0.99
10	-2.51	0.14	-88.59	1.31
11	-2.79	0.12	-96.49	1.56
12	-3.08	0.10	-104.14	1.74
13	-3.35	0.06	-111.69	1.80
14	-3.63	0.04	-119.09	1.77
15	-3.94	0.03	-126.37	1.78
16	-4.21	0.03	-133.52	1.85
17	-4.50	0.02	-140.86	1.68
18	-4.82	0.03	-148.02	1.65
19	-5.24	0.06	-154.75	1.89
20	-5.54	0.12	-161.73	2.33
21	-5.83	0.16	-167.02	1.96
22	-6.11	0.17	-174.95	0.36
23	-6.72	0.31	-179.35	0.13
24	-6.69	0.30	-172.54	2.07
25	-7.34	0.06	-167.66	0.78
26	-7.05	0.44	-162.39	1.50

On-state 20 V

S22-dB	Stn. Dev.	S22-pha	Stn. Dev
-2.04	0.06	-24.55	18.18
-5.54	0.45	-39.32	23.04
-8.66	1.08	-49.25	20.71
-10.70	1.26	-53.68	14.28
-10.01	0.15	-56.04	12.69
-9.92	0.50	-62.70	12.32
-10.43	0.35	-71.23	11.65
-11.17	0.19	-79.50	10.45
-11.87	0.09	-87.23	8.76
-12.57	0.03	-94.36	6.85
-13.12	0.00	-100.99	4.80
-13.64	0.03	-107.42	2.90
-14.13	0.01	-113.73	1.08
-14.59	0.03	-119.97	0.52
-15.09	0.12	-125.38	3.18
-15.49	0.16	-130.58	6.00
-15.77	0.19	-135.90	8.69
-15.97	0.23	-140.94	11.65
-16.04	0.18	-145.45	15.04
-16.34	0.08	-152.80	14.96
-15.81	0.06	-156.73	16.51
-16.30	0.66	-163.26	16.89
-16.39	0.62	-163.00	23.25
-16.32	0.13	-166.17	6.94
-16.49	0.42	-163.90	4.54
-15.96	0.03	-167.65	5.94

Wafer: MEMS-4 B-800

No data

Wafer: MEMS-4 B-800-20 (4/6)

Off-state **On-state 20 V**

Freq-GHz	S11-dB	Stn. Dev.	S11-pha	Stn. Dev.	S11-dB	Stn. Dev.	S11-pha	Stn. Dev
1	-0.04	0.00	-6.20	0.12	-2.19	0.49	-37.07	2.30
2	-0.17	0.00	-12.20	0.29	-5.66	0.75	-52.33	0.16
3	-0.37	0.01	-17.92	0.43	-7.93	0.61	-55.06	2.32
4	-0.62	0.00	-22.87	0.69	-8.60	0.14	-54.75	3.41
5	-0.81	0.04	-27.48	0.91	-8.51	0.22	-61.02	0.95
6	-0.99	0.08	-32.19	0.84	-8.77	0.21	-69.90	1.87
7	-1.18	0.09	-36.93	0.63	-9.27	0.02	-78.51	3.66
8	-1.42	0.07	-41.61	0.49	-9.87	0.26	-85.87	4.26
9	-1.67	0.05	-46.08	0.41	-10.44	0.42	-92.24	4.27
10	-1.94	0.03	-50.35	0.41	-10.97	0.53	-97.85	4.08
11	-2.24	0.01	-54.42	0.43	-11.44	0.61	-102.92	3.84
12	-2.53	0.01	-58.21	0.49	-11.83	0.65	-107.48	3.58
13	-2.81	0.02	-61.74	0.50	-12.18	0.64	-112.09	3.56
14	-3.06	0.02	-65.23	0.53	-12.46	0.62	-116.38	3.58
15	-3.32	0.03	-68.82	0.53	-12.77	0.59	-120.64	3.70
16	-3.58	0.03	-72.22	0.40	-13.03	0.60	-124.44	4.06
17	-3.82	0.04	-75.58	0.43	-13.25	0.54	-128.15	4.29
18	-4.10	0.04	-78.93	0.34	-13.52	0.51	-131.54	4.53
19	-4.37	0.03	-82.22	0.11	-13.66	0.44	-135.45	4.80
20	-4.64	0.03	-85.82	0.04	-13.95	0.40	-139.97	6.49
21	-4.89	0.11	-88.67	0.38	-14.01	0.50	-142.40	6.20
22	-5.20	0.02	-91.63	0.09	-14.08	0.11	-145.04	6.20
23	-5.50	0.20	-95.15	1.67	-14.12	0.76	-148.19	7.01
24	-5.78	0.18	-97.92	2.02	-14.08	0.45	-152.64	8.26
25	-5.93	0.30	-99.90	1.85	-13.88	0.49	-156.49	8.35
26	-6.01	0.38	-105.53	3.20	-14.04	0.88	-166.68	10.11

Wafer: MEMS-4 B-800-20 (4/6)

Off-state

Freq-GHz	S21-dB	Stn. Dev.	S21-pha	Stn. Dev.
1	-21.69	0.05	80.25	0.36
2	-15.50	0.09	69.10	0.49
3	-12.30	0.12	57.95	0.81
4	-10.37	0.26	47.04	1.29
5	-9.36	0.45	38.80	0.22
6	-8.46	0.43	33.17	1.30
7	-7.55	0.28	27.83	2.14
8	-6.72	0.15	22.04	2.18
9	-6.00	0.06	15.90	1.93
10	-5.43	0.01	9.94	1.64
11	-4.92	0.02	3.78	1.31
12	-4.52	0.03	-2.12	1.11
13	-4.18	0.02	-7.64	0.86
14	-3.82	0.02	-13.23	0.75
15	-3.53	0.00	-18.37	0.70
16	-3.25	0.00	-23.74	0.57
17	-3.04	0.01	-29.45	0.52
18	-2.84	0.03	-34.36	0.54
19	-2.65	0.05	-39.98	0.66
20	-2.52	0.02	-45.24	0.84
21	-2.40	0.01	-50.06	0.33
22	-2.31	0.11	-56.25	0.90
23	-2.29	0.07	-61.47	0.41
24	-2.16	0.01	-66.08	0.78
25	-2.28	0.04	-71.30	0.94
26	-2.23	0.30	-74.23	0.76

On-state 20 V

S21-dB	Stn. Dev.	S21-pha	Stn. Dev
-4.69	0.52	45.86	4.27
-2.19	0.06	20.76	3.58
-1.83	0.09	6.60	2.68
-2.00	0.27	-1.68	1.89
-2.11	0.32	-5.85	0.11
-1.92	0.17	-9.37	0.98
-1.66	0.02	-13.50	1.03
-1.45	0.06	-18.11	0.69
-1.28	0.09	-22.86	0.33
-1.17	0.08	-27.46	0.08
-1.07	0.08	-32.10	0.09
-1.00	0.06	-36.58	0.15
-0.94	0.04	-40.95	0.24
-0.86	0.02	-45.45	0.23
-0.81	0.01	-49.69	0.24
-0.77	0.01	-54.03	0.17
-0.78	0.01	-58.67	0.16
-0.77	0.01	-62.74	0.10
-0.77	0.04	-67.19	0.18
-0.79	0.04	-71.52	0.03
-0.81	0.05	-75.41	0.02
-0.85	0.07	-79.95	0.56
-0.97	0.04	-83.96	0.28
-0.93	0.06	-87.94	0.22
-1.00	0.06	-91.91	0.70
-1.00	0.11	-95.26	0.33

Off-state

Freq-GHz	S22-dB	Stn. Dev.	S22-pha	Stn. Dev.
1	-0.07	0.01	-13.03	0.05
2	-0.28	0.04	-25.62	0.12
3	-0.73	0.09	-38.26	0.28
4	-1.49	0.23	-48.85	0.92
5	-2.06	0.19	-56.65	2.61
6	-2.37	0.01	-64.25	3.31
7	-2.58	0.16	-72.28	3.10
8	-2.81	0.24	-80.59	2.53
9	-3.03	0.25	-88.92	2.02
10	-3.31	0.24	-97.13	1.66
11	-3.58	0.20	-105.07	1.35
12	-3.85	0.13	-112.76	1.15
13	-4.11	0.10	-120.37	1.27
14	-4.36	0.05	-127.94	1.31
15	-4.65	0.02	-135.46	1.39
16	-4.94	0.02	-142.69	1.69
17	-5.22	0.04	-150.00	1.93
18	-5.54	0.05	-157.22	2.28
19	-5.90	0.03	-164.16	1.92
20	-6.28	0.17	-171.50	2.07
21	-6.57	0.27	-177.26	2.68
22	-7.09	0.10	-176.08	4.95
23	-7.69	0.18	-171.03	0.99
24	-7.97	0.30	-163.64	2.82
25	-8.51	0.16	-159.80	6.53
26	-8.51	0.24	-155.53	0.34

On-state 20 V

S22-dB	Stn. Dev.	S22-pha	Stn. Dev.
-2.30	0.55	-44.11	2.34
-6.27	1.00	-66.60	0.57
-9.69	1.17	-74.86	4.36
-12.06	0.90	-72.09	10.73
-12.14	0.18	-71.03	11.42
-12.17	0.61	-77.03	8.10
-12.41	0.63	-84.36	5.35
-12.78	0.50	-91.37	4.01
-13.12	0.32	-97.86	3.41
-13.53	0.19	-103.89	3.32
-13.81	0.08	-109.32	3.61
-14.08	0.05	-115.03	4.10
-14.36	0.05	-120.57	4.84
-14.62	0.07	-126.10	5.28
-14.97	0.07	-130.48	5.83
-15.29	0.04	-134.06	6.73
-15.46	0.06	-138.26	6.84
-15.58	0.15	-142.15	6.90
-15.63	0.13	-145.23	6.47
-15.99	0.08	-150.43	8.30
-15.64	0.17	-153.76	8.77
-15.83	0.73	-157.47	7.63
-15.47	0.05	-158.61	5.49
-15.67	0.08	-165.49	8.09
-15.83	0.64	-169.66	10.63
-15.91	0.28	-173.42	5.99

Wafer: MEMS-4 B-800-30 (4/6)

Off-state

Freq-GHz	S11-dB	Stn. Dev.	S11-pha	Stn. Dev.
1	-0.06	0.02	-5.87	0.01
2	-0.15	0.01	-11.39	0.00
3	-0.29	0.04	-16.74	0.09
4	-0.43	0.07	-21.88	0.33
5	-0.61	0.08	-26.93	0.62
6	-0.81	0.07	-31.75	0.84
7	-1.00	0.09	-36.39	1.00
8	-1.22	0.10	-41.09	1.38
9	-1.46	0.09	-45.59	1.71
10	-1.72	0.06	-49.95	1.94
11	-2.00	0.03	-54.17	2.16
12	-2.28	0.01	-58.07	2.27
13	-2.57	0.05	-61.77	2.28
14	-2.83	0.07	-65.32	2.20
15	-3.10	0.10	-68.99	2.06
16	-3.37	0.12	-72.48	1.89
17	-3.62	0.13	-75.95	1.79
18	-3.90	0.15	-79.35	1.68
19	-4.18	0.15	-82.64	1.23
20	-4.46	0.17	-86.38	1.13
21	-4.72	0.10	-89.48	0.78
22	-5.11	0.17	-92.63	0.83
23	-5.32	0.05	-95.82	0.18
24	-5.70	0.11	-99.74	0.86
25	-6.15	0.05	-102.65	1.12
26	-6.36	0.14	-103.62	0.41

On-state 20 V

S11-dB	Stn. Dev.	S11-pha	Stn. Dev
-2.12	0.64	-28.84	8.59
-3.98	1.66	-43.60	5.25
-5.39	1.93	-53.10	2.34
-6.36	1.90	-62.18	1.18
-7.33	1.62	-70.22	2.57
-8.15	1.41	-76.56	2.28
-8.63	1.52	-83.05	2.42
-9.18	1.39	-90.15	3.87
-9.77	1.18	-96.38	4.29
-10.30	0.99	-102.09	4.37
-10.79	0.82	-107.48	4.02
-11.21	0.66	-112.33	3.49
-11.63	0.51	-117.12	2.78
-11.97	0.42	-121.57	1.98
-12.33	0.33	-125.95	1.33
-12.66	0.26	-129.83	0.63
-12.95	0.18	-133.82	0.06
-13.27	0.10	-137.29	0.78
-13.46	0.01	-141.20	1.21
-13.89	0.08	-145.58	3.17
-14.06	0.02	-148.58	3.63
-14.30	0.22	-150.83	3.34
-14.11	0.09	-154.23	3.27
-14.51	0.28	-159.55	5.72
-14.83	0.10	-162.90	6.37
-14.68	0.28	-165.64	6.49

Off-state

Freq-GHz	S21-dB	Stn. Dev.	S21-pha	Stn. Dev.
1	-22.71	0.67	75.66	4.06
2	-16.93	0.73	67.94	0.03
3	-13.92	0.74	59.75	1.27
4	-11.75	0.56	53.14	2.93
5	-10.14	0.35	45.71	3.08
6	-8.92	0.25	38.42	2.49
7	-8.01	0.29	32.04	2.69
8	-7.15	0.19	26.10	3.24
9	-6.40	0.06	19.79	3.17
10	-5.80	0.03	13.71	2.86
11	-5.25	0.09	7.50	2.49
12	-4.81	0.12	1.59	2.05
13	-4.44	0.15	-4.10	1.71
14	-4.05	0.16	-9.80	1.39
15	-3.74	0.16	-14.97	1.14
16	-3.44	0.15	-20.41	0.90
17	-3.20	0.16	-26.18	0.71
18	-2.98	0.16	-31.13	0.57
19	-2.75	0.17	-36.77	0.25
20	-2.62	0.12	-42.17	0.10
21	-2.44	0.11	-47.02	0.28
22	-2.32	0.16	-53.43	0.03
23	-2.37	0.08	-57.90	0.25
24	-2.09	0.06	-62.80	0.03
25	-2.00	0.06	-68.64	0.03
26	-2.17	0.03	-72.91	0.85

On-state 20 V

S21-dB	Stn. Dev.	S21-pha	Stn. Dev.
-7.09	2.81	41.93	1.20
-4.14	1.56	27.58	8.97
-3.09	1.00	16.34	8.68
-2.45	0.52	8.99	8.33
-1.99	0.24	1.69	6.56
-1.76	0.19	-4.94	4.98
-1.64	0.22	-10.08	4.87
-1.44	0.09	-15.06	4.68
-1.29	0.01	-20.19	4.07
-1.19	0.02	-25.00	3.52
-1.09	0.05	-29.82	3.03
-1.02	0.06	-34.43	2.61
-0.96	0.05	-38.95	2.30
-0.89	0.06	-43.53	2.04
-0.84	0.06	-47.77	1.86
-0.79	0.05	-52.19	1.69
-0.79	0.05	-56.83	1.51
-0.78	0.05	-60.98	1.34
-0.76	0.06	-65.44	1.30
-0.79	0.06	-69.84	1.07
-0.79	0.06	-73.88	0.92
-0.84	0.08	-78.39	0.49
-0.88	0.06	-81.94	0.92
-0.87	0.06	-86.36	0.80
-0.88	0.06	-90.70	0.57
-0.94	0.03	-93.96	0.36

Wafer: MEMS-4 B-800-30 (4/6)

Off-state **On-state 20 V**

Freq-GHz	S22-dB	Stn. Dev.	S22-pha	Stn. Dev.	S22-dB	Stn. Dev.	S22-pha	Stn. Dev
1	-0.20	0.11	-12.06	0.84	-2.56	0.51	-32.84	11.73
2	-0.40	0.02	-22.61	1.94	-4.76	1.91	-48.81	10.03
3	-0.74	0.03	-33.02	2.78	-6.63	2.37	-58.76	8.00
4	-1.06	0.19	-41.85	3.51	-7.95	2.69	-65.73	4.94
5	-1.33	0.29	-51.34	3.25	-8.99	2.50	-73.44	2.31
6	-1.71	0.26	-60.43	3.04	-10.10	2.16	-79.44	1.83
7	-2.08	0.25	-68.25	4.01	-10.78	2.22	-83.40	3.27
8	-2.33	0.38	-76.18	4.29	-11.30	2.31	-88.86	1.97
9	-2.58	0.46	-84.27	3.98	-11.79	2.19	-94.28	0.82
10	-2.88	0.50	-92.16	3.69	-12.30	2.04	-99.41	0.25
11	-3.16	0.51	-99.85	3.35	-12.68	1.86	-104.13	0.30
12	-3.45	0.51	-107.43	2.97	-13.08	1.75	-109.13	0.62
13	-3.74	0.45	-114.90	2.65	-13.48	1.53	-114.00	0.77
14	-4.03	0.41	-122.27	2.51	-13.83	1.39	-118.77	0.75
15	-4.36	0.37	-129.49	2.55	-14.27	1.28	-122.48	0.61
16	-4.65	0.36	-136.54	2.20	-14.59	1.13	-125.60	1.22
17	-4.93	0.32	-143.70	2.01	-14.81	0.94	-129.31	1.09
18	-5.24	0.27	-150.82	1.54	-14.95	0.75	-133.25	1.06
19	-5.61	0.17	-157.87	1.93	-15.11	0.75	-136.52	0.56
20	-6.03	0.26	-164.98	1.83	-15.56	0.75	-140.35	2.25
21	-6.28	0.29	-171.37	0.85	-15.35	0.27	-144.60	2.70
22	-6.88	0.10	-177.59	0.66	-15.46	0.24	-147.19	1.01
23	-6.92	0.23	-177.57	1.98	-14.92	0.47	-154.24	0.95
24	-7.57	0.12	-168.95	0.96	-15.59	0.06	-155.93	1.66
25	-8.12	0.04	-162.74	0.16	-15.71	0.25	-158.85	1.09
26	-8.11	0.46	-160.58	1.97	-14.90	0.14	-166.06	3.50

Wafer: MEMS-4 B-800-40 (4/6)

Off-state

Freq-GHz	S11-dB	Stn. Dev.	S11-pha	Stn. Dev.
1	-0.10	0.05	-7.32	1.81
2	-0.25	0.10	-13.59	2.76
3	-0.48	0.19	-19.75	3.95
4	-0.70	0.25	-24.96	4.41
5	-0.90	0.29	-30.30	5.24
6	-1.13	0.38	-35.15	5.68
7	-1.32	0.45	-39.80	5.61
8	-1.49	0.45	-44.31	5.02
9	-1.65	0.35	-48.73	4.52
10	-1.81	0.21	-53.22	4.36
11	-2.00	0.07	-57.73	4.44
12	-2.21	0.06	-62.05	4.65
13	-2.46	0.14	-66.11	4.84
14	-2.70	0.21	-69.92	4.94
15	-2.95	0.27	-73.52	4.69
16	-3.19	0.34	-76.88	4.29
17	-3.41	0.42	-80.20	3.87
18	-3.66	0.51	-83.46	3.35
19	-3.84	0.63	-86.32	2.10
20	-4.05	0.82	-90.00	2.15
21	-4.32	0.84	-93.09	1.45
22	-4.62	1.01	-95.92	0.71
23	-4.79	1.09	-98.61	0.03
24	-5.16	1.21	-101.30	1.47
25	-5.51	1.30	-104.00	2.11
26	-5.69	1.44	-105.47	2.29

On-state 20 V

S11-dB	Stn. Dev.	S11-pha	Stn. Dev
-2.50	0.22	-30.25	1.23
-4.44	0.08	-40.99	2.19
-5.80	0.14	-48.14	2.18
-6.46	0.23	-53.95	2.66
-7.00	0.21	-60.74	2.73
-7.39	0.05	-66.70	4.30
-7.66	0.03	-73.29	7.78
-7.92	0.36	-79.86	11.69
-8.21	0.92	-86.18	14.11
-8.51	1.39	-92.41	15.03
-8.85	1.75	-98.23	15.45
-9.21	2.00	-103.45	15.87
-9.57	2.17	-108.38	16.47
-9.90	2.28	-112.70	17.41
-10.26	2.33	-116.65	18.73
-10.58	2.42	-119.90	20.37
-10.84	2.53	-123.30	22.25
-11.14	2.71	-126.39	23.86
-11.52	2.50	-129.17	25.98
-11.66	2.86	-130.36	30.78
-11.77	3.03	-134.59	31.84
-12.21	3.16	-135.77	33.98
-12.11	2.81	-136.16	37.54
-12.46	3.02	-139.93	38.65
-12.60	3.12	-142.31	39.69
-12.67	2.95	-140.97	47.19

Off-state

Freq-GHz	S21-dB	Stn. Dev.	S21-pha	Stn. Dev.
1	-21.97	0.03	75.67	1.89
2	-16.25	0.05	64.19	2.33
3	-13.44	0.08	54.37	2.91
4	-11.54	0.07	46.51	2.49
5	-10.25	0.06	38.67	2.99
6	-9.31	0.00	31.93	3.74
7	-8.53	0.04	26.29	5.49
8	-7.81	0.29	20.84	6.90
9	-7.18	0.60	15.18	7.22
10	-6.64	0.83	9.90	6.63
11	-6.14	0.98	4.45	5.83
12	-5.70	1.06	-0.87	5.05
13	-5.31	1.11	-6.01	4.26
14	-4.91	1.15	-11.32	3.68
15	-4.59	1.15	-16.20	3.12
16	-4.28	1.15	-21.36	2.69
17	-4.03	1.17	-26.82	2.24
18	-3.81	1.16	-31.47	1.79
19	-3.47	1.02	-36.77	1.65
20	-3.40	1.15	-42.69	2.01
21	-3.18	1.14	-47.06	1.43
22	-3.02	1.16	-53.34	1.22
23	-3.01	1.11	-58.16	1.78
24	-2.72	1.02	-63.04	0.92
25	-2.64	0.98	-68.50	0.10
26	-2.68	0.82	-73.34	1.73

On-state 20 V

S11-dB	Stn. Dev.	S21-pha	Stn. Dev.
-6.42	0.61	38.99	3.59
-4.28	0.62	22.22	0.85
-3.53	0.61	10.88	0.98
-3.24	0.58	4.32	0.27
-2.94	0.47	-1.65	0.60
-2.79	0.43	-6.79	1.35
-2.60	0.48	-11.08	2.40
-2.39	0.64	-15.40	2.74
-2.16	0.75	-20.03	2.35
-1.99	0.78	-24.54	1.78
-1.83	0.75	-29.25	1.54
-1.69	0.71	-33.99	1.55
-1.59	0.69	-38.67	1.63
-1.50	0.69	-43.48	1.86
-1.44	0.67	-47.88	1.97
-1.37	0.67	-52.44	2.21
-1.36	0.69	-57.27	2.48
-1.34	0.71	-61.60	2.72
-1.29	0.65	-66.22	2.63
-1.37	0.71	-71.45	3.92
-1.41	0.81	-75.38	3.94
-1.44	0.83	-80.42	4.10
-1.45	0.83	-85.15	5.66
-1.52	0.88	-88.49	4.22
-1.65	1.01	-92.50	3.72
-1.62	0.94	-97.36	6.17

Wafer: MEMS-4 B-800-40 (4/6)

Off-state

Freq-GHz	S22-dB	Stn. Dev.	S22-pha	Stn. Dev.
1	-0.17	0.01	-12.83	0.11
2	-0.49	0.01	-23.95	0.18
3	-0.95	0.04	-34.78	0.29
4	-1.48	0.11	-43.48	0.43
5	-1.87	0.18	-52.02	0.98
6	-2.30	0.23	-59.82	2.09
7	-2.59	0.13	-66.97	3.33
8	-2.81	0.05	-74.32	3.62
9	-3.00	0.16	-82.04	3.12
10	-3.24	0.16	-89.68	2.59
11	-3.45	0.11	-97.24	2.29
12	-3.66	0.02	-104.95	2.34
13	-3.91	0.05	-112.77	2.53
14	-4.17	0.13	-120.40	2.98
15	-4.47	0.22	-127.90	3.66
16	-4.74	0.26	-135.30	4.39
17	-4.99	0.31	-142.93	5.46
18	-5.25	0.31	-150.77	6.72
19	-5.64	0.26	-158.40	6.47
20	-6.03	0.58	-166.44	8.83
21	-6.34	0.35	5.77	243.18
22	-6.91	0.31	-2.22	242.02
23	-6.87	0.62	-10.78	238.83
24	-7.95	0.27	-10.86	230.15
25	-8.77	0.13	-12.32	220.87
26	-8.29	0.23	-14.39	210.28

On-state 20 V

S22-dB	Stn. Dev.	S22-pha	Stn. Dev
-2.84	0.06	-35.01	2.70
-5.22	0.55	-47.89	2.14
-7.12	0.85	-56.42	0.61
-8.36	1.14	-60.72	2.14
-9.08	1.20	-66.67	5.59
-9.69	1.05	-72.03	8.95
-10.02	0.70	-78.09	10.69
-10.34	0.54	-85.23	10.92
-10.71	0.59	-92.80	11.55
-11.20	0.68	-99.98	13.36
-11.61	0.72	-107.14	15.83
-12.08	0.68	-114.54	18.95
-12.68	0.51	-121.85	22.39
-13.27	0.29	-128.88	26.11
-13.92	0.06	-135.06	30.19
-14.62	0.66	-141.59	34.85
-15.40	1.52	-148.60	40.09
-16.24	2.58	-149.40	34.98
-17.16	3.38	-150.83	30.46
-18.24	4.39	-136.87	10.05
-20.22	7.68	-135.76	0.90
-22.36	10.41	-116.74	30.08
-20.55	7.36	-103.99	59.79
-24.93	13.62	-98.22	67.02
-19.52	6.18	-116.23	47.90
-20.51	7.42	-112.08	69.87